Coden: JPLPAY
Volume 9, Part A-2, No. 2, February 1971

Journal of Polymer Science
Part A-2: Polymer Physics

Contents

Published by INTERSCIENCE PUBLISHERS a division of John Wiley & Sons, Inc.

Journal of Polymer Science **Part A-2: Polymer Physics**

The Journal of Polymer Science is published in four sections as follows: Part A-1, Polymer Chemistry, monthly; Part A-2, Polymer Physics, monthly; Part B, Polymer Letters, monthly; Part C, Polymer Symposia, irregular.

Published monthly by Interscience Publishers, a Division of John Wiley & Sons, Inc., covering one volume annually. Publication Office at 20th and Northampton Sts., Easton, Pa. 18042. Executive, Editorial, and Circulation Offices at 605 Third Avenue, New York, N.Y. 10016. Second-class postage paid at Easton, Pa. Subscription price, $325.00 per volume (including Parts A-1, B, and C). Foreign postage $15.00 per volume (including Parts A-1, B, and C).

JOURNAL OF POLYMER SCIENCE: PART A-2 VOL. 9, 193–208 (1971)

Structure and Optical Activity of a Crystalline Modification of Isotactic Poly-(S)-4-methyl-1-hexene

I. W. BASSI, *S. p.A. Montecatini-Edison, Milan, Italy*, O. BONSIGNORI, G. P. LORENZI, and P. PINO, *Technisch-Chemisches Laboratorium, Eidg. Technische Hochschule, Zürich, Switzerland*, and P. CORRADINI and P. A. TEMUSSI, *Istituto Chimico, Università di Napoli, Italy*

Synopsis

The results of an x-ray and polarimetric study of a crystalline modification (form I) of isotactic poly-(S)-4-methyl-1-hexene are reported and discussed. The x-ray fiber spectra of this polymer are practically indistinguishable from those of isotactic poly-(R)-(S)-4-methyl-1-hexene. Although the crystal structure of the latter can be described on the basis of helices of different screw sense packed in a $P\bar{4}$ space group, the crystal structure of poly-(S)-4-methyl-1-hexene is better described on the basis of a $P1$ space group. The conclusion of the x-ray investigation, that in the crystals of the optically active polymer an equal number of right-handed and left-handed helices must be present, is supported by the polarimetric measurements, which have shown that the polymer in the crystalline form I possesses a rather low rotatory power.

INTRODUCTION

Preliminary x-ray studies[1] have revealed a strong similarity between the fiber spectra of isotactic specimens of poly-(S)-4-methyl-1-hexene (henceforth called SPMH) and poly-(R)(S)-4-methyl-1-hexene (henceforth called PMH). In turn, the spectrum of PMH has previously[2] been shown to be like that of isotactic poly-4-methyl-1-pentene (PMP), whose crystal structure has been preliminarily described[3] on the basis of 7/2 helices packed in a $P\bar{4}$ space group.

The $P\bar{4}$ space group is possible in principle for PMH; in fact, owing to the stereoselectivity of the catalytic systems which have been used for the polymerization of the racemic monomer,[4] macromolecules formed predominantly by (R) or (S) monomeric units are present in such a polymer, and therefore the chains can assume truly enantiomorphic helical conformations. On the contrary, the $P\bar{4}$ space group is not consistent, in principle, with SPMH because, in this case, a right-handed and a left-handed helical chain are not mirror images.

Measurements[5] of optical activity in crystalline vinyl polymers have stimulated our interest to investigate in more detail the crystalline structure of isotactic SPMH. In fact, if the chain conformation in the crystalline

state is known, the comparison of the optical activity in the crystalline state and in solution may give useful indications on the conformation in solution. It appeared possible, therefore, to check the validity of hypotheses concerning the conformational equilibria for SPMH in solution, which have been put forward previously.[6] Moreover, SPMH seemed particularly well suited for a study of the packing of crystalline isotactic polymers characterized by complex helices. This problem, first tackled by Frank, Keller, and O'Connor[3] and later by Noether,[7] has been recently discussed to some length by Corradini[8] on the basis of close packing considerations.

The present paper reports the results of an x-ray and polarimetric study of a crystalline modification of isotactic SPMH. Since the fiber spectrum of SPMH bears a very close resemblance to the spectrum of PMP, the results of a reinvestigation of the crystalline structure of the latter polymer are also included.

RESULTS AND DISCUSSION

Poly-4-methyl-1-pentene

The x-ray fiber photographs of isotactic PMP can be interpreted on the basis of a tetragonal unit cell with the axes (a = 18.66 Å; c = 13.80 Å) given by Frank, Keller and O'Connor.[3] On the other hand, the number of well defined reflections which can be observed in our x-ray photographs is consistently larger than was utilized by Frank et al.[3]

These improved experimental data can be used not only for a refinement of the structure proposed by Frank et al.[3] but also to test with complete

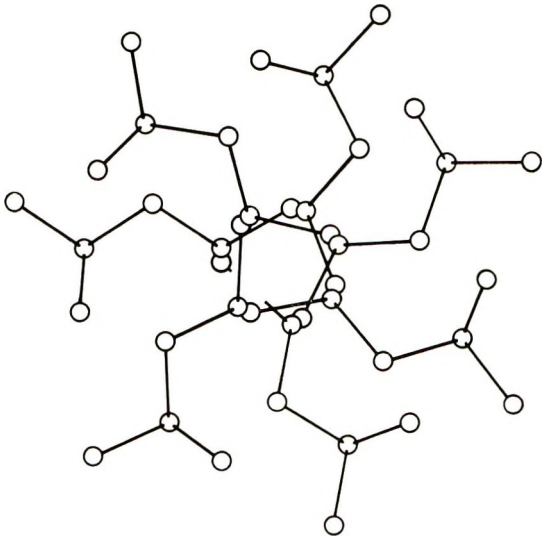

Fig. 1. End view of the molecular model of a chain of poly-4-methyl-1-pentene.

structure factor calculations, the possibility discussed by the above authors[3] of packing in the $P4$ space group rather than in the proposed $P\bar{4}$ group.

A reliable molecular model can be built by taking into account the data on internal conformational parameters which have become available in the last few years from structural work on polymers[9] and on model compounds.[10] In conformity with the studies cited, the two C—C—C valence angles along the chain ϕ_1 for 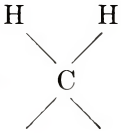 and ϕ_2 for 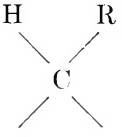 were assumed to be respectively 113° and 110°.

The two internal rotation angles σ_1 and σ_2 which characterize the chain conformation were calculated[11] with the assumption that the C–C distances are all 1.54 Å and by using the experimental value 13.80/7 for p, the identity period of the monomeric unit, and $4\pi/7$ for θ, the rotation about the helix axis. The following values were found:

$$\sigma_1 = 72°30', \ \sigma_2 = 193° \begin{cases} \theta = 103°22' \\ p = 1.970 \text{ Å} \end{cases}$$

Similar values of the internal coordinates were used for the side group. It can be seen from Figure 1 that in the chosen conformation all the carbon atoms of the side group not directly bonded to the main chain are placed as far away as possible from the chain skeleton.

On trying to fit four chains like that shown in Figure 1 in the experimental unit cell, even very simple packing considerations, based on the order of magnitude of closest contact distances between atoms belonging to adjacent chains, show that the $P4$ space group must be rejected. The data reported in Table II show the satisfactory agreement between observed intensities and structure factors calculated by using the coordinates reported in Table I, obtained in the case of the $P\bar{4}$ group.

No further attempts were made to improve the calculations by means of slight modifications of the molecular model.

TABLE I

Fractional Coordinates of One Monomeric Unit of Poly-4-methyl-1-pentene Employed in the Calculations of Table II[a]

	x/a	y/b	z/c
C_1	0.250	0.306	0.925
C_2	0.264	0.307	0.038
C_3	0.304	0.373	0.067
C_4	0.255	0.439	0.045
C_5	0.193	0.441	0.119
C_6	0.300	0.507	0.054

[a] The coordinates of the other six monomeric units are generated through the operation of a local 7/2 screw axis.

TABLE II
Comparison between Observed Intensities I and the Calculated NF_c^2 (where n is the Multiplicity of the Reflection) for Poly-4-methyl-1-pentene, B = 8 Å^2

h	k	l	I	nF_c^2 ($P\bar{4}$)	h	k	l	I	nF_c^2 ($P\bar{4}$)
1	0	0		1	10	1	0		23
1	1	0		2	10	2	0		20
2	0	0	vs	763	9	5	0		8
2	1	0		2	10	3	0		16
2	2	0	m	127	1	0	1		2
3	0	0		—	1	1	1		4
3	1	0		—	2	0	1	vw	12
3	2	0		2	2	1	1	w	88
4	0	0	w	44	2	2	1	w	174
4	1	0		2	3	0	1		48
3	3	0		—	3	1	1	m	218
4	2	0	ms	170	3	2	1	ms	706
5	0	0	vw	1	4	0	1		70
4	3	0		2	4	1	1	m	230
5	1	0		1	3	3	1		24
5	2	0		11	4	2	1		32
4	4	0	w	75	5	0	1		6
5	3	0		—	4	3	1		6
6	0	0	vw	18	5	1	1		20
6	1	0		3	5	2	1		8
6	2	0		18	4	4	1		14
5	4	0		1	5	3	1		10
6	3	0		4	6	0	1		5
7	0	0		7	6	1	1		26
7	1	0		1	6	2	1	vvw	62
5	5	0		—	5	4	1		18
6	4	0		—	1	0	2		28
7	2	0		14	1	1	2	w	2
7	3	0		2	2	0	2		2
6	5	0	vw	5	2	1	2	vs	1428
8	0	0		6	2	2	2		4
8	1	0	w	4	3	0	2	vw	180
7	4	0		6	3	1	2		18
8	2	0		17	3	2	2	mw	380
6	6	0		19	4	0	2		32
8	3	0		3	4	1	2	w	34
7	5	0		8	3	3	2		68
8	4	0	vw	36	4	2	2	w	68
9	0	0		1	5	0	2	mw	184
9	1	0		9	4	3	2		164
9	2	0		—	5	1	2		60
7	6	0		2	5	2	2	vw	258
8	5	0		10	4	4	2		96
9	3	0		9	5	3	2		112
9	4	0		24	6	0	2		7
7	7	0		14	6	1	2		22
10	0	0		14	6	2	2		70
8	6	0		24	5	4	2		54

TABLE II (*continued*)

h	k	l	I	nF_c^2 ($P\bar{4}$)	h	k	l	I	nF_c^2 ($P\bar{4}$)
1	0	3		—	4	2	4		18
1	1	3	ms	726	5	0	4		36
2	0	3	s	578	4	3	4		81
2	1	3		—	5	1	4		66
2	2	3		16	5	2	4		46
3	0	3		7	4	4	4		62
3	1	3	mw	212	5	3	4		15
3	2	3		22	6	0	4		1
4	0	3		6	6	1	4		20
4	1	3		30	6	2	4		11
3	3	3		2	5	4	4		19
4	2	3	vw	4	1	0	5		2
5	0	3		10	1	1	5		1
4	3	3		10	2	0	5		—
5	1	3		13	2	1	5	s	315
5	2	3		3	2	2	5		—
4	4	3		2	3	0	5		6
5	3	3		12	3	1	5	vw	2
6	0	3		5	3	2	5		6
6	1	3		1	4	0	5		4
6	2	3		6	4	1	5	vw	—
5	4	3		9	3	3	5		11
1	0	4		—	4	2	5		22
1	1	4	ms	152	5	0	5		—
2	0	4	w	134	4	3	5		2
2	1	4		2	5	1	5		23
2	2	4		11	5	2	5		2
3	0	4		6	4	4	5		46
3	1	4	vw	42	5	3	5		52
3	2	4		32	6	0	5		4
4	0	4		3	6	1	5		2
4	1	4	vw	61	6	2	5		23
3	3	4		—	5	4	5		3

Poly-(S)-4-methyl-1-hexene and poly-(R)(S)-4-methyl-1-hexene

Two different crystalline modifications have been observed for SPMH. One of them (form I, Fig. 2) is present in melt-spun fibers and in powders prepared by finely grinding polymer samples obtained by slow cooling from the molten state. As is shown by Figure 2, such a modification has a crystal structure similar to that of the polymer of the racemic monomer (PMH). The second modification (form II, Fig. 3) has been detected in samples obtained by precipitation from benzene solutions with methanol. The latter modification changes into form I by heating at temperatures slightly above 120°C. Our present study concerns only form I; the structural features of form II are still under investigation.

The fiber spectra of PMH and SPMH are practically indistinguishable and resemble very closely that of PMP. All the experimental reciprocal

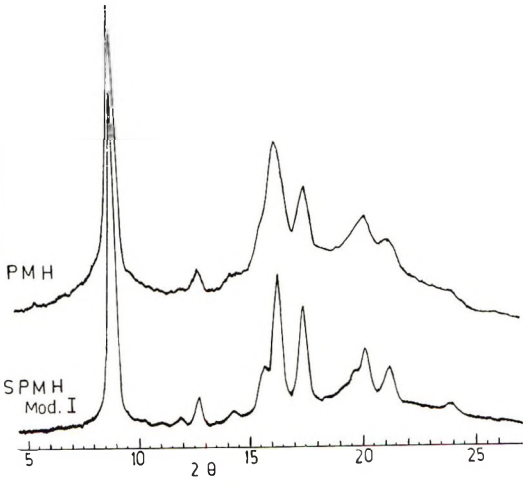

Fig. 2. Geiger counter recorded x-ray powder spectra (CuKα) of poly-(S)-4-methyl-1-hexene, form I, (SPMH, Mod. I), and of poly-(R)(S)-4-methyl-1-hexene (PMH).

distances can be interpreted on the basis of a tetragonal unit cell characterized by the following parameters: $a = b = 19.85$ Å; $c = 13.50$Å. Such a result holds true within experimental error both for PMH and SPMH, form I. Also, the values of the intensities can be considered to be the same in the spectra of both polymers.

The molecular model, apart from the additional methylene group, has been built by using the same values for bond lengths and valence angles as were used for PMP. The following internal rotation angles (around the chain bonds) are consistent with the repetition of seven monomeric units in two pitches and with an identity period per monomeric unit of 1.93 Å:

$$\sigma_1 = 72°30', \sigma_2 = 196° \begin{cases} \theta = 102°24' \\ p = 1.933 \text{ Å} \end{cases}$$

A schematic model is shown in Figure 4. This model has been tested for the $P\bar{4}$ space group by means of structure factor calculations. The coordinates of one monomeric unit are reported in Table III. The structure factor calculation is reported in Table IV. The calculation, which implies the existence in equal amounts of macromolecules (R) made up of monomeric units spiraled in the right-handed sense and of macromolecules (S) made up of monomeric units spiraled in the left-handed sense, appears to be acceptable as far as the accord between calculated and observed intensities is concerned. However, this calculation is not consistent with the identical configuration of the asymmetric carbon atoms in the side chains of the optically active polymer. Also, for the polymer of the racemic monomer, the model chosen would imply complete stereoselectivity of the polymerization process. This is because, in principle, in this $P\bar{4}$ space group calculation, helices of opposite screw sense should be built up of monomeric units having opposite chirality. These considerations prompted

TABLE III
Fractional Coordinates of One Monomeric Unit of
Poly-4-methyl-1-hexene Employed in the Calculations of Table IV[a]

	x/a	y/b	z/c
C_1	0.250	0.303	0.925
C_2	0.263	0.304	0.038
C_3	0.302	0.368	0.067
C_4	0.255	0.430	0.045
C_5	0.196	0.432	0.119
C_6	0.298	0.495	0.054
C_7	0.358	0.493	0.980

[a] The coordinates of the other six monomeric units are generated through the operation of a local 7/2 screw axis.

us to perform further calculations, in which more appropriate and still consistent symmetries of the unit cell were taken into account.

For SPMH a structure factors calculation was tried by using, for the atoms of the main chain, coordinates consistent with the $P\bar{4}$ space group while for the side group of all four helices the coordinates correspond to only one of the two possible configurations (thus reducing the actual symmetry of the unit cell to *P1*). For PMH a calculation was performed for the $P\bar{4}$ space group, allowing for a statistical distribution of the configurations. It can be seen from Table V that these last calculations do give better agreement than the previous one. It is gratifying that the two structures (*P1* for SPMH and $P\bar{4}$ for PMH) give rise to practically identical calculated intensities, in accordance with our previously reported experimental remarks.

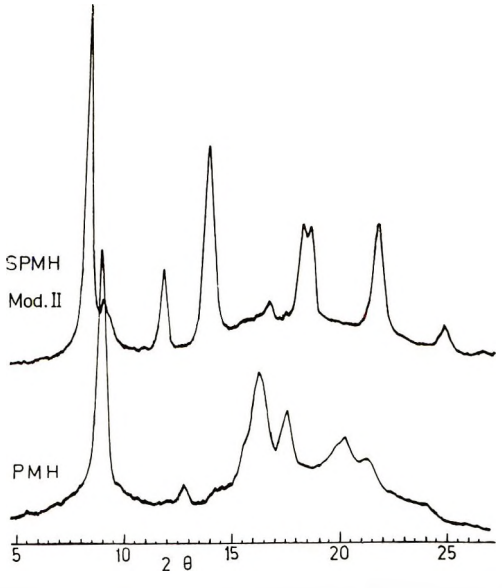

Fig. 3. Geiger counter recorded x-ray powder spectra (CuKα) of poly-(S)-4-methyl-1-hexene, form II, (SPMH, Mod. II), and of poly-(R)(S)-4-methyl-1-hexene (PMH).

TABLE IV
Comparison between Observed Intensities I and Calculated nF_c^2 (where n is the Multiplicity of the Reflection) for Poly(R)(S)-4-methyl-1-hexene, B = 8 Å^2.

h	k	l	I	nF_c^2 ($P4$)	h	k	l	I	nF_c^2 ($P4$)
1	0	0		—	10	1	0		12
1	1	0		—	10	2	0		42
2	0	0	vs	673	9	5	0		4
2	1	0		—	10	3	0		27
2	2	0	m	60	1	0	1		1
3	0	0		1	1	1	1		4
3	1	0		—	2	0	1		13
3	2	0		5	2	1	1	vw	119
4	0	0	w	92	2	2	1	vw	137
4	1	0		28	3	0	1		65
3	3	0		—	3	1	1	mw	227
4	2	0	ms	286	3	2	1	s	849
4	3	0	vw	49	4	0	1		98
5	0	0		26	4	1	1	mw	302
5	1	0		—	3	3	1		66
5	2	0		31	4	2	1		24
4	4	0		66	4	3	1		24
5	3	0		—	5	0	1		5
6	0	0		9	5	1	1		16
6	1	0		6	5	2	1		40
6	2	0		10	4	4	1		12
5	4	0		—	5	3	1		26
6	3	0		—	6	0	1		22
7	0	0		10	6	1	1		20
7	1	0		—	6	2	1		62
5	5	0		—	5	4	1		38
6	4	0		3	1	0	2		114
7	2	0		7	1	1	2	vvw	—
7	3	0		2	2	0	2		—
6	5	0		36	2	1	2	vs	1740
8	0	0		—	2	2	2		8
8	1	0		16	3	0	2	w	188
7	4	0		20				diff.	
8	2	0		—	3	1	2		24
6	6	0		2	3	2	2		364
8	3	0		7	4	0	2	w	11
7	5	0		2				diff.	
8	4	0		13	4	1	2		32
9	0	0		—	3	3	2		99
9	1	0		3	4	2	2	mw	50
9	2	0		2				diff.	
7	6	0		4	4	3	2		200
8	5	0		7	5	0	2		254
9	3	0		3	5	1	2	w	122
9	4	0		29	5	2	2		338
7	7	0		7	4	4	2		96
10	0	0	w	24	5	3	2		144
8	6	0		47	6	0	2		5

TABLE IV (*continued*)

h	k	l	I	nF_c^2 ($P\bar{4}$)	h	k	l	I	nF_c^2 ($P\bar{4}$)
6	1	2		22	4	1	3		34
6	2	2		38	3	3	3		—
5	4	2		62	4	2	3		14
1	0	3		—	4	3	3		7
1	1	3	s	1208	5	0	3		5
2	0	3	s	270	5	1	3		8
2	1	3		4	5	2	3		8
2	2	3		8	4	4	3		2
3	0	3		18	5	3	3		2
3	1	3	w	250	6	0	3		32
3	2	3		39	6	1	3		13
					6	2	3		23
4	0	3		102	5	4	3		45

Optical Activity of Crystalline Poly-(S)-4-methyl-1-hexene

The optical activity of crystalline SPMH has proved to be remarkably dependent upon the type of crystalline structure and the degree of crystallinity.

The dependence of the optical activity of the polymer on the type of crystalline structure is evident from the data of Table VI, which refer to a specimen in which the relative content of form I was gradually raised by annealing at suitable temperatures. The gradual transition of form II to form I (indicated in Table VI by the increase of the ratio between the intensities

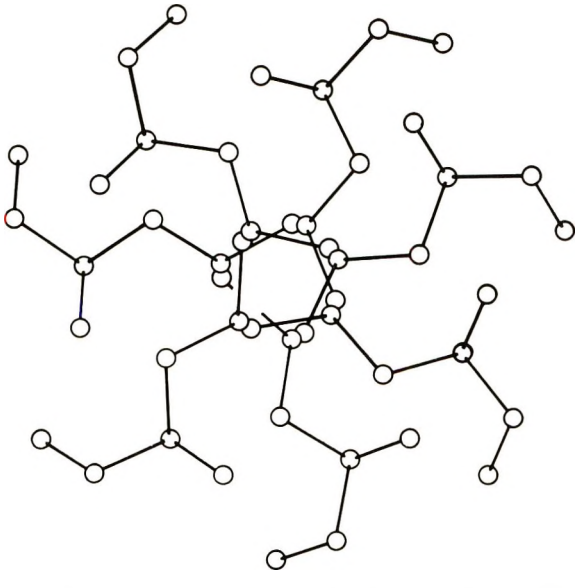

Fig. 4. End view of the molecular model of a chain of poly-(S)-4-methyl-1-hexene, form I.

TABLE V

Comparison between Observed Intensities I and Calculated nF_c^2 for Poly-(R) (S)-4-methyl-1-hexene ($P\bar{4}$, Statistical Distribution of the Configurations of the Side Groups) and for Poly-(S)-4-methyl-1-hexene, form I (*P1*, pseudo $P\bar{4}$, all S Configurations of the Side Groups), $B = 8$ Å^2

h	k	l	I	nF_c^2 ($P\bar{4}$, statistical)	nF_c^2 (*P1*)	h	k	l	I	nF_c^2 ($P\bar{4}$ statistical)	nF_c^2 (*P1*)
1	0	0		—	—	7	7	0		15	15
1	1	0		—	—	10	0	0	w	24	25
2	0	0	vs	677	677	8	6	0		47	47
2	1	0		—	—	10	1	0		13	13
2	2	0	m	59	59	10	2	0		42	42
3	0	0		—	1	9	5	0		9	9
3	1	0		—	—	10	3	0		24	24
3	2	0		4	6	1	0	1		2	1
4	0	0	w	92	93	1	1	1		3	4
4	1	0		20	22	2	0	1		6	6
3	3	0		—	—	2	1	1	vw	188	216
4	2	0	ms	287	288	2	2	1	vw	72	72
4	3	0	vw	36	37	3	0	1		115	124
5	0	0		19	20	3	1	1	mw	128	216
5	1	0		—	—	3	2	1	s	857	861
5	2	0		21	22	4	0	1		72	72
4	4	0		68	68	4	1	1	mw	280	282
5	3	0		—	—	3	3	1		59	61
6	0	0		10	10	4	2	1		28	30
6	1	0		3	2	4	3	1		23	33
6	2	0		10	9	5	0	1		5	9
5	4	0		—	—	5	1	1		30	38
6	3	0		—	—	5	2	1		33	38
7	0	0		10	9	4	4	1		32	38
7	1	0		1	6	5	3	1		32	53
5	5	0		—	—	6	0	1		18	19
6	4	0		3	2	6	1	1		20	24
7	2	0		6	6	6	2	1		56	59
7	3	0		2	3	5	4	1		34	35
6	5	0		27	26	1	0	2		24	50
8	0	0		—	—	1	1	2	vvw	—	—
8	1	0		15	14	2	0	2		—	—
7	4	0		17	16	2	1	2	vs	1763	1765
8	2	0		—	—	2	2	2		—	7
6	6	0		2	3	3	0	2	w	233	239
8	3	0		6	6				diff.		
7	5	0		4	5	3	1	2		7	8
8	4	0		13	10	3	2	2		426	436
9	0	0		—	—	4	0	2	w	2	13
9	1	0		10	10				diff.		
9	2	0		2	2	4	1	2		33	33
7	6	0		3	3	3	3	2		42	44
8	5	0		6	6	4	2	2	w	24	52
9	3	0		10	9				diff.		
9	4	0		25	25						

TABLE V (*continued*)

h	*k*	*l*	*I*	nF_c^2 ($P\bar{4}$, statistical)	nF_c^2 (*P1*)	*h*	*k*	*l*	*I*	nF_c^2 ($P\bar{4}$ statistical)	nF_c^2 (*P1*)
4	3	2		164	173	3	1	3	w	222	252
5	0	2		198	200	3	2	3		25	57
5	1	2	w	66	79	4	0	3		38	38
5	2	2		268	284	4	1	3		22	42
4	4	2		76	85	3	3	3		—	6
5	3	2		107	116	4	2	3		4	4
6	0	2		3	7	4	3	3		4	6
6	1	2		22	23	5	0	3		3	5
6	2	2		56	63	5	1	3		8	9
5	4	2		72	72	5	2	3		5	7
1	0	3		—	—	4	4	3		—	—
1	1	3	s	1179	1199	5	3	3		2	6
2	0	3	s	566	567	6	0	3		10	11
2	1	3		2	3	6	1	3		10	10
2	2	3		18	18	6	2	3		6	7
3	0	3		6	14	5	4	3		20	31

of the diffraction peaks at $2\theta = 9.0°$ and $2\theta = 8.3°$ which are characteristic of form I and form II, respectively) is accompanied by a marked decrease of the polymer optical activity which eventually reaches a constant value. At this stage, as revealed by the x-ray diffraction spectrum, form II is no longer present and, therefore, the rotatory power derives only from the contributions of the amorphous phase and of form I.

The contribution of form I to the polymer optical activity could be evaluated through examination of additional specimens crystallized in form I only, but having different degrees of crystallinity. The data of Figure 5 indicate that, whereas completely amorphous specimens should

TABLE VI

Variation of the Crystalline Structure and the Optical Activity of a Sample of SPMH upon Stepwise Annealing at Increasing Temperatures

Annealing temperature, °C[a]	$\frac{I_{2\theta=9.0°}}{I_{2\theta=8.3°}}$	Crystalline structure[b]	$[M]_D^{25}$[c]
—	1.7	I + II	+211
90	2.0	I + II	+172
90	2.1	I + II	+175
100	2.7	I + II	+151
130	4.1	I[d]	+91
130	4.0	I[d]	+102

[a] Duration of each annealing treatment: 2 hr.

[b] See text.

[c] Referred to one monomeric unit. The approximation of the reported values is about ±10°.

[d] Approximative degree of crystallinity: 60%.

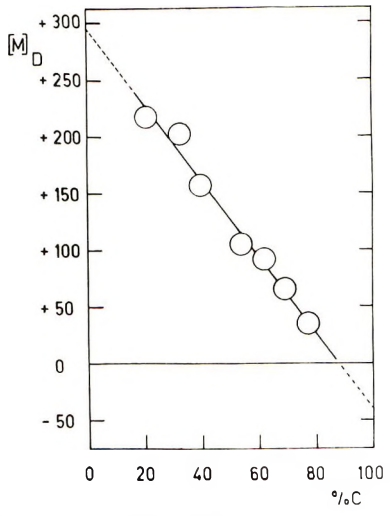

Fig. 5. Molar optical rotation at 25°C, referred to one monomeric unit, vs. degree of crystallinity for isotactic poly-(S)-4-methyl-1-hexene specimens crystallized in form I only. ($[M]_D^{25}$ for the polymer in hydrocarbon solution is +288.)

have a rotatory power which is very high and practically identical to that found in solution in hydrocarbons ($[M]_D^{25} = +288$), a much smaller and negative value of $[M]_D^{25}$ (about −40) can be expected for specimens completely crystallized in form I.*

It is worth noting that the specimens regain the initial optical activity after dissolution, and thus only a negligible racemization, if any, takes place at the high temperatures used for their preparation.

The relatively small and possibly negative optical activity of form I does not seem to be related to any specific vicinal effect[12] due to the close packing of the chains in the crystals. In fact, the ORD study of SPMH in the crystalline state shows[5,14] that the λ_0 value of the one-term Drude equation, which is followed in the investigated range (from 600 mμ to 310 mμ) is very close to that found previously[6] for the polymer in dilute solution, and therefore the chromophoric systems primarily responsible for the optical rotation are very likely the same in both states. Consequently, the large difference between the optical activity of form I and that of the polymer in solution must be related to conformational differences only.

A reasonable way to explain the above difference of optical activity can be found by considering values of the molar rotatory power which can be calculated by Brewster's semiempirical method[13] for monomeric units of SPMH belonging to either a right-handed or left-handed 3/1 helix (Table

* As an amorphous component deriving from the contributions of folds, chain ends etc. is expected to be present in the total x-ray scattering even of completely crystallized specimens, the values of the degree of crystallinity determined by us (see experimental part) make the extrapolation of the data of Figure 5 to 100% crystallinity somewhat questionable. The extrapolated value of $[M]_D^{25}$ can, however, be used for qualitative considerations.

TABLE VII
Experimental Molar Optical Rotation of SPMH in the Crystalline and in the Dissolved State and Molar Optical Rotation Calculated According to Brewster[13] for SPMH 3/1 Helices

		Optical activity of SPMH 3/1 helices calculated according to Brewster		
Physical state of polymer	$[M]_D^{25}$ (obsd.)[a]	Handedness of the helices	Conformation of monomer units	$[M]_D$[b]
Dissolved	+288[b]	left	A	+180
		left	B	+300
		right	C	−300
Crystalline (form I)	−40[c]	left + right	A + C	−60
		left + right	B + C	0

[a] Referred to one monomeric unit.
[b] Maximum observed value.[6]
[c] Extrapolated value (see Fig. 5).

VII).* It has already been observed[6] that the molar rotatory power experimentally found for isotactic SPMH in hydrocarbon solution not only has the same sign, but is also very close to the calculated average molar rotatory power in the two conformations, indicated in Table VII by A and B, corresponding to left-handed helices; this result has led[6] us to postulate for isotactic SPMH in solution the existence of helical main-chain sections mainly spiraled in the left-handed sense. It can be observed now (Table VII), that both the above two conformations belonging to left-handed helices and the conformation C, for a right-handed helix, have a rotatory power which is much higher, as far as the absolute value is considered, than that experimentally found for the crystalline polymer. However, according to Brewster, a mixture of right-handed and left-handed helices of the same length formed by monomeric units with the conformation C and A respectively, would have a molar optical rotation, referred to one monomeric unit, of −60, and a similar mixture consisting of helices of opposite handedness formed by monomeric units with the conformation C and B respectively, would be, according to Brewster's calculations, optically inactive. In both cases, the calculated value of the molar optical rotation compares well enough with that of form I.

Even if the approximation in the Brewster method and, in particular, the difference between the type of helical conformation allowed according to Brewster (3/1) and that found experimentally (7/2), limit the validity of the comparison, it strongly suggests the possibility that the low rotatory

* The right-handed and the left-handed 3/1 helices are the only conformations which, according to Brewster's conformational analysis[13] can be envisaged for the main chain of isotactic SPMH. According to the same conformational analysis approach, as discussed in detail elsewhere,[17] only one conformation (C) is allowed to monomeric units inserted in the right-handed helix, while two conformations (A and B) are allowed, when they are inserted in a left-handed helix.

power of form I arises from the presence in the crystals of both right-handed and left-handed helical sections, and thus supports the hypothesis put forward on the basis of the x-ray data.

EXPERIMENTAL

Polymers

The samples of isotactic poly-(S)-4-methyl-1-hexene were prepared by polymerizing the monomer (minimal optical purity: 93%) with catalysts obtained from $TiCl_3$ and $Al(i\text{-}C_4H_9)_3$ or $TiCl_4$ and $Zn(i\text{-}C_4H_9)_2$. Some of the samples were a kind gift of Dr. F. Ciardelli and Dr. C. Carlini, Industrial Organic Chemistry Institute, University of Pisa. Polymer fractions insoluble in boiling ethyl acetate and soluble in diethyl ether were used.

Measurements of Optical Activity in the Crystalline State

The determination of the optical rotatory power of crystalline SPMH has been carried out by the techniques described in detail elsewhere.[14]

Evaluation of the Degree of Crystallinity

The degree of crystallinity of the samples of SPMH crystallized in form I, has been evaluated by using Geiger counter tracings of x-ray diffraction diagrams. The points at $2\theta = 7°$ and $2\theta = 30°$ in such diagrams were joined by a straight line and the closed surface so obtained was separated into two regions by a suitable curve having the features of the diffraction pattern of a completely amorphous sample, namely that of the polymer above its melting point. The degree of crystallinity was then calculated as the percentage ratio between the area of the upper region, related to the scattering of the crystalline phase, and the total area.

CONCLUSIONS

The results of the x-ray investigation, while suggesting that helices of opposite screw sense are simultaneously present in the crystalline form I of SPMH, do not contradict the hypothesis[6] that in solution the polymer macromolecules are spiraled predominantly in one of the two possible screw senses. In fact, the optical activity study has revealed a very large difference between the rotatory power of the polymer in the crystalline form I and in solution, and it has suggested that such a difference arises from different positions of the conformational equilibrium. Actually, the finding that the crystalline form I, in which, according to the x-ray investigation, helices of both screw senses are packed together, has a low rotatory power, gives additional support to the idea that the very high rotatory power in solution is connected with the existence of helical conformations in which a single screw sense largely prevails.

The different positions of conformational equilibrium in solution and in the crystalline form I are not surprising in view of the following considera-

tions. In solution, each macromolecule of an isotactic polymer has a conformation[15] in which chain segments of right-handed helix sense alternate with segments of left-handed sense, the average length of the right-handed and left-handed segments being the same. If an isotactic polymer has a side group containing an asymmetric carbon atom, the side group may assume a different number of allowed conformations, depending on whether it is pendant from a right-handed or from a left-handed helix. In the case of SPMH (Table VII), two stable, almost isoenergetic, conformations are permitted to the S lateral group pendant from a left-handed helix, whereas only one stable conformation is permitted when the S lateral group is pendant from a right-handed helix.

In accordance with the statistical thermodynamic calculations[16,17] in SPMH, taking into account the cooperativeness of the phenomenon, a very large prevalence of the left-handed helix is expected, mainly for entropic reasons.

In the solid state, good packing is achieved in the pseudo-$P\bar{4}$ space group, because it allows a good fitting of bulges and hollows.[8] Therefore, in the crystals, an equal number of right-handed and left-handed helices must be present. This is evidently in accordance with the very low optical rotation which is observed in the most crystalline specimens of the form I of SPMH.

According to the above considerations it is possible to anticipate that in the crystalline form II (having a high value of optical rotation) helices should be present which have the left-handed sense of rotation only.

References

1. P. Pino, G. P. Lorenzi, and L. Lardicci, *Chim. Ind.* (Milan), **42**, 712 (1960).

2. G. Natta, P. Corradini, and I. W. Bassi, *Atti Accad. Nazl. Lincei Rend. Classe Sci. Fi. Mat. Nat.*, [8] **19**, 404 (1955).

3. F. C. Frank, A. Keller, and A. O'Connor, *Phil. Mag.*, **4**, 200 (1958).

4. P. Pino, F. Ciardelli, G. P. Lorenzi, and G. Natta, *J. Amer. Chem. Soc.*, **84**, 1487 (1962).

5. P. Pino, G. P. Lorenzi, and O. Bonsignori, *Chimica della Macromolecole*, Consiglio Nazionale delle Ricerche, Roma, 1968, p. 3.

6. P. Pino, F. Ciardelli, G. P. Lorenzi, and G. Montagnoli, *Makromol. Chem.*, **61**, 207 (1963).

7. H. D. Noether, in *Macromolecular Chemistry, Prague 1965* (*J. Polym. Sci. C*, **16**), O. Wichterle and B. Sedlàček, Eds., Interscience, New York, 1967, p. 725.

8. P. Corradini, paper presented at The Robert A. Welch Foundation Conferences on Chemical Research, X, Polymers, Houston, Texas (1966).

9. G. Natta, P. Corradini, P. Ganis, and P. A. Temussi, in *Macromolecular Chemistry, Prague 1965* (*J. Polym. Sci. C*, **16**), O. Wichterle and B. Sedlàček, Eds., Interscience, New York, 1967, p. 2477.

10. P. Corradini, P. Ganis, C. Pedone, A. Sirigu, and P. A. Temussi, in *Macromolecular Chemistry, Prague 1965* (*J. Polym. Sci. C*, **16**), O. Wichterle and B. Sedlàček, Eds., Interscience, New York, 1967, p. 2877.

11. P. Ganis, *Europ. Polym. J.*, **2**, 397 (1966).

12. W. Kauzmann and H. Eyring, *J. Chem. Phys.*, **9**, 41 (1941).

13. J. H. Brewster, *J. Amer. Chem. Soc.*, **81**, 5475 (1959).
14. O. Bonsignori and G. P. Lorenzi, *J. Polym. Sci. A-2*, **8**, 1639 (1970).
15. G. Allegra, P. Ganis, and P. Corradini, *Makromol. Chem.*, **61**, 225 (1963).
16. G. Allegra, P. Corradini, and P. Ganis, *Makromol. Chem.*, **90**, 60 (1966).
17. P. L. Luisi and P. Pino, *J. Phys. Chem.*, **72**, 2400 (1968).

Received May 4, 1970

JOURNAL OF POLYMER SCIENCE: PART A-2 VOL. 9, 209–213 (1971)

Viscoelastic Behavior of Low Molecular Weight Polystyrene

DONALD J. PLAZEK* and V. MICHAEL O'ROURKE, *Mellon Institute, Pittsburgh, Pennsylvania 15213*

Synopsis

The shear creep and creep recovery behavior of narrow molecular weight distribution polystyrene samples of low molecular weight, 1.1×10^3, 3.4×10^3, and 1.57×10^4 are reported as a function of temperature, near and above the glass temperature. Time-temperature equivalence for the total creep compliance is found to be nonapplicable, and in fact the steady-state recoverable compliance, J_e, is a strong function of temperature. The time-scale shift factors for the recoverable compliance are analyzed in the light of free volume theory. Viscosity data are presented for samples with molecular weights between 1.1×10^3 and 6.0×10^5. The temperature dependence of the characteristic time constant ηJ_e can be explained in terms of free volume concepts whereas that of viscosity η cannot. Effects of residual molecular weight heterogeneity are demonstrated.

INTRODUCTION

The availability of narrow molecular weight specimens[1–3] has made it possible to investigate the molecular weight dependence of the viscoelastic response of polymers in the terminal zone.[4] A definitive study could not be made in the past because usually the mechanical response at "long times" is more a function of the distribution of chain lengths than it is of the molecular weight itself.[5]

Stress relaxation measurements by Tobolsky, Aklonis, and Akovali[6] on anionically polymerized polystyrenes with molecular weights from 9.4×10^4 to 2.6×10^5 revealed that the steady-state compliance J_e did not increase proportionally with the molecular weight. Instead, it is sensibly constant. This constancy of J_e has been confirmed by several groups of investigators.[7–9]

Dynamic mechanical property measurements on rather dilute solutions of similar polymers have been made by Ferry et al.[10,11] investigating the terminal zone of response as a function of concentration and molecular weight. The results have been compared with the predictions of current dilute solution theories derived for monodisperse polymer samples.

* Present address: Department of Metallurgical and Materials Engineering, University of Pittsburgh, Pittsburgh, Pennsylvania 15213.

We are reporting here the results of creep and creep recovery studies on three low molecular weight polystyrenes of narrow molecular weight distribution. Our measurements on each of these samples revealed an unexpected striking decrease in J_e with temperature in the neighborhood of the glass temperature, T_g. In addition, it was found that the upper limits of J_r approached asymptotically with increasing temperature were lower than the calculated Rouse values.[4]

Changes in the shape of the relaxation spectrum of poly(vinyl acetate) near T_g have been reported by Kovacs, Stratton, and Ferry.[12] Evidence obtained from dielectric measurements[13] indicates a rapid loss of long-range molecular motion with decreasing temperature near T_g, above and beyond the shifting of the effective time scale to longer times. The large spectrum changes with temperature that we are reporting are in accord with both these sets of data.

The creep compliance curves obtained have all been analyzed according to the classic representation[4]

$$J(t) = J_g + J_d\Psi(t) + t/\eta$$

where the total creep compliance, $J(t)$ (in cm^2/dyne), is the sum of the recoverable contributions $J_g + J_d\Psi(t)$ and that representing the permanent viscous deformation, t/η. J_g is the glassy compliance which is the long-time steady-state value for relaxations occurring at very short times and includes the stretching and bending of inter and intra-molecular bonds. $\Psi(t)$, the normalized retardation function for the primary dispersion increases monotonically with time t from zero at $t = 0$ to one at $t = \infty$. The steady-state compliance, $J_e = J_g + J_d$, where J_d is the steady-state delayed compliance and η is the viscosity. We will identify the recoverable compliance as $J_r(t) = J(t) - t/\eta$.

EXPERIMENTAL TECHNIQUES

All creep and recovery measurements were made with a magnetic bearing torsional creep apparatus.[14] This instrument consists essentially of a magnetically suspended rotor that transmits known torques, induced by a drag cup motor, to one end of a cylindrical polymer sample. Distinctive features of the instrument include the frictionless magnetic bearing enabling precise recovery measurements that may extend to very long times; an adjustable lower sample platen permitting a manipulation of the sample shape; and a controlled atmosphere which was essential for the removal of entrapped gas and residual solvent from the samples.

The characteristics of samples studied for this paper appear in Table I. "A" prefixed samples were prepared by T. Altares, Jr.; "L" prefixed samples by Samuel Lee; PC-11 was obtained from Pressure Chemicals Company (Pittsburgh, Pennsylvania 15201). The sample M102 represents an incomplete recovery from solution of the Dow Chemical anionically polymerized S102. The samples of polystyrene were prepared *in vacuo*

by using well known anionic polymerization techniques.[1-3] Because of its low molecular weight, polymer A67 was fractionated by elution chromatography in a silica gel-packed column.* All other fractions were precipitated from acetone or butanone by an appropriate mixture of methyl alcohol and water. All samples, including a mixture of A58 and A16[5], were freeze-dried from benzene.

Viscosity-average molecular weights were determined from dilute solution viscosity measurements.† For molecular weights greater than 4000 the relationship[15] used was $[\eta]_\Theta = 8.5 \times 10^{-4} M^{0.5}$. For PC11 and A67, the relationship[16] was $[\eta]_\Theta \sim [\eta]_{\text{benzene}} = 1.0 \times 10^{-3} M^{0.5}$.

TABLE I
Sample Characterization

Designation[a]	Cut	$[\eta_\Theta]$, dl/g[b]	$\bar{M}_v \times 10^{-3}$	$\bar{M}_w/\bar{M}_n$[c]	Method
A-67[7]	3–99%	0.0344[d]	1.1	1.03[e]	VPO + cryoscopy[f]
PC-11[2]	22–64%	0.058[d]	3.3$_6$	—	—
A-61[g]	Whole	0.106$_6$	15.$_7$	<1.08	Sedimentation
A-61[3]	~10–90%	0.1087	16.4	—	—
A-58	Whole	0.118$_6$	20.0	<1.08	Sedimentation
A-25[4–6]	25–64%	0.184	46.$_9$	1.04$_7$	Fractionation
M-102	Whole	0.260	94	<1.08	Sedimentation
A-63	Whole	0.28	104	<1.08	Sedimentation
L-5[5,8]	{25–50% / 75–80%}	0.29$_7$	122	1.05$_5$	Fractionation
L-2[1_2][h]	6–8%	0.36$_9$	189	1.01$_5$	Fractionation
A-19[7–12]	24–80%	0.65$_4$	592	1.05$_6$	Fractionation
A-16[5]	80–93%	0.76	800	—	—

[a] Bracketed numbers denote fractions.
[b] Θ solvent = cyclohexane at 34.5°C.
[c] Values given apply to whole polymer.
[d] Intrinsic viscosities of A-67[7] and PC-11[2] determined in benzene at 30°C.
[e] Assumes $\bar{M}_w \simeq \bar{M}_v$.
[f] $\bar{M}_n$ obtained from vapor phase osmometry and cryoscopy.
[g] Sometimes called A-61T.
[h] Indicates cut 2 of refractionation of first cut of whole polymer.

In the post-polymerization handling of the polystyrenes, great care was taken to avoid contamination with vacuum sealing and stopcock greases. As previously reported,[14] for measurements of the creep rate near T_g, the effect of a small amount of plasticizer, lowering the glass temperature about 1°C, is roughly equivalent to a decrease in molecular weight of more than 30%. Although greases could apparently be removed by coacervation of the polystyrene from cyclohexane at about 20°C, whenever possible, conventional glassware joints—especially those in the freeze-drying

* Fractionations were carried out by Marguerite Fulton, Timothy Altares, Jr., Elizabeth Frommel, and S.-P. S. Yen.

† Dilute solution viscosities were determined by Elizabeth Frommel.

glassware—were replaced by grease-free O-ring sealed joints to reduce contamination.

Degradation of the samples was avoided by limiting the temperature to 180°C. This precaution and the purging of the sample chamber made it unnecessary to add antioxidants to the polystyrene samples.

Before installation of the sample in the instrument, the freeze-dried material was compressed and fused at an appropriate temperature (greater than T_g) in an evacuated glass tube mold. For these low molecular weight samples a very short time was necessary to relax the molding stresses. When the mold was cooled to room temperature the glass could be broken away to yield a small cylindrical sample.

After installation of the sample, the sample chamber of the instrument was alternately evacuated and filled with dry nitrogen several times to eliminate oxygen and water vapor. All samples were heated under vacuum well above their glass temperatures to remove residual solvents and dissolved gasses. Since measurements on one sample near its glass temperature indicated that nitrogen, acting as a plasticizer, could lower the glass temperature about 0.03°C, subsequent measurements were made with the sample chamber evacuated to about 10^{-2} Torr.

At an elevated temperature (usually about 150°C), the degassed samples were manipulated by means of the movable bottom sample platen and applications of torque to the rotor to yield a cylinder completely filling the gap between the sample platens. The maximum instrument sensitivity required that measurements of compliance below about 10^{-8} cm^2/dyne be on samples drawn into a thin rod shape.[14]

Sample coefficients (defined as the second moment of the cross-sectional area, j, divided by the height, h), entering the compliance calculation, were computed from the expression $j/h = m^2/(2\pi\rho^2h^3)$ where m is the mass, and ρ the density. Densities were calculated[17] from expression

$$1/\rho = 0.767 + 5.5 \times 10^{-4}T + 643 \times 10^{-4}T/M$$

where T is in degrees Kelvin. Since the sample platen radius r was known, the sample coefficient calculation could be checked by using the equivalent relation $j/h = \pi r^4/2h$. However, the former expression was normally preferred since it partially compensates for the deviation of the sample from a perfectly cylindrical shape.

When samples were drawn into thin rods for low compliance measurements, a sample coefficient was empirically determined at some reference temperature. For subsequent measurements at lower temperatures, this sample coefficient was multiplied by the factor $h_0^3\rho_0^2/h^3\rho^2$, where the subscript refers to the value at the reference temperature, T_0. The empirical coefficient was obtained by matching data for the drawn sample to the compliance and/or viscosity determined for an undrawn sample at T_0. To prevent sample sagging, T_0 was necessarily near T_g. $J(t)$ and η change rapidly with temperature near T_g so that great care was taken to reproduce the reference temperature to about 0.01°C.

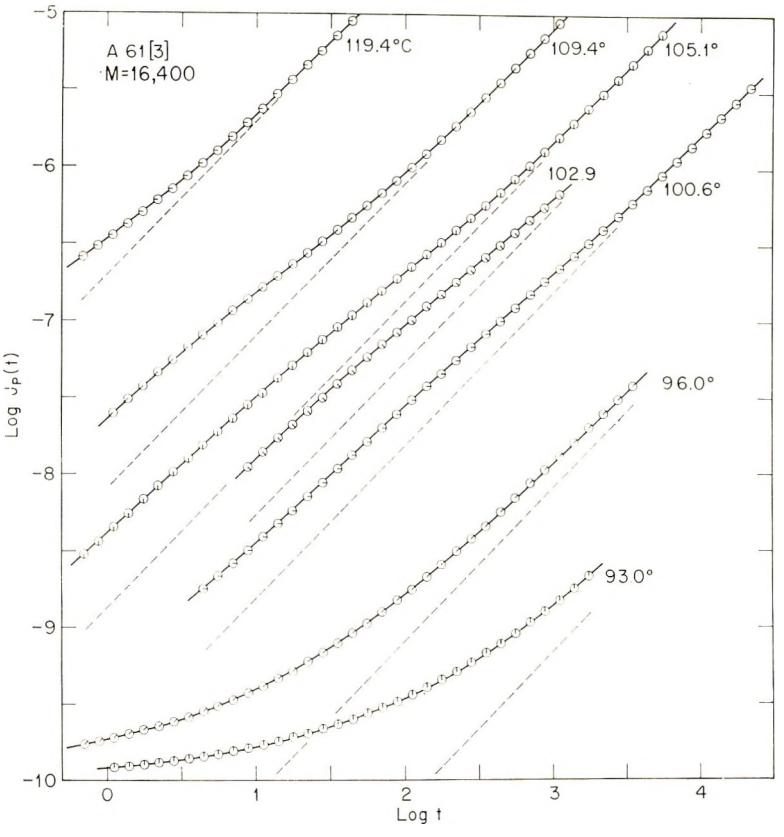

Fig. 1. Plots of the logarithm of the total creep compliance, $J_p(t)$ (cm²/dyne) vs. the logarithm of time t (sec). Curves are for a 16,400 molecular weight sample measured at the indicated temperatures. Subscript p indicates amplitude adjustment for the temperature dependence of the rubberlike response: (○) calculated from the measured recoverable compliance, $[J_p(t) - t/\eta_p]$ and the measured viscosity, η_p; (- - -) dashed lines represent the viscous contribution to the total creep.

Although the recoverable compliance has been denoted on the graphs by $[J(t) - t/\eta]$, recoveries were normally measured directly after steady state flow in creep had been obtained. In fact, since, for the measurements reported here, the viscous deformation was usually the dominant contribution to creep, the indicated subtraction would lead to imprecise recoverable compliance values. On the other hand, by adding the known viscous deformation to the known recoverable compliance it was possible to precisely reconstruct total creep curves as shown in Figure 1.

When more than about 3 hr was required for steady-state flow, a technique suggested by Leaderman et al.[18] was often employed. At a temperature above that for which the recovery was desired, the torque was applied to the sample and steady-state flow was attained in a relatively short time. Then, the stress being maintained the sample was cooled to the temperature of interest. The torque was then removed to obtain the recovery.

Among other verifications of this technique the following may be mentioned: In Figure 12, discussed in a later section, one set of half-solid circles represents measurements made by using Leaderman's technique; the other set of half-solid circles represents the recovery obtained after creeping at 129.3°C until steady flow had been obtained. The agreement between the two sets of points indicates the possibility of applying the technique even to materials behaving nonlinearily.

The use of this technique also simplified the shear viscosity determinations. If the stress on the sample were maintained after attaining steady state flow, it was necessary only to measure the rate of sample deformation at any desired temperature (above T_g) to obtain a precise viscosity value. Other methods sometimes used for determining viscosities have been previously summarized.[19]

RESULTS

Torsional shear measurements of the recoverable creep compliance, $J(t) - t/\eta$, were carried out at seven temperatures between 93 and 119.4°C on the A61[3] sample ($\bar{M}_v = 16{,}400$). Values for the shear viscosity η (in dynes sec/cm^2) were obtained at temperatures between 93 and 160°C. Over this span in temperature η decreased nearly nine orders of magnitude from 1.43×10^{12} to 2.97×10^3 poises. The total creep response is presented in Figure 1 in terms of the creep compliance $J_p(t)$, cm^2/dyne, over four logarithmic decades of time. The subscript p indicates that the usual small correction was made which accounts for the temperature dependence of the assumed entropic nature of the response; $J_p(t) = J(t) \times T\rho/T_0\rho_0$, where ρ is the density at the temperature T of the measurement and ρ_0 is the value at the chosen reference temperature T_0. Dashed lines representing the viscous contribution to the compliance, t/η_p, indicate that only as the glass temperature, $T_g = 91.5$°C, for this material is approached does the recoverable part of the deformation become the dominant part of the creep in the measured region of the time scale; $\eta_p = \eta T_0\rho_0/T\rho$. It is eminently clear that very little can be concluded about the form of the recoverable compliance from the total creep compliance curves. Subtraction of the viscous deformation, as indicated by didactic portrayals of creep, to ascertain the recoverable contribution is not practical in regions where $t/\eta > 0.8\,J(t)$.

The recoverable compliance curves, $J_p(t) - t/\eta_p$, which were measured directly following the attainment of steady-state deformation, are shown in Figure 2. Reliable results were possible up to 119.4°C, where a recoverable deformation was seen that is too high by about 30% to be compatible with successful temperature superposition with the curve previously obtained at 109.4°C. This apparent decrease in the steady-state compliance with a decrease in temperature persisted down to 105.1°C. To confirm our conclusion that these changes in the level of recoverable compliance were far beyond our experimental uncertainty, which admittedly

does increase as the viscosity decreases, extra time and trouble were taken with the measurements made at 100.6°C. Attainment of steady state was insured by allowing the sample to creep at 110°C for about 36 hr. After cooling and thermally equilibrating the samples at 100.6°C, the imposed torque was removed and the recovery was monitored for a week. Indeed, the steady-state compliance level dropped another 80% with a temperature decrease of 4.5°C. When the transition portions of the recovery curves are superimposed by reducing the time scale at each temperature to 100°C, the pattern of divergence becomes exceptionally clear, as seen in Figure 3. At this point in our investigation it was not clear that reduction should be attempted without normalizing the dispersion. It now appears

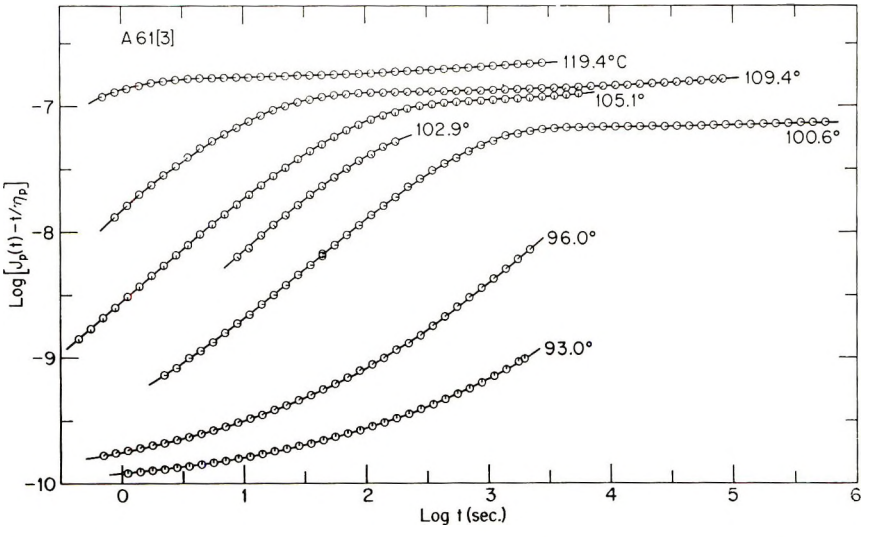

Fig. 2. Plots of the logarithm of the recoverable compliance, $[J_p(t) - t/\eta_p]$, (cm²/-dyne) vs. the logarithm of time t for M = 16,400 measured at the indicated temperatures.

that this procedure most correctly represents the changes in response that occur with decreasing temperature in the neighborhood of T_g. We will try to clarify the reasons for this conclusion below. It still remains a point of academic, but no practical, concern whether the rubberlike vertical shift should be applied to the portion of the recoverable deformation above the glassy level. We have not made this small correction to most of the data presented subsequently on the two lowest molecular weight samples.

Total creep measurements on sample PC11[2], $\bar{M}_v$ = 3400, show a smaller fractional contribution of the recoverable deformation even though our measurements were extended to times shorter than were normally measured. Results obtained at seven temperatures from 70.0 to 100.6°C, shown in Figure 4, indicate the dominance of the viscous deformation. Here again the t/η contributions are presented as dashed lines. Examination of the directly measured recoverable compliance curves, $J(t)$ —

t/η, presented logarithmically in Figure 5, reveals several unexpected salient features.

It is unmistakable that two dispersive regions on the time scale are present. Only at molecular weights substantially greater than the molecular weight between entanglements, 14,100 for polystyrene,* is a second dispersion beyond the rise from a glass to a rubber plateau level expected. Only at these high molecular weights can there exist a well developed entanglement network, which can further delay retarded deformation several orders of magnitude. At the same time, it is well known that the steady-state compliance J_e and the retarded deformation immediately

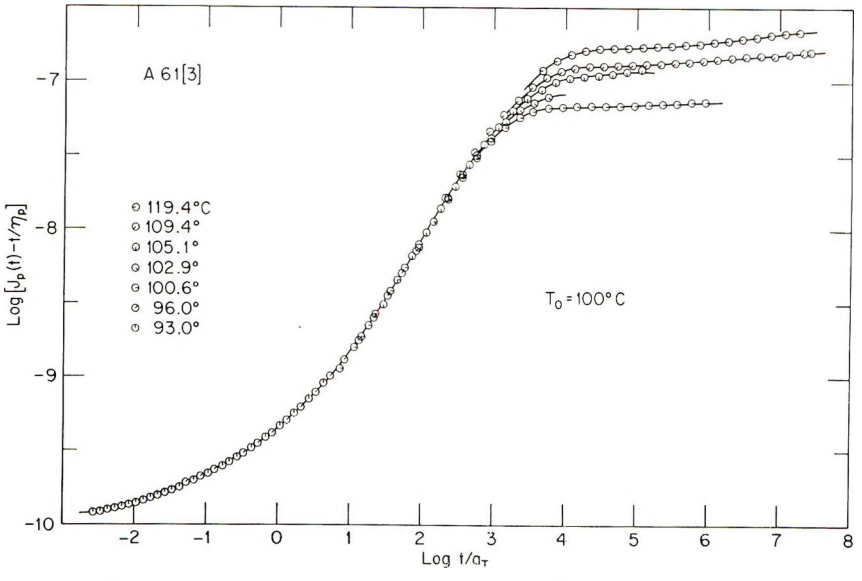

Fig. 3. Plots of the recoverable compliance curves of Figure 2, against the logarithm of the reduced time, t/a_T (sec). Temperature-dependent horizontal shift factors, a_T, relative to 100°C, have been empirically determined to give best superposition below knees of curves.

preceding steady-state deformation can be profoundly influenced by the molecular weight distribution of the sample.[5] We will present an example, later, of a sample where an otherwise undetectable high molecular weight tail gave rise to an enormous second dispersion: a 1000-fold increase in the recoverable compliance. Therefore, in spite of the fact that PC11-[2] is a central cut of a narrow distribution sample we believe the second dispersion here is the result of such a tail. Continuing work at the University of Pittsburgh has confirmed this proposition. The first plateau is taken to be the J_e for the predominant species present, in this case with a molecular weight of 3400.

* Determined from recoverable compliance measurements on sample A16 (not reported here).[20]

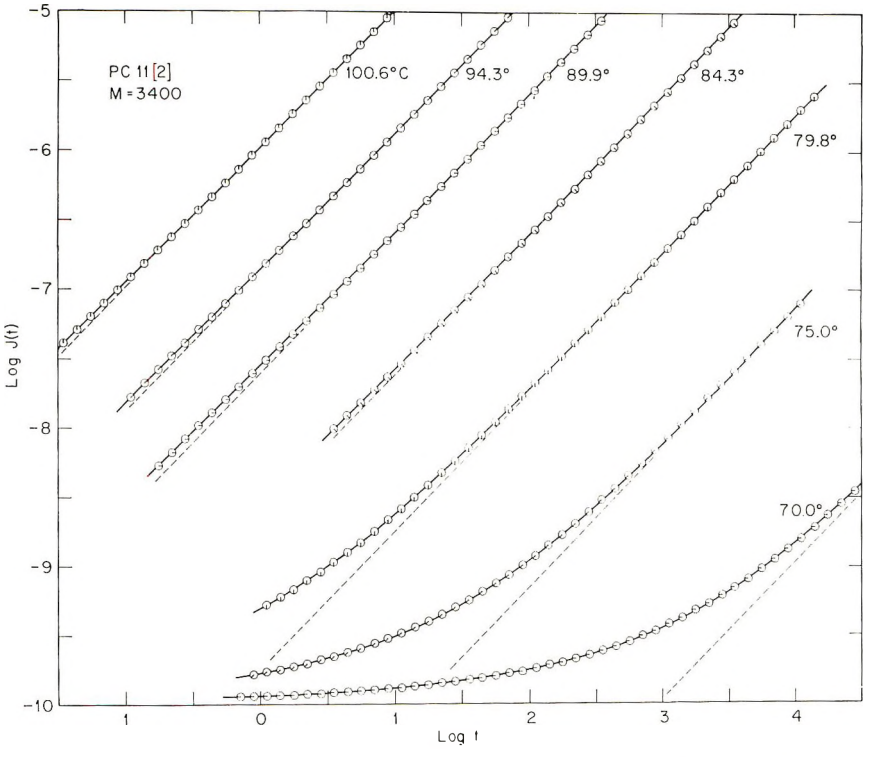

Fig. 4. Logarithmic plots of the total creep compliance, $J(t)$ (cm²/dyne), against time t (sec), for $M = 3400$ at the indicated temperatures. Dashed lines represent viscous contributions to the total creep: (O) measured recoverable compliances plus calculated viscous contributions.

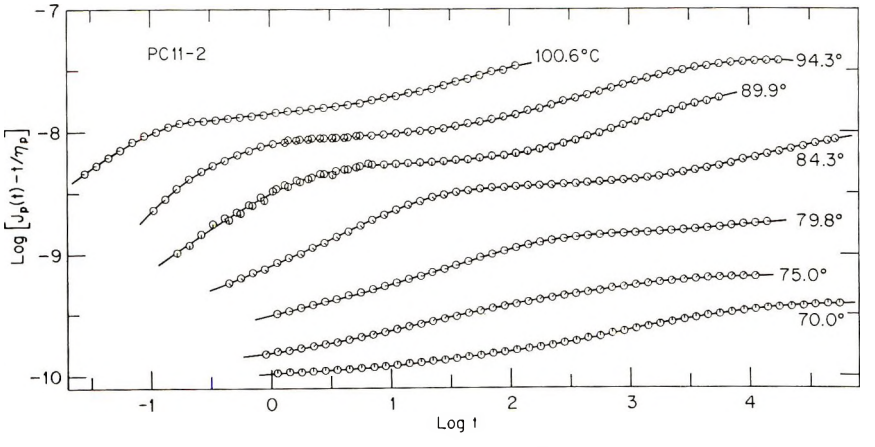

Fig. 5. Logarithmic plots of recoverable creep compliances, $[J_p(t) - t/\eta_p]$ (cm²/dyne), at indicated temperatures for $M = 3400$ plotted against time t (sec). Subscript p indicates amplitude correction for entropic $T_0 = 100°C$ response.

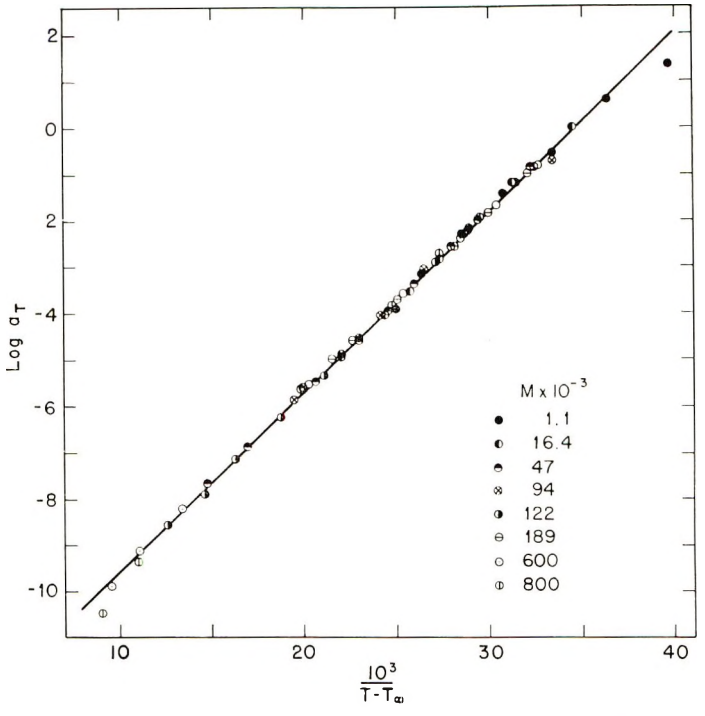

Fig. 6. Recoverable compliance shift factors a_T plotted semilogarithmically against $10^3/(T - T_\infty)$ for samples of indicated molecular weight. For each sample the reference temperature for reduction is T_g so that log $a_T = 0$ at $T = T_g$. Equation of line is: log $a_T = -13.46 + 389/(T - T_\infty)$.

Steady-state deformation in creep is achieved when the time independent recoverable deformation is reached. It is sometimes assumed that this is equivalent to a rate of deformation that is constant within experimental accuracy. This assumption can be erroneous if the recoverable deformation is only a small part of the total creep. The response of PC11[2] as seen in Figures 4 and 5 serves as an example of this. Note that a constant rate of deformation (within experimental uncertainty) is reached in about 1 sec at 94.3°C but the recoverable compliance does not attain a constant value until about 10^4 sec.

The most startling feature seen in Figure 5 is a marked decrease in recoverable deformation as the temperature of measurement approaches T_g (70°C). This is an exaggerated case of the behavior exhibited by A-61[3] in Figure 2. In the interval between 100 and 70°C the J_e for the 3400 molecular weight species decreases by thirtyfold. It is evident that many retardation mechanisms are lost as the temperature of measurement approaches T_g. The time scale of the response of the remaining mechanisms still shifts rapidly toward longer times with decreasing temperature, but because of the changing shape of the recoverable compliance curves the amount of time scale shift is impossible to determine with this data.

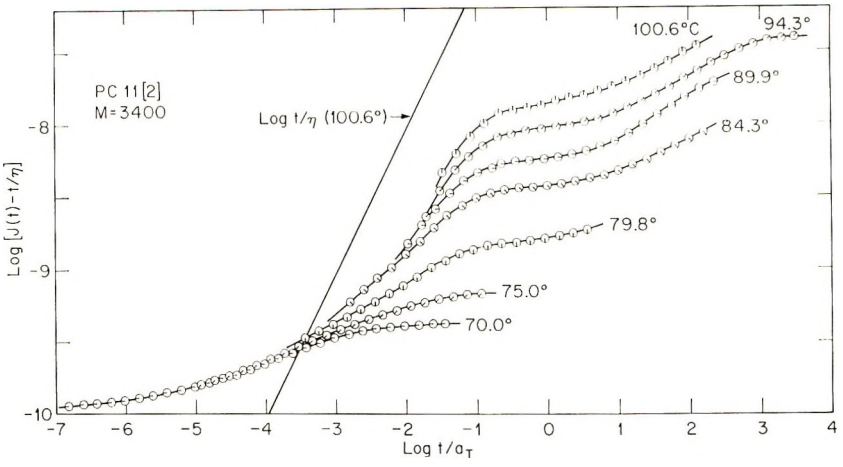

Fig. 7. Recoverable compliance for $M = 3400$ reduced to 100°C by plotting logarithmically against the reduced time, t/a_T. Horizontal shift factors a_T for the indicated temperatures have been calculated by assuming the applicability of the results of Figure 6 and $T_g = 70$°C. The straight line is the viscous contribution to total creep at 100.6°C.

However, it was found that within experimental error the time scale shift factors, a_T, for all of the other narrow distribution polystyrene samples studied in our laboratory could be described as the same function of $T - T_g$. This result is shown in Figure 6, where data are presented from samples with molecular weights that range from 1.1×10^3 to 8.0×10^5. The procedure used in obtaining the fit of the data in Figure 6 and its possible significance is discussed below in the section entitled Temperature Dependences.

By using this relation, shift factors were calculated for PC11[2] and curves from Figure 5 were plotted in Figure 7 in their appropriate position at the reference temperature T_0 of 100°C. The pattern of behavior can be clearly seen as an exaggeration of the anomaly present in the response of A61[3] (see Fig. 3). There is a limiting high temperature envelope of recoverable compliance. Since J_e at 100.6°C is close to the high-temperature asymptotic value as seen in plot of log J_e versus T, shown below, the curve for 100.6°C is nearly representative of this envelope. At all of the lower temperatures the curves fan out reflecting the disappearance of retardation mechanisms to which we have alluded. The viscous contribution to the total creep deformation, t/η, at 100.6°C is shown plotted against the reduced time of the recoverable compliance to indicate the amount of permanent deformation which accompanies the retarded elastic component during creep. It can be seen that when log t/a_T is between -2.5 and -1.0, t/η is roughly an order of magnitude greater than $J(t) - t/\eta$, so that only about 10% of the creep deformation is recoverable in this region of the time scale. By using the 100.6°C viscosity value we are indicating the relative contributions as observed at 100.6°C. We have not used the reference temperature value of η to emphasize the fact that not only would the re-

coverable compliance curve be different at 100°C but quantitatively the relative amounts of permanent and recoverable deformation at any given reduced time would differ. This is so because the two forms of deformation, recoverable and viscous, have different temperature dependences. This fact, which was reported earlier,[19] has been found to be true for all of the samples of polystyrene measured.

In Figure 8 the recoverable compliance curves for PC11[2] at 70.0 and 75.0°C have been plotted as functions of the cube root of time. Semiquantitatively the curves bear a striking resemblance to the response found for the nonpolymeric 1,3,5-tri-α-naphthylbenzene, ($T\alpha$NB) in the neighborhood of T_g. This kind of behavior has been called terminating

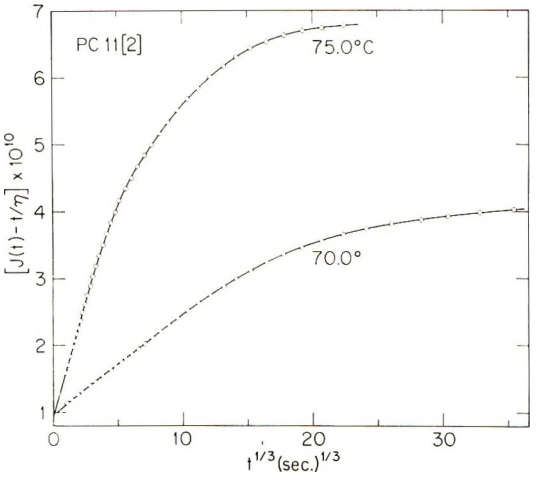

Fig. 8. Plots of the recoverable compliance, $[J(t) - t/\eta]$, (cm²/dyne) for M = 3400 vs. the cube root of time t (sec). Both curves extrapolate to a value of 1.0×10^{-10} cm²/dyne at $t = 0$.

Andrade creep.[21] The short-time portions of the curves are linear and extrapolate to intercepts, J_A, of 1.0×10^{-10} cm²/dyne. This value appears to be the short-time limiting value of the dominating dispersion. The J_e at 70.0°C is slightly greater than 4×10^{-10} cm²/dyne. The corresponding values at T_g for $T\alpha$NB are 1.0×10^{-10} and 2.5×10^{-10} cm²/dyne. The persistent appearance of Andrade creep in the viscoelastic response of various materials continues to suggest that some unrecognized mechanism is responsible and that fortuitous curve fitting is not involved. When it appears as the dominating form it is usually best recognized in the logarithmic display of the retardation spectrum where a slope of $^1/_3$ is often present for several orders of magnitude in time. Such is the case for polystyrene between log $\tau = -1.0$ and 2.0 at T_g. Empirically speaking, it appears that the Andrade intercept has a very weak temperature dependence and that the $t^{1/3}$ linearity is valuable to obtain an objective value of the short time limiting compliance which immediately precedes the dis-

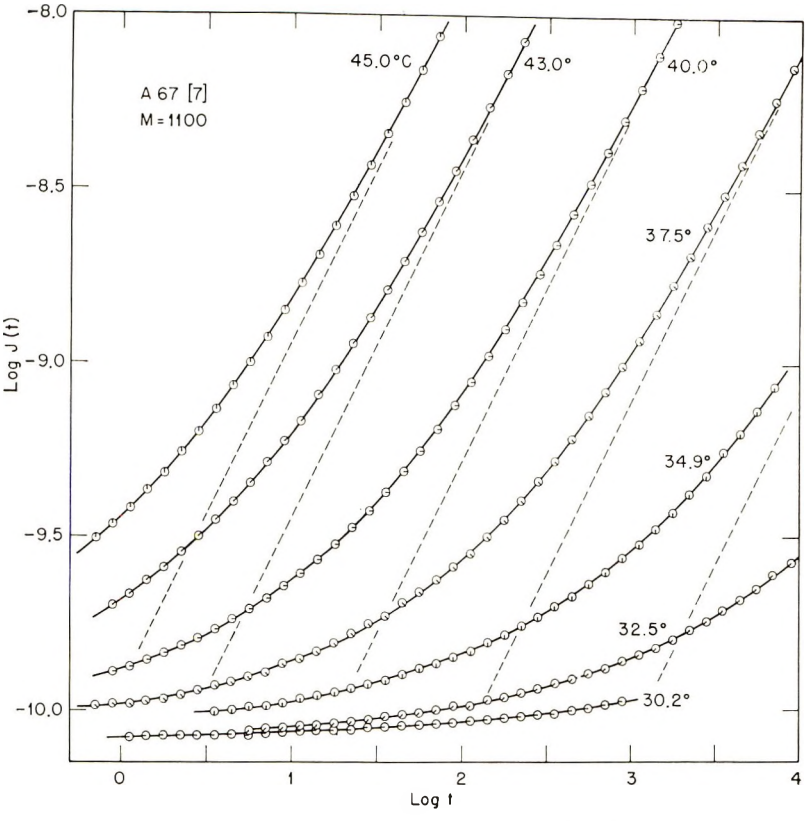

Fig. 9. Logarithmic plots of the creep compliance, $J(t)$, (cm²/dyne) vs. time t (sec) calculated from measured recoverable compliance and viscosity data: (---) viscous contributions to the total creep.

persion in question. It can also be useful in calculating the viscosity before steady-state deformation is achieved.[22]

The total creep compliance curves of sample A67[7], $M = 1100$, at temperatures between 30 and 45°C are shown with an expanded ordinate in Figure 9. This undecamer hardly qualifies as a high polymer, and the character of its memory certainly is not apparent from its response under constant torque nor would it be from stress relaxation measurements, if it were possible to make such measurements on this fragile material. We wish to emphasize that pains were taken to insure that equilibrium volume obtained before creep measurements were made near and below the conventional glass temperature of 40°C. For example at 30.2°C the specimen was held at temperature for 4 days before any measurements were made. During the subsequent 4 days, repetitive short runs were made to ascertain that no further time-scale shifting to longer times due to isothermal volume contraction was occurring. Previous or concurrent dilatometric measurements on a specimen from the same stock can be used to determine when equilibrium volume is achieved.

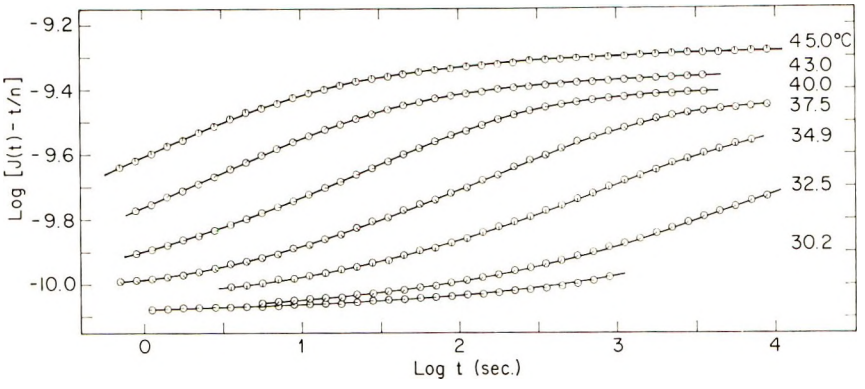

Fig. 10. Logarithmic plots of the measured recoverable compliance, $[J(t) - t/\eta]$ (cm^2/dyne) against time t. Measurements were made on sample A67[7], $M = 1100$.

The recoverable response in this temperature range is presented in Figure 10. Although the dispersion seen is not great, the dimunition of J_e is still readily apparent at this low molecular weight. Notice that at the three highest temperatures of measurement about the same time is required to reach steady state, i.e., several thousand seconds. This is a consequence of the increasing population of long time retardation mechanisms with increasing temperature. It would have been desirable to obtain additional information on the recoverable compliance at temperatures above 45°C because, as will be seen, the high temperature limiting behavior apparently is substantially larger than the response measured to date. Measurements at higher temperatures were precluded with our intrumentation because of detection limitations.

If long-time retardation mechanisms are preferentially being lost with decreasing temperature, as proposed above, then it would not, in principle, be proper to normalize the dispersion with a simple factor to obtain complete superposition with temperature reduction. Such a normalization

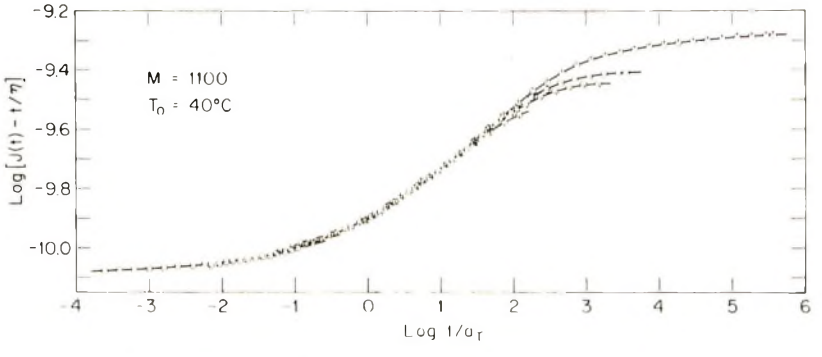

Fig. 11. Data of Figure 10 shifted horizontally to the temperature reduced time, t/a_T. Shift factors a_T were determined empirically for best superposition. Pip directions correspond to temperatures indicated in Figure 10.

would erroneously effect the level and hence the apparent shift factor of the short time portion of the recovery curve. It would take data of greater precision than that available to convincingly test this opinion. The result of the reduction effected by a simple logarithmic time axis shift is presented in Figure 11. Satisfactory reduction is achieved over five decades of reduced time, but at longer times the same kind of spreading is observed as in the response of the higher molecular weight samples. The degree of spreading is less, principally because of the limited accessible temperature range. Of course, as the strength of the dispersion diminishes with molecular weight—to the point that the maximum J_e is not much larger than J_g—any divergence will be correspondingly less.

DISCUSSION

Dependence on Molecular Weight Distribution

At the outset of this investigation we were of the opinion that samples of whole anionically polymerized polystyrene had molecular weight distributions that were sufficiently narrow ($\bar{M}_w/\bar{M}_n \simeq 1.05$) to justify investigating the molecular weight dependence of the terminal viscoelastic zone.[4] The first six samples studied had molecular weights above 45,000. One of these was a whole polymer and others were single fractionation cuts or combinations of central cuts of so-called "mono-disperse" samples.

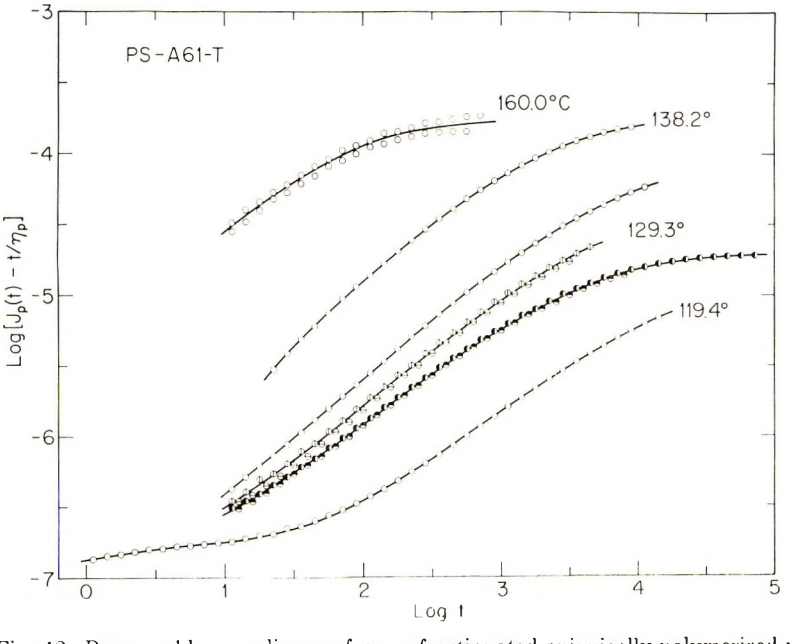

Fig. 12. Recoverable compliance of an unfractionated anionically polymerized polystyrene, M = 15,700. Open and marked circles correspond to separate samples. At 129.3°, maximum sample stresses are: (○) 1.3 × 10^3 dyne/cm², (⊖, ⊕) 3.9 × 10^3 dyne/cm², (◐, ◓) 8.6 × 10^3 dyne/cm².

The results obtained (not described in this paper) led us to suspect that the terminal response was not necessarily representative of a single molecular weight moiety.

Our growing suspicion concerning the sensitivity of the terminal zone response to molecular weight dispersity was confirmed when the recoverable compliance of the whole polymer, designated A-61 ($\bar{M}_w$ = 15,700), was measured. The unexpected results are presented in Figure 12, where the results at four temperatures, 119.4, 129.3, 138.2, and 160.0°C, are depicted. Several features should be noted. First of all, and most important, at the two highest temperatures, recoverable compliances approaching 2×10^{-4} cm²/dyne are obtained. This is astonishing because this level is

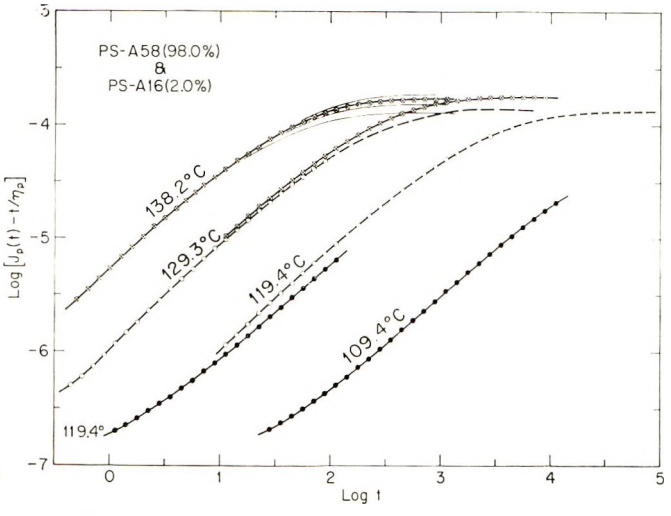

Fig. 13. Logarithmic plots of the recoverable compliance, $[J_p(t) - t/\eta_p]$ (cm²/dyne) vs. time t (sec) for $M = 2 \times 10^4$ containing 2% $M = 8 \times 10^5$ for various maximum sample stresses: (●) 14.6×10^3 dyne/cm², (○) 3.8×10^3 dyne/cm², (⊗) 1.00×10^3 dyne/cm²; solid light curves at 138.2°C correspond (from top to bottom) to 0.24×10^3, 2.3×10^3, and 6.2×10^3 dyne/cm²; dashed curve at 129.3°C is an extrapolation.

about 100 times greater than that observed for a sample with a molecular weight of 6×10^5. The reproducibility at 160°C was checked because the instrumental limit of normal accuracy had been reached. We have found that instrumental drift influences recovery results when the product ηJ_e is less than about 1 sec. The two sets of points shown for 160°C were obtained following torsional creep deformation in opposite directions.

In addition, it can be seen from the data at 129.3°C obtained at three levels of applied torque that the reponse of the material is highly nonlinear with the recoverable compliance, decreasing about fivefold at long times as the maximum stress in the sample increases from 1300 to 8600 dyne/cm². Since the stress in a torsionally deformed sample is not homogeneous and since no correction was made for the nonlinearity in calculating the data

points in Figures 12 and 13 the resultant values are somewhat in error. The degree of error is probably less than 20% at worst and does not negate any of the conclusions drawn from these two graphs. A correction formula for such recoverable compliance data does not exist and one analogous to that of Weissenberg (often called the Rabinowitz) correction for non-Newtonian flow[23] would be desirable.

The same torques were applied to the specimen at 138.2 and 160.0°C. There is an indication that $J_e(T\rho/T_0\rho_0)$ is the same at the two temperatures at the same stress.

The plateau level seen between 1 and 20 sec at 119.4°C is reasonable for the steady-state compliance of a sample composed solely of species with a molecular weight of 15,700. This fact suggests that the enormous enhancement of the recoverable compliance is the result of residual heterogeneity in sample A-61. However, examination of the resultant curves from gel-permeation chromatographic and velocity ultracentrifuge measurements did not reveal the presence of the suspected high molecular weight tail.* The polymerization of sample A61 had proceeded without extraordinary incident and there was no known reason to expect an unusual tail in the molecular weight distribution. Since direct evidence for such a tail was wanting, indirect evidence was sought. A portion of the stock of A-61 was subjected to a molecular weight fractionation by means of solution coacervation with the solvent-precipitant pair, benzene and methanol. The viscoelastic response of the central cut, fraction [3] was then measured and the results that have already been presented in Figures 1 and 2 were obtained. Notice that in Figure 2 the steady-state compliance at 119.4°C is the same as the plateau seen at the same temperature in the whole polymer; $\log (J_e)_p \simeq -6.8$. The unexpected enhanced and nonlinear recoverable compliance was thus eliminated and explained.

To confirm this explanation, a blend was prepared by mixing in solution 2.0% of a high molecular weight sample, A16 ($\bar{M}_v = 8 \times 10^5$) with 98.0% of a low molecular weight sample of anionically polymerized polystyrene, A58 ($\bar{M}_v = 2 \times 10^4$) in benzene. Sample A58 was chosen after a preliminary investigation showed its behavior was not anomalous. The benzene solution was then freeze-dried to avoid segregation upon drying. The recoverable compliance behavior of the blend at four temperatures, 109.4, 119.4, 129.3, and 138.2°C is presented in Figure 13. All of the features noted in the response of the whole polymer A-61 are qualitatively present in the blend; in fact, the J_e values are close, quantitatively. In Figure 13 similar kinds of data point designations indicate similar stresses in the specimen. The four maximum stresses present in the specimen during the four creep measurements at 138.2°C are 240, 1000, 2300, and 6200 dyne/cm^2. Again the lowest recoverable compliance is associated with the highest stress, and the reduced J_e values are, within the experimental precision, the same at different temperatures, when the stresses are the same.

* The GPC analysis was directed by Dorothy J. Pollack at Koppers Company, Inc. Research Center, Monroeville, Pennsylvania.

It is significant that while the recoverable compliance is highly nonlinear, the viscous contribution is linear for both the blend and the whole polymer A-61; i.e., at the highest applied torques the viscosity was only a few per cent lower than the limiting low rate of shear value. It is, therefore, clear that the predominant species present, the low molecular weight molecules, principally determine the steady state rate of shear and do not contribute additional increments to the recoverable deformation at relative long times. The large recoverable compliances seen in Figure 13 can be attributed only to the high molecular weight molecules present in a diluted state, with the polymer A58 playing the role of diluent at long times. The viscosity or alternatively the fractional free volume of the diluent plays an influential role in determining where on the time scale a recoverable response will be found, but obviously in the linear range of response the rate of shear plays no role in determining the level of recoverable compliance attained. The requirement of stress–strain linearity precludes such a dependence. Accurate values of the true J_e values of the blend and A16 have not been obtained but the recoverable deformations obtained are not inconsistent with a simple linear dependence of J_e upon the concentration of the high molecular species. Since at a concentration of 2% an entanglement network is not expected to be well developed, the decrease in apparent J_e is believed to be associated with molecular coil extensions into a non-Gaussian segment distribution regime.

At the time of our investigation, the A-61 sample was unique in its anomalous behavior. However, at the 39th Annual Meeting of the Society of Rheology Stratton[24] reported some unexpectedly high die swell results obtained on two low molecular weight polystyrene samples. They were anionically polymerized narrow distribution samples whose molecular weights were 1.05×10^4 and 1.98×10^4. In a discussion following his report the possibility of the presence of some high molecular weight species was considered. Stratton's subsequent investigations revealed the same kind of recoverable compliance behavior as found for the A-61 sample: a nonlinear response and steady-state compliances that were far too large for the molecular weights of the specimens.[25] His search for the then suspected high molecular component was successful. A gel-permeation chromatographic analysis of the 1.98×10^4 molecular weight sample made at 16 times the normal sensitivity revealed a distinct small satellite peak with a molecular weight of about 7×10^5. The material responsible for the peak constituted 0.3% by weight of the sample. Apparently the polymerization procedures used to prepare these low molecular weight samples not infrequently lead to a small amount of high molecular weight contaminant, which for some studies must be removed.

Temperature Dependences

The temperature dependence of the recoverable compliance, $J_r(t) = [J(t) - t/\eta]$, is measured by a_T, the relative rates of recovery for a given $J_r(t)$ level. On a logarithmic plot the shift along the time scale necessary

to obtain superposition of the log $J_r(t)$ curves with the one measured at a chosen reference temperature, T_0, is $-\log a_T$. Strict adherence to the principles of temperature reduction requires that the amplitude dependence of the compliance (the vertical shift factor) be taken into account and that all of the retardation mechanisms contributing to the recoverable deformation have the same temperature dependence.[4] It is usually assumed, with good reason, that the recovery of a polymer is rubberlike in nature. Therefore, the amplitude temperature dependence of the compliance is reduced with the elasticity factor $T\rho/T_0\rho_0$, where ρ_0 is the density at the chosen reference temperature, T_0°K, and ρ is the density at the temperature of measurement T.[4] The data for the samples of higher molecular weight were multiplied by this factor. Upon finding strong decreases in $J_r(t)$ at relative long times in the response of the low molecular weight samples, we were reluctant to (and did not) apply this amplitude factor, since it enhanced the unexpected anomalous behavior. At this writing we still feel, in principle, that the rubberlike correction should be made to that portion of the compliance above the glassy level. The derived parameters presented below may be in slight error because of this omission.

We propose that our reduction of recoverable compliance curves with slopes differing at relative long times may not violate the requirement that all the mechanisms contributing to the retarded deformation have the same temperature dependence. In fact, we are assuming that those present do, but that the population of mechanisms diminishes with decreasing temperature. This loss of mechanisms is biased toward those with large retardation times. Thus, the shape of the curve is maintained at relative short times and the time scale shifts obtained reflect the temperature dependence of all the mechanisms operative at the temperature of measurement.

Since the temperature dependence of a viscoelastic mechanism can be measured by the magnitude of its retardation time, τ_i, we can follow the example of Williams, Landel, and Ferry[26] and make explicit the indirect effect of temperature on τ_i, which is a function of free volume. Assuming that the volume, v, is a linear function of temperature, the Doolittle free volume equation,[27]

$$\log \tau_i = \log A + [(B/2.303)/\phi] \tag{1}$$

is easily shown to be equivalent to the Vogel equation,[26,28]

$$\log \tau_i = \log A + [(C/2.303)/(T - T_\infty)] \tag{2}$$

A, B, C, and T_∞ are characterizing constants and ϕ is the relative free volume,

$$\phi = (v - v_0)/v_0 \tag{3}$$

where v_0 is the occupied volume. v_0 is considered operationally to be that volume which is unavailable to the molecular process of interest. In this

TABLE II
Temperature Dependences

M	T_0, °C	T, °C	log η	log a_T[a]	log J_e
1.10×10^3	40	30.2	—	3.66	—
		32.5	—	2.90	—
		34.9	—	1.75	—
		37.5	12.113	0.88	−9.45
		40.0	11.283	0.00	−9.41
		43.0	—	−0.86	—
		45.0	9.936	−1.62	−9.28
		47.6	9.252	—	−9.22[b]
		50.0	8.705	—	−9.10[b]
		55.0	7.716	—	−8.95[b]
		60.0	6.817	—	−8.78[b]
		65.0	6.055	—	−8.66[b]
		70.0	5.355	—	−8.51[b]
		80.0	4.294	—	−8.42[b]
		90.0	3.317	—	−8.24[b]
		100.0	2.603	—	−8.19[b]
		110.0	2.011	—	−8.15[b]
		120.0	1.518	—	−8.22[b]
		130.0	1.120	—	−8.15[b]
		140.0	0.797	—	−8.19[b]
		150.0	0.510	—	−8.22[b]
		165.0	0.162	—	−8.28[b]
		180.0	−0.113	—	−8.37[b]
3.4×10^3	100	70.0	12.967	—	−9.37
		75.0	11.152	—	−9.15
		79.8	9.749	—	−8.80
		84.3	8.619	—	−8.40
		89.9	7.609	—	−8.23
		94.3	6.888	—	−8.03
		100.6	5.995	—	−7.89
		109.4	5.047	—	−7.77[c]
		130.3	3.418	—	−7.71[c]
		144.6	2.627	—	−7.72[c]
1.57×10^4	100	109.4	7.966	—	—
		111.4	6.628	—	—
		129.3	5.593	—	—
		138.2	4.837	—	—
		160.0	3.463	—	—
		180.0	2.578	—	—
1.64×10^4	100	93.0	12.156	2.62	−7.94[c]
		96.0	11.088	1.43	−7.54[c]
		100.6	9.820	−0.21	−7.16
		102.9	9.270	−0.91	−7.05[d]
		105.1	8.882	−1.41	−6.96
		109.4	8.116	−2.28	−6.90
		119.4	6.730	—	−6.79
		134.1	5.257	—	−6.75[c]

TABLE II (*continued*)
Temperature Dependences

M	T_0, °C	T, °C	log η	log a_T[a]	log J_e
4.7×10^4	100	97.0	—	1.13	—
		100.6	—	−0.22	—
		101.8	—	−0.58	—
		104.5	10.499	−1.39	−6.45[b]
		106.7	10.033	−1.96	−6.37[b]
		109.5	9.463	−2.58	−6.27[b]
		114.5	8.667	−3.49	−6.24[b]
		125.0	7.323	−4.87	−6.17
		133.8	6.406	−5.67	−6.18
		144.9	5.484	—	−6.18
		160.0	4.506	—	−6.18[c]
9.4×10^4	100	97.9	—	0.67	—
		102.9	—	−0.93	—
		105.7	—	−1.66[5]	—
		109.4	—	−2.67	—
		113.4	10.088	−3.49	−5.94[c]
		119.4	—	−4.49	—
		134.1	7.602	—	−5.88
		144.6	6.698	—	−5.88[c]
		160.0	5.661	—	−5.88[c]
		180.0	4.668	—	—
1.89×10^5	100	100.7	—	−0.22	—
		102.9	—	−1.07	—
		105.1	—	−1.76	—
		109.4	—	−2.92	—
		113.7	11.085	−3.81	−5.90[c]
		116.0	—	−4.21	—
		119.7	10.244	−4.83	−5.90[c]
		144.9	7.700	—	−5.90
		160.3	6.657	—	−5.90
		180.3	5.665	—	−5.85
6.0×10^5	100	100.6	—	−0.23	—
		102.9	—	−1.09	—
		105.1	—	−1.80	—
		109.4	—	−2.98	—
		113.4	—	−3.93	—
		119.4	12.077	−4.94	—
		144.6	9.491	−7.61	—
		160.0	8.434	−8.51	−5.85
		180.0	7.386	−9.29	—
8.0×10^5	100	99.8	—	0.07	—
		102.9	—	−1.06	—
		105.6	—	−1.77	—
		109.4	—	−2.89	—
		119.4	—	−4.70	—
		160.0	8.706	−8.44	—
		180.0	7.666	−9.55	—

[a] From recoverable compliance data.
[b] Calculated from extrapolations in Figure 18.
[c] Value from reasonable extrapolations.
[d] Interpolated values.

context different kinds of molecular motions would see different v_0 values. If v_0 is substantially insensitive to temperature[21] then

$$v = v_0 + \alpha_p(T - T_\infty) \tag{4}$$

where $\alpha_p = dv/dT$, for the polymer melt and T_∞ is the temperature at which the free volume, $v - v_0$, would disappear were it not for the intervention of glass formation. Substitution for ϕ in eq. (1) yields

$$\log \tau_i = \log A + [(Bv_0/2.303\alpha_p)/(T - T_\infty)] \tag{5}$$

Therefore,

$$C = v_0B/\alpha_p \tag{6}$$

Since $a_T = \tau_i/\tau_{i,0}$, where $\tau_{i,0}$ is the value of the retardation time of the mechanism of interest at the chosen reference temperature T_0,

$$\log a_T = I + [(C/2.303)/(T - T_\infty)] \tag{7}$$

where $I = -C/(T_0 - T_\infty)2.303$.

The original Williams-Landel-Ferry (WLF) equation is

$$\log a_T = -c_1(T - T_0)/(c_2 + T - T_0)$$

where T_0 is an arbitrarily chosen reference temperature. When T_g is chosen for the reference temperature the constants c_1 and c_2 are designated as c_1^g and c_2^g and are related to the fractional free volume at the glass temperature, f_g, and the thermal expansion coefficient of the free volume f which is denoted as α_f.

The relations between the Vogel parameters, C and T_∞; the WLF parameters c_1, c_2, f_g, and α_f; and the Doolittle relative free volume, ϕ, and B are

$$C = 2.303\ c_1c_2 = (1/f_g)\Delta = 1/\alpha_f = (B/\phi)(T - T_\infty) = (B/\phi_g)\Delta$$

where $\Delta \equiv T_g - T_\infty$. Williams, Landel, and Ferry assumed $B = 1$. Note that

$$c_2 = T_0 - T_\infty$$

$$c_1 = c_1^g(T_g - T_\infty)/(T_0 - T_\infty).$$

When the experimentally determined shift factors for each sample listed in Table II are fitted to eq. (7), the free volume parameters presented in Table III are obtained. The temperature difference Δ_T is determined from $J_r(t)$ data; the relative free volume at the glass temperature, ϕ_g, is equal to $\alpha_p\Delta/v_0$. To determine values for B it is necessary to make some additional assumption about the temperature dependence of v_0. We have chosen, as mentioned above, to hold v_0 constant. Then with values of the Vogel parameters, α_p, and T_g a value for B can be calculated from $B = C\phi_g/\Delta$. Except for the lowest molecular weight sample, A67[7], v_0 is remarkably constant. There is no doubt that the decrease in v_0 at very

TABLE III
Free-Volume Parameters from the Recoverable Compliance

Mol. wt. $\times 10^{-3}$	T_g, °C		T_∞, °C		Δ_r	B	v_0, cm³/g	$\phi_g \times 10^2$
	Calcd[a]	Combined fit	Individual fit	Combined fit				
1.1	40[b]	34	5	5	29.0[c]	0.571[d]	0.927[d]	1.90[d]
16.4	91.5	93	65	64	26.5	0.500	0.954	1.54
47	95.8	95	70	66	25.8	0.425	0.956	1.48
94	96.9	96.9[e]	68	68[e]	28.9	0.516	0.955	1.67
122	97.2	96.5	68	66.5	29.2	0.490	0.955	1.68
189	97.5	98	68	69	28.5	0.537	0.955	1.70
600	97.8	98	69	69	28.8	0.532	0.955	1.65
800	97.9	99	69	70	28.9	0.504	0.955	1.67
All samples from Figure 6			..	..	28.9	0.516	0.955_3	1.67

[a] From $T_g = 98.0 - 1.02 \times 10^5/M$ as determined by Altares.
[b] Estimated from differential scanning calorimetry data.
[c] In this case alone we used the T_g from the combined fit.
[d] Based on a specific volume at T_g, $v_g = 0.9447$ from Ueberreiter and Kanig,[30] directly. Equation in text not applicable.
[e] Individually determined values for sample M102 accepted as correct and used to fix other relative values.

low molecular weights is real. Because the degree of purity of a polymer is not generally known and because small amounts of residual solvent or even absorbed moisture can significantly decrease the T_g of any given sample, normally one cannot be sure of the actual T_g of a sample being studied within a degree or two.

Positions of $J_r(t)$ curves on the unreduced time scale indicate that the values of our T_g's for samples with $M > 3 \times 10^4$ are relatively correct within $\pm 0.3°C$. Such comparisons are not possible at lower M because the shape of the primary dispersion varies with temperature.

In addition, any T_∞ value cannot be considered dependable to better than a few degrees. With these limitations in mind, examination of the free volume parameters obtained from individual samples indicates sufficient latitude for one equation to serve adequately well for all of the shift data relative to T_g or T_∞. Δ_r can be seen to be as independent of molecular weight as we could expect. Minor manipulations of T_∞ values allowed all of the a_T data to adopt the slope of the line in Figure 6 (referred to in Table III as "combined fit" values). The T_g and Δ_r for sample M102 were assumed to be correct so that the reference temperature chosen would be a reliable T_g. Only two of our points, which are among our least reliable, are significantly off the line. The assumption of a constant Δ_r allows one

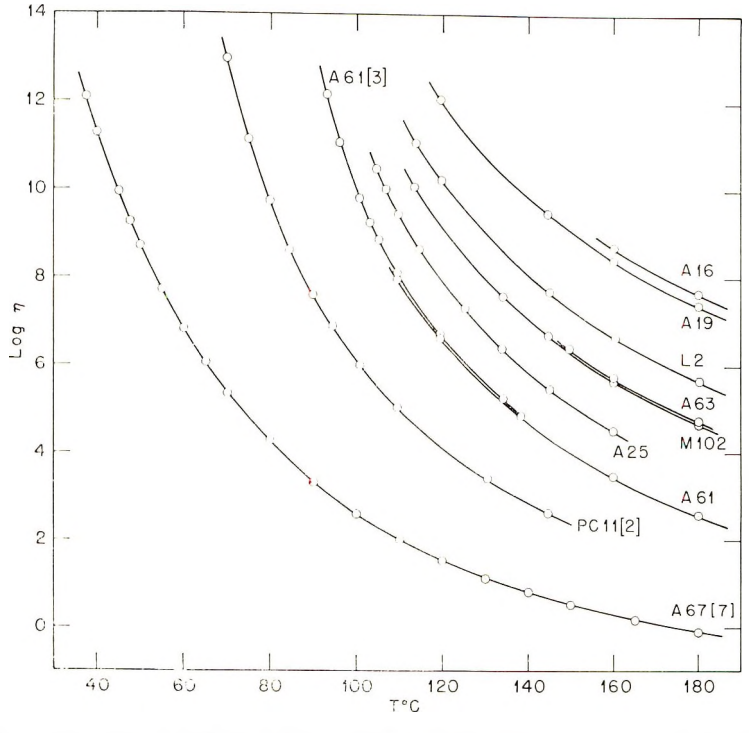

Fig. 14. Plots of the logarithm of the viscosity η (poise) vs. temperature T. Molecular weights of indicated samples are tabulated in Table I.

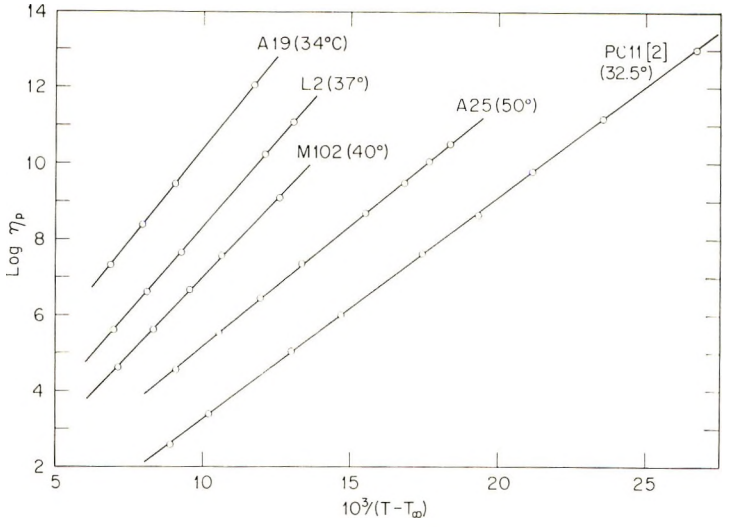

Fig. 15. Semilogarithmic plots of the reduced (corrected for entropic forces) viscosity η_p against the reciprocal of the temperature difference, $(T - T_\infty)$. Molecular weights of samples are given in Table I. T_∞ values empirically determined to give best straight lines are indicated in parentheses.

to calculate effective relative T_g values as determined by the recoverable compliance measurements (see Table III). It is, therefore, expected that with one determined T_g for any given polymer the value for any other molecular weight can be determined from the temperature dependence of viscoelastic data. A glass temperature of 70°C is deduced for sample PC 11[2]. We wish to emphasize that no deviation from the free volume equation (7) is found below the conventional glass temperature so long as an equilibrium density is obtained.[21] The equation for the line in Figure 6 is $\log a_T = -13.46 + 389\,(T - T_\infty)^{-1}$.

Let us now turn to the temperature dependence of the viscosity and note that it is the viscosity which is most often used in testing rate process theories. All of the viscosities that have been determined on the samples described in Table I are shown in Figure 14 and listed in Table II as a function of temperature. Most of the samples were measured from the neighborhood of T_g up to 180°C. We include in this paper on low molecular weight samples our data on high molecular weight polystyrenes so that a more complete picture of the viscosity temperature dependence for the polystyrene system can be given. Over the entire molecular weight range studied the usual characteristic increase in temperature sensitivity is seen as T_g is approached. Plots of log η versus $1/T$ show strong positive curvature, so, as is well known, Arrhenius temperature dependence is not observed. This viscosity behavior is therefore not simply thermally activated process behavior. However, the data for all the samples with the exception of that of the lowest molecular weight sample, A67[7], can be satisfactorily fitted to a Vogel equation. Figure 15 presents five examples

TABLE IV
Free-Volume Parameters from Viscosity Behavior

Mol. wt. × 10^{-3}	Graphical fit of data					Computer fit of data			
	T_∞, °C	Δ_η	B	v_0, cm³/g	ϕ_g × 10^2	T_∞, °C	C	log A	ϕ_g × 10^2
1.1[a]	−13	53	1.33	0.916[b]	3.12[b]	−14.0	2061	−5.27	3.19[a]
3.4	32.5	37	0.81	0.941	2.15	32.6	1333	−2.52	2.26
15.7	40	51.5	1.00	0.940	3.04	39.3	1734	−2.77	3.08
16.4	55	36.5	0.67	0.949	2.14	—	—	—	—
47	50	45.8	0.85	0.945	2.67	46.5	1626	−1.69	2.88
94	40	56.9	1.14	0.940	3.33	39.6	1939	−1.31	3.36
189	37	60.5	1.22	0.938	3.55	38.7	1994	−0.46	3.45
600	34	63.8	1.32	0.936	3.65	35.6	2156	0.91	3.65

[a] Eight highest temperature points omitted from calculations.

[b] Based on a specific volume at T_g, v_g = 0.9447 from Ueberreiter and Kanig[39] directly. Equation in text not applicable.

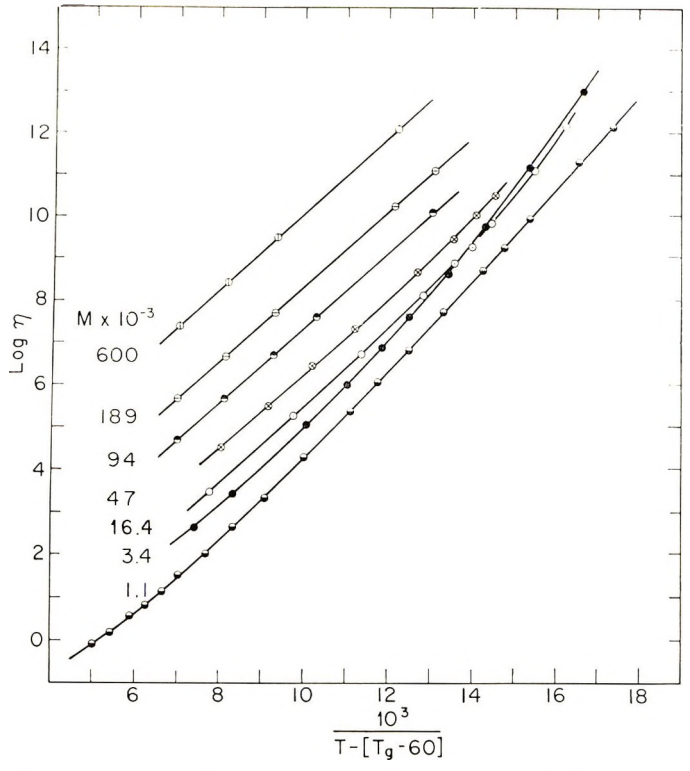

Fig. 16. Plots of the logarithm of the viscosity η (poise) vs. the reciprocal of the temperature, $T - [T_g - 60°C]$ for the molecular weights as indicated.

of the excellent fits that were obtained over a large range of molecular weights, 3.4×10^3 to 6.0×10^5. As far as we know, all polymer viscosity data in the literature can be accommodated by the Vogel expression within experimental scatter.

The Vogel expression is just one of the expressions that is associated with WLF free volume theory.[21,26,27] We have chosen to work with this form because the quality of the fit can be judged by means of simple visual inspection. With the Vogel parameters C and T_∞, the free volume parameters can be determined; see relations given above. The best values that we could determine graphically, treating the viscosity values determined for each sample separately, are presented in Table IV. In the last four columns, for comparison, are objective computer determinations of the best Vogel parameters carried out through the kindness of André Kovacs.* Examination of the resultant parameters reveals that as a function of molecular weight they make no more sense than does human behavior. T_∞ doesn't parallel T_g; it goes through a maximum as does the insensitive V_0. The parameter B, which Turnbull and Cohen associate with the

* Computer calculations were carried out at the Centre de Recherches sur les Macromolecules, Strasbourg, France, by R. Suzuki.

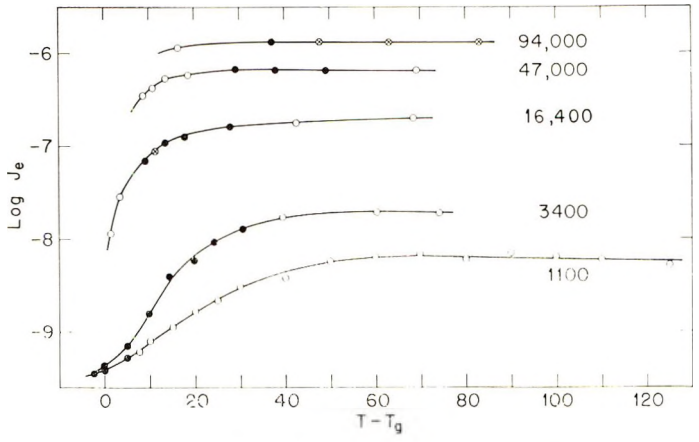

Fig. 17. Semilogarithmic plots of the equilibrium recoverable compliance J_e (cm²/-dyne) as a function of the temperature, $T - T_g$, for the identified molecular weights: (●) measured values; (⊗) interpolated or extrapolated values; (○) calculated from analysis of Fig. 18.

critical relative volume necessary for a molecular jump[29] varies by over a factor of 2. ϕ_g jumps about and goes through a well-defined minimum (if we temporarily ignore sample A-61). The only conclusions one can draw are that the data are poor or a free volume interpretation of the temperature dependence of the viscosity is not proper.

Let us examine how the data behave if we assume the desirable feature that $T_g - T_\infty = \Delta_\eta$ is a constant as was found in the behavior of the recoverable compliance shift factors. In Figure 16 we have chosen a Δ_η of 60, which is characteristic of the high molecular weight samples. Instead of yielding a set of parallel straight lines, as is hoped, not only do the data from the lower molecular weights form curved lines, but that of sample PC-11[2] even crosses that of A61[3]. This appears to be a clear indictment of the free volume theory as propounded in recent years.

If at this point we reflect on the unexpected behavior of the recoverable compliances of the low molecular weight samples, described above, we realize that the viscosity curves in Figure 16 with positive curvature were obtained from these same samples.

The steady-state compliances determined on the lower molecular weight samples are presented as a function of $T - T_g$ in Figure 17. The solid circles represent well-defined determinations and the crossed circles short extrapolations. The open circles are predictions which will be explained presently. Even if the open circles are ignored, a pattern can be discerned which has the following features: (1) J_e decreases substantially as T_g is approached from above; (2) above T_g a fairly constant asymptote is approached; and (3) the asymptote is approached in an increasingly smaller temperature interval as the molecular weight increases. Many of the predicted points are subject to experimental verification. Such verification where deemed necessary will be attempted in the future. However,

two regions of response do not appear to be accessible. The J_e for samples with molecular weights above 10^5 cannot be measured in the neighborhood of T_g, because of the excessively long times required to achieve steady state creep. Creep recovery studies on very low molecular weight materials are exceedingly demanding at temperatures well above T_g. The viscosity decreases so rapidly with increasing temperature that the condition of negligible inertial forces cannot be met. It is likely that dynamic mechanical measurements will be possible at temperatures 30–40°C above the glass temperature. It does not appear that present day instrumentation can extract information on the recoverable deformation at still higher temperatures.

Now if we stop to consider the dictates of the eminently successful theory of linear viscoelasticity[4,31,32] the measure of the relative time scale or rate of response is not the viscosity but the relaxation times τ_i involved. We can make use of the measured temperature dependence of J_e in determining the temperature dependence of the relaxation times that govern the terminal zone[4] of viscoelastic response and hence the viscous deformation processes. In terms of the generalized Maxwell model for viscoelastic behavior and existing molecular model theories the last few relaxation times largely determine the viscosity.[4] Markovitz has shown[33] that when temperature reduction is applicable the time scale reduction factor is

$$a_T = \eta(T)J_e(T)/\eta(T_0)J_e(T_0) \tag{8}$$

where $\eta(T_0)$ and $J_e(T_0)$ are the limiting low rate of shear viscosity and the steady-state compliance, respectively, at a chosen reference temperature and $\eta(T)$ and $J_e(T)$ are the corresponding values at the temperature of measurement. Although temperature reduction fails for the recoverable compliance response of low molecular weight polystyrene in the neighborhood of the glass temperature it is clear that since η and J_e are steady-state parameters that determine the final form of the terminal zone of viscoelastic response together, their product ηJ_e is the proper measure for the time-scale behavior. In other words their product can be considered to be a "terminal characteristic time" whose magnitude fixes the time scale of response. Experimentally, all previous data allowed $\eta(T)$ as well as a_T to represent the temperature dependence of the time scale of response simply because most of the $\eta(T)$ data in the literature[34] were obtained at temperatures sufficiently removed from T_g where $J_e(T)$ is a very weak function of the temperature. The dramatic decrease in J_e of the 3400 molecular weight sample with decreasing temperature is seen to be the reason for the curvature and the cross-over seen in Figure 16. To check this conclusion we examine whether the temperature dependence of the product ηJ_e can be effectively rationalized with the above outlined free volume analysis. Figure 18 where $\log \eta J_e$ is plotted against $[T - (T_g - 60)]^{-1}$ testifies that relative to T_g one set of free volume constants can satisfactorily describe the temperature dependence of our "terminal relaxation time" over the molecular weight range studied. In this plot we

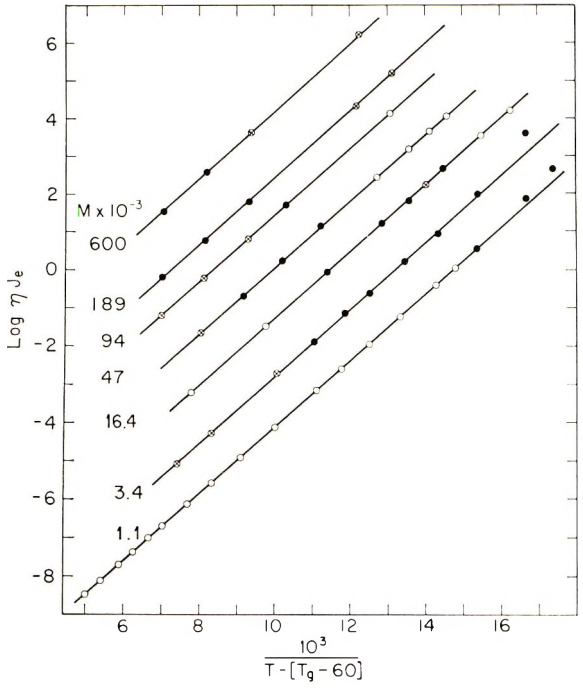

Fig. 18. Semilogarithmic plots of the product of the viscosity η (poise) and the equilibrium recoverable compliance J_e (cm²/dyne) against the reciprocal of the temperature, $T - [T_u - 60°C]$. Viscosities for all plotted points were measured. (●) J_e measured, (⊗) J_e extrapolated or interpolated from creep data; (○) extrapolations to permit calculation of J_e. Molecular weights of samples are shown. The line for M = 1100 has been drawn parallel to that for M = 3400.

have assumed a constant $\Delta_T = 60$. The filled points in Figure 18 represent data where both η and J_e were measured. To obtain the crossed circle points an interpolation or an extrapolation in a temperature range where J_e was not changing appreciably was used to obtain J_e. The viscosities for all the data points were measured and in the case of the open circles the data were used to predict the open points in Figure 17.

The curves for the 3400 and 16,400 molecular weight samples are crucial for this assessment and fortunately are well defined. The fact that the lowest temperature points for the two lowest molecular weight samples deviate from the lines almost certainly is an indication that the glassy compliance, J_g, may not be involved in determining the time scale for viscous deformation and that the terminal relaxation time should be calculated as ηJ_d. At higher temperatures and molecular weights the difference between J_d and J_e is negligible. The use of J_d is strictly required for the same reasons that Ferry and Fitzgerald[35] subtract the glassy compliance before reducing their dynamic data; the temperature dependence of mechanisms contributing to J_g is distinctly different from that of the mechanisms contributing to the principal dispersion.

TABLE V
Free-Volume Parameters from Terminal Characteristic Times

$$\log \eta J_r = \log A + C/2.303\,[T - (T_g - 60)]$$

Mol. wt. $\times 10^{-3}$	$-\log A$	$C/2.303$	v_0, cm³/g	$\phi_g \times 10^2$	B	$\phi_g/B \times 10^2$
1.1	12.62	—	0.908	4.02	1.34	3.00
3.4	11.35	874	0.928	3.68	1.24	2.98
16.4	9.87	877	0.937	3.54	1.20	2.97
47	8.53	877	0.937	3.54	1.19	2.98
94	7.13	876	0.938	3.53	1.19	2.98
189	6.23	886	0.938	3.52	1.20	2.94
600	4.49	887	0.938	3.52	1.20	2.94
		878 Avg.				

In Table V, we see the slopes observed in Figure 18 are constant to within ±1%. Therefore, within our homologous system, the data for the "terminal characteristic times" are compatible with a constant Δ_τ and a constant Vogel parameter C. It must be noted that the parameters, $\Delta_\tau = 60$ and $C = 2{,}022$ which apply to the "terminal characteristic time," ηJ_e, are substantially different from those that apply to the recoverable compliance behavior, $\Delta_r = 29$ and $C = 896$. Since α_p increases with decreasing molecular weight, a constant Δ demands that B and ϕ_g be dependent on molecular weight.

It is obvious that if Δ and C are constants for the entire range of molecular weight covered in the polystyrene system, their ratio is constant and hence so is the ratio ϕ_g/B.

Three levels of constancy of free volume parameters must be recognized: (1) constancy between different molecular mechanisms; (2) constancy within a homologous series of polymers; i.e., constancy with only a variation of molecular weight; (3) constancy between different materials. It has been pointed out above that Δ and C are constants for polystyrene of various molecular weight; but it can be seen from Tables IV and V that different values are obtained from the analysis of $J_r(t)$ and ηJ_e data. However, for the $J_r(t)$ data, $\phi_g/B = 0.032_4$ and for the ηJ_e data $\phi_g/B = 0.029_7$. The difference is a mere 9% that could result from experimental error and from any one of the specific assumptions we have made in our analysis which is only approximate. However, since

$$\phi_g/B = \Delta/C \tag{9}$$

and Δ and C are the primary parameters extracted from the data, the assumption that v_0 is insensitive to temperature is not involved in determining ϕ_g/B. Δ, which is equal to the WLF constant c_2^g, is often about 50°C for polymers.[26] Nonequivalent T_g's (i.e., measured at different rates) for different materials will, of course, cause a variation of the ratio Δ/C.

TABLE VI
Temperature Dependence Parameters for Various Materials

	T_v, °K	Measurement[a]	C	Δ	$\phi_v/B \times 10^2$	Reference
Polystyrene	371	$J_r(t)$	896	29	3.24	This work
		ηJ_e	2,002	60	2.97	This work
		η	1,790	60	3.36	34
Polyisobutylene	202	J^*	3,980	104.4	2.62	4
		η	3,125	80	2.56	34
Poly(vinyl acetate)	305	J^*	1,686	46.8	2.78	4
		η	2,183	57	2.61	34
Poly(methyl acrylate)	276	J^*	1,876	45	2.40	4
		η	2,304	61	2.65	34
Poly(methyl methacrylate) (ideally atactic)	379	$J(t)$	2,850	86	3.02	37
		η	2,718	80	2.95	38
Poly(ethyl methacrylate)	335	J^*	2,653	65.5	2.47	4
		η	2,880	70	2.43	34
Poly(*n*-butyl methacrylate)	300	J^*	3,780	96.6	2.56	4
		η	3,080	80	2.60	34
Poly(*n*-hexyl methacrylate)	268	J^*	5,310	129.4	2.44	4
		η	3,310	90	2.72	34
Polydimethylsiloxane	150	η	1,405	120	0.85	39
Poly(dimethyl diphenyl zinc phosphinate)	324	$J(t)$	1,135	22	1.94	40
1,3,5-tri(α-naphthyl)benzene	342	g	1,570	42	2.68	41
		η	9,440	142	1.50	21

[a] $J(t)$, total creep compliance; $J_r(t)$, recoverable compliance; J_e, steady state compliance; J^*, complex dynamic compliance; g, crystal growth rate; η, viscosity (high temperature data for polymers, $T > T_v + 30$°C, on high molecular weight polymers used).

The WLF free volume equation[26] with "universal" constants, c_1^g = 17.44 and c_2^g = 51.6 is impressive in approximating the temperature dependence of relaxation and transport behavior of many glass-forming substances, but even in its original presentation the lack of true universality was clearly pointed out. A greater degree of constancy from system to system in one of the derived free volume parameters, f_g, was noted over that of α_f. Williams, Landel, and Ferry pointed out that "the existence of a universal value of f_g is, of course, consistent with the view of Fox and Flory[36] that the glass transition is an iso-free-volume state."[26] We wish to suggest a slightly different criterion for the glass temperature: the constancy of ϕ_g/B alone. *At T_g, the free volume is a fixed proportion of the critical volume necessary for a molecular relaxation process.* We interpret this to mean that holes larger than the required critical size must spontaneously appear at a rate compatible with the rate of measurement of T_g. Since we have demonstrated that the free volume expression is appropriate strictly to molecular relaxation and not to molecular transport, we are in a position to show a greater universality of ϕ_g/B than could Williams, Landel, and Ferry[26] and Berry and Fox.[34] In Table VI, we have selected examples of free-volume parameters where the temperature dependence of primary relaxation has been determined by more than one method. The temperature dependence of the viscosity can generally, but not always, be used to describe that of the relaxation behavior. The necessary conditions apparently are that the polymer be of high molecular weight and that the span of temperature covered be appreciably above T_g. Examination of the first eight materials listed reveals that the parameters C and Δ vary over a factor of 5, but the standard deviation from the mean of ϕ_g/B = 0.0273 is 10%. We can conclude that this value appears to be the sole criterion for the glass temperature in the most general sense listed above. If the parameters T_∞ and C for primary relaxation, are known, it should be possible to estimate an unknown T_g, which is likely to be within 5°C of a conventionally measured value, by using

$$T_g = T_\infty + 0.0273C \tag{10}$$

The last three materials entered in Table VI are examples of the substances that exhibit behavior that appears to depart from the criterion of constant ϕ_g/B. However, the properties that indicate the departure are total creep and viscosity, and the observed temperature dependences have not been proved to be that of relaxation. In fact, the temperature dependence of the transport factor involved in the crystal growth g of the nonpolymeric glass-former 1,3,5-tri-α-naphthylbenzene does yield a ϕ_g/B ratio that is within 2% of the average found above. Crystal growth is assumed to be proportional to self-diffusion, which has been assumed to involve relaxation.[29] It has already been suggested that the difference between the temperature dependences of g and η is a result of a strong temperature dependence of the modulus of rigidity involved in the pertinent relaxation times.[42]

CONCLUSIONS

The time-scale shift factors for the recoverable and the viscous deformation of polystyrene are different. Therefore, temperature reduction of the total creep compliance data is not correct.

The steady-state compliance of low molecular weight polystyrene decreases appreciably with decreasing temperature as the glass temperature is approached.

A single pair of free volume parameters can successfully describe the time scale shift factors of the recoverable compliance over most of the molecular weight range studied.

It has been demonstrated that a free-volume analysis should not be applied to the viscosity temperature dependence, but to the temperature dependence of the characteristic time ηJ_e.

Additional evidence for the concept of a single criterion for glass formation, a universally constant value of $\phi_0/B = 0.0273$, is presented.

Sizable effects on the recoverable compliance from residual molecular weight heterogeneity are possible.

This work was supported in part by the Office of Naval Research, Contract No. Nonr 2693(00) and the development of the principal instrument used in this investigation was supported by the National Aeronautics and Space Administration under Research Grant NsG 147-61. The authors wish to also thank those mentioned who helped in the sample characterization and preparation. Valuable discussions with Drs. Hershel Markovitz and Guy Berry are gratefully acknowledged.

References

1. R. Waach, A. Rembaum, J. D. Coombes, and M. Szwarc, *J. Amer. Chem. Soc.*, **79**, 2026 (1959).
2. D. J. Worsfold and H. Bywater, *Can. J. Chem.*, **38**, 1894 (1960).
3. F. Wenger and S. P. S. Yen, *Makromol. Chem.*, **43**, 1 (1961).
4. J. D. Ferry, *Viscoelastic Properties of Polymers*, Wiley, New York, 1961.
5. H. Leaderman, R. G. Smith, and L. C. Williams, *J. Polym. Sci.*, **36**, 233 (1959).
6. A. V. Tobolsky, J. J. Aklonis, and G. Akovali, *J. Chem. Phys.*, **42**, 723 (1965).
7. G. Akovali, *J. Polym. Sci.*, **5**, 875 (1967).
8. J. M. O'Reilly and W. M. Prest, Jr., paper presented at 37th Annual Meeting of the Society of Rheology, Atlantic City, October 31–November 2, 1966.
9. H. Odani, S. Kitamura, N. Nemoto, and M. Kurata, 5th International Congress on Rheology, October 7–11, 1968, Kyoto, Japan.
10. J. E. Frederick, N. W. Tschoegl, and J. D. Ferry, *J. Phys. Chem.*, **68**, 1974 (1964).
11. L. A. Holmes and J. D. Ferry, in *Macromolecular Chemistry, Kyoto–Tokyo 1966* (*J. Polym. Sci. C*, **23**), I. Sakurada and S. Okamura, Eds., Interscience, New York, 1968, p. 291.
12. A. J. Kovacs, R. A. Stratton, and J. D. Ferry, *J. Phys. Chem.*, **67**, 152 (1963).
13. C. A. F. Tuijnman and H. C. Booij, *Rheol. Acta*, **5**, 292 (1966).
14. D. J. Plazek, *J. Polym. Sci. A-2*, **6**, 621 (1968).
15. T. Altares, Jr., D. P. Wyman, and V. R. Allen, *J. Polym. Sci. A*, **2**, 4533 (1964).
16. C. Rossi, V. Bianchi, and E. Bianchi, *Makromol. Chem.*, **41**, 31 (1960).
17. T. G. Fox and S. Loshaek, *J. Polym. Sci.*, **15**, 371 (1955).
18. H. Leaderman, R. G. Smith, and R. W. Jones, *J. Polym. Sci.*, **14**, 47 (1954).
19. D. J. Plazek and V. M. O'Rourke, *J. Phys. Chem.*, **69**, 3480 (1965).

20. D. J. Plazek, to be published.
21. D. J. Plazek and J. H. Magill, *J. Chem. Phys.*, **45**, 3038 (1966).
22. D. J. Plazek, *J. Colloid Sci.*, **15**, 50 (1960).
23. B. D. Coleman, H. Markovitz, and W. Noll, *Viscometric Flows of Non-Newtonian Fluids*, Springer-Verlag, New York, 1966, p. 87.
24. R. A. Stratton, paper presented at 39th Annual Meeting of the Society of Rheology, January 1969.
25. R. A. Stratton, private communication.
26. M. L. Williams, R. F. Landel, and J. D. Ferry, *J. Amer. Chem. Soc.*, **77**, 3701 (1955).
27. A. K. Doolittle, *J. Appl. Phys.*, **22**, 1471 (1951).
28. H. Vogel, *Physik* Z., **22**, 645 (1921).
29. D. Turnbull and M. H. Cohen, *J. Chem. Phys.*, **34**, 120 (1961).
30. K. Ueberreiter and G. Kanig, *J. Colloid Sci.*, **7**, 569 (1952).
31. B. Gross, *Mathematical Structure of the Theories of Viscoelasticity*, Herman, *et al.*, Paris, 1953.
32. A. V. Tobolsky, *Properties and Structure of Polymers*, Interscience, New York, 1962.
33. H. Markovitz, *J. Phys. Chem.*, **69**, 671 (1965).
34. G. C. Berry and T. G. Fox, *Fortschr. Hochpolym. Forsch.*, **5**, 261 (1968).
35. J. D. Ferry and E. R. Fitzgerald, *J. Colloid Sci.*, **8**, 224 (1953).
36. T. G. Fox and P. J. Flory, *J. Appl. Phys.*, **21**, 581 (1950).
37. D. J. Plazek and V. M. O'Rourke, unpublished data.
38. S.-P. S. Yen, unpublished data.
39. D. J. Plazek, W. Dannhauser, and J. D. Ferry, *J. Colloid Sci.*, **16**, 101 (1961).
40. D. J. Plazek, *Trans. Soc. Rheol.*, **91**, 119 (1965).
41. J. H. Magill and D. J. Plazek, *J. Chem. Phys.*, **46**, 3757 (1967).
42. D. J. Plazek and J. H. Magill, *J. Chem. Phys.*, **49**, 3678 (1968).

Received February 12, 1970
Revised July 2, 1970

JOURNAL OF POLYMER SCIENCE: PART A-2 VOL. 9, 245–265 (1971)

Axial Dispersion of Solute Zones in Gel Permeation Chromatography

HERBERT R. HALVORSON and GARY K. ACKERS,
Department of Biochemistry, University of Virginia, Charlottesville, Virginia 22901

Synopsis

The two essential aspects of axial dispersion in gel permeation chromatography have been studied: (1) the relationship of axial dispersion to the continuity equations of chromatographic transport, and (2) the relationship to molecular size and the system parameters of an individual column. Theoretical analyses are presented for both of these problems and are applied to an experimental study of axial dispersion by both zonal (small-zone) and frontal (large-zone) experiments with a series of macromolecular species having discrete, precisely known molecular weights. Theoretically predicted non-Gaussian elution profiles were observed for the small-zone experiments, and axial dispersion coefficients for each molecular species were determined as a function of flow rate. Resulting values were found to be in good agreement with the theoretical equation relating axial dispersion to molecular size, flow rate, and two "calibration constants" of the column. These results provide a rational basis for axial dispersion effects in terms of the fundamental processes and system parameters of gel columns. Extension of the analysis to multicomponent systems is discussed.

INTRODUCTION

Gel permeation chromatography is used extensively for polymer fractionation, for characterization of molecular size and weight distributions, and for studies of macromolecular interaction. In each of these applications it is important to have an accurate quantitative understanding of the fundamental processes which underlie the technique so that experimental design may be optimized and maximum information extracted from the data. In this paper we present results of an experimental study in which the basic theory of axial dispersion in gel columns has been verified.

The behavior of single-component solute zones in gel chromatography can be fully characterized by two phenomenological parameters: (1) the partition coefficient, which determines the average rate of solute transport within the column and reflects the degree of gel penetration by the solute molecule; and (2) the axial dispersion coefficient (or equivalent plate height), which describes spreading of the solute zone on the column under specified operating conditions. For noninteracting multicomponent systems the behavior of solute zones is determined by the values of these two parameters for each species plus the weight fraction of each species

in the sample. With interacting systems of macromolecules it is necessary also to know values of the interaction constants involved. In studies of macromolecular solutes primary attention has usually been focused on the first of the above parameters (partition coefficient) and advantage taken of its dependence on molecular size or weight. Either the axial dispersion effects have been ignored or corrections have been made based on some arbitrarily assumed shape such as a Gaussian distribution curve. The latter approach has been applied (usually via the Tung equation[1]) to the analysis of molecular weight distributions in heterogeneous polymer samples with reasonable accuracy in certain cases.[2-4] The success of this method lies in the fact that, although elution curves of individual components are not strictly Gaussian, the error introduced by the Gaussian approximation is small under most operating conditions, as will be seen. It is clear that an adequate basis for such analyses requires solution of the appropriate differential equations of chromatographic transport within the gel column, and experimental testing of the resulting equations for single, homogeneous solutes covering a range of molecular size. In this paper we present results of an investigation in which the theoretically predicted non-Gaussian shapes of solute profiles have been experimentally studied and the basic continuity equation for gel permeation chromatography verified.

An important feature of gel permeation chromatography is that the axial dispersion coefficient depends on molecular size in addition to flow rate, gel porosity and column packing. Consequently theoretical plate models in which the height equivalent theoretical plate is assumed constant for all molecular species show large discrepancies with experimental results.[5] In the present study we have verified a theoretical relationship based on a "continuous" model of chromatography. The new relationship explicitly includes the effects of molecular size as well as flow rate and column packing. It is also simple, in that only two adjustable constants are required and the constants have a readily attributable physical meaning.

In this investigation we have used single, homogeneous macromolecular solutes to test theories of chromatographic behavior. In critical studies of axial dispersion even a small degree of molecular weight heterogeneity (resulting in a slight skewing of boundary shapes) can produce highly misleading results. We have therefore used selected biopolymers of precisely known, discrete molecular weights rather than narrow (heterogeneous) molecular weight fractions of synthetic polymer materials.

THEORY

The theory of gel permeation chromatography and its analytical applications has been treated extensively elsewhere.[6-8] The presentation here will summarize the analysis which leads to solutions of the continuity equation for the system. These solutions predict the shape and position of solute zones both within the column and as elution profiles. Subse-

quently we review the analysis leading to a relationship between the coefficient of axial dispersion, column parameters, and solute molecular size. First we define the basic variables to be used.

Definition of Variables

The bulk flow rate F is assumed constant. The distribution volume $\bar{V}$ is the volume within the column which is accessible to a given solute. The void volume V_0 is the distribution volume of a totally excluded solute and the internal volume V_i is the difference between the distribution volumes of a totally nonexcluded solute and a totally excluded solute. The partition coefficient σ is $(\bar{V} - V_0)/V_i$, i.e., the fraction of the internal volume accessible to the solute.* For the low concentrations used here it is a valid assumption that σ and $\bar{V}$ are independent of the concentration C.[6] A useful parameter is $\xi = \bar{V}/V_t$, where V_t is the total volume of the column. By defining $\alpha = V_0/V_t$, and $\beta = V_i/V_t$, it follows directly that $\bar{V} = V_0 + \sigma V_i$ and $\xi = \alpha + \beta\sigma$. The cross-sectional area of the column a, multiplied by ξ, gives the cross-sectional area accessible to the solute.

Description of Solute Zones

The continuity equation for partitioning between stationary and mobile phases with simultaneous axial dispersion is[6]

$$\frac{\partial C}{\partial t} + \frac{F}{\xi a}\frac{\partial C}{\partial x} = L\frac{\partial^2 C}{\partial x^2} \tag{1}$$

where L is a coefficient of axial dispersion (with units of square centimeters per second) and x is distance from the top of the column. The flow equation for total solute flux is

$$J = (FC/\xi a) - L(\partial C/\partial x) \tag{2}$$

J is the rate of solute transport per unit cross-sectional area occupied by solute (ξa).

Equation (2) follows directly from eq. (1) and the general continuity equation,

$$\frac{\partial C}{\partial t} = -\partial J/\partial x$$

* The analysis could also be carried out in terms of a partition coefficient defined relative to the total gel volume:

$$K_{AV} = (\bar{V} - V_0)/(V_t - V_0)$$

The relation between this coefficient and σ is:

$$\sigma = K_{AV}(1 + \bar{V}_g/S_r)$$

where $\bar{V}_g$ is the anhydrous partial specific volume of the gel-forming material and S_r is the solvent regain (grams of solvent imbibed per gram of gel-forming material at swelling equilibrium).

Equation (2) has the form of Fick's first law of diffusion for a moving frame of reference. The reference frame is located at the position of the "average solute molecule" (e.g., the peak of a profile within the column) and moves with a velocity $F/\xi a$. Let $\phi = x - (Ft/\xi a)$ be the new position coordinate. Since $F(\partial C/\partial V) = \partial C/\partial t$ where V is volume of solvent passed through the column (F constant), eq. (1) becomes

$$\partial C/\partial V = L_V(\partial^2 C/\partial \phi^2) \tag{3}$$

with $L_V = L/F$. This coefficient of axial dispersion L_V is the quantity determined directly in experiments. The coefficient L can subsequently be calculated since F is known.

Two types of elution experiments were performed in this study, requiring different solutions of eq. (3). In the "small-zone" experiment (zonal analysis) the solute is applied as an instantaneous pulse (amount s). The solution to eq. (3) for this case is best formulated with the Dirac delta function $\delta(x)$. For the boundary conditions

$$\begin{aligned} C(x,0) &= \delta(x)\cdot s \quad x \geq 0 \\ C(0,V) &= 0 \qquad\quad V > 0 \end{aligned}$$

the solution of eq. (3) is

$$C = (s/2\xi a\sqrt{\pi L_V V}) \exp\{-\phi^2/4L_V V\}$$

Substituting for ϕ and noting that $x = \bar{V}/\xi a$ at the bottom of the column, we have

$$C = (s/2\xi a\sqrt{\pi L_V V}) \exp\{-(\bar{V} - V)^2/4\xi^2 a^2 L_V V\} \tag{4}$$

It is apparent that, although C is Gaussian with respect to ϕ (and hence x) at fixed V, it is clearly a non-Gaussian function with respect to V at constant x (equal to the column length in an elution experiment). Whereas the solute distribution along the column at any instant is Gaussian, the distribution with respect to time as a zone moves past any point of the column is non-Gaussian. The physical basis of this effect is simply the prolonged time for dispersion of the latter part of the solute zone. It is thus an "end effect" of elution from a column of finite length.

A second consequence of this "end effect" is that the distribution volume $\bar{V}$ does not correspond exactly to the maximum (peak) concentration of the elution profile. At the peak volume V_M, we have from eq. (4):

$$\frac{dC}{dV} = \left[\frac{\bar{V} - V_M}{2\xi^2 a^2 L_V V_M} + \frac{(\bar{V} - V_M)^2}{\xi^2 a^2 L_V V_M{}^2} - \frac{1}{2V_M}\right] C = 0$$

and by rearrangement, $\bar{V} = V_M\sqrt{1 + (2\xi^2 a^2 L_V/V_M)}$
or, since $\xi \approx V_M/V_t$, the distribution volume is given by:

$$\bar{V} = V_M\sqrt{1 + 2\xi a^2 L_V/V_t}.$$

The square root is roughly 1.002 for real systems, producing an error in $\bar{V}$ of 0.01 ml. If $\bar{V}$ is determined independently this relationship provides an additional determination of L_V:

$$L_V = \frac{\bar{V}^2 - V_M^2}{2\xi^2 a^2 V_M}.$$

In practice $\bar{V}$ may be rigorously determined as the measured centroid of the elution profile. For most purposes, however, use of V_M represents a sufficiently accurate approximation.

In the second type of experiment, a "large-zone" experiment (frontal analysis), solute of concentration $C = C_0$ is applied in a volume sufficiently large to produce a plateau ($C = C_0$) in the elution profile. The leading and trailing edges of the profile have separate solutions.

Leading edge:*

$$C(x,0) = 0$$

$$C(0,V) = C_0$$

$$C(x,V) = \frac{C_0}{2} \operatorname{erfc}\left[\frac{\phi}{\sqrt{4L_V V}}\right]$$

or, at fixed x:

$$C(V) = \frac{C_0}{2} \operatorname{erfc}\left[\frac{\bar{V} - V}{\sqrt{4\xi^2 a^2 L_V V}}\right] \tag{5}$$

Trailing edge:

$$C(x,0) = C_0$$

$$C(0,V) = 0$$

$$C(V) = \frac{C_0}{2} \operatorname{erfc}\left[\frac{(V - \bar{V})}{\sqrt{4\xi^2 a^2 L_V V}}\right]. \tag{6}$$

It is apparent from these relations that the concentration profile of an elution experiment is not a simple error function complement of the volume, since the V coordinate appears in a nonsimple manner in both numerator and denominator of the argument of the error function complement. This deviation represents the same "end effect" as that mentioned above for the small-zone case. It can be seen from the above solutions—eqs. (4) and (6)—to the continuity equation that the two types of experiment provide independent means for determination of column parameters and verification of theory.

* The error function complement is defined by

$$\operatorname{erfc}(x) = \frac{2}{\sqrt{\pi}} \int_x^\infty e^{-t^2}\, dt = 1 - \frac{2}{\sqrt{\pi}} \int_0^x e^{-t^2}\, dt$$

The inverse error function complement is defined as $\operatorname{inverfc}(y) = x$, where $y = \operatorname{erfc}(x)$.

Analysis of L_V

The following analysis provides the basis for quantitatively determining the dependence of L_V on system parameters: solute molecular size, flow rate, gel particle characteristics (size and shape), and column characteristics (physical dimensions and packing). This analysis uses the approach developed originally by Glueckauf[9,10] but is formulated without recourse to theoretical plates and incorporates the system parameters peculiar to gel chromatography. Total axial dispersion is analyzed as the sum of dispersions contributed by nonuniformities in packing, axial diffusion (in both phases), and nonequilibrium between phases:

$$L_V = L_P + L_D + L_N. \tag{7}$$

The first term, L_P, comes from the finite size of the gel particles and the random variations in particle packing. Such variations produce variations in velocity between microscopic regions within the column. By summing the velocity fluctuations over the whole column, even a column of impenetrable glass beads will produce a solute distribution which closely approximates a Gaussian curve.[11,12] This effect is independent of F (at moderate flow rates), directly proportional to gel particle size d, and to an unknown extent unique to the particular column.

The diffusional second term is evaluated from

$$J = -\xi D\left(\frac{\partial C}{\partial \phi}\right)$$

or

$$\frac{\partial C}{\partial V} = \frac{\xi D}{F}\frac{\partial^2 C}{\partial \phi^2}$$

to give

$$L_D = \xi D/F$$

where D is the free diffusion coefficient. This term varies inversely with flow rate and becomes small in a nonsimple fashion for large solute molecules.

In the presence of a net flow, the finite time necessary for exchange of solute between the two phases introduces a nonequilibrium perturbation within the zone. As a result the actual amount of solute within the stationary phase differs slightly from that prescribed by the equilibrium partition isotherm. This isotherm is written $Q = \beta\sigma C$, where Q is the equilibrium amount of solute per unit column length in the stationary phase and C is the corresponding solute concentration in the mobile phase. Similarly, $Q^* = \beta\sigma C^*$, with Q^* the actual (nonequilibrium) solute in the stationary phase and C^* the (nonequilibrium) solute concentration in the mobile phase. Further, the total solute Q_T^* is given by $Q_T^* = \alpha C + Q^*$. Conservation of mass requires that

$$(\partial C/\partial x) + (\partial Q_T^*/\partial V) = 0$$

or

$$(\partial C/\partial x) + \alpha(\partial C/\partial V) + \beta\sigma(\partial C^*/\partial V) = 0 \tag{8}$$

Assume that the rate of approach to equilibrium is first order with respect to the deviation from equilibrium for these small perturbations and let Δt_D be the mean time required to reach equilibrium, so that

$$(\partial Q^*/\partial t) \approx (Q - Q^*)/\Delta t_D$$

The mean equilibration time is related to D by

$$\Delta t_D = qd^2/\beta\sigma D$$

where d is particle diameter, q is a factor reflecting the geometry of the gel particles, and $\beta\sigma D$ is the diffusion coefficient within the stationary phase. Since

$$\partial Q^*/\partial t = F(\partial Q^*/\partial V) \tag{9}$$

we now have

$$\partial Q^*/\partial V = (\beta\sigma D/qd^2F)\,(Q - Q^*) \tag{10}$$

which after differentiation with respect to V becomes

$$\partial Q^*/\partial V = (\partial Q/\partial V) - (qd^2F/\beta\sigma D)(\partial^2 Q^*/\partial V^2). \tag{11}$$

Recalling the defining relationships for Q and Q^* and substituting into eq. (8), we have

$$(\partial C/\partial x) + \xi a(\partial C/\partial V) = \frac{qd^2F}{D}\,(\partial^2 C^*/\partial V^2) \tag{12}$$

Referring again to eq. (8), we see that

$$\partial C^*/\partial V = -(1/\beta\sigma)[(\partial C/\partial x) + \alpha(\partial C/\partial V)]$$

and

$$\partial^2 C^*/\partial V^2 = -(1/\beta\sigma)[(\partial^2 C/\partial V\partial x) + \alpha(\partial^2 C/\partial V^2)]. \tag{13}$$

With the approximation (valid for small deviations from equilibrium)

$$\begin{aligned}\partial C/\partial x &\approx -(dV/dx)(\partial C/\partial V)\\ &= -\xi a(\partial C/\partial V)\end{aligned} \tag{14}$$

the expression becomes

$$\frac{\partial C}{\partial V} + \frac{1}{\xi a}\frac{\partial C}{\partial x} = \frac{qd^2F}{\xi^3 a^2 D}\frac{\partial^2 C}{\partial x^2}. \tag{15}$$

Recalling that $\partial C/\partial t = F(\partial C/\partial V)$ and $L_V = L/F$, comparison with eq. (1) shows that

$$L_N = \frac{qd^2F}{\xi^3 a^2 D} \tag{16}$$

Summing the contributions leads to

$$L_V = L_P + \frac{\xi D}{F} + \frac{qd^2F}{\xi^3 a^2 D}. \tag{17}$$

Several features of this relation should be emphasized: (*1*) it contains only two parameters (L_P and qd^2) which are not determined independently; (*2*) axial dispersion of a solute zone as a function of flow rate exhibits a minimum, the second term dominating at low flow rates and the last term at moderate to high flow rates; (*3*) at moderate flow rates axial dispersion increases with increasing molecular size (decreasing σ,ξ,D).*

MATERIALS AND METHODS

The gels used for these experiments were dextrans crosslinked with epichlorohydrin (Sephadex, Pharmacia). Sephadex G-100 (lot 6164) was used for the small-zone experiments; large-zone experiments were done on columns of Sephadex G-75 (lot 9393).

The following solutes were the finest grades commercially available: glycylglycine (Mann 1719, lot S2891), horse heart cytochrome *c* (Mann 179, lot R3282), sperm whale myoglobin (Mann 6649, lot S4714), and human gamma globulin (Mann 457, lot S3451). Southern bean mosaic virus was a gift of Dr. Russell Steere (USDA Plant Virology Laboratory, Beltsville, Md.). Molecular weights for these solutes are shown in Table I along with other physical characteristics.

TABLE I
Molecular Species

Molecular species	Molecular weight	$D_{20,w} \times 10^7$, cm²/sec[a]
Glycylglycine	132	70.7[b]
Cytochrome c (horse heart)	13,400	13.0
Myoglobin (sperm whale)	16,890	11.3
γ-Globulin (human)	153,000	4.00
Southern bean mosaic virus	6.6×10^6	1.39

[a] Unless otherwise identified, values are taken from the *Handbook of Biochemistry*.[13]
[b] Corrected to 20°C from the value determined at 25°C by Longsworth.[14]

The solvent for all experiments was 0.1 *M* potassium phosphate buffer (pH 7.4.).

After soaking the gel in solvent for at least 24 hr and decanting the fine particles, columns were poured in glass tubes made from sections of burets (this assures constant cross-sectional area and makes it simple to deter-

* An important distinction is necessary between the absolute amount of zone spreading observed after a sample has been eluted from the column and the rate of spreading during the time it is on the column. A smaller molecular species which spends more time on the column prior to its elution may exhibit a large amount of absolute dispersion relative to a larger molecule, even though the larger molecule spreads at a greater rate (larger L_V).

mine total column volume). The columns were fitted with porous polyethylene disks at the top and bottom of the gel bed. A constant pressure head sufficient to provide flow greater than one column volume an hour was applied to a buret filled with solvent (eluent reservoir). The eluate from the water-jacketed (20 ± 0.5°C) column passed through a flow cell into a syringe pump (Sage 255W-2) operating in the withdrawal mode. This arrangement produced constant flow rates within the accuracy of buret readings (±0.02 ml/hr).

Since a stable baseline is vital to the analyses performed here, the absorbance at 220 nm was monitored in a double-beam spectrophotometer (Bausch and Lomb Spectronic 600) for the small-zone experiments and in a single-beam spectrophotometer equipped with an automatic sample changer and automatic blank compensator (Gilford 2000) for the large-zone experiments.

Elution profiles were recorded on a strip chart recorder (Sargent SRL) simultaneous with the taking of digital data. A digital voltmeter (Hewlett-Packard 3440A), coupler (Hewlett-Packard 2547A), teletype/paper tape punch, and an external timer constituted the digital data acquisition system which collected 240 to 2400 data points/hr. For the large zone experiments the sample changer of the Gilford 2000 was used as a trigger for the data collecting system.

Small-Zone Experiments

As the meniscus of the solvent entered the porous disk, one drop of solute (1–2 mg/ml) was applied and the time was recorded. As soon as the sample entered the porous disk, one or two drops of solvent were applied. When this had entered the disk, the space above the gel was rinsed with solvent and filled. The solvent reservoir was then connected and flow rate was determined by measuring the rate at which solvent entered the column.

Large-Zone Experiments

The samples were roughly 10 ml of solution (0.05–0.1 mg/ml). In all cases sufficient volume was applied to achieve a "plateau" of constant concentration equal to that initially applied. The times when the sample began and finished entering the column were recorded. The sample was followed by a small amount of solvent and and a rinse as described above. The flow rate was determined from the rate at which the sample entered the column as well as the rate at which solvent entered. These procedures gave reproducible elution profiles.

Computations

Computations were carried out on a Hewlett-Packard 2114A digital computer, or in some cases on a Burroughs B5500 computer. Figures were plotted with a Hewlett-Packard 9100A programmable calculator equipped with a 9125A plotter.

RESULTS

Small-Zone Profiles

A typical small-zone elution profile is shown in Figure 1. Inspection reveals skewing to the left (leading edge), as predicted by eq. (4). This qualitative evidence of skewing is equivocal at best, however, and more powerful analysis is required to test rigorously the fit of the data to eq. (4) versus the fit to a normal Gaussian curve. If the data describe a Gaussian curve ($C = 1/\sqrt{2\pi\mu}\exp\{-(\bar{V} - V)^2/2\mu\}$, where μ is the second moment or variance), then a plot of ln C versus $(\bar{V} - V)^2$ will produce a straight line, whereas skewed data will show a systematic deviation from the line corresponding to the best Gaussian fit (Fig. 2). On the other hand, if the

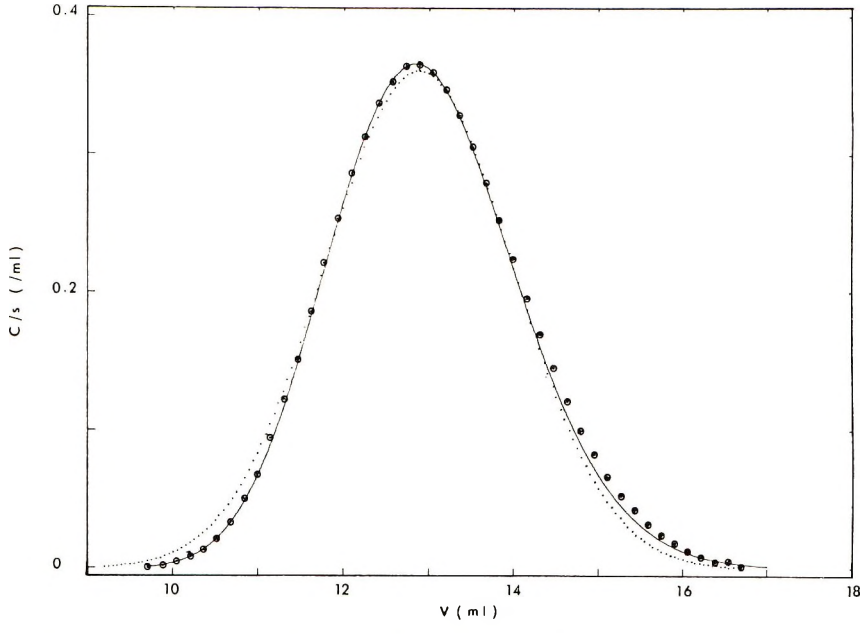

Fig. 1. Representative small-zone elution profile for cytochrome c on Sephadex G-100 (column B, Table II) at a flow rate of 9.49 ml/hr: (⊙) every 40th point of the data taken is shown; (——) best fit of eq. (4) to the data; (· · ·) best fit of a Gaussian curve to the data. On the ordinate, solute concentrations are normalized with respect to total amount s of solute.

data fit eq. (4), $\ln(C\sqrt{V})$ will be linear with respect to $(\bar{V} - V)^2/V$ (Fig. 3). It is clear that eq. (4) provides a much better fit to the data than does the Gaussian curve. In Figure 3, small systematic deviations from the straight line occur. These deviations are less than the difference between the two curves. Furthermore the data points and the best Gaussian curve always lie on opposite sides of the straight line. The origin of the small systematic deviations seen in Figures 2 and 3 is likely due to a systematic

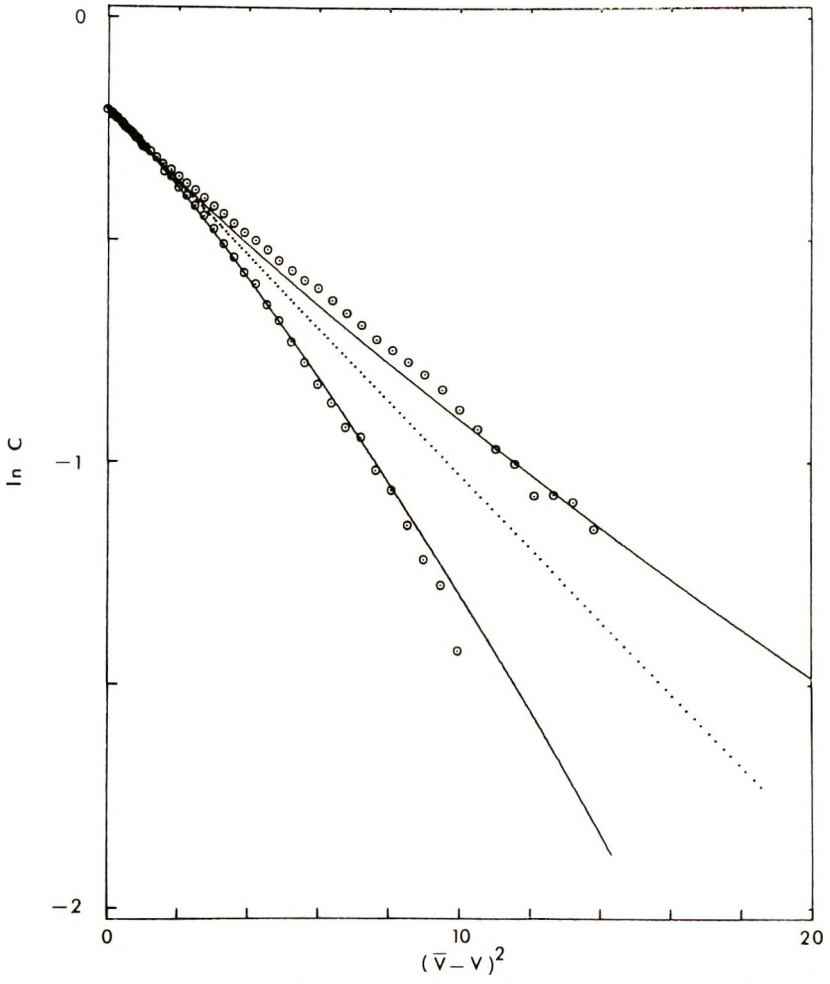

Fig. 2. Linear transformation for Gaussian curve: (⊙) applied to the data; (· · ·) the best Gaussian fit; (—) eq. (4). In this graph and Figure 3 the same data are plotted as in Figure 1, except every 20th point is shown.

error in measured flow rate, initial time, or $\bar{V}$. Small errors of this kind would be amplified greatly by the transformations used in these plots.

Evaluation of L_V

Equation (4) provides a means of evaluating the axial dispersion coefficient. Five virtually independent determinations were performed on each profile. Results of these determinations are shown in Table II.

Height/Area Methods. Numerical evaluation of $\int_0^\infty Cdv$ gives s, the mass of sample applied to the column. Analytic integration of eq. (4) verifies that

$$\int_0^\infty CdV = s$$

When $V = \bar{V}$, the exponential term is unity and $C_{max} = s/(2\xi a\sqrt{\pi L_V V})$ or

$$L_V = (s/2\xi a C_{max})^2/\pi\bar{V}.$$

Curve-Fitting Method. An interval-dividing routine on L_V was used for a least-squares fit of eq. (4) to the data.

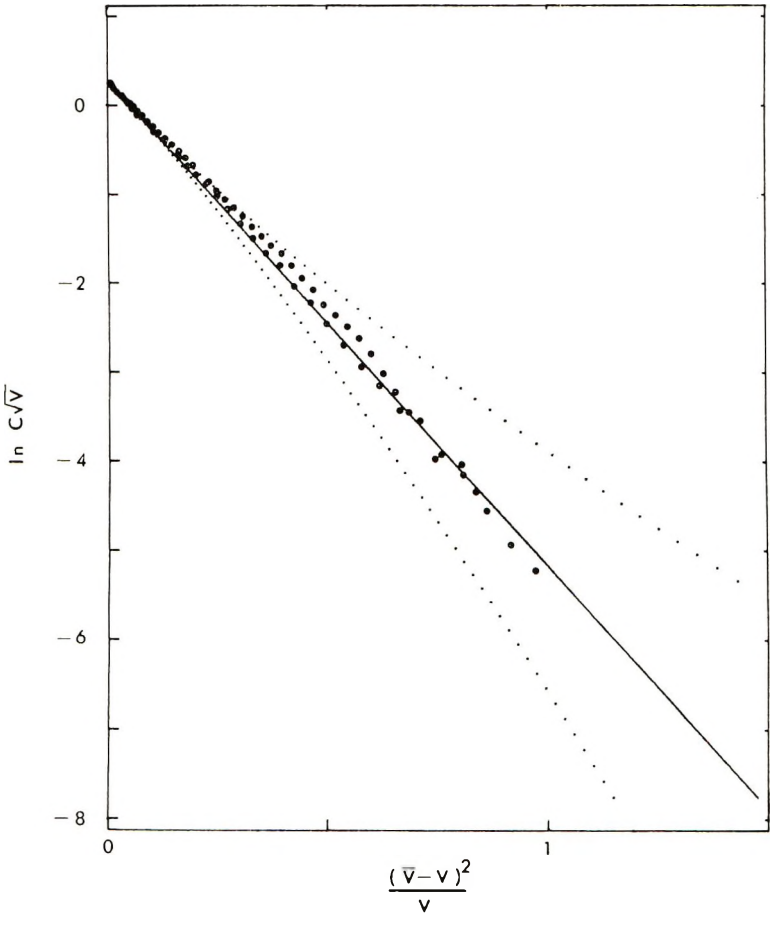

Fig. 3. Linear transformation for eq. (4): (⊙) applied to data; (· · ·) best Gaussian fit; and (—) eq. (4). The slope $(-1/4\xi^2a^2L_V)$ and intercept $\ln(s/2\xi a\sqrt{\pi L_V})$ are used to determine L_V (see text).

Slope Method. As can be seen directly from eq. (4), $L_V = -1/4\xi^2a^2A$, where A is the slope of the regression line (cf. Fig. 3).

Intercept Method. Again referring to eq. (4) and Figure 3, we see that $L_V = (s/4\pi\xi^2a^2)\exp\{-2B\}$, where B is the intercept of the regression line. This method is quite sensitive to the scatter in the data.

TABLE II
L_V for Small-Zone Experiments on G-100

Sample	Column	F, ml/hr	L_V, cm^{-1} Height/area	Curve fitting	Regression Slope	Regression Intercept	Inflection points	
	A	12.85	0.0230	0.0234	0.0326	0.0679	0.0408	0.0404
Glycylglycine	B	4.64	0.0205	0.0211	0.0311	0.0453	0.0294	0.0302
	B	9.59	0.0212	0.0214	0.0210	0.0217	0.0227	0.0130
	B	14.47	0.0254	0.0254	0.0150		0.0211	0.0236
	A	12.08	0.0798	0.0792	0.0483	0.0194	0.0885	0.0835
Cytochrome *c*	B	9.49	0.0665	0.0669	0.0470	0.0306	0.0756	0.0835
	B	13.93	0.1482		0.1529		0.1028	0.1413
	B	14.11	0.0533	0.0534	0.0335		0.0576	0.0977
	A	12.08	0.1113	0.1000	0.0678	0.0333	0.1018	0.1609
Myoglobin	B	9.82	0.0742	0.0752	0.0978	0.1586	0.0426	0.1089
	B	14.11	0.1219		0.1820		0.0880	0.2081

Inflection Point Method. Differentiating eq. (4) twice with respect to V gives

$$\frac{d^2C}{dV^2} = \left\{\frac{3}{4V} + \frac{1}{4\xi^2a^2L_VV}\left[1 - 3\left(\frac{\bar{V}}{V}\right)^2\right] + \left(\frac{1}{4\xi^2a^2L_V}\right)^2\left[1 - \left(\frac{\bar{V}}{V}\right)^2\right]^2\right\} C$$

At the inflection points, d^2C/dV^2 is zero and

$$L_V = V_I[3(\bar{V}/V_I)^2 - 1 - \sqrt{6(\bar{V}/V_I)^4 - 2}]/6\xi^2a^2$$

where V_I is the volume at the inflection point. Unfortunately, this expression is hypersensitive to small errors in the values of V_I or $\bar{V}$ and gives values of L_V only to about one order of magnitude. From a theoretical viewpoint, however, this expression is quite significant, as it shows explicitly that L_V is related to the peak position and the extent of spreading only and is independent of the zone size s.

Large-Zone Experiments

The leading and trailing boundaries for a typical large-zone experiment are shown in Figure 4. These data from the Gilford spectrophotometer show much greater scatter than was present in the small-zone experiments, which were monitored with the Bausch and Lomb 600 spectrophotometer. For the large-zone experiments, $\bar{V}$ is determined as the volume at the centroid of the appropriate boundary. If the transition from $C = 0$ to $C = C_0$ (from C_0 to 0 for the trailing boundary) takes place over the range V_a to V_b, then for the leading boundary $\bar{V} = V_b - \int CdV/C_0$, where $\int CdV$ is the area under the curve, evaluated numerically. For the trailing boundary $\bar{V} = V_a + \int C\,dV/C_0$. An appropriate test of eq. (5) would be to compare inverfc $(2C/C_0)$ versus $(\bar{V} - V)/\sqrt{V}$ with inverfc $(2C/C_0)$

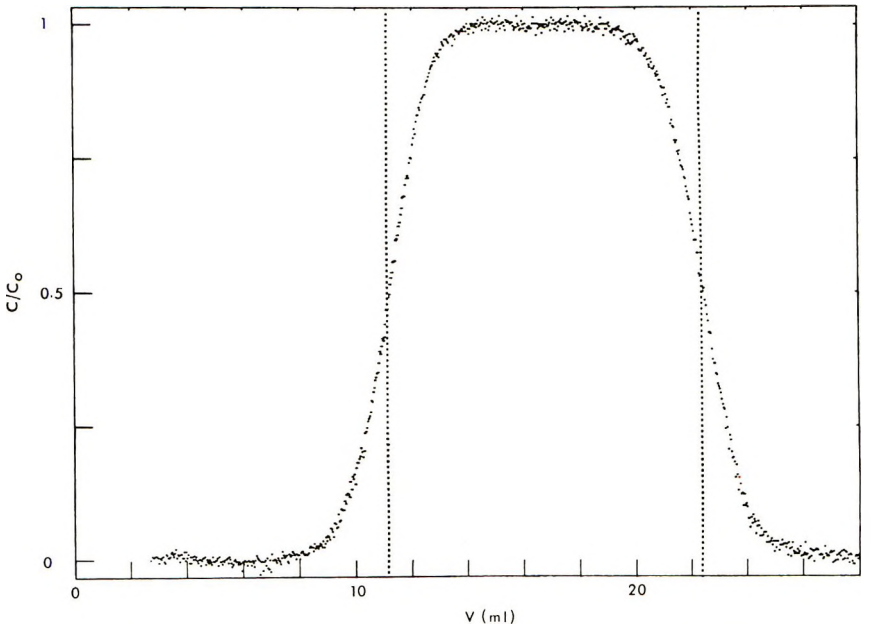

Fig. 4. Leading and trailing boundaries of large-zone experiments for cytochrome *c* run on G-75. Data obtained with a Gilford 2000 spectrophotometer at a flow rate of 8.15 ml/hr.

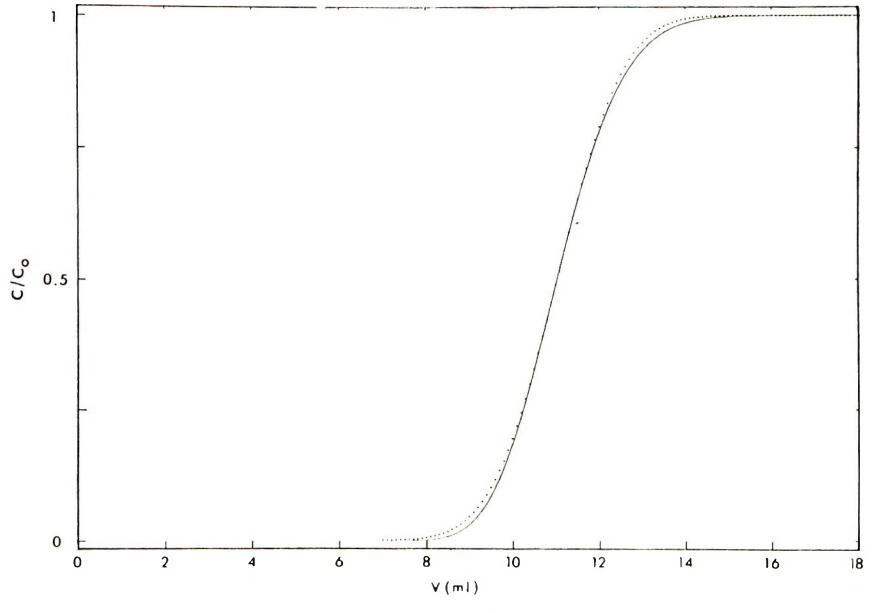

Fig. 5. Predicted leading boundary elution profile: (- -) plot of the best error function complement for the data shown in Figure 4; (——) plot according to eq. (5).

versus $(\bar{V} - V)$. However the large-zone experiments are relatively insensitive for detection of small amounts of skewing, since eq. (5) is the integral of eq. (4) in terms of ϕ. Figure 5 shows the relative insensitivity of the large-zone experiment for detecting skewing. As a result of this and the scatter in the data it was not possible to detect any significant difference in linearity between the two plots. By rearrangement of eq. (5) one could, in principle, calculate L_V from:

$$L_V = \left[\frac{\bar{V} - V}{2\xi a \cdot \text{inverfc}(2C/C_0)}\right]^2 \Big/ \text{V}$$

This expression, however, is next to useless for calculating L_V, owing to large relative errors in C at the ends of the boundary and uncertainty near $\bar{V}$ as both numerator and denominator go to zero. Therefore each boundary was analyzed by determining the regression line of inverfc $(2C/C_0)$ on $(\bar{V} - V)/\sqrt{\bar{V}}$. Letting A be the slope of the regression line, we write $L_V = \pm 1/(2a\xi A)^2$, where the sign is determined by whether the boundary is leading (+) or trailing (−). The results are shown in Table III.

TABLE III
L_V for Large-Zone Experiments on G-75

Sample	Column	F, ml/hr	L_V cm^{-1}	
			Leading	Trailing
Glycylglycine	C	8.21	0.0333	0.0405
	C	14.91	0.0578	0.0522
	D	6.50	0.0261	0.0320
	D	12.71	0.0349	0.0493
Cytochrome *c*	C	8.15	0.1210	0.1429
	C	14.73	0.1951	0.1898
Myoglobin	C	8.22	0.0952	0.0895
	C	15.39	0.2017	0.1954
	D	6.91	0.1021	0.0993
	D	12.75	0.1838	0.2007

Analysis of L_V

Rearrangement of eq. (17) to

$$L_V - \frac{\xi D}{F} = L_P + \frac{qd^2 F}{\xi^3 a^2 D}$$

gives a linear equation relating the known terms. Figures 6 and 7 show the data plotted in this fashion for small-zone and large-zone experiments, respectively. Table IV contains the values of L_P and qd^2 for the columns used in these experiments. Reasonable estimates of d indicate that q is of the order of 1 (i.e., $0.3 < q < 3$). Figure 8 shows the general behavior of L_V with flow rate for two of the columns used.

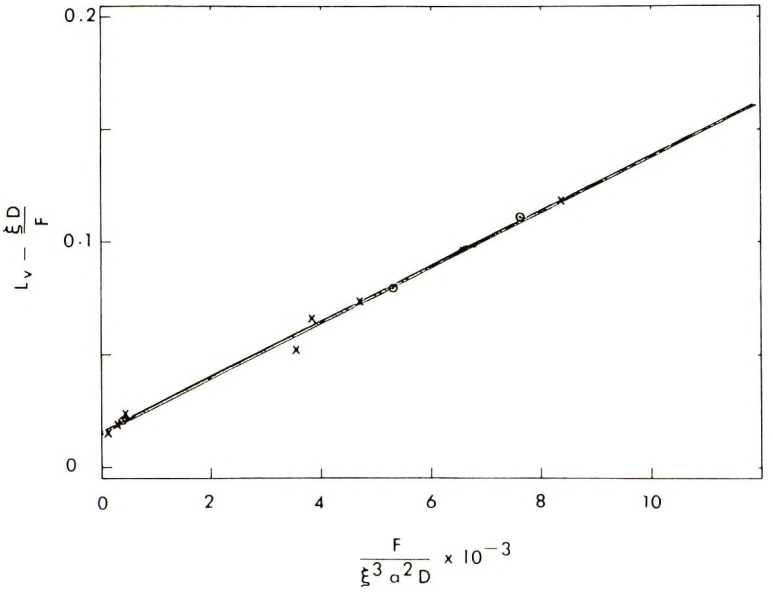

Fig. 6. Analysis of L_V based on eq. (17) for data from small-zone experiments: (⊙) column A; (×) column B. The upper line is a regression plot for data of column A and the lower is for column B. The slope of the regression line (——) is qd^2, and the intercept is L_P.

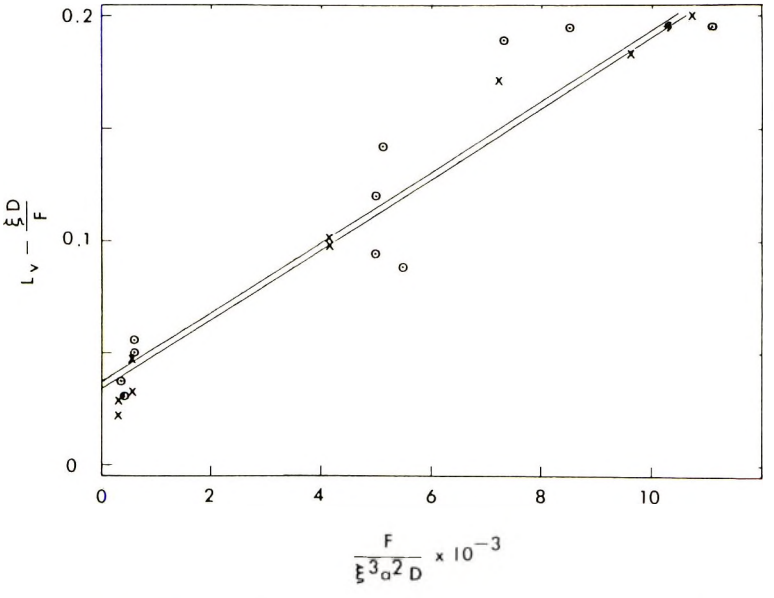

Fig. 7. Analysis of L_V based on eq. (17) for data from large-zone experiments: (⊙) column C; (×) column D. The upper line is a regression plot for data of column C and the lower line is that for column D. The slope of the regression line (——) is qd^2, and the intercept is L_P.

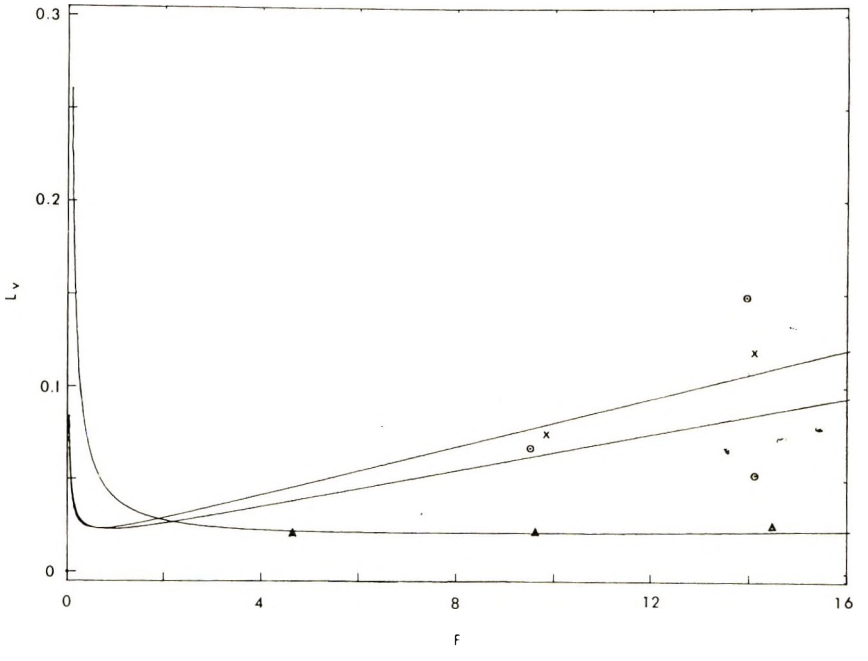

(*a*)

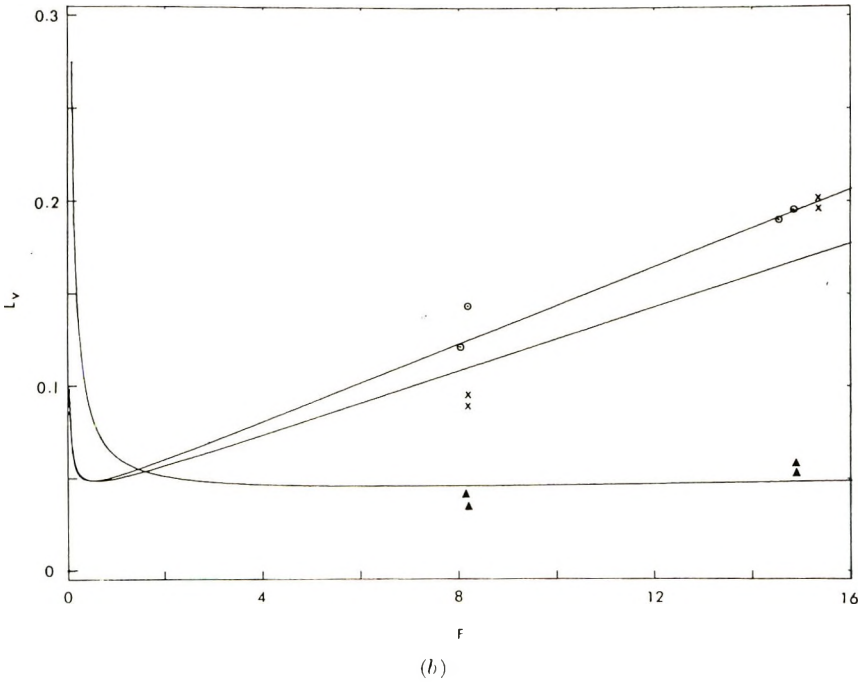

(*b*)

Fig. 8. Behavior of L_V as a function of flow rate with (*a*) Sephadex G-100 and (*b*) Sephadex G-75 columns: (▲) glycylglycine; (⊙) cytochrome *c*; (×) myoglobin.

TABLE IV
Column Parameters

Gel	Column	L_V, cm^{-1}	$qd^2 \times 10^5$, cm^2
G-100	A	0.0158	1.23
	B	0.0148	
G-75	C	0.0384	1.57
	D	0.0340	

DISCUSSION

This study has been directed toward the two essential aspects of axial dispersion in gel-permeation chromatography: (1) the relationship of axial dispersion to the continuity equations of chromatographic transport and (2) the relationship to molecular size and the system parameters of an individual column. The first of these relationships defines the general form of elution profiles and provides a basis for experimental determination of the phenomenological coefficient of axial dispersion. In the present study we have verified the basic continuity equation for gel chromatography and have used its solutions to obtain axial dispersion coefficients of single discrete macromolecular components. These results can be readily extended to the analysis of multicomponent systems.

For heterogeneous mixtures of noninteracting components, an equation analogous to the empirical Tung equation can be written, on the basis of eq. (4). On the assumption of an effectively continuous distribution of molecular size, the elution profile (between two arbitrary points V_a and V_b) is given by:

$$C(V) = \int_{V_a}^{V_b} \frac{W(\bar{V})}{2\xi a\sqrt{\pi L_V V}} \exp\left\{-\frac{(\bar{V} - V)^2}{4\xi^2 a^2 L_V V}\right\} d\bar{V} \tag{18}$$

In this equation, $\bar{V}$, ξ, and L_V are now continuous variables, and $W(\bar{V})$ is a distribution function reflecting the distribution in molecular size. Although no general solution exists for integral equations of this kind, the solution for $W(\bar{V})$ may be obtained numerically. Using the technique of direct optical scanning in gel permeation chromatography,[15] it is of interest to study concentration profiles of solute zones prior to their elution from the column. Experimentally, the column is scanned at constant V and the solute concentration is recorded as a function of x. The corresponding equation for the nonelution case would be:

$$C(x) = \int_{x_a}^{x_b} \frac{W(\bar{x})}{2\xi a\sqrt{\pi L_V V}} \exp\left\{-\frac{(x - \bar{x})^2}{4L_V V}\right\} d\bar{x} \tag{19}$$

where $\bar{x} = \bar{V}/\xi a$. It is seen that this equation in the distance coordinate bears a closer resemblance to the Tung equation than does eq. (18) and would reduce to it if ξ were independent of molecular size.

For many multicomponent systems of biopolymers there are interactions between discrete macromolecular species which lead to reversible association–dissociation equilibria having definite stoichiometry. For such systems gel-permeation chromatography may be used to study the associations and to determine thermodynamic parameters for the interactions involved.[16,17] Results of the present study can be used to predict the shapes of both "small" and "large" solute zones for such systems, and these shapes provide diagnostic indications of the type of association complexes formed. Results of such a study, now underway, will be presented at a later time.

The second aspect of this work, mentioned above, has resulted in a useful approach to the analysis of peak broadening in terms of molecular size, flow rate, and column parameters. Equation (17) provides a good correlation of axial dispersion with column parameters over the range of conditions employed in this study. Although it is not presently possible to assess the overall range of applicability, eq. (17) would clearly have to be modified to describe behavior of molecules having very small partition coefficients. The necessary modification would be a different expression for Δt_D in the expression,

$$L_V = L_P + \frac{\xi D}{F} + \frac{B\sigma F}{\xi^3 a^2}\,\Delta t_D$$

which is the more general form of eq. (17). The parameter Δt_D could be determined experimentally as a function of solute size as the slopes of plots of $L_V - (\xi D/F)$ versus $B\sigma F/\xi^3 a^2$.

Equation (17) has the general form of the well-known van Deemter equation[18] for height equivalent to theoretical plate: $H = A + (BD/F) + (CF/D)$, where A, B, and C are adjustable constants of the column. It has long been known that theoretical plate models derived by analogy to fractional distillation and countercurrent distribution do not conform to the physical reality of chromatographic systems.[19] In spite of this inadequacy their use appears deeply entrenched in tradition. Later versions of the van Deemter equation have been extensively modified and expanded to allow for variations in solute diffusion coefficient and other system parameters while retaining the fiction of theoretical plates. Since there is no physical justification for use of theoretical plates, these efforts would appear somewhat similar to the continued description of planetary orbits in terms of epicycles, which persisted after the time of Kepler. It is possible to "translate" axial dispersion coefficients, based on the continuity equation (which is physically realistic) into the corresponding "equivalent theoretical plate height" by the relation, $H = 2\xi a L_V$.

By combining results of the present study with previously known procedures for calibrating columns, it is possible to characterize the entire chromatographic system much more completely. The goal of such a characterization would be the possibility of predicting for a known solute the

position and shape of an elution profile from a given column. The procedures necessary for such a characterization are outlined below.

Characterization of the Gel

The useful parameters for characterizing a given batch or lot of gel are (1) the partial specific volume of the anhydrous gel-forming material, (2) its volume fraction in the swollen gel, (3) the factor qd^2 of eq. (17), and (4) calibration constants for partitioning of solute into the gel. The partial specific volume of the anhydrous gel-forming material v_g is normally available from the manufacturer or may be determined experimentally. After weighing an amount of gel W_g, on making a column and determining V_t and V_0, one can calculate $k' = \bar{v}_g W_g/(V_t - V_0)$. The value of k' is normally about 0.05, and represents the volume fraction in the swollen gel occupied by the gel-forming material. On this same column qd^2 is determined by means of equation (17) (see Figs. 6 and 7). The next step is to calibrate the gel with respect to partitioning properties in terms of molecular size or weight. A variety of procedures can be used. For example, if molecular radius a is of interest, the relations[20] $\sigma = \text{erfc}[(a - a_0)/b_0]$

or

$a = a_0 + b_0 \text{ inverfc } (\sigma)$ can be used for molecules of known radius a and partition coefficient σ to determine gel parameters a_0 and b_0. (A comprehensive review of gel-calibration procedures has been given by Ackers.[6])

Calibration of the Individual Column

Once the lot of gel has been characterized, any column prepared from a known weight of gel can be calibrated with a single (internal volume) elution experiment. The void volume is found from $V_0 = V_t - (v_g W_g/k')$, and L_P is determined as above. With such a column it is possible either to predict for a known solute the position and shape of the elution profile or to determine the molecular radius and diffusion coefficient of an unknown (single-component) solute. A sample calculation on cytochrome c, according to eq. (17) solved for D,

$$D = 2qd^2 F \Big/ \left\{ (L_V - L_P)\xi^3 a^2 \left[1 + \sqrt{1 - \frac{4\,qd^2}{(L_V - L_P)^2 \xi^2 a^2}} \right] \right\}$$

gave a value of 1.20×10^{-6} cm^2/sec, compared to a literature value of 1.30×10^{-6} cm^2/sec (Table I).

Finally, it should be pointed out that the method of analysis developed here provides a powerful means of detecting polydispersity in a system of macromolecules. During the course of this study we found that some preparations of solutes could not be used, since small amounts of additional components led to anomalously high values of L_V. Preparing a "calibration chart" like Figures 6 and 7 makes this effect immediately apparent.

For most purposes, planimetric determination of $s = \int CdV$ should be sufficiently accurate.

This work has been supported by Grant GM-14493 from the U. S. Public Health Service.

References

1. L. H. Tung, *J. Appl. Polym. Sci.*, **10**, 375 (1966).
2. P. E. Pierce and J. E. Armonas, in *Analytical Gel Permeation Chromatography* (*J. Polym. Sci. C*, **21**), J. F. Johnson and R. S. Porter, Eds., Interscience, New York, 1968, p. 23.
3. J. H. Duerksen and A. H. Hamielec, in *Analytical Gel Permeation Chromatography* (*J. Polym. Sci. C*, **21**), J. F. Johnson and R. S. Porter, Eds., Interscience, New York, 1968, p. 83.
4. M. Hess and R. F. Kratz, *J. Polym. Sci. A-2*, **4**, 731 (1966).
5. J. C. Giddings and K. L. Mallik, *Anal. Chem.*, **38**, 997 (1966).
6. G. K. Ackers, *Advan. Protein Chem.*, **24**, 343 (1969).
7. G. K. Ackers and R. L. Steere, in *Methods in Virology*, K. Maramorosch and H. Koprowski, Eds. Vol. II, Academic Press, New York, 1967, p. 325.
8. K. H. Altegelt, *Advan. Chromatog.*, **4**, 3 (1967).
9. E. Glueckauf, K. H. Barker, and G. P. Kitt, *Discussions Faraday Soc.*, **7**, 199 (1949).
10. E. Gleuckauf, *Trans. Faraday Soc.*, **51**, 34 (1955).
11. K. O. Pedersen, *Arch. Biochem. Biophys.* (*Suppl.* **1**), 157 (1962).
12. R. N. Kelly and F. W. Billmeyer, Jr., *Anal. Chem.*, **41**, 874 (1969).
13. *Handbook of Biochemistry*, Chemical Rubber Co., Cleveland, 1968.
14. L. G. Longworth, in *Electrochemistry in Biology and Medicine*, T. Shedlovsky, Ed., Wiley, New York, 1955, p. 225.
15. E. E. Brumbaugh and G. K. Ackers, *J. Biol. Chem.*, **243**, 6315 (1968).
16. G. K. Ackers and T. E. Thompson, *Proc. Nat. Acad. Sci. U.S.*, **53**, 342 (1965).
17. G. K. Ackers, *J. Biol. Chem.*, **242**, 3026 (1967).
18. T. J. van Deempter, F. J. Zuiderweg, and A. Klinkenberg, *Chem. Eng. Sci.*, **5**, 271 (1956).
19. J. C. Giddings, *Dynamics of Chromatography. Part I. Principles and Theory*, Dekker, New York, 1965, p. 20.
20. G. K. Ackers, *J. Biol. Chem.*, **242**, 3237 (1967).

Received May 4, 1970
Revised July 16, 1970

JOURNAL OF POLYMER SCIENCE: PART A-2 VOL. 9, 267–281 (1971)

Oscillatory Shear Measurements on Polystyrene Melts in the Terminal Region

N. J. MILLS* and A. NEVIN,
Petrochemical & Polymer Laboratory, Imperial Chemical Industries Limited, The Heath, Runcorn, Cheshire, England

Synopsis

Oscillatory shear measurements have been made on a range of anionic polystyrene melts of molecular weights 1000–500,000. For $M < 5000$ the polymer chain is too short to act as a Gaussian coil and hence the compliance of the melt is very low. For $10,000 < M < 100,000$ the compliance of the melt follows the Rouse model of the elasticity of isolated polymer molecules. It is necessary to use the Ferry, Landel and Williams extension of the Rouse theory for $M > 40,000$ to allow for the effect of entanglements on the complex modulus. For $M > 200,000$ the entangelment network dominates the compliance and the Rouse theory is no longer applicable.

INTRODUCTION

Oscillatory shear measurements have been made by a number of workers[1–5] on polystyrene melts of narrow molecular weight distribution (MWD). However, the change in behavior down to very low molecular weights has not been investigated except by Burge,[5] who showed that there was little difference in the transition region (the shear modulus G between 10^6 and 10^8 N/m^2) for molecular weights 20,000 to 860,000 except for the shift in frequency due to change in T_g. Now that anionic polystyrenes, of narrower MWD's than the polystyrene fractions used by earlier workers,[1,2] are available it is possible to find more nearly the behavior of a monodisperse polymer melt. This then will allow the molecular theories of polymer viscoelasticity[6] to be tested more thoroughly. Experiments on blends have also been carried out to confirm the effects of polydispersity observed in polydimethylsiloxane[7] and test whether the MWD could be inferred from the rheological behavior. Our results can be compared with recent dynamic data[8] on anionic polystyrenes and blends therefrom.

EXPERIMENTAL

Materials

Anionic polystyrenes from three sources were used; Pressure Chemical Co., Dow Chemical Co., and those prepared in our laboratory by R.

* Now at Department of Physical Metallurgy and Science of Materials, The University of Birmingham, P. O. Box 363, Birmingham B15 2TT, England

Denyer. In addition a series of blends of anionic polystyrenes with weight-average molecular weights $\bar{M}_w$ of 86,000 and 500,000 were prepared by mixing dilute solutions and evaporating the solvent. Details of the molecular weight averages measured by gel-permeation chromatography, or supplied by the manufacturers, are given in Table I. Molecular weight averages of the blends were computed and are given in Table II.

TABLE I
Molecular Weights of Polystyrene Samples

Source	$\bar{M}_n$ (method)[a]	$\bar{M}_w$ (method)[a]	$\bar{M}_z/\bar{M}_w$[b]
Pressure Chemicals Co.			
Batch 15a	1,050 ± 10% (VPO)		
" 11a	2,900 ± 7% (VPO)	3,800 (GPC)	1.2
" 8a	10,900 ± 5% (MO)	10,000 ± 10% (LS)	1.1
" 2a	19,800 ± 3% (MO)	19,800 ± 2% (LS)	1.1
" 7a	50,100 ± 5% (MO)	50,500 ± 4% (LS)	1.1
" 1a		160,000 ± 3% (V)	1.1
" 5a	404,000 ± 5% (MO)	507,000 ± 4% (LS)	1.2
R. Denyer	28,900 (GPC)	31,600 GPC	1.1
"	76,000 (GPC)	87,000 GPC	

[a] VPO, vapor pressure osmometry; MO, membrane osmometry; LS, light scattering; V, viscometry.
[b] $\bar{M}_z$ by GPC.

TABLE II
Molecular Weight Distribution of Blends

Polymer	Weight fraction 1	Weight fraction 2	$\bar{M}_n$	$\bar{M}_w$	$\bar{M}_z$	$10^{-6}\,\bar{M}_z\bar{M}_{z+1}/\bar{M}_w$	$J \times 10^{-4}$, m^2/N
1	100	0	425,000	500,000	600,000	0.865	0.20
Blend A	50	50	128,300	292,000	529,000	1.26	0.7
Blend B	25	75	95,500	189,000	432,000	1.51	1.51
Blend C	12.5	87.5	84,600	138,000	328,000	1.47	1.9
Blend D	6.25	93.75	80,000	112,000	241,000	1.15	1.6
2	0	100	75,700	86,800	102,000	0.139	0.11

Rheological Equipment

A model 16 Weissenberg cone-and-plate viscometer with 2.5 cm diameter platens and gap angle 4° was used. A torsion bar was used to measure the transmitted torque for G in the range 10–1000 N/m^2 for the relatively elastic blends. A piezoelectric measuring head of high stiffness, described previously,[9] was used for G in the range 10^3–10^7 N/m^2. The oscillatory drive is no longer through the manufacturers normal force shaft and diaphragm. The torsional stiffness of the stainless steel tube between the oscillatory drive mechanism and the cone is 2800 N-m/rad and of the tube between the plate and the stress measuring head is 1470 N-m/rad. This means that for the sample geometry used the steady-state shear

compliance (defined later) of the melt can be as low as 4×10^{-8} m^2/N before the melt contributes as little to the total measured compliance as does the upper stainless steel tube. A Solatron digital transfer function analyzer was used to calculate the components of the complex modulus as before. These values were corrected, for the low molecular weight polystyrenes, for the stiffness of the measuring system. In all cases the applied frequency was well below the natural frequency of the measuring system and the damping in the air bearing and torque measuring head was negligible.

Continuous shear measurements were made by using the Weissenberg apparatus with torsion bar torque measurement, and at higher shear stresses with a small capillary viscometer.[10]

THEORY

The continuum rheological theory[11] for a second-order fluid predicts that the limiting low-frequency behavior of the in-phase G' and out-of-phase G'' components of the complex modulus in oscillatory shear flow are given by

$$\lim_{\omega \to 0} \frac{G'(\omega)}{\omega^2} = \eta_0^2 J \tag{1}$$

$$\lim_{\omega \to 0} \frac{G''(\omega)}{\omega} = \eta_0 \tag{2}$$

where η_0 is the limiting viscosity, J the steady-state shear compliance, and ω the frequency.

The Rouse[12] molecular theory for the viscoelastic properties of dilute polymer solutions has been modified and extended for use with polymer melts. A useful brief summary of the theory has been given by Tobolsky et al.[13] The results that we wish to use are those of Rouse that the compliance of a monodisperse polymer of molecular weight M (of sufficiently high molecular weight to have a number of possible Rouse modes) is

$$J = 0.4M/\rho RT \tag{3}$$

where ρ is the density, R the gas constant, and T the absolute temperature. This has been extended to polydisperse polymers by Ferry[14] giving

$$J = (0.4/\rho RT)\ (\bar{M}_z \bar{M}_{z+1})/\bar{M}_w \tag{4}$$

The components of the complex modulus are given by:

$$G'(\omega) = \rho RT \sum_{i,p} \frac{W_i}{M_i} \frac{\omega^2 \tau_{pi}^2}{1 + \omega^2 \tau_{pi}^2} \qquad p = 1,2,3,\ldots,z \tag{5}$$

$$G''(\omega) = \rho RT \sum_{i,p} \frac{W_i}{M_i} \frac{\omega \tau_{pi}}{1 + \omega^2 \tau_{pi}^2}$$

when the weight fraction of polymer of molecular weight M_i is W_i and there are z Gaussian submolecules per molecule.

The relaxation times τ_{pi} associated with the modes of vibration of the molecule are given in terms of the measured viscosity by

$$\tau_{pi} = (6/\pi^2)\ (\eta M_i^2/\rho RT_P^2 \bar{M}_w) \qquad p = 1,2,3,\ldots \tag{6}$$

Ferry, Landel, and Williams[15] empirically modified this equation for polymers of molecular weight greater than a critical value M_c so that it only applied for modes for which $p < (M/M_c)$. For higher modes the relaxation times were shortened by a factor $(M_c/M_i)^{2.4}$ so that

$$\tau_{pi} = \frac{6\eta}{\pi^2 \rho RT\ \bar{M}_w\ p^2} \frac{M_c^{2.4}}{M_i^{0.4}}$$

$$(Z > P > M_i/M_c) \tag{7}$$

This effectively means that the shorter relaxation times are unaltered but the longer ones are shifted to longer times to allow for the change in the slope of the log viscosity versus log molecular weight relation from 1 to 3.4 at about M_c. This automatically ensures that the low frequency behavior of $G''(\omega)$ gives the measured viscosity. Also for a polymer of rather narrow MWD and high molecular weight, G' will reach a plateau value of $\rho RT/M_c$ at frequencies higher than the reciprocal of all the long τ_{ip} and less than the reciprocal of the short τ_{ip}.

RESULTS

Oscillatory Shear on Whole Polymers

The components G' and G'' of the complex modulus are shown as a function of the normalized angular frequency $\eta_0\omega$ in Figures 1, 2, 4, and 5 for a series of polystyrenes of increasing molecular weight. The limiting viscosities and temperatures of measurement are given in Table III. This presentation is preferred to the more usual one of η' and G' versus frequency, since there is no reason to divide only one of the measured

TABLE III
Limiting Viscosities and Temperature of Measurement

Polymer $\bar{M}_w$	T, °C	η_0, poise	J_0, m²/N
3,800	90	1.2×10^7	
3,800	100	5.6×10^6	1.1×10^{-7}
10,000	115	8.6×10^6	1.0×10^{-6}
20,000	130	5.0×10^6	2.4×10^{-6}
31,000	135	2.7×10^6	2.6×10^{-6}
51,000	155	1.0×10^6	5.6×10^{-6}
87,000	190	5.0×10^5	1.1×10^{-5}
160,000	190	7.2×10^4	8.5×10^{-6}
500,000	190	4.2×10^6	2.0×10^{-5}

quantities by ω, and the relative values of G' and G'' are more easily seen. The component G' was not detectable for polystyrene of molecular weight 1000. It is always very low relative to G'' for the polystyrene of molecular weight 3800, and G'' barely deviates from a linear dependence on frequency in the range of measurement. The number of possible Rouse modes of

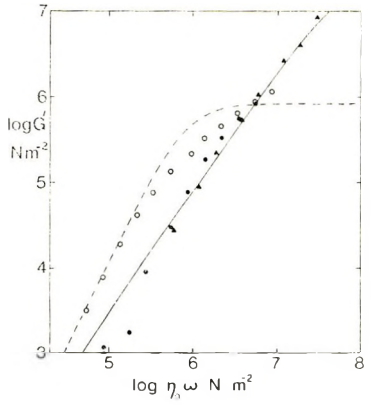

Fig. 1. Plots of log G' vs. log $\eta_0\omega$ for polystyrene of molecular weight 3800 (▲) at 90°C and (●) at 100°C and (○) for molecular weight 10,000 at 115°C; (——), of model Barlow et al.; (- - -) Maxwell element.

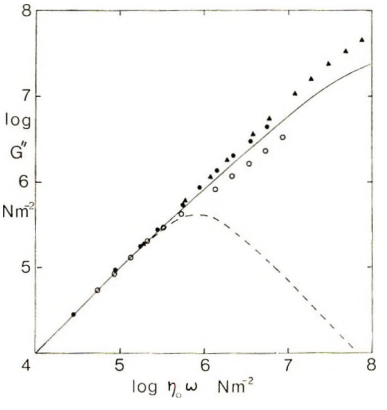

Fig. 2. Plots of log G'' vs. log $\eta_0\omega$ for same samples and notation as Fig. 1.

oscillation for this polymer is small. If the Gaussian submolecule contains five freely jointed segments, then its molecular weight is ca. 4000 (see discussion) and there are one and two modes, respectively, for the 3800 and 10,000 molecular weight polystyrene. For the 3800 molecular weight polymer at 100°C therefore, the Rouse theory reduces to a single Maxwell element with relaxation time given by

$$\tau/\eta = M/\rho RT = 1.2 \times 10^{-6}\ \mathrm{m^2/N} \tag{8}$$

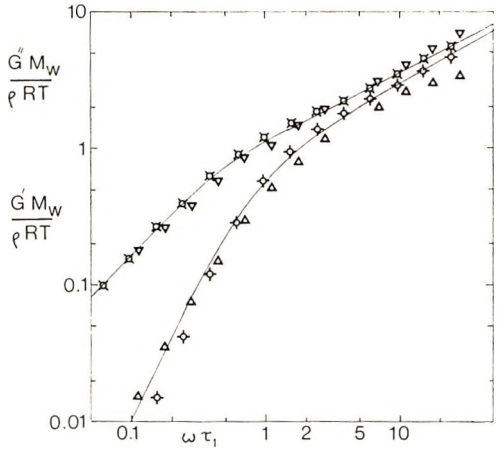

Fig. 3. Plots of log reduced complex modulus vs. log $\omega\tau_1$, for polystyrene of molecular weight 20,000 (▽, △) and 30,000 (▽,-◇-) compared with the Rouse model (——); upper curves G' in each case.

This is compared with the experimental results in Figures 1 and 2. Not only is the limiting compliance J predicted to be too high by a factor of 12, but the G'' behavior is also quite different at high frequencies. The first might be explained by the occurrence of non-Gaussian behavior at higher molecular weights than expected, leading to a lower effective compliance of the polymer chain. The second indicates that there are other relaxation mechanisms contributing to the modulus of the 3800 molecular weight polystyrene at high frequencies. The empirical model of Barlow et al.[16] (BEL model) which fits the behavior of pure low molecular weight liquids is also shown in Figures 1 and 2. (The parameter G_∞, the modulus at infinite frequency, is taken as 2×10^8 Nm^2 at the temperature of measurement, a reasonable value considering Burge's[5] results on polystyrenes with

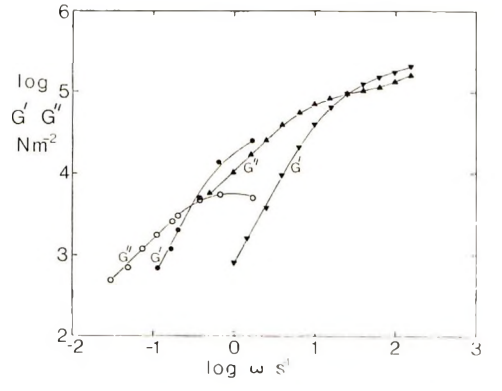

Fig. 4. Plots of log of complex modulus components G' and G'' versus log ω for polystyrene of molecular weight 51,000 at 155°C: (▼, ▲) our data; (●, ○) data of Chartoff and Maxwell.[3]

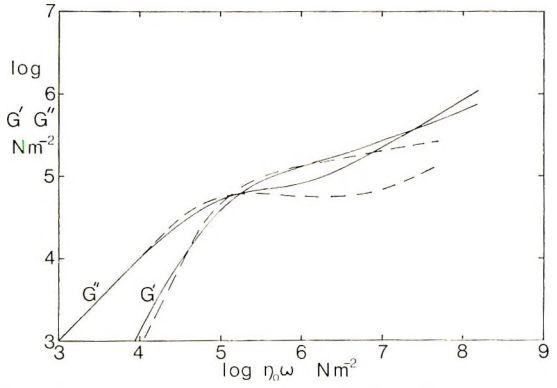

Fig. 5. Plots of log G' and G'' vs. log $\eta_0\omega$ for anionic polystyrenes: (——) molecular weight 87,000; (---) molecular weight 160,000.

$M > 20{,}000$.) The BEL model is close to the 3800 molecular weight polystyrene result, except that it predicts $G' \propto \omega^{3/2}$ at low frequencies instead of the observed ω^2 behavior. If, therefore, the G^* behavior is a sum of that for low molecular weight liquids and the Rouse model, then there is a Rouse mode of sorts for the 10,000 molecular weight polystyrene, but none for the 3800 molecular weight polystyrene.

To show the similarity of the behavior of the 20,000 and 30,000 molecular weight samples to the high molecular weight Rouse model, the reduced variables $G' \bar{M}_w/\rho RT$ and $G'' \bar{M}_w/\rho RT$ were plotted against $\omega\tau_1$, where τ_1 is given by eq. (6), with $M_i = \bar{M}_w$ in Figure 3. The fit is very good for the 30,000 molecular weight polystyrene and less good for the 20,000 molecular weight polystyrene. This suggests that it is only for $M \geqslant 30{,}000$ that there are sufficient modes acting for the Rouse model to apply.

Figure 4 compares our complex modulus results on an anionic polystyrene of $M = 51{,}000$ at 155°C with those of Chartoff and Maxwell.[3] Although the viscosities are nearly the same at low frequencies, their values of G' are far greater than ours; and correspondingly there is a deviation from $G'' \propto \omega$ at much lower modulus values. In the case of the 160,000 molecular weight sample measured by Chartoff and Maxwell the same differences were found, their G'' reaching a maximum value of 2×10^3 N/m² at 200°C instead of our value of 6×10^4 N/m² (Fig. 5) which agrees with Den Otter's[4] result. The apparent large increase in compliance with increasing temperature in Chartoff's results is another disturbing feature since it has generally been found to increase little if at all. We suspect that either the theoretical justification of the orthogonal rheometer[17] is at fault, or the strain-gauge measuring system that Chartoff and Maxwell[18] use has a relatively large compliance that has not been corrected for. At molecular weights of 87,000 and above the terminal region covers too great a frequency range for convenient measurement at one temperature. Therefore measurements were made at two or three temperatures and the results shifted along the frequency axis to get super-

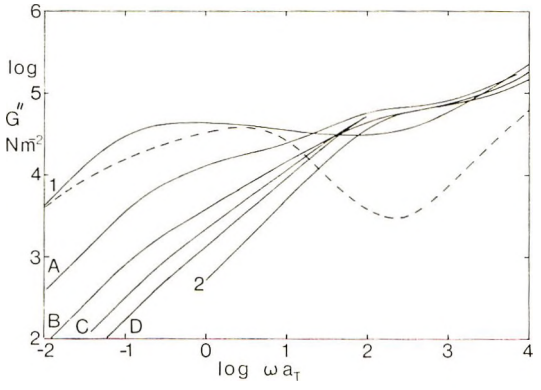

Fig. 6. Plots of log G'' vs. log ωa_T for (——) blends at 190°C and (- - -) for modified Rouse model. Data for blends C and D are suppressed above log $\omega a_T = 10^2$ since they are the same as for blend B in this range.

position, by shift factors a_T given in Table IV. The reduction factor $\rho_0 T_0/\rho T$ used by Ferry[13] for the modulus was ignored, since it involved less than a 7% change in G and did not always give a better superposition of experimental data. The slope of log G'' versus log ω in the region of 10^5 N/m^2 falls with increasing molecular weight until it is zero for $\bar{M}_v$ = 160,000 and has a shallow minimum for molecular weights higher than this. With increasing molecular weight the rubberlike plateau extends over a greater frequency range, and tan $\delta = G''/G'$ decreases in this region.

Den Otter[4] showed that the Williams-Landel-Ferry (WLF) modification of the Rouse theory is satisfactory for Dow anionic polystyrene S111 of $\bar{M}_w$ = 224,000 if M_e is taken as 30,000. Presumably the WLF modification of the Rouse theory will also fit our results for 51,000 < M < 160,000 although there would be some difficulty when the number of modes, for which $M > M_e$, is small. Figures 6 and 7 show a similar comparison between this theory and a 500,000 molecular weight polystyrene calculated for M_e = 31,000. The theory predicts lower values of G'' than those observed in the region of $\omega a_T = 10^{-1}$ sec^{-1}, and the minimum in G'' at ωa_T = 200 sec^{-1} is far too large because of the arbitrary splitting of

TABLE IV
Shift Factors a_T Referred to 190°C

Polymer $\bar{M}_w$	T, °C	a_T
87,000	150	80
160,000	155	43
500,000	150	95
	230	0.115
Blend A	155	46
Blend B	150	98
Blend C	150	96
Blend D	150	82

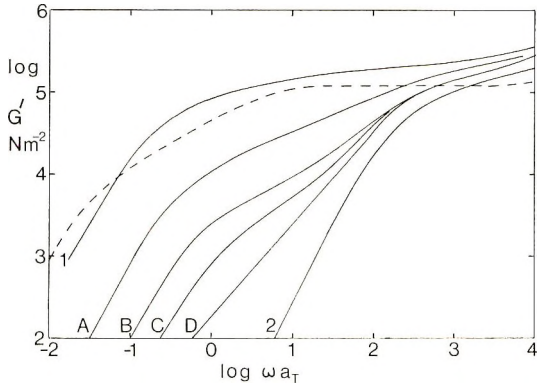

Fig. 7. Plots of log G' vs. log ωa_T (——) for blends at 190°C and (- - -) for modified Rouse model. Data for blends C and D are suppressed above $\omega a_T = 500$ sec^{-1} since they are the same as for blend B in this range.

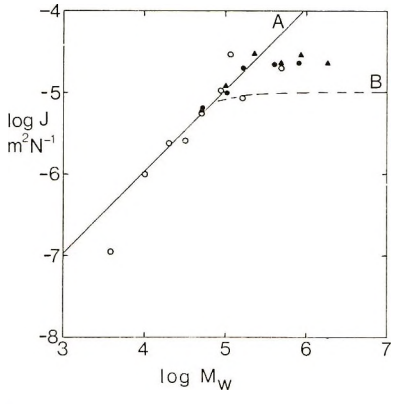

Fig. 8. Plots of log of limiting low-frequency compliance J vs. log $\bar{M}_w$ for polystyrene (mainly at 190°C): (O) oscillatory measurements; (▲) flow birefringence; (●) normal stress; (A) Rouse theory; (B) combination of Rouse theory and entanglement-network theory.

the relaxation time spectrum at $p = M/M_c$. The predicted low frequency values of G' are too large, but above $\omega a_T = 10^{-1}$ sec^{-1} the values are too small. The fit of this model to experiment will deteriorate further with increasing molecular weight.

The limiting low frequency compliances (values in Table III) of anionic polystyrenes are plotted against $\bar{M}_w$ in Figure 8 together with published results involving use of flow birefringence[19] and normal stress in steady-shear flow[20] measurements. The Rouse theory is shown to fit the data for $10{,}000 < \bar{M}_w < 200{,}000$, although the upper limit might be 100,000 if truly monodisperse polystyrene were available. Outside this range the compliance falls below the line, and the various methods of measurement all indicate a constant compliance above $\bar{M}_w = 200{,}000$. Onogi's compliance data[8] for polymers with $M < 100{,}000$ falls above ours, but his

GPC characterization indicates a broader molecular weight distribution for these polymers.

Oscillatory Shear on Blends

The limiting compliance J for the polystyrene blends is compared with the extended Rouse theory in Figure 9 and with the empirical correlation with $\bar{M}_z/\bar{M}_w$, used previously[7] for polydimethylsiloxane and published stress relaxation data for polystyrene, in Figure 10. In Figure 9

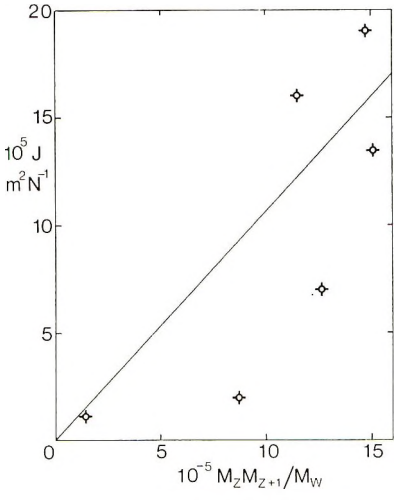

Fig. 9. Plot of J vs. $\bar{M}_{z+1}$ $\bar{M}_z/\bar{M}_w$ for blends.

the points fall widely on either side of the Rouse theory prediction, confirming the more limited results of Akovali[21] from stress relaxation. In Figure 10 the data fall on the line given by

$$J = 1.0 \times 10^{-5} (\bar{M}_z/\bar{M}_w)^{3.7} \tag{9}$$

where J is in units of square meters per Newton. The data of Onogi et al.[8] for binary blends of polystyrene are included in Figure 10. Onogi's $\bar{M}_w$ values calculated from intrinsic viscosities were used, and $\bar{M}_z/\bar{M}_w$ for the components of the blends deduced from the compliance data given and eq. (9). The calculated molecular weight averages for the blends are given in Table V. The limiting viscosity of our blends and whole polymers at 190°C was found to fit the relation

$$\log \eta_0 = 3.57 \log \bar{M}_w - 13.81 \tag{10}$$

Although the limiting low frequency values of G″ and G′ in Figures 6 and 7 are proportional to $\bar{M}_w^{3.7}$ and $(\bar{M}_w\bar{M}_z)^{3.7}$, respectively, at a given frequency, this relation breaks down at higher frequencies. Thus G'' for blends A–D lies above that for either component at $\omega a_T = 10^2$ and a closing up of G' for blends B–D is also seen at this frequency. The weight

TABLE V
Compliance Data for Blends of Onogi et al.[8] at 160°C

Blend	$\bar{M}_w$	$\bar{M}_z/\bar{M}_w$	$J_e \times 10^{-5}$, m^2/N
BB25	283,000	1.29	2.0
BB15	320,000	1.96	8.2
BB32	143,000	1.20	1.7
BB34	119,000	1.36	3.8
BB36	95,000	1.44	4.5
BB38	71,000	1.61	7.0

fraction addition laws associated with the Rouse theory and used to obtain equations 4 and 5, fail for the complex modulus components of the blends.

Continuous Shear Measurements on Blends

Figure 11 shows the log shear stress log shear rate relation of the polystyrene blends in continuous shear flow. The Weissenberg and capillary viscometer results do not coincide exactly either because of temperature differences between the two instruments (should not be >2°C), or because of the effect of pressure on viscosity. The values of p_{12} (shear stress) and G'' coincide fairly well in Newtonian region at shear rate $\dot{\gamma}$ = fre-

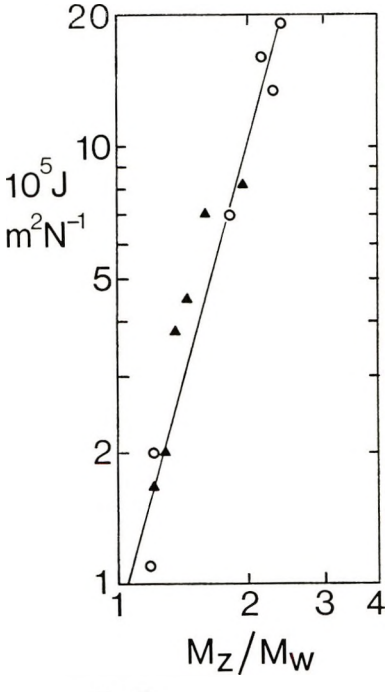

Fig. 10. Plot of log J vs. log $(\bar{M}_z/\bar{M}_w)$ for blends: (▲) Onogi's data; (○) our data.

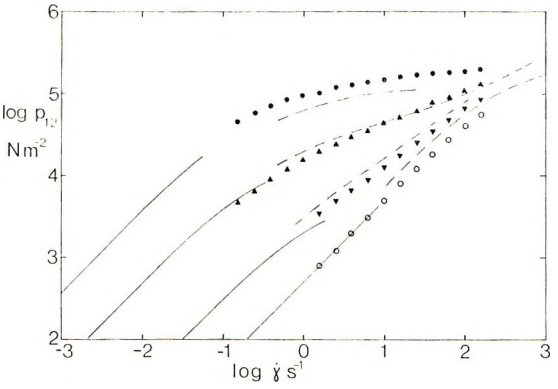

Fig. 11. Shear stress p_{12} versus shear rate $\dot{\gamma}$ in steady-shear flow for polystyrene blends obtained with (——) Weissenberg and (- - -) capillary viscometer: (●) 1, (▲) A, (▼) C, (○) 2 are $|G|$ at $\omega = \dot{\gamma}$.

quency ω. At higher frequencies, G'' falls below p_{12}, but the empirical correlation[22] between p_{12} and $|G|$ works reasonably well. For the 500,000 molecular weight polymer, G' is the major contributor to $|G|$, and in this case $|G|$ is somewhat higher than P_{12}.

The postulated relation[7] between the flow curve (p_{12} versus $\dot{\gamma}$) and the molecular weight distribution was tried for these polystyrene blends. The flow curve was smoothed over the instrument discontinuity then differentiated at points 0.5 apart in log $\dot{\gamma}$. The molecular weight distribution $W(\ln M)$, where W is the weight fraction on a logarithmic scale, was calculated from

$$W(\ln M) = (p_{12}J_M)^{0.27}\left[\frac{d \ln p_{12}}{d \ln \dot{\gamma}} - \left(\frac{d \ln p_{12}}{d \ln \dot{\gamma}}\right)^2 - \frac{d^2 \ln p_{12}}{d(\ln \dot{\gamma})^2}\right] \quad (11)$$

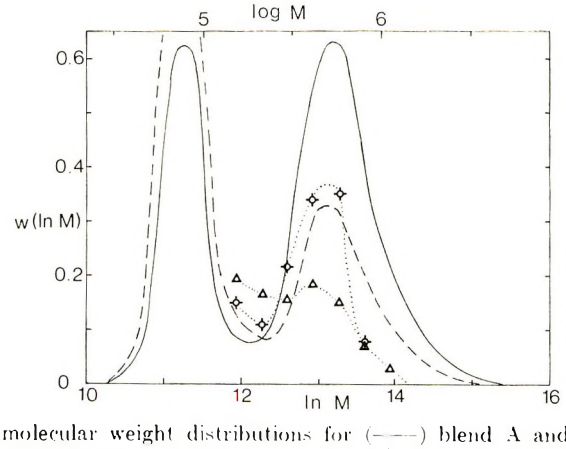

Fig. 12. GPC molecular weight distributions for (——) blend A and (- - -) blend B compared with the rheological prediction (-◇-) for A and (△) for B.

where $J_M\ \eta(M) = 1/\dot{\gamma}$, by using the viscosity molecular weight relation $\eta(M)$ and the monodisperse compliance $J_M = 1.0 \times 10^{-5}$ m²/N.

The results for blends A and B are compared with the GPC molecular weight distributions in Figure 12. The theoretical curves considerably underestimate the amount of high molecular weight material in the blends. Thus although this method is hardly exact at predicting the molecular weight distribution, it may be a useful first approximation.

Similar blending experiments were carried out by using 500,000 and 30,000 molecular weight polystyrenes, and in this case the rheological predication of the amount of the high molecular weight component was quite good. However, this was not felt to be a fair trial since the low molecular weight component is probably nonentangled, not a typical situation in a polymer melt.

DISCUSSION

The low-frequency compliance of organic glasses of low molecular weight has been shown[23] to be in the range between 10^{-9} and 10^{-8} m²/N. The compliance is expected to increase when the molecule is long enough to act as a deformable Gaussian coil, i.e., when the chain contains more than five freely joined segments. For polystyrene the molecular weight of one segment of rubber elasticity theory is 770 (this is calculated from the unperturbed mean square end to end distance in dilute solution, and the maximum length of the molecule possible by rotating bonds but not deforming bond angles). Therefore entropy elasticity is expected to occur for molecular weights greater than 4000. If the empirical model of Barlow, Erginsav, and Lamb is assumed to apply to all pure low molecular weight liquids in the glass transition region, then the polystyrene of $M = 3800$ is no different from these. Although the limiting compliance of the 10,000 molecular weight polystyrene agrees with the value for the Rouse theory, eq. (3), this is somewhat fortuitous. The behavior is best explained in terms of one or two Rouse modes superimposed upon the BEL model.

The frequency dependence of the complex modulus only coincides with the high molecular weight Rouse model at about $M = 30{,}000$, there being insufficient Rouse modes at lower molecular weights, and the effects of entanglements changing the behavior at higher molecular weights. It is assumed that a type of entanglement network described by Lodge[24] exists in high molecular weight polymer melts. Rheological data gives information on the number of lifetime function of the entanglements. If the kinetic theory of rubberlike elasticity is valid, then the average molecular weight of polymer per entanglement M_L is related to the shear modulus for an instantaneous strain G_I by

$$G_I = M_L/\rho RT \tag{12}$$

where ρ is the density and T the absolute temperature of the melt, and R is the gas constant. Previous work on polydimethylsiloxane[7] indicated

that G_I was experimentally equal to $1/J_M$ for steady shear measurements, and this would be justified by the Lodge theory if the entanglement lifetime function had a particular form and molecular weight dependence. Taking the monodisperse compliance J_M from eq. 9 gives a value of $M_L = 38000$ for polystyrene at 190°C (compared to a value of 42,000 at 115°C calculated[7] from published stress relaxation data). The entanglement network does not become completely effective until M is much greater than 38,000. The simplest method (and at this stage only an approximation is required) of allowing for chain ends that are not effective in the network is to use the expression of Flory[25]

$$G_1 = (\rho RT/M_L)\,[1 - (2M_L/\bar{M}_n)] \tag{13}$$

for the effective number of network chains, adapted for an entanglement network. $\bar{M}_n$ is the number-average molecular weight of the polymer melt. If it is assumed that the complex shear modulus of the melt is a sum of the Rouse-type behavior [eq. (3)] and the entanglement network behavior [eq. (13)], the compliance J of a monodisperse polymer will be given by eq. (3) for $M < 2M_L$ and by

$$\frac{1}{J} = \frac{2.5RT}{M} + \rho RT\left(\frac{1}{M_L} - \frac{2}{M}\right) \tag{14}$$

for $M > 2M_L$. This relation is shown in Figure 8 as line B, with $M_L = 38{,}000$. Bearing in mind that high molecular weight polystyrenes have $\bar{M}_z/\bar{M}_w \approx 1.2$ so that the correction for polydispersity $(\bar{M}_z/\bar{M}_w)^{3.7}$ is about 2, the agreement is quite good. The contribution of the two types of behavior to the compliance are equal at $M = 4.5\,M_e$ or 170,000 for polystyrene.

The log viscosity–log $\bar{M}_w$ relation changes its slope from roughly 1 to 3.7 in the region of the critical molecular weight M_c defined as the intercept of the extrapolated first and 3.7th power regions; and M_c is found to be in the region 30,000 to 40,000. It must therefore be assumed that entanglements between isolated pairs or groups of chains not forming part of a network begin to have a marked effect on the viscosity at this molecular weight. That the modification of the Rouse theory is needed in the range $100{,}000 > M > 30{,}000$ is confirmation of an entanglement effect. This WLF modification does not change the molecular weight dependence of the limiting low frequency compliance, hence J follows the Rouse theory value for $100{,}000 > M > 10{,}000$.

The molecular weight dependence of J is approximately the same as the molecular weight dependence of the tensile strength[25] of unoriented anionic polystyrene in that it rises rapidly from a low value at $M = 50{,}000$ to a plateau value above $M = 150{,}000$. This together with the examination of fracture surfaces of anionic polystyrenes[26] of molecular weights 35,000, 82,000, and 222,000 suggests that a complete entanglement network is necessary in glassy polystyrene to achieve adequate mechnical properties. This entanglement network then allows the formation of

small highly extended filaments during the fracture of the polystyrene at room temperature.

We would like to thank R. Denyer for supplying some anionic polystyrenes and J. W. Maddock for GPC measurements.

References

1. W. P. Cox, L. E. Nielsen, and R. Keeney, *J. Polym. Sci.*, **26**, 365 (1957).
2. S. Onogi, H. Kato, S. Ueki, and T. Ibaragi, in *U.S.-Japan Seminar in Polymer Physics* (*J. Polym. Sci. C*, **15**), R. S. Stein and S. Onogi, Eds., Interscience, New York, 1966, p. 481.
3. R. P. Chartoff and B. Maxwell, *Polym. Eng. Sci.*, **8**, 126 (1968).
4. J. L. Den Otter, *Rheol. Acta*, **8**, 355 (1969).
5. D. E. Burge, *J. Appl. Polym. Sci.*, **13**, 1993 (1969).
6. S. Middleman, *The Flow of High Polymers*, Interscience, New York, 1968, Chap. 4.
7. N. J. Mills, *Europ. Polym. J.*, **5**, 675 (1969).
8. S. Onogi, T. Masuda, and K. Kitagawa, *Macromolecules*, **3**, 109 (1970).
9. N. J. Mills, A. Nevin, and J. McAinsh, *J. Macromol. Sci. (Phys.)*, **B4**, 863 (1970).
10. N. J. Mills, *Rheol. Acta*, **8**, 226 (1969).
11. B. D. Coleman and H. Markovitz, *J. Appl. Phys.*, **35**, 1 (1964).
12. P. E. Rouse, *J. Chem. Phys.*, **21**, 1272 (1953).
13. A. V. Tobolsky, J. J. Aklonis, and G. Akovali, *J. Chem. Phys.*, **42**, 723 (1965).
14. J. D. Ferry, *Viscoelastic Properties of Polymers*, Wiley, New York, 1961, p. 171.
15. J. D. Ferry, R. F. Landel, and M. L. Williams, *J. Appl. Phys.*, **26**, 359 (1955).
16. A. J. Barlow, A. Erginsav, and J. Lamb, *Proc. Roy. Soc.* (London), **A298**, 481 (1967).
17. R. B. Bird and E. K. Harris, *AIChE J.*, **14**, 758 (1968).
18. B. Maxwell and R. P. Chartoff, *Trans. Soc. Rheol.*, **9**:**1**, 41 (1965).
19. H. Janeschitz-Kriegl, *Fortschr. Hochpolym. Forsch.*, **6**, 170 (1969).
20. H. J. M. A. Mieras and C. F. N. van Rijn, *Nature*, **218**, 865 (1968).
21. G. Akovali, *J. Polym. Sci. A-2*, **5**, 875 (1967).
22. W. P. Cox and E. H. Merz, *J. Polym. Sci.*, **28**, 619 (1958).
23. J. J. Benbow, *Proc. Phys. Soc.*, **B67**, 120 (1954).
24. A. S. Lodge, *Elastic Liquids*, Academic Press, New York, 1964, p. 118.
25. P. J. Flory, *Principles of Polymer Chemistry*, Cornell Univ. Press, Ithaca, N. Y., 1953.
26. H. W. McCormick, F. M. Bower, and L. Kin, *J. Polym. Sci.*, **39**, 87 (1959).
27. R. N. Haward and I. Brough, *Polymer*, **10**, 724 (1969).

Received May 1, 1970
Revised July 30, 1970

JOURNAL OF POLYMER SCIENCE: PART A-2 VOL. 9, 283–294 (1971)

Adhesion of Viscoelastic Materials to Rigid Substrates. II. Tensile Strength of Adhesive Joints

A. N. GENT, *Institute of Polymer Science, The University of Akron, Akron, Ohio 44304**

Synopsis

Measurements have been made of the tensile force required to pull a disk of a model viscoelastic adhesive away from an inert rigid substrate. Over a wide range of temperature and rate of deformation of the adhesive the results were found to yield a single master relation in terms of deformation rate by means of the Williams, Landel and Ferry rate–temperature equivalence for viscous materials. Thus, the strength of adhesion is due mainly to dynamic effects in the adhesive of a viscous nature, in a similar way to the cohesive strength of viscoelastic materials. This similarity is attributed to a common failure mechanism: initial failure at a highly stressed point, followed by spreading of the failure zone under local stresses which are governed by the dynamic response of a compliant material. An increase in the strength of adhesion is observed with decreasing thickness of the adhesive layer. This is also explained by the proposed failure mechanism if failure starts at a critical amount of local deformation energy, a form of Griffith's fracture criterion.

INTRODUCTION

In a previous publication,[1] a study of the mechanics of adhesive failure by peeling apart two flexible adherends was reported. We now consider separation of adherends by a simple tensile pull. An experimental investigation has been carried out of the effects of rate of separation and temperature, and to some extent of the thickness of the adhesive layer, on the force required to cause tensile failure of a "sandwich" testpiece (Fig. 1). The same viscoelastic material was employed as before[1] as a model adhesive, and it was sandwiched between two layers of one of the same substrate materials used before. Thus, only the method of separation has been changed. This change had profound consequences, however, as described below.

The experimental results are presented in the following section of the paper. They are then discussed in terms of a concept of tensile adhesive failure as catastrophic peeling from an initial flaw where bonding is imperfect or absent. Although not applied before (to the author's knowledge) to adhesion, a similar concept has been widely employed to treat cohesive tensile rupture of glassy and rubbery solids in terms of tearing from a small

* Visiting Professor, Department of Materials, Queen Mary College, University of London, 1969–70.

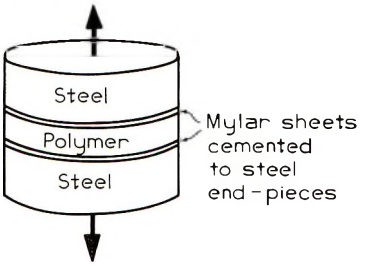

Fig. 1. Sketch of tensile testpiece.

nick or flaw acting as a stress raiser. This view of tensile rupture of materials which are primarily elastic, like crosslinked rubbers or brittle glasses, has been reviewed recently by Greensmith et al.,[2] Berry,[3] Landel and Fedors,[4] Halpin,[5] and Andrews.[6] It was put forward originally by Griffith.[7,8]

Less attention has been paid to the rupture of elastic liquids, like the uncrosslinked polymer used in the present experiments. At high rates of deformation it behaves like an elastic solid because intermolecular entanglements prevent rapid flow,[9,10] whereas at low rates of deformation it behaves like a Newtonian liquid of high viscosity. Measurements of cohesive tensile rupture for the present polymer over a wide range of deformation rate have been described elsewhere.[11,12] They are compared here with the measured adhesive bond strengths in tension.

Finally, the effect on the bond strength of the thickness of the adhesive layer is examined. As is well known, the thinner the adhesive layer, the greater is the adhesive strength of a bond in tension.[13,14] In contrast, the thinner the adhesive layer, the smaller is the force required to peel apart two bonded films.[15,16] This paradox does not appear to have been resolved before. It is accounted for here in a qualitative way, assuming that in both cases failure occurs in accordance with a critical energy criterion, a generalized form of Griffith's fracture criterion.

EXPERIMENTAL

Preparation of Testpieces

The viscoelastic substance used as a model adhesive in the present experiments was the same as before, a high molecular weight amorphous polymer consisting of butadiene (60%) and styrene (40%) randomly copolymerized to yield a linear polymer with a number-average molecular weight of about 70,000, and a glass transition temperature T_g of about $-40°C$ (Amperipol 1513, Goodrich—Gulf Chemical Company). It was pressed between two sheets of a glassy plastic film, poly(ethylene terephthalate) (Type 300 A Mylar, E. I. du Pont de Nemours & Co.), for 15 min at a temperature of 75°C, to form a "sandwich." Measurements of the force P required to peel off one of the Mylar films from such a sandwich were described previously.[1] For the present experiments, disk-shaped test-

pieces were cut from the sandwich with a circular die, 2.5 cm in diameter, and then the outer surfaces of the two Mylar disks were cemented to steel blocks (Fig. 1) to confer rigidity and to provide a means of applying a tensile force normal to the plane of the Mylar/adhesive interfaces.

As it proved rather difficult to obtain satisfactory bonding of the Mylar films to steel, the technique adopted is now described in some detail. The Mylar surfaces were first treated with 90% sulfuric acid for 3 min. They were then washed with cold water and allowed to dry at room temperature. Sulfuric acid reacts with Mylar, leaving a corroded surface with a chalky deposit clinging to it. This deposit was removed by rubbing the surface with a tetrahydrofuran-soaked cloth and then allowing it to dry again. The treated Mylar surfaces were then bonded to the steel blocks with an epoxy cement, consisting of resin and hardener in equal parts, which was allowed to set for 24 hr at room temperature. The bonds obtained in this way between Mylar and steel were able to withstand tensile loads of over 50 kg/cm^2 without failure.

Testpieces were made with two quite different thicknesses of Ameripol 1513 between the Mylar surfaces, 0.1 cm and 2.5 cm, corresponding to relatively thin and relatively thick adhesive layers. Most of the experiments were carried out with the thinner test-pieces.

Measurement of Tensile Strength σ_b

The steel end-pieces (Fig. 1) were pulled apart in a tensile testing machine at various speeds in the range 0.83×10^{-4} to 0.83 cm/sec and temperatures in the range $-40°$C to $+50°$C. The corresponding tensile forces set up in the adhesive were measured as a function of time, and hence of displacement of the end-pieces, by means of a strain gauge bridge and high-speed chart recorder.

Different types of relation were obtained between the mean tensile stress σ, i.e., the tensile force per unit bonded area, and the fractional displacement e of one bonded surface with respect to the other, under different circumstances. At high rates of extension and low temperatures, the stress–displacement relations were substantially linear up to the (small) extensions at which abrupt separation occurred at a Mylar–adhesive interface. At somewhat lower rates and higher temperatures the relations were nonlinear, but adhesive failure still occurred at a well-defined maximum force. The strength of the adhesive bond in all these cases has been taken as the mean tensile stress at break, σ_b.

In some instances, internal rupture of the adhesive occurred for the thinner testpieces[17] at intermediate rates of extension and temperatures. Cavities appeared in the central region of the testpiece and grew, causing rupture of the adhesive rather than failure of the bond, often at a final force less than that at which the cavitation occurred. Sometimes, however, failure still took place at the interface, even though the adhesive layer had already suffered internal rupture.

In these cases where failure was caused or accompanied by cavitation, the strength of the testpiece has still been taken as the maximum tensile stress attained before failure. To distinguish them from other modes of failure the corresponding experimental values are represented, respectively, by full or half-filled circles in the Figures, although in fact they were found not to differ greatly in magnitude from results for purely adhesive failures without cavitation, under similar experimental conditions.

At low rates of extension and high temperatures the adhesive was soft, liquidlike and highly deformable. In consequence, the tensile force was always small and rose on extension to a maximum value at about 20–40% elongation. It then decreased, the sample elongating further in a nonuniform way by forming a narrow-waisted central region. Rupture took place eventually at large extensions and at a much smaller force than the maximum value. Even the true stress at break calculated from the reduced cross-sectional area was less than the maximum value attained at small extensions. The maximum value has been taken here as a measure of the strength of the testpiece for consistency, but it must be regarded as an overestimate of the cohesive strength of the polymer and as an underestimate of the true bond strength, because the interface does not fail under these conditions.

RESULTS

The tensile strength σ_b is plotted in Figure 2 against the rate of extension $\dot{e}$. A logarithmic scale is used for $\dot{e}$ in view of the wide range of rates employed. Results are shown for a number of different temperatures.

The values obtained for σ_b range from less than 1 to more than 50 kg/cm^2, increasing continuously with increasing rate of extension and with decreasing temperature. Clearly, there is no single value for the strength of adhesion between the adhesive and substrate. Indeed, the variation observed in σ_b is similar to that which would be expected for several mechanical properties of the adhesive itself. Its cohesive tensile strength, for example, will increase with increasing rate of deformation and decreasing temperature in a similar way, reflecting the general transition from a liquidlike to a glasslike response in a viscoelastic material.[10,18]

The fundamental variable in such cases is the ratio of the rate of deformation $\dot{e}$ to the frequency ϕ_T with which molecular segments move to new positions. The variation of ϕ_T with temperature T follows a characteristic law for simple glass-forming substances, like the present model adhesive,

$$\log (\phi_T/\phi_{T_g}) = -17.4(T - T_g)/(52 + T - T_g) \qquad (1)$$

depending only upon the temperature difference $T - T_g$.[9,10] Accordingly, the results shown in Figure 2 have been replotted in Figure 3 against equivalent rates of extension $\dot{e}a_T$ at a convenient reference temperature T_s of 23°C, where the factor $a_T (= \phi_{T_s}/\phi_T)$ was calculated from eq. (1) for each temperature by using the appropriate value of T_g, 233°K for the present adhesive.

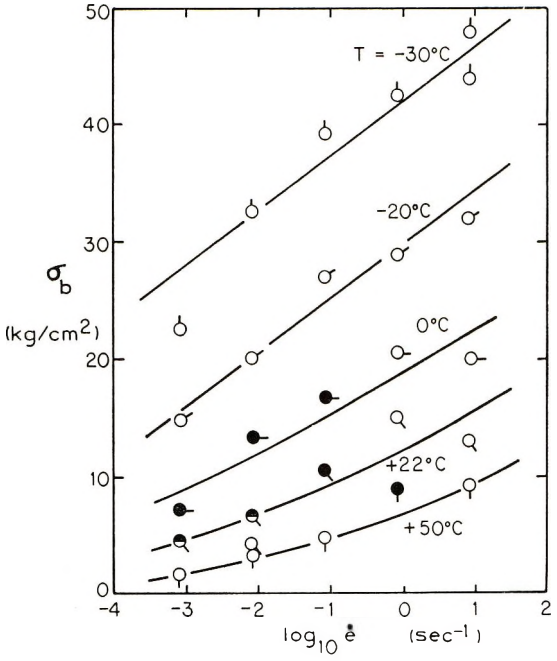

Fig. 2. Tensile breaking stress σ_b for a thin adhesive layer (1 mm thick) vs. rate of extension $\dot{e}$. Filled circles denote internal rupture or cohesive failure, instead of adhesive failure. Pips vertically down, +50°C; successive 45° intervals counterclockwise, +22°C, 0°C, −20°C, −30°C, −40°C.

In this representation the results obtained at different test temperatures all superimpose satisfactorily to yield a single master relation for adhesive strength as a function of rate of extension. The good superposition shows

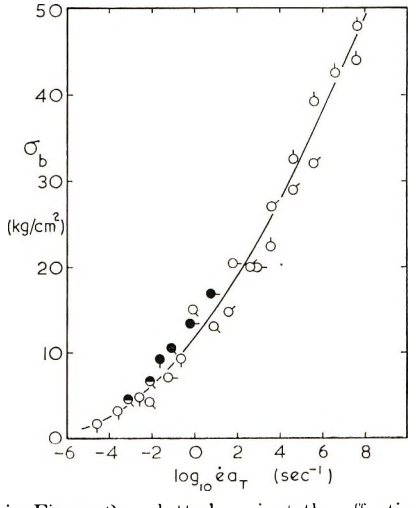

Fig. 3. Results shown in Figure 2 replotted against the effective rate of extension $\dot{e}a_T$ at 23°C, calculated by means of eq. (1).

that the strength of adhesion is associated with dynamic effects of a viscous nature, rather than with equilibrium thermodynamic properties, for example bond dissociation energies. A similar conclusion has been reached for the cohesive strength of viscoelastic materials.[2,19]

At first sight, this similarity appears to support Bikerman's conjecture that purely adhesive failure does not occur.[20] Instead, cohesive failure takes place in the adhesive itself, in the vicinity of the interface. However, there are several reasons for discounting this hypothesis,[21] and it seems more likely that the similarity arises from a common failure mechanism in both cases, which may be stated as follows:

Proposed Failure Mechanism

Failure (or adhesive separation) first occurs at a site of high local stress, for example at the tip of an edge flaw, and then propagates under the influence of the stress field acting at its moving boundary. These local stresses are governed by the dynamic response of the material. They will be smaller for materials which exhibit mechanical hysteresis (as viscoelastic materials do) and consequently the applied forces necessary to cause failure will be larger than for ideally elastic materials. This is basically the mechanism of "reinforcement" proposed by Andrews[22,23] to account for the high cohesive strengths of imperfectly elastic rubbery materials. It can clearly apply to the strength of an adhesive joint also, and then accounts both for the success of the Williams, Landel, and Ferry temperature reduction scheme for a simple viscoelastic adhesive, and for the surprisingly high values of bond strength attained at high rates of extension (Fig. 3), when the material is becoming glasslike, its mechanical hysteresis is high, and Andrews' reinforcement mechanism is most effective.

The proposed failure mechanism leads to a generalization of Griffith's fracture criterion, that bond failure will occur when the energy stored elastically in the adhesive (assumed to be the compliant member, the substrate being regarded as rigid) in the vicinity of the initial flaw and released by growth of the initial flaw is sufficient to meet the energy requirements for growth. This criterion was put forward for cohesive failure by Rivlin and Thomas[24] and shown to describe several different modes of fracture in a unified way.[2,24] It is applied to adhesive testpieces in the following section.

Strength of Thicker Testpieces

The maximum tensile stress required to break the 2.5-cm testpieces was also measured over a range of rates of extension and temperature. Again, the Williams-Landel-Ferry rate–temperature equivalence was found to hold with reasonable success. Results obtained at different temperatures superimposed to form a single curve when plotted against the equivalent rate of extension $\dot{e}a_T$ at a reference temperature of 23°C, as shown in Figure 4. Also, the values obtained increased markedly with increasing rate of extension. However, they were much smaller than for the thinner testpieces,

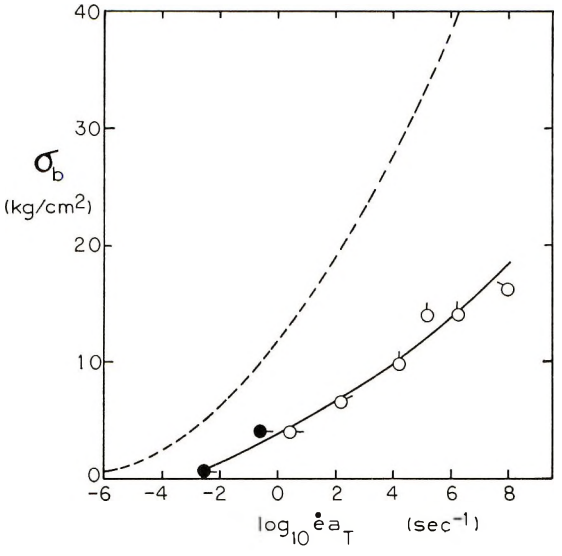

Fig. 4. Tensile breaking stress σ_b for a thick adhesive layer (2.5 cm thick) vs. effective rate of extension $\dot{e}a_T$ at 23°C. The actual test temperatures are represented by the same symbols as in Fig. 2 and 3. The broken curve represents the relation obtained for a thin adhesive layer, Figure 3.

about one-third as large at all rates of extension. This effect of an increase in adhesive thickness causing a decrease in bond strength is well known[13,14] but not previously accounted for; it is also discussed in the following section in terms of the proposed energy criterion for fracture.

Effect of Crosslinking

Measurements were also made of the tensile strength of thin adhesive layers, about 1 mm thick, crosslinked after preparing them as disks between two Mylar films. Crosslinking was effected by adding 1% of dicumyl peroxide to the polymer before molding, and subsequently heating the sandwich testpieces for 1 hr at a temperature of 150°C.

The adhesion of the crosslinked samples proved to be easily broken at room temperature and low rates of extension, so that great care had to be taken in handling the testpieces. However, over the entire range of test temperatures and rates of extension they were found to give substantially the same breaking stresses as the uncrosslinked specimens (although with considerably greater experimental scatter). The experimental difficulties in handling these testpieces are therefore attributed to the much reduced extensibility of the crosslinked material, compared to the uncrosslinked one, at low rates of extension; the actual bond strengths appear to be quite similar for both materials.

This is in sharp contrast to peel adhesion measurements, where crosslinking brings about a considerable reduction in strength at low rates of peel.[1] The difference is due to the importance of adhesive extensibility in

peel strength, which is proportional to the energy of deformation up to the point of detachment or rupture[1,15] rather than to the maximum stress the bond can withstand. Similarly, internal ruptures and subsequent large deformations before final failure, usually of a cohesive nature, were not associated with unduly large tensile strength values (filled circles, Figs. 3 and 4), although this behavior would result in high peel strength because of the large work of deformation.[25]

Cohesive Strength of the Adhesive Material

Measurement were made of the tensile breaking stress σ_b for molded rods of the model viscoelastic adhesive material, Ameripol 1513, at various temperatures and rates of extension.[11,12] The values obtained are plotted in Figure 5 against the effective rate of extension $\dot{e}a_T$ at 23°C, calculated by means of eq. (1). Logarithmic scales are used for both axes in view of the wide ranges. There is a high degree of experimental scatter, due in part to molding and gripping difficulties, but the general character of the results is clear. They fall into two distinct regions. (*1*) At low rates, less than 10^2 sec^{-1}, the material behaved primarily like a viscous fluid, and extended in a ductile manner at low stresses. The maximum stress in this case depends primarily on the viscous resistance to flow, increasing rapidly with rate of extension. (*2*) At rates greater than about 10^2 sec^{-1} (at this temperature) liquidlike flow ceased and the material responded in a rubberlike way, as an entangled molecular network. As the rate of extension increased further, the material became harder and stronger and eventually responded like a glassy solid. This second change in fracture properties has been studied

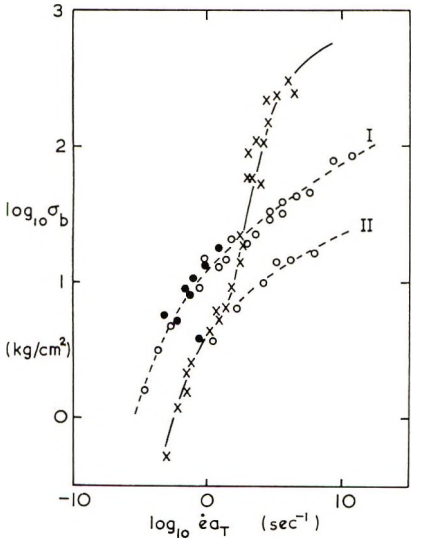

Fig. 5. Plot of (×) cohesive tensile breaking stress σ_b vs. effective rate of extension $\dot{e}a_T$ at 23°C; (---) relations obtained for the adhesive strength of thin (I) and thick (II) adhesive layers (replotted from Figs. 3 and 4).

by Smith[18] for a crosslinked material of similar composition to the present one.

The experimental relations obtained previously for adhesive strength (Figs. 3 and 4) are replotted in Figure 5 for comparison with the cohesive strength results. At high rates, approaching the glassy state, the cohesive strength is seen to be about 20–30 times larger than the adhesive strength of the thicker testpieces. Part of this difference can be ascribed to the presence of abnormally large stress concentrations at the edges of the disk in the adhesion experiments, so that the real adhesive bond strength appears to be quite high, of the order of $^1/_{16}$ or more of the cohesive strength under similar conditions. At low rates of extension, when the material deformed in a ductile manner before separation into two pieces, the test material sometimes broke "cohesively" in the adhesion experiment (filled circles). The values of "adhesive" and "cohesive" strength in these cases were necessarilly the same. It thus appears that the intrinsic strength of adhesion is not much smaller than the instrinsic cohesive strength when molecular rupture occurs, i.e., at high rates of extension, and is similar to or even larger than the cohesive strength at low rates of extension, when the molecules separate by flowing apart rather than by rupture.

EFFECT OF TESTPIECE THICKNESS ON ADHESIVE STRENGTH: THEORETICAL CONSIDERATIONS

Peel Testpiece

In this case the peel energy, or work of separation per unit area, is given directly by the peel force per unit width. This energy is accounted for mainly by work expended in deforming the adhesive so that a critical stress (or energy) condition is set up at the tip of the peel front.[1] It is therefore predicted to be directly proportional to the thickness of the adhesive layer, neglecting any energy of deformation of the backing layer. Experimental measurements are in reasonably good agreement with this prediction,[15,16] departing seriously from proportionality only for extremely thin adhesive layers when the bending stiffness of the backing is probably no longer negligible in comparison with that of the adhesive.

Tensile Testpiece

The shear strain γ near the outer edges of thin cylinders in tension may be calculated on certain simplifying assumptions[26] in terms of the fractional tensile strain e and the ratio a/h of cylinder radius to thickness,

$$\gamma = 3ea/h$$

This calculation will be in error right at the edges because it fails to take account of the absence of complementary shear stresses on the free surface of the cylinder (although it should be satisfactory somewhat away from the edges). We therefore expect the actual edge strains to differ from this

value, depending on the detailed shape of the cylinder edges, and represent them by the relation

$$\gamma = 3kea/h$$

where the factor k denotes the unknown stress-concentration effect of the edge geometry.

The total strain energy density W in the edge regions is given by the sum of shear and tensile contributions,

$$W = {}^1/_2Ee^2(1 + 3k^2a^2/h^2) \tag{2}$$

taking the shear modulus of elasticity as one-third of Young's modulus E. The corresponding average tensile stress is obtained from the effective value E_e of Young's modulus for thin bonded cylinders,[26]

$$\sigma = E_e e = Ee(1 + a^2/2h^2) \tag{3}$$

Hence, the breaking stress σ_b necessary to develop a critical strain energy W in the edge regions is given by substituting for e from equation (2) in eq. (3),

$$\sigma_b = (2EW)^{1/2}(1 + a^2/2h^2)(1 + 3k^2a^2/h^2)^{-1/2} \tag{4}$$

When the disc radius a is much larger than its thickness h, this relation yields an inverse proportionality between the breaking stress σ_b and h. When the radius a is much smaller than h, the breaking stress is predicted to be independent of the testpiece thickness. Dependence on thickness of this general form is commonly observed in tensile tests on adhesives. We see that it arises as a result of two competing effects: the greater stiffness of thin testpieces, necessitating a greater average tensile stress to achieve the same level of strain energy, and the increased concentration of shear strain, and hence strain energy, in the edge regions of thinner testpieces, causing failure at lower mean stresses than would otherwise be required.

The ratio of breaking stresses for the two testpiece sizes employed in the present experiments, with values of the dimensional ratio a/h of 12.7 and 0.5, was found to be about 3 over the entire range of rates of extension (Fig. 5). This value corresponds to a reasonable value for the stress concentration factor k of about 3, on substituting in eq. (4). A more detailed comparison of theory and experiment, for example between the tensile strain energy W for adhesive failure and the corresponding peel energy, is not warranted at present because of two serious deficiencies in the theoretical treatment outlined above. First, the relation employed for strain energy, eq. (2), is only valid for linear stress–strain behavior and is therefore unlikely to be satisfactory when large deformations occur. Secondly, the rate at which the adhesive separates from the substrate in a tensile experiment is not known, and an appropriate rate of peel cannot be chosen

for comparative purposes. However, at least in a qualitative way the theory accounts for the increase in breaking stress with rate of extension, Figures 3–5, because both Young's modulus E and the fracture energy W on the right-hand side of eq. (4) increase with increasing rate of deformation.

CONCLUSIONS

The tensile strength of a model viscoelastic adhesive joint, like the peel strength,[1] has been shown to depend on rate of deformation and temperature in accordance with the WLF rate–temperature equivalence for viscoelastic materials. This feature proves that the measured strength of adhesion does not directly reflect thermodynamic equilibrium bond strengths but instead is determined by viscous effects within the adhesive. The tensile breaking stress differs from the peel strength in being much less influenced by high extensibility or ductile flow of the adhesive. Also, the tensile strength decreases with increasing thickness of the adhesive layer whereas the peel strength increases. These differences have been shown to arise from a single failure criterion: that a critical strain energy density is required to cause bond failure. For peel testpieces the breaking force is then proportional to the total work of deformation, whereas for tensile testpieces the breaking stress is that necessary to generate the critical strain energy in the neighborhood of a (hypothetical) small flaw. Both the effects of extensibility and adhesive thickness are accounted for in this way.

The proposed failure criterion is a generalization of Griffith's fracture criterion for the cohesive rupture of solids.[7,8] However, the critical strain energy density is not associated here directly with a thermodynamic quantity, for example the differing surface energies of the unbroken and broken joints, but rather with the inelastic character of the adhesive. Much larger stresses must be imposed for inelastic materials than for elastic ones, as Andrews has shown,[22,23] to develop the fracture stress at the point of rupture. The critical stresses and hence strain energy densities required for failure are not necessarily constant, therefore, but will generally depend upon the degree to which the material is imperfectly elastic. This may change with rate of deformation, temperature and other factors. The particular advantage of the present model adhesive is that the dependence of its inelastic, i.e., viscoelastic, properties on rate and temperature is simple and well-understood, and this permits conclusions to be reached which, although equally valid, would be difficult to recognize in more complex adhesive systems.

This work was supported by a research grant from the Engineering Division of the National Science Foundation. The author is also indebted to Mr. I. Nazeni for experimental assistance and the preparation of testpieces, to Mr. R. L. Henry of the University of Akron and Mr. M. Fujimori of the Bridgestone Tire and Rubber Company (Visiting Scientist at the University of Akron, 1968–70) for assistance with high-speed measurements, and to Prof. E. H. Andrews of Queen Mary College, University of London, for helpful comments.

References

1. A. N. Gent and R. P. Petrich, *Proc. Roy. Soc.* (London), **A310,** 433 (1969).
2. H. W. Greensmith, L. Mullins, and A. G. Thomas, in *The Chemistry and Physics of Rubberlike Substances*, L. Bateman, Ed., Wiley, New York, 1963, Chap. 10.
3. J. P. Berry, in *Rupture Processes in Polymeric Solids*, B. Rosen, Ed., Interscience, New York, 1964, Chap. II.
4. R. F. Landel and R. F. Fedors, in *Rupture Processes in Polymeric Solids*, B. Rosen, Ed., Interscience, New York, 1964, Chap. IIIB.
5. J. C. Halpin, *Rubber Chem. Technol.*, **38,** 1007 (1965).
6. E. H. Andrews, *Fracture in Polymers*, Oliver and Boyd, London, 1968.
7. A. A. Griffith, *Phil. Trans. Roy. Soc.*, **A221,** 163 (1921).
8. A. A. Griffith, *Proc. 1st Intern. Congr. Appl. Mech. (Delft)*, 55 (1924).
9. J. D. Ferry, *Viscoelastic Properties of Polymers*, Wiley, New York, 1961.
10. F. Bueche, *Physical Properties of Polymers*, Interscience, New York, 1962.
11. R. P. Petrich, Ph.D. Thesis, The University of Akron, 1968.
12. M. Fujimori, private communication.
13. J. W. McBain and W. B. Lee, *J. Phys. Chem.*, **31,** 1674 (1927).
14. H. P. Meissner and G. H. Baldauf, *Trans. Am. Soc. Mech. Engrs.*, **73,** 697 (1951).
15. J. L. Gardon, in *Treatise on Adhesion and Adhesives*, R. L. Patrick, Ed., Dekker, New York, 1967, Chap. 8.
16. D. W. Aubrey, G. N. Welding, and T. Wong, *J. Appl. Polym. Sci.*, **13,** 2193 (1969).
17. A. N. Gent and P. B. Lindley, *Proc. Roy. Soc.* (London), **A249,** 195 (1958).
18. T. L. Smith, *J. Polym. Sci.*, **32,** 99 (1958).
19. G. J. Lake and A. G. Thomas, *Proc. Roy. Soc.* (London), **A300,** 108 (1967).
20. J. J. Bikerman, *The Science of Adhesive Joints*, Academic Press, New York, 1961.
21. J. R. Huntsberger, *J. Polym. Sci. A*, **1,** 1339 (1963).
22. E.H. Andrews, *J. Appl. Phys.*, **32,** 542 (1961).
23. E. H. Andrews, *J. Mech. Phys. Solids*, **11,** 231 (1963).
24. R. S. Rivlin and A. G. Thomas, *J. Polym. Sci.*, **10,** 291 (1953).
25. D. H. Kaelble, *Trans. Soc. Rheol.*, **9:2,** 135 (1965).
26. A. N. Gent and E. A. Meinecke, *Polym. Eng. Sci.*, **10,** 48 (1970).

Received June 29, 1970

JOURNAL OF POLYMER SCIENCE: PART A-2 VOL. 9, 295–311 (1971)

Scattering of Light by Deformed Three-Dimensional Spherulites

J. J. VAN AARTSEN* and R. S. STEIN, *Polymer Research Institute and Department of Chemistry, University of Massachusetts, Amherst, Massachusetts 01002*

Synopsis

A theoretical calculation of the H_V light-scattering patterns for deformed three-dimensional spherulites is presented. Affine deformation is assumed. The optic axis of the scattering element is allowed to lie at an arbitrary angle β to the radius which is permitted to change in the course of the deformation in a manner that may depend upon the angular location in the spherulite. The consequences of twisting of the optic axis about the spherulite radius are also explored.

Introduction

It is known that the stretching of a spherulitic polymer produces very specific changes in the corresponding light scattering patterns from such samples.[1–6] A theory of scattering from deformed two-dimensional spherulites has been presented[3] as well as a semiempirical theory for the deformation of three-dimensional spherulites.[7] Both theories qualitatively account for the form of the scattering patterns but differ in detail. In this paper, the previous two-dimensional approach[3] will be extended to three dimensions.

The assumption of affine deformation of the spherulite will be used so that all parts of the spherulite deform equally and any point in the undeformed spherulite having coordinates (x,y,z) will assume coordinates (x',y',z') in the deformed state such that $x' = \lambda_1 x$, $y' = \lambda_2 y$, and $z' = \lambda_3 z$. We will restrict our considerations to uniaxial deformation so that $\lambda_1 = \lambda_2$. It is realized, of course, that this represents a simplification for real systems, in that it has been observed[8–10] that spherulites often deform differently in different regions.

We shall consider the case where the optic axis of the scattering element is initially oriented at some arbitrary angle β_0 with respect to the spherulite radius (Fig. 1) which may change in the course of deformation according to some assumed empirical equation. We shall also assume that the twist angle ω of the optic axis about the radius is initially random but may achieve some preferential orientation in the course of stretching.

* Present address: AZKO Research Laboratories, Arnhem, Netherlands.

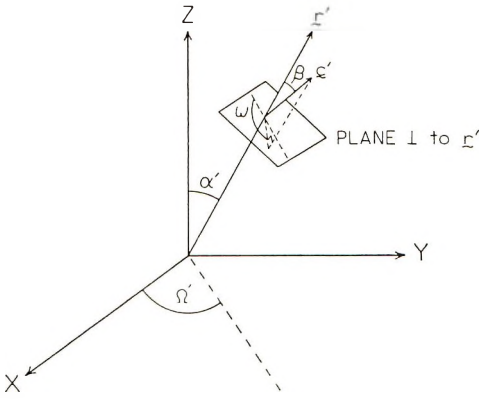

Fig. 1. Coordinates describing the orientation of the optic axis of the scattering element with respect to the spherulite radius.

General Theory[11]

For a scattering element located at coordinates (r',α',Ω') in the spherulite (see Fig. 1), where the primed quantities designating the deformed state, the scattered amplitude is given by

$$E = C \int_{r'=0}^{R'} \int_{\alpha'=0}^{\pi} \int_{\Omega'=0}^{2\pi} N'(r',\alpha'\Omega')(\mathbf{M}'\cdot\mathbf{O}) \cos\,[k(\mathbf{r}'\cdot\mathbf{s})]\,\sin\,\alpha' d\Omega' d\alpha' (r')^2 dr. \quad (1)$$

where $N'(r',\alpha',\Omega')$ is a distribution function for density of scattering elements in the deformed state, $\mathbf{M}'$ is the induced dipole moment in the

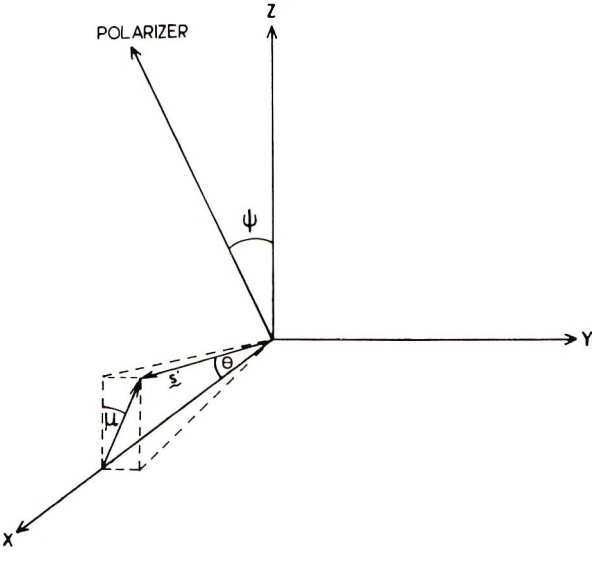

Fig. 2. Coordinate system of the scattering and polarization angles.

scattering element, $\mathbf{O}$ is a unit vector normal to the scattered ray and in the plane of polarization of the scattered ray transmitted by the analyzer, and the propagation vector $\mathbf{s}$ is defined by $\mathbf{s} = \mathbf{s}_0 - \mathbf{s}'$, where $\mathbf{s}_0$ and $\mathbf{s}'$ are unit vectors along the incident and scattered ray. Thus, it follows that

$$\mathbf{s} = 2 \sin (\theta/2)[(\sin \theta/2)\mathbf{i} - (\cos \theta/2 \sin \mu)\mathbf{j} - (\cos \theta/2 \cos \mu)\mathbf{k}] \quad (2)$$

where θ and μ are the polar and azimuthal scattering angles as shown in Figure 2, where the incident beam travels along the x axis and z is the "vertical" direction. The wavenumber k is $2\pi/\lambda$.

The calculation of the scattering is dependent upon obtaining expressions for N' and $\mathbf{M}'$ as a function of coordinates in the deformed state. If $\mathbf{c}'$ and $\mathbf{d}'$ are unit vectors along and perpendicular to the optic axis of the scattering element (which is assumed to be uniaxial with principal polarizabilities α_1 and α_2), the induced dipole moment resulting from an incident electric field $\mathbf{E}$ is

$$\mathbf{M}' = \alpha_1(\mathbf{E}\cdot\mathbf{c}')\mathbf{c}' + \alpha_2(\mathbf{E}\cdot\mathbf{b}')\mathbf{b}' \quad (3)$$

$\mathbf{b}'$ lies perpendicular to $\mathbf{c}'$ and in the plane formed by $\mathbf{c}'$ and $\mathbf{E}$.

The plane of polarization of the incident ray is oriented at the angle ψ (Fig. 2) to the vertical so that

$$\mathbf{E} = E_0[(-\sin \psi)\mathbf{j} + (\cos \psi)\mathbf{k}] = E_0\mathbf{t}_p \quad (4)$$

The vector $\mathbf{c}'$ may be located in terms of the angles α',Ω',β', and ω' (Fig. 1) by

$$\begin{aligned}\mathbf{c}' = {} & [(\cos \beta' \sin \alpha' - \sin \beta' \cos \omega' \cos \alpha')\cos \Omega' \\ & + \sin \beta' \sin \omega' \sin \Omega']\mathbf{i} + [(\cos \beta' \sin \alpha' - \sin \beta' \cos \omega' \\ & \cos \alpha') \sin \Omega' - \sin \beta' \sin \omega' \cos \Omega']\mathbf{j} + (\cos \beta' \cos \alpha' \\ & + \sin \beta' \cos \omega' \sin \alpha')\mathbf{k} \quad (5)\end{aligned}$$

The vector $\mathbf{c}'$ may be obtained from this by using the relation

$$\mathbf{b}' = [1 - (\mathbf{c}'\cdot\mathbf{t}_p)^2]^{-1/2}[\mathbf{t}_p - (\mathbf{c}'\cdot\mathbf{t}_p)\mathbf{c}'] \quad (6)$$

Equations (4), (5), and (6) may then be substituted into eq. (3) to obtain an expression for $\mathbf{M}'$.

The vector $\mathbf{O}$ depends upon the orientation of the polarization plane of the analyzer which will be assumed to include the primary beam direction $\mathbf{i}$ and can be rotated about it. As in earlier papers, two conditions of polarization will be considered; one designated $\mathbf{O}_\parallel$ where the polarization planes of the polarizer and analyzer are parallel, and a second designated $\mathbf{O}_\perp$ where those planes are perpendicular. It then follows that[12]

$$\begin{aligned}\mathbf{O}_\parallel = {} & \pm [\cos^2 (\mu + \psi) + \cos^2 \theta_p \sin^2 (\mu + \psi)]^{-1/2} \\ & [\cos (\mu + \psi)\mathbf{p} + \cos \theta_p \sin (\mu + \psi)\mathbf{q}] \quad (7)\end{aligned}$$

where θ_p is the scattering angle in the polaroid filter, and

$$\mathbf{p} = (-\sin\theta)\mathbf{i} + (\cos\theta\sin\psi)\mathbf{j} + (\sin\mu)\mathbf{k}$$

$$\mathbf{q} = (-\cos\mu)\mathbf{j} + (\sin\mu)\mathbf{k}.$$

This expression greatly simplifies in the case where θ is small (to which we will restrict our calculations) so that $\mathbf{O}$ may be approximated by

$$\mathbf{O}_{\parallel} = (-\sin\psi)\mathbf{j} + (\cos\psi)\mathbf{k} \tag{8}$$

and also, in this approximation

$$\mathbf{O}_{\perp} = (\cos\psi)\mathbf{j} + (\sin\psi)\mathbf{k} \tag{9}$$

It has been shown that at values of ψ other than 0° and 90°, the scattering pattern may be appreciably affected by the birefringence of the oriented medium[13–15] so that in practice, our considerations are restricted to $\psi = 0°$ and $\psi = 90°$ where this birefringence effect is minimized. In this paper we shall adopt the notation used to identify photographic patterns: V_V for the intensity $I_{\parallel}$ with $\psi = 0°$ and H_V for $I_{\perp}$ with $\psi = 0°$.

By using Eqs. (3), (4), (6), (8), and (9), it follows that

$$(\mathbf{M}'\cdot\mathbf{O})_{\parallel} = \mathbf{E}_0\{(\alpha_1 - \alpha_2)[\cos^2\psi(\mathbf{c}'\cdot\mathbf{k})^2 + \sin^2\psi(\mathbf{c}'\cdot\mathbf{j})^2 - \sin 2\psi(\mathbf{c}'\cdot\mathbf{k})(\mathbf{c}'\cdot\mathbf{j})] + \alpha_2\} \tag{10}$$

and

$$(\mathbf{M}'\cdot\mathbf{O})_{\perp} = E_0(\alpha_1 - \alpha_2)\{\cos 2\psi(\mathbf{c}'\cdot\mathbf{k})(\mathbf{c}'\cdot\mathbf{j}) + \tfrac{1}{2}\sin 2\psi[(\mathbf{c}'\cdot\mathbf{k})^2 - (\mathbf{c}'\cdot\mathbf{j})^2]\} \tag{11}$$

The vector $\mathbf{r}'$ in the deformed state is related to that in the undeformed state through the affine transformation to give

$$\mathbf{r}' = r[(\lambda_2\sin\alpha\cos\Omega)\mathbf{i} + (\lambda_2\sin\alpha\sin\Omega)\mathbf{j} + (\lambda_3\cos\alpha)\mathbf{k} \tag{12}$$

It is assumed that in uniaxial deformation, the distribution function for scattering elements is cylindrically symmetrical in the deformed state so that $\Omega' = \Omega$ and thus

$$N'(\alpha',\Omega',r') = N'(\alpha',\Omega,r') = N(\alpha',r') \tag{13}$$

Calculations are carried out for the two types of transformation of $N'(\alpha',r')$ considered in the earlier paper.[3]

In model I, a constant density of scattering material is preserved so that

$$N'(\alpha',r')(r')^2\sin\alpha' d\alpha' dr' = N(\alpha,r)r^2\sin\alpha d\alpha dr \tag{14}$$

where in the undeformed state $N(\alpha,r) = N$ and is a constant. This leads to

$$N'(\alpha',r') = N \tag{15}$$

for deformation at constant volume.

In model II, the radial density of scattering elements remains constant but the angular distribution changed affinely. This model appeared less

realistic physically but led to an analytical solution in two dimensions. In this case we have

$$N'(\alpha',r) \sin \alpha' d\alpha' = N(\alpha,r) \sin \alpha d\alpha \tag{16}$$

which leads to

$$N'(\alpha',r') = N[\lambda_2^2 \sin^2 \alpha + \lambda_3^2 \cos^2 \alpha]^{3/2} \tag{17}$$

for constant volume deformation.

Numerical Calculations

Two cases are considered for calculation. The first of these is with ω random so that it may be averaged prior to integrating over other angles. A second case is that for which this optic axis twist angle assumes a preferred value as the spherulite deforms, as in the case of previous birefringence calculations.[16] An empirical function is assumed for an orientation parameter g

$$\begin{aligned} g &= 2\langle \cos^2 \omega' \rangle_{av} - 1 \\ &= 1 - \exp\{-\eta(\lambda_3^2 - \lambda_2^2) \sin^2 \alpha'\} \end{aligned} \tag{18}$$

where $g = 0$ corresponds to random orientation of ω and $g = 1$ corresponds to alignment of optic axes in the plane through the radius vector **r** and the stretching direction. The proposed equation allows for such alignment to occur to a greater extent near $\alpha' = 90°$ (the equatorial part of the spherulite) and to an increasing degree at increasing elongations at a rate which is describable in terms of the parameter η. This model is intended to account approximately for the type of crystal orientation actually observed in deforming spherulites by x-ray diffraction studies.

A second consideration involves the angle β between the optic axis and the spherulite radius. As previously discussed,[16] this angle may change with deformation. Optic axes are initially oriented at some angle β_0 to the radius. With elongation, β_0 changes so as to align the optic axes more nearly parallel to the stretching direction. A possible empirical function having the desired variation is

$$\beta' = \beta_0 \exp\{-K(\lambda_3^2 - \lambda_2^2) \cos^2 \alpha'\} \tag{19}$$

where β' approaches 0° with increasing deformation at a rate which is greater as α' approaches 0° (the polar regions of the spherulite). Here K is a compliance parameter which specifies the ease with which β changes upon deformation. Values of the birefringence have been calculated as functions of the parameters K and η.[16]

The results of the calculations of H_V scattering patterns are presented in Figures 3–10 for the case of uniaxial deformation ($\lambda_1 = \lambda_2$) at constant volume ($\lambda_1\lambda_2\lambda_3 = 1$). These were obtained by the CDC 3600 computer of the Research Computing Center of the University of Massachusetts and a FORTRAN program which has been published.*[11] The intensities are

* Available from one of the authors (R.S.S.).

plotted as first quadrants of polar contour diagrams where the distance from the origin is $U = 4\pi(R/\lambda)\sin(\theta/2)$ and the azimuthal angle measured clockwise from the vertical is μ. The dotted line on each figure is the locus of the μ for which intensity is a maximum. Calculations were made

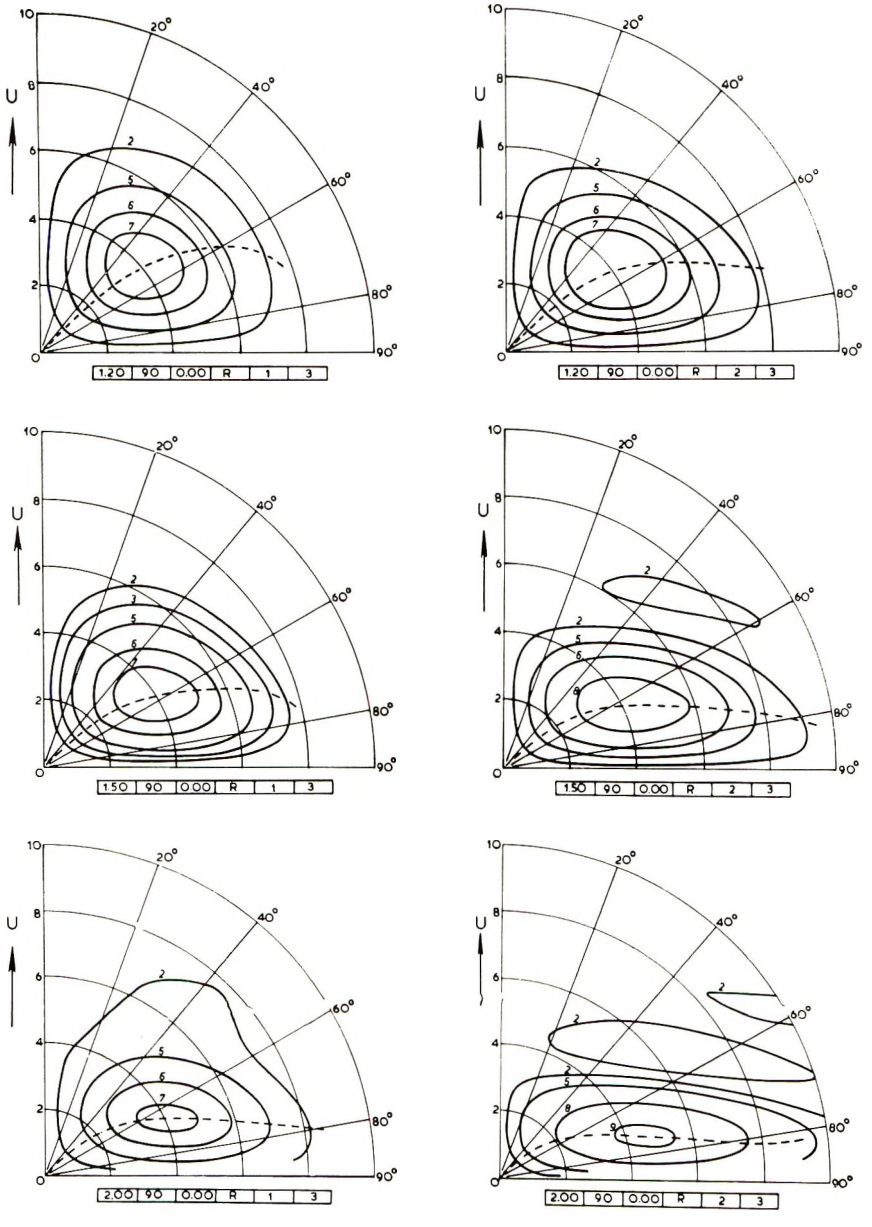

Fig. 3. Variation of H_V scattered intensity for a three-dimensional spherulite for the crystal reorganization compliance $K = 0.00$ at elongation ratios of 1.20, 1.50, and 2.00 for model I (left) and Model II (right).

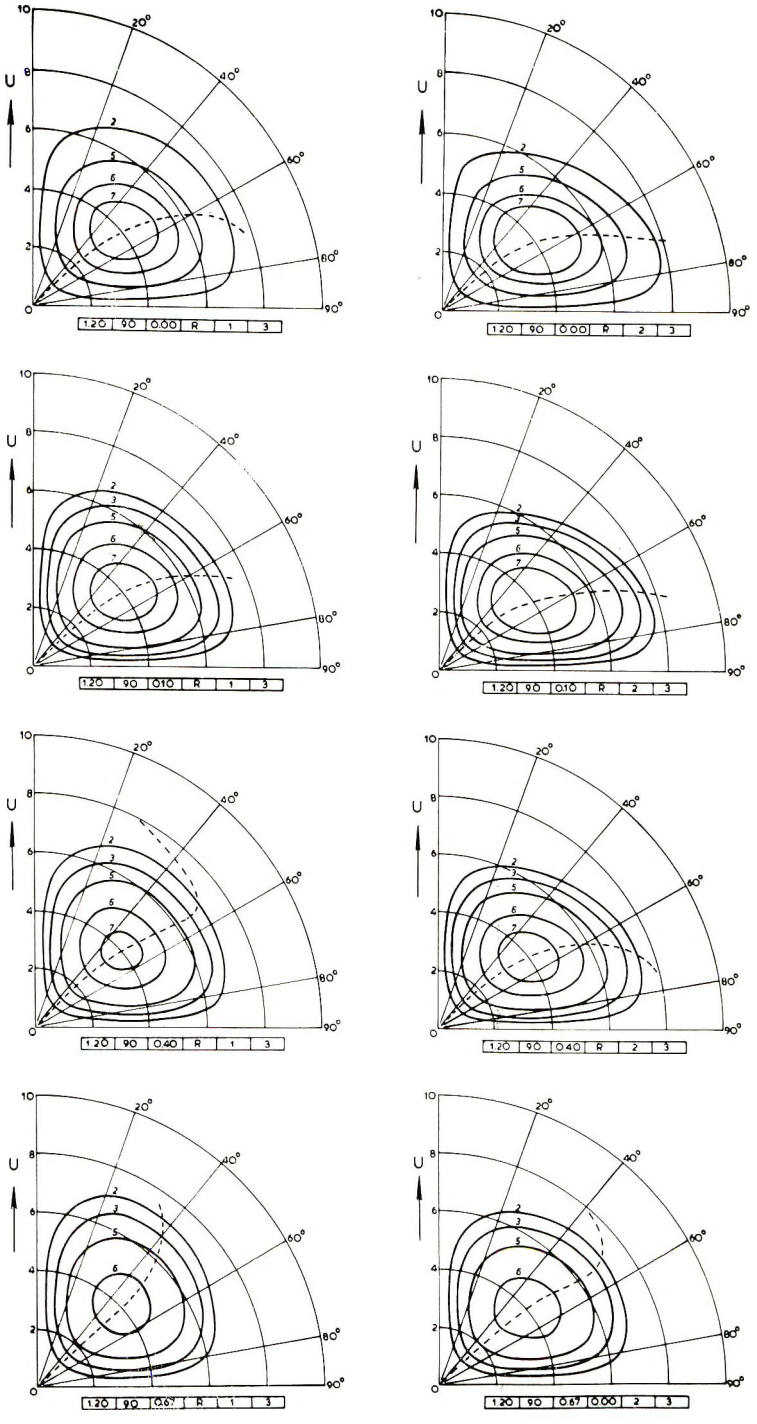

Fig. 4. Variation of H_V scattered intensity for a three-dimensional spherulite for values of the reorientation compliance K = 0.00, 0.10, 0.40, 0.67, for model I (left) and model II (right), for an elongation ratio λ_3, of 1.20.

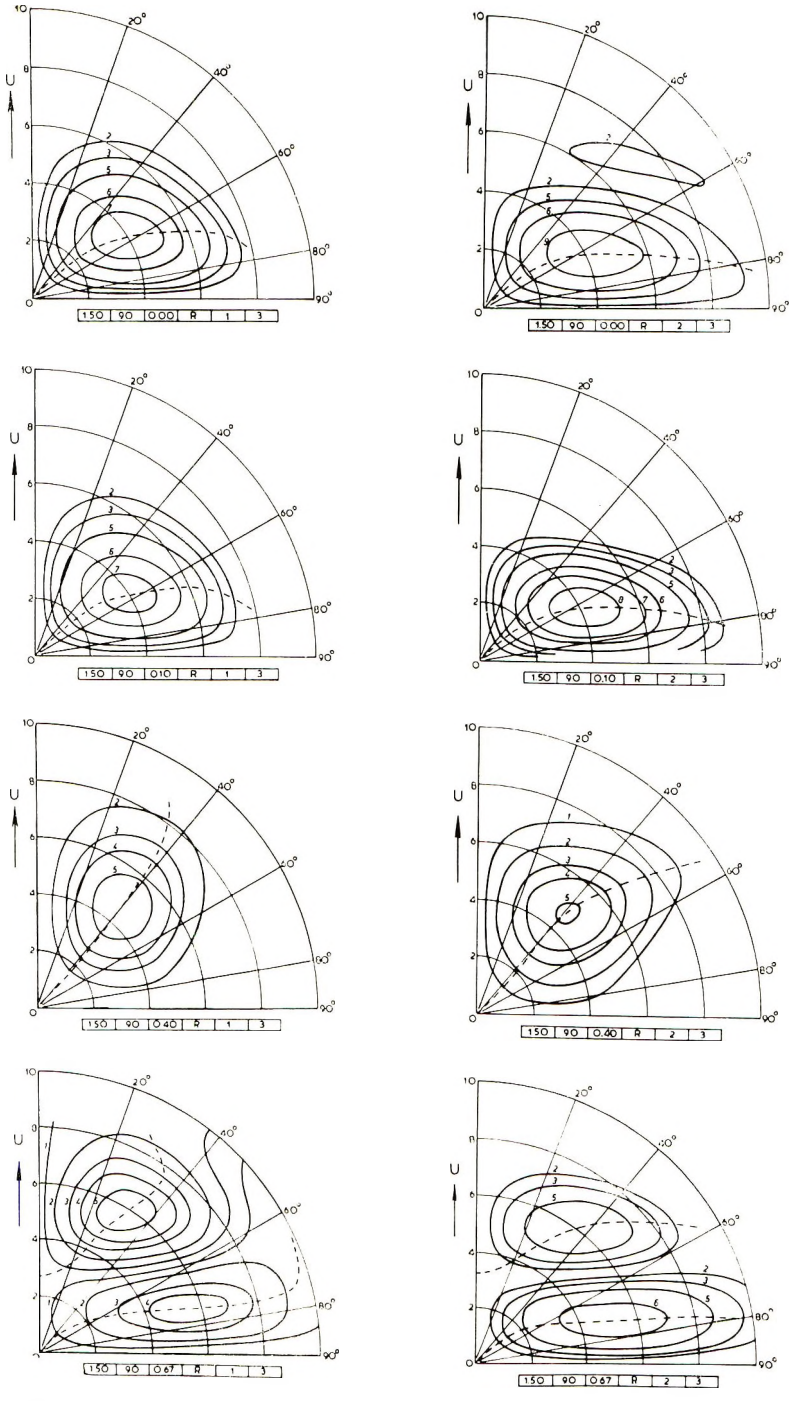

Fig. 5. Variation of H_V scattered intensity, as in Fig. 4 but with $\lambda_3 = 1.50$.

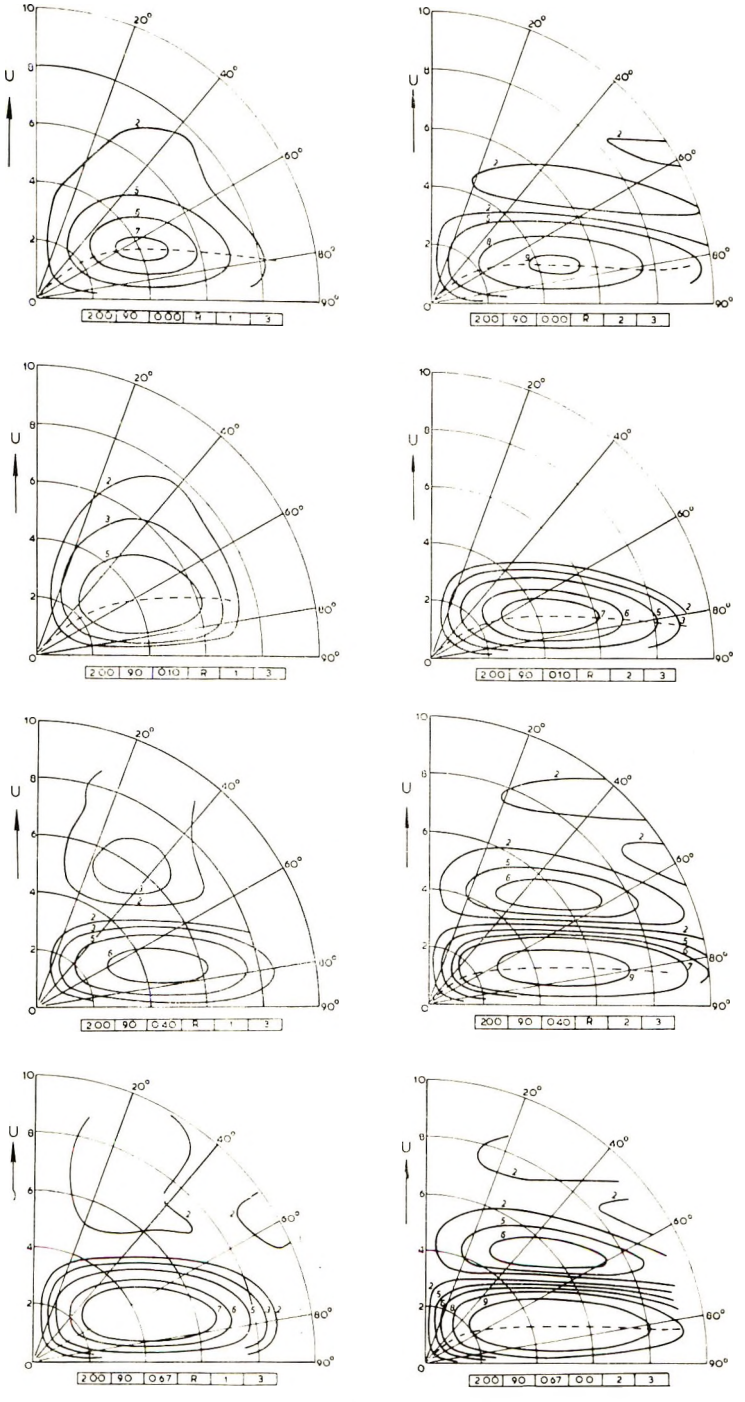

Fig. 6. Variation of H_V scattered intensity, as in Fig. 4 but with $\lambda_3 = 2.00$.

up to an elongation ratio of 2.00 although it seems doubtful that the proposed deformation mechanism will be valid at such a high elongation.

The box underneath each figure specifies the parameters used for the calculation. The first entry is the elongation ratio λ_3, the second is the

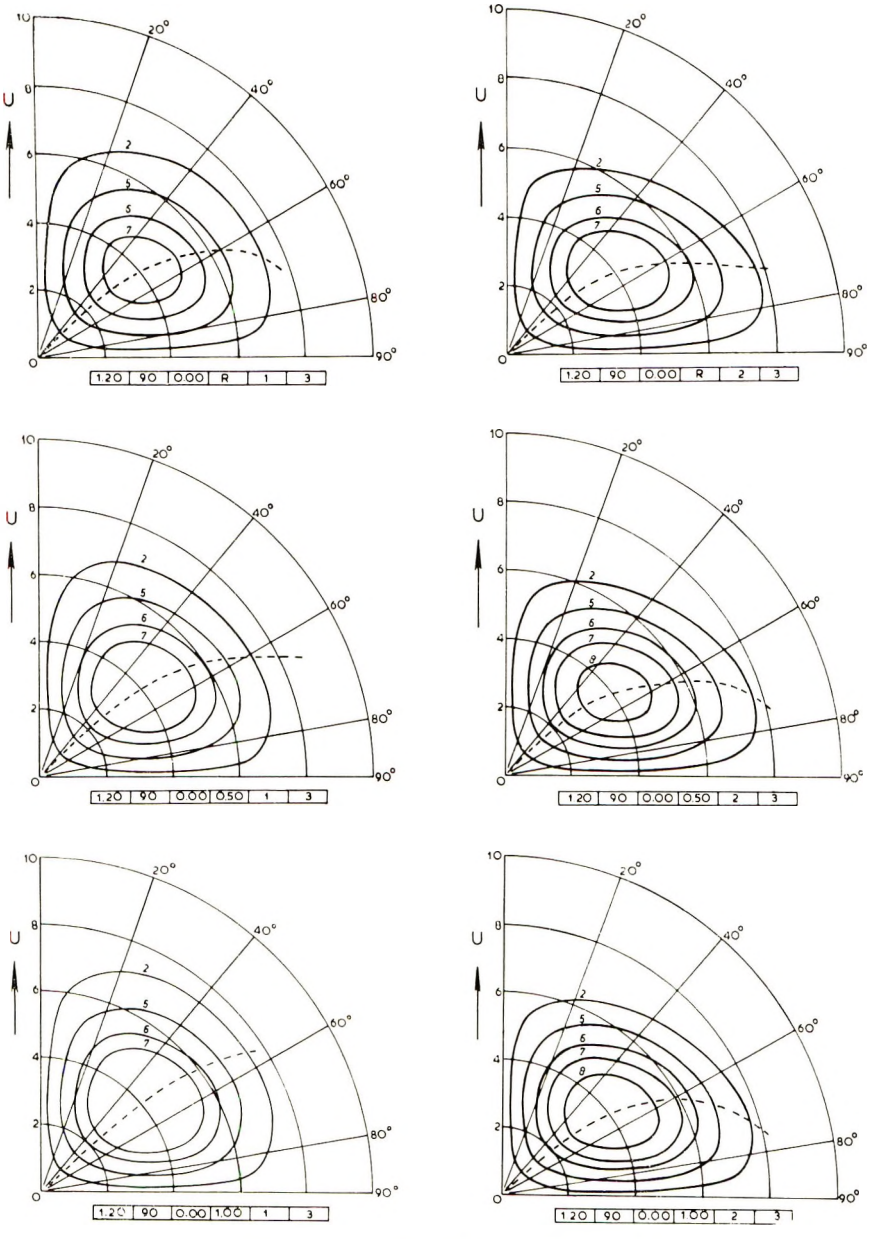

Fig. 7. Variation of H_V scattered intensity for a three-dimensional spherulite at an elongation ratio λ_3 of 1.20 for $K = 0.00$ and values of the crystal rotation compliance parameter η of 0.0, 0.5, and 1.0 for model I (left) and model II (right).

value of the initial orientation angle of the optic axis to the radius β_0, the third is the value of the parameter K in eq. (19) and the fourth is the value of η in eq. (18). The letter R in this position designates random values of the angle ω. The number 1 or 2 in the fifth position designates whether the deformation assumption of model I or model II is used. The

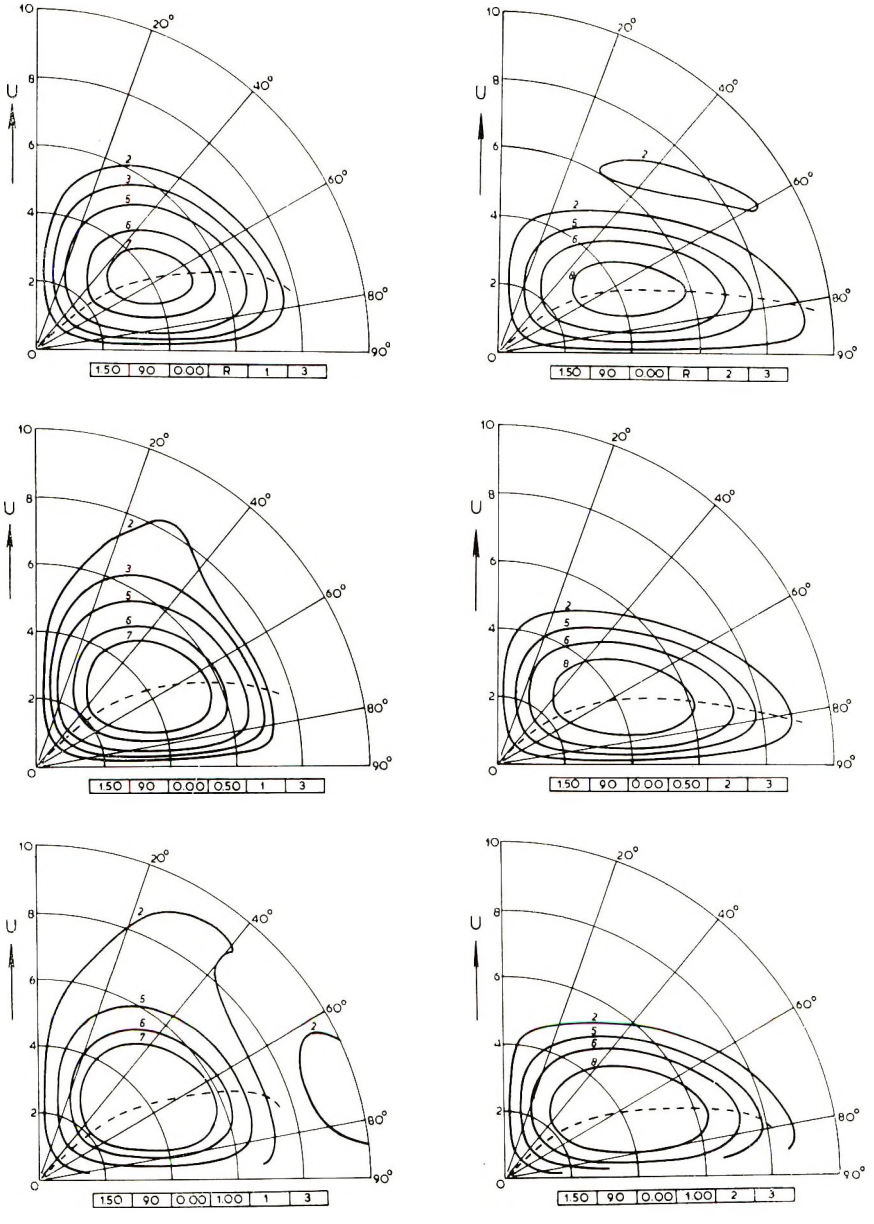

Fig. 8. Variation of H_V scattered intensity as in Fig. 7 but with $\lambda_5 = 1.50$.

number 2 or 3 in the sixth position designates whether the calculation is for a two-dimensional or three-dimensional spherulite.

The number next to each of the isointensity contour lines indicates the value of logarithmic intensity associated with that contour. These ln H_V values in arbitrary units are as follows: 1, −12.50; 2, −10.00; 3, −9.00;

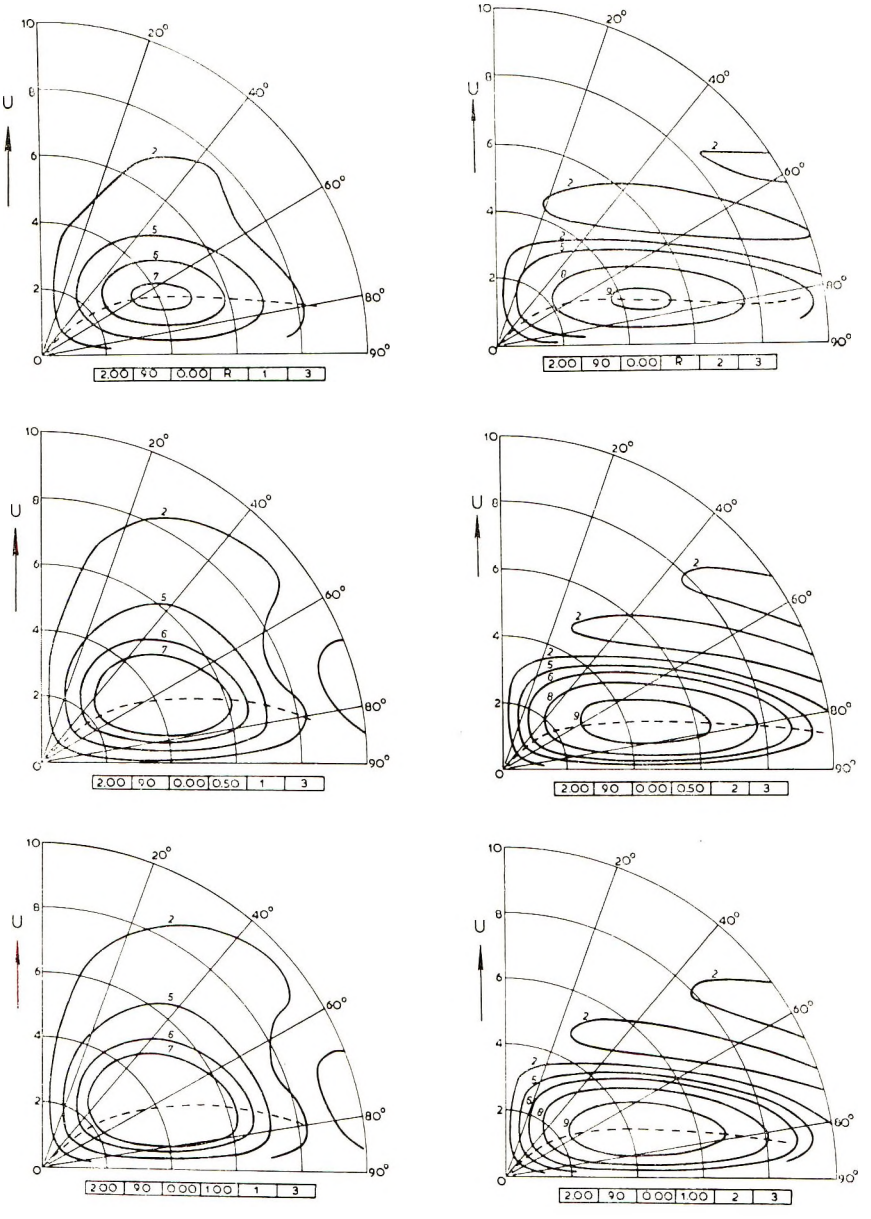

Fig. 9. Variation of H_V scattered intensity for a three-dimensional spherulite, as in Fig. 7 but with $\lambda_0 = 2.00$.

4, −8.50; 5, −8.00; 6, −7.00; 7, −6.50; 8, −6.00; 9, −5.00; 10, −4.00.

It is seen for the case $K = 0.0$ shown in Figure 3 that with increase in elongation the lobes of maximum scattering move from their initial position at $\mu = 45°$ toward $\mu = 90°$. That is, the pattern becomes more elongated in a direction perpendicular to the stretching direction. This general

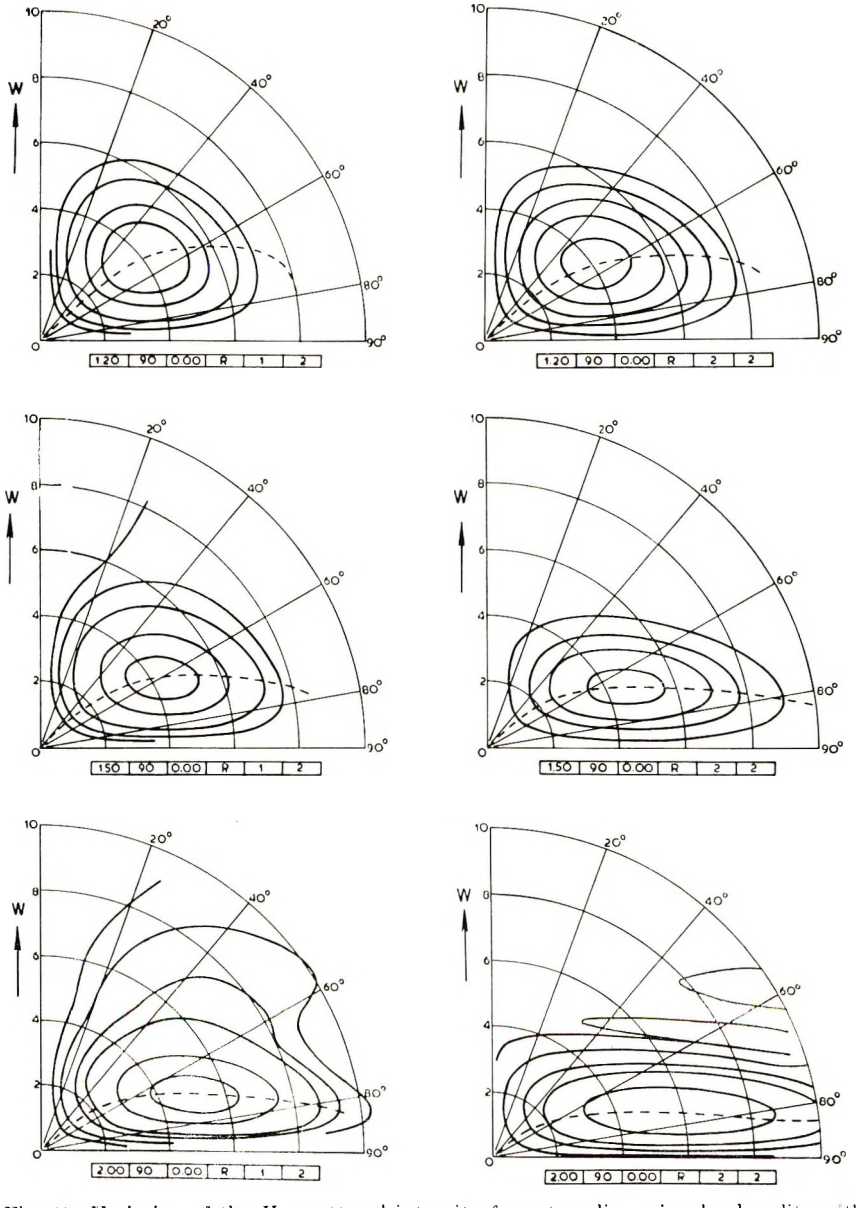

Fig. 10. Variation of the H_V scattered intensity for a two-dimensional spherulite with elongation ratios of 1.20, 1.50, and 2.00 for $K = \eta = 0.0$.

feature of the light-scattering patterns was observed in the two-dimensional calculations[3] and was also predicted by Samuels' semiempirical theory.[6,7]

With increasing elongation, also, the absolute maximum in intensity with respect to both U and μ moves to a slightly higher value of U and appreciably toward the equatorial regions of the pattern. This shift in intensity peak position is greater for model II than for model I. Since the difference between the predictions for the two models is only a few degrees, it is unlikely that one could distinguish between these two deformation mechanisms on this basis. In view of this fact we can use an intermediate model in order to make the mathematics simpler. If we put

$$N'(\alpha',\nu') = N(\lambda_2^2 \sin^2 \alpha + \lambda_3^2 \cos^2 \alpha) \tag{20}$$

the whole H_V calculation can be carried out, leading to

$$I_{HV} = \sin^2 \epsilon \cos^2 \epsilon \{4 \sin U^* - U^* \cos U^* - 3\mathrm{Si}U^*\}^2 (U^*)^{-6} \tag{21}$$

where

$$U^* = U[\lambda_2^2 \sin^2 (\theta/2) + \cos^2 (\theta/2)(\lambda_2^2 \sin^2 \mu + \lambda_3^2 \cos^2 \mu)]^{1/2} \tag{22}$$

and

$$\cos \epsilon = \lambda_3 \cos (\theta/2)(\cos \mu)(U/U^*) \tag{23}$$

For this case it can be shown that the maximum intensity [where $(\partial I/\partial \mu)_U = 0$ and $(\partial I/\partial U)_\mu = 0$ simultaneously] is to be found at $U^* = 4.09$ and $\cos^2 \mu = [(\lambda_3^3 + 1) \cos^2 (\theta/2)]^{-1}$. Thus, for small scattering angles we have the approximate relations

$$\tan \mu_{max} = \lambda_3^3$$

and

$$U_{max} = 4.00$$

The shift in intensity peak position toward higher values of μ, as found experimentally,[3,17] is a point of difference between our calculations and the theoretical and experimental results of Samuels.[7]

Upon comparing the results in Figures 4, 5, and 6 with those in Figure 3, it is seen that there is little effect from small amounts of reorientation of the optic axes, as represented by low values of K. (Compare the patterns for $K = 0.00$ with those for $K = 0.10$ which show hardly any difference.) For higher values of K, there is a shift of the intensity peak toward smaller values of μ in somewhat the opposite manner than results from an increase in λ_3. However, because of the strong dependence of β on both α and λ_3, this tendency is not always evident. For instance, for $\lambda_3 = 2.00$ and $K = 0.40$, the results are much more like those for $\lambda_3 = 1.50$, $K = 0.67$ than for the lower K value ($K = 0.40$, $\lambda_3 = 1.50$).

It is noted from Figure 5 that for $K = 0.67$ and $\lambda_3 = 1.50$, the four-leaf clover is split into eight segments, four of which can be regarded as the result of a continuation of the tendency to shift the lobes toward the

stretching direction with increasing K, whereas the four leaves in the equatorial region of the pattern appear as extra lobes. We do not know of any case which shows such a split-up pattern. It is likely that with the extent of spherulite reorganization represented by these values of parameters, the affine deformation assumption fails so that the theoretical predictions are not fulfilled.

Experiments from our laboratory[3] are in qualitative agreement with the theoretical predictions. However, it appears that light scattering patterns are not sufficiently discriminating to distinguish among the various deformation mechanisms.

The calculated patterns for nonrandom values of ω characterized by values of 0.5 and 1.0 for the parameter η are given in Figures 7, 8, and 9. The influence of a nonrandom ω appears to mainly increase the overall intensity without appreciably affecting the shape of the pattern.

In Figure 10, the patterns calculated for a two-dimensional spherulite with $K = \eta = 0.0$ and $\beta_0 = 90°$ are given. These patterns are to be compared with the corresponding patterns for a three-dimensional spherulite in Figure 3. It is evident that the shift in the maximum intensity with respect to U and μ is always more pronounced for the two-dimensional case. The shape of the patterns is rather similar, however.

Conclusions

It was the initial hope in this investigation that light scattering patterns might prove sufficiently discriminating to distinguish among various deformation mechanisms. It is apparent that qualitative features of the patterns are predictable but their unique assignment to any specific deformation process is difficult. Even the relatively simple model I and model II affine deformation schemes accompanied by the simple phenomenological mechanisms of optic axis reorientation expressed by eqs. (18) and (19) lead to more parameters than may be readily evaluated. The observed variation of the pattern with elongation may be compared with the predicted values according to the different mechanisms as a means for selecting the appropriate mechanism. For this purpose it is convenient to plot an experimental parameter such as μ_{max} at which the intensity maximum occurs versus elongation.[18]

It is cautioned that the affine deformation ratio for the spherulite is not necessarily that of the sample so that it is useful to compare the two in cases where spherulite deformation ratios may be directly observed by microscopy. If one assumes a particular deformation mechanism, then the theory permits one to determine the spherulite deformation ratio from light scattering observations. This proves useful when the spherulites are too small or the deformation is too rapid for direct microscopic observation.[18]

In this theory it has been assumed that the spherulite is internally uniform so that, for example, the scattered intensity of the undeformed

spherulite is zero at $\vartheta = 0$ for all U. In practice this is not found to be the case and a "background intensity" is found to be superposed upon the spherulite scattering.[3,7,12] It is the practice[3,7] to subtract out this background contribution when comparing the experimental scattering patterns with the theoretical predictions.

The source of this background scattering is spherulite imperfection which may arise from internal disorder, boundary regions, or interspherulitic interference. Upon deformation of the polymer, such background scattering will change together with the spherulitic contribution; and an unambiguous subtraction is often difficult. Furthermore, a study of the change in this background contribution with elongation is of interest in elucidating the deformation mechanism.

One approach[12] to the treatment of this background contribution is to assume that it may be treated as an added contribution describable by a random orientation correlation type theory.[19] This contribution then changes with deformation as described, for example, by the approach of Stein and Hotta.[20] Experiments indicate,[21] however, that a random orientation correlation theory is not always sufficient and that nonrandom orientation correlations[22,23] need be considered for this contribution. The effect of deformation on such contributions has been studied.[24]

Another and perhaps more direct approach is to consider the background scattering to be a result of the perturbation of perfect spherulite scattering by disorder and to treat it as a modification of spherulite scattering theory. The results of having correlated fluctuations in the optic axis angle β characterized by an internal correlation function have been explored by Stein and Chu,[25] and the effects of deformation upon these internal fluctuations have been analyzed.[26]

One purpose of these analyses is to interpret dynamic birefringence experiments in which the sample is subjected to a small oscillatory strain and the variation of scattered intensity is analyzed or else the change in light scattering is observed during relaxation at constant length.[27–31] The change in light scattering with time is a consequence of both the changes in the spherulitic and in the background contributions. The time dependence of the spherulitic contribution must be related to the time dependence of the parameters such as λ_3, K, and η which characterize the change in scattering with deformation.

While it is not possible to uniquely characterize structural parameters by light scattering, a goal is to describe scattering in terms of parameters that are common to other phenomena such as high-angle and low-angle x-ray diffraction and birefringence. Thus, a model for the structural change occurring upon deformation must be chosen so as to account simultaneously for these various observations. This has been an objective of the rheo-optical techniques employed in this laboratory.[30,32]

This work was supported in part by a contract with the Office of Naval Research and in part by a grant from thd Petroleum Research Fund of the American Chemical Society.

References

1. R. S. Stein and M. B. Rhodes, *J. Appl. Phys.*, **31**, 1873 (1960).

2. P. Erhardt, K. Sasaguri and R. S. Stein, in *Rheo-optics of Polymers* (*J. Polym. Sci. C*, **5**), R. S. Stein, Ed., Interscience, New York, 1964, p. 170.

3. S. Clough, J. J. van Aartsen, and R. S. Stein, *J. Appl. Phys.*, **36**, 3072 (1965).

4. R. S. Moore and S. Matsuoka, in *Rheo-optics of Polymers* (*J. Polym. Sci. C*, **5**), R. S. Stein, Ed., Interscience, New York, 1964, p. 163.

5. R. S. Moore, *J. Polym. Sci. A*, **3**, 4093 (1965).

6. R. J. Samuels, *J. Polym. Sci. A*, **3**, 1741 (1965).

7. R. J. Samuels, in *Small Angle Scattering from Fibrous and Partially Ordered Systems* (*J. Polym. Sci. C*, **13**), R. H. Marchessault, Ed., Interscience, New York, 1966, p. 37.

8. I. L. Hay and A. Keller, *Kolloid Z.*, **204**, 43 (1965).

9. R. Yang and R. S. Stein, *J. Polym. Sci. A-2*, **5**, 939 (1967).

10. K. Kobayashi and T. Nagasawa, in *U.S.–Japan Seminar on Polymer Physics* (*J. Polym. Sci. C*, **15**), R. S. Stein and S. Onogi, Eds., Interscience, New York, 1966, p. 163.

11. J. J. van Aartsen, ONR Technical Report No. 83, Project: NR 056-378, Contract: Nonr 3357(01), Polymer Research Institute, University of Massachusetts, 1966.

12. A. E. M. Keijzers, J. J. van Aartsen, and W. Prins, *J. Amer. Chem. Soc.*, **90**, 3167 (1968).

13. R. S. Stein, P. F. Erhardt, and W. Chu, *J. Polym. Sci. A-2*, **7**, 271 (1969).

14. W. Chu and R. S. Stein, *J. Polym. Sci. A-2*, **8**, 489 (1970).

15. M. Motegi, M. Moritani, and H. Kawai, *J. Polym. Sci. A-2*, **8**, 499 (1970).

16. K. Sasaguri, R. Yamada, and R. Stein, *J. Appl. Phys.*, **35**, 3188 (1964).

17. K. A. Gasparyan et al., *Polym. Sci. USSR*, **10**, 96 (1968).

18. P. F. Erhardt and R. S. Stein, *J. Appl. Phys.*, **39**, 4898 (1968).

19. R. S. Stein and P. R. Wilson, *J. Appl. Phys.*, **33**, 1914 (1962).

20. R. S. Stein and T. Hotta, *J. Appl. Phys.*, **35**, 2237 (1964).

21. W. Chu, Ph.D. Thesis, University of Massachusetts, Amherst, 1969.

22. R. S. Stein, P. F. Erhardt, S. B. Clough, and G. Adams, *J. Appl. Phys.*, **37**, 3980 (1966).

23. T. Hashimoto and R. S. Stein, *J. Polym. Sci. A-2*, **8**, 1127 (1970).

24. R. S. Stein and T. Hashimoto, *J. Polymer Sci. A-2*, **8**, 1503 (1970).

25. R. S. Stein and W. Chu, *J. Polym. Sci. A-2*, **8**, 1137 (1970).

26. R. S. Stein and T. Hashimoto, in preparation.

27. P. F. Erhardt and D. G. LeGrand, *J. Polym. Sci.*, **62**, S47 (1962).

28. P. F. Erhardt and D. G. LeGrand, *J. Appl. Phys.*, **34**, 68 (1963).

29. T. Hashimoto and R. S. Stein, *J. Polymer Sci. A-2*, in press.

30. R. S. Stein, *Polym. Sci. Eng.*, **9**, 320 (1969).

31. D. G. LeGrand and W. R. Haaf, in *Rheo-Optics of Polymers* (*J. Polym. Sci. C*, **5**), R. S. Stein, Ed., Interscience, New York, 1964, p. 153.

32. R. S. Stein, in *U.S.–Japan Seminar on Polymer Physics* (*J. Polym. Sci. C*, **15**), R. S. Stein and S. Onogi, Eds., Interscience, New York, 1966, p. 185.

Received May 7, 1970
Revised July 10, 1970

JOURNAL OF POLYMER SCIENCE: PART A-2 VOL. 9, 313–329 (1971)

Light Scattering by Cellulose. III. Morphology of Wood

JENS BORCH, P. R. SUNDARARAJAN, and R. H. MARCHESSAULT,
Chemistry Department, Université de Montréal, Montréal, Québec, Canada

Synopsis

Radial, tangential and cross cuts of Eastern spruce are examined by a solid-state light-scattering method which allows study of light scattering due to fluctuations in density and fluctuations in anisotropy. All of the samples investigated show well-defined scattering maxima which are related to their anisotropic texture with limited contributions from random density fluctuations. The radial cuts give rise to scattering similar to that by a grating with orthogonal characteristic spacings. The gratinglike character is due mainly to the pit structure and their periodic spacings, which can be deduced from the "unit-cell" dimensions of the scattering pattern. The scattered intensity is maximum when the fiber direction is at 45° to the polarization direction; when it is either horizontal or vertical, a distinct "spherulitic" scattering is observed from which size and asymmetry of the pits can be deduced.

Introduction

Light-scattering analysis has recently been applied to the study of natural polymers in the solid state[1,2] and in the gel state.[3–5] This technique complements classical microscopy and requires very little sample preparation so that the structure can be analyzed in its true native state. The scattering pattern contains information about structural entities of the size from 0.1 μ to 50–100 μ, depending upon the angular scattering range which is recorded. Although this scattering envelope is often rather complex, it has been demonstrated[1–5] that approximate procedures of analysis are feasible and that the scattering entities can be identified and described in terms of superstructural "models" such as, for example, spherulitic, rodlike or random organizations. When a successful analysis is accomplished it is often possible to deduce parameters from the scattering patterns which are difficult or time-consuming to derive by other techniques. Thus, the average size of a granular starch sample is determined by just one measurement and calculation.[1] Similarly, this technique shows promise for determining the degree of orientation and average fibrillar length of paper materials and cellulosic films.[6]

Scattering may advantageously be viewed in parallel with light microscopy, since the scattering pattern is observable on the microscope stage itself by viewing the back focal plane of the objective by means of a Ber-

(*a*)

(*b*)

Fig. 1. Photomicrograph of a radial section of Eastern spruce between crossed Nicols: (*a*) fibers parallel to the polarization direction; (*b*) fibers rotated 45° in the field of view.

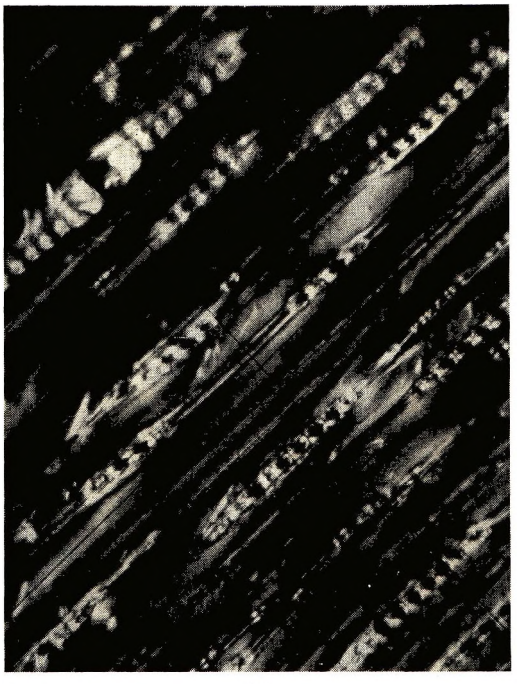

(*a*)

(*b*)

Fig. 2. Photomicrograph of a tangential section of Eastern spruce between crossed Nicols: (*a*), (*b*) sample positioning same as for Fig. 1.

trand lens.[7] This approach is effective when scattering is due to fluctuations in anisotropy, since ill-defined polarization often yields a scattering pattern which is easily classified as due to a particular material texture or in the case of a well-defined texture, such as spherulitic, a crowded sample which could not be size-averaged accurately is immediately averaged via the overall scattering pattern.

Since wood sections show rich details in the polarizing microscope, it was to be expected that scattering analysis would be rewarding. The types of structures examined in this preliminary study were first observed microscopically with the following results.

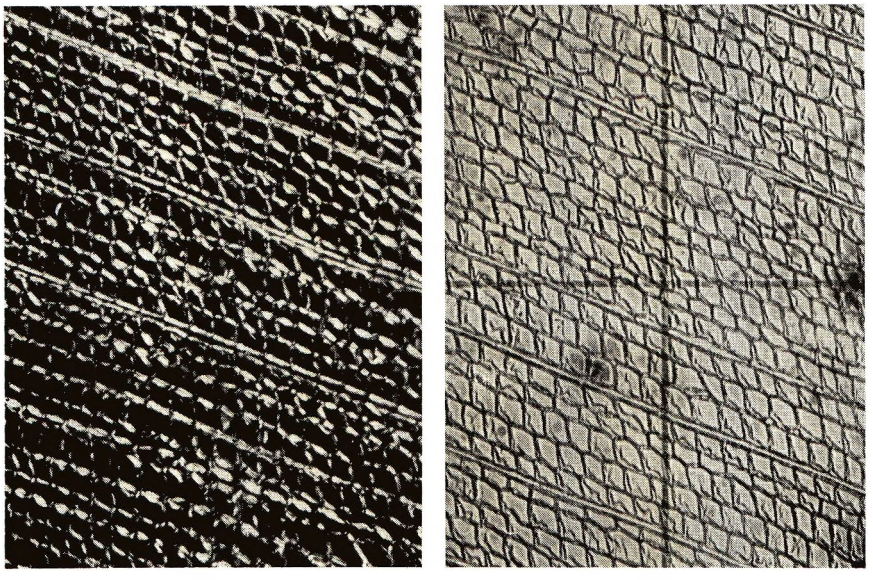

(*a*) (*b*)

Fig. 3. Photomicrograph of a cross section of Eastern spruce (*a*) between crossed Nicols; (*b*) parallel Nicols.

The specimens (thickness approximately 10 μ) were mounted in Canada balsam on microscope slides. The radial, tangential, and cross sections of Eastern spruce are shown in Figures 1, 2, and 3 as they appear in the light microscope between crossed Nicols. Figure 1*a* is heavily populated with bordered pits showing the familiar spherulitic isocline cross which results from the predominantly tangential orientation of the cellulose microfibrils in the borders of the pit aperture.[8]

On introduction of a first-order wave-plate, the quadrants of the pits parallel to the fast direction show a yellow subtraction color and those perpendicular to this direction show a blue addition color, indicating a negative birefringence.

The cross-sectional view shows that the cells have a parallelepiped shape.

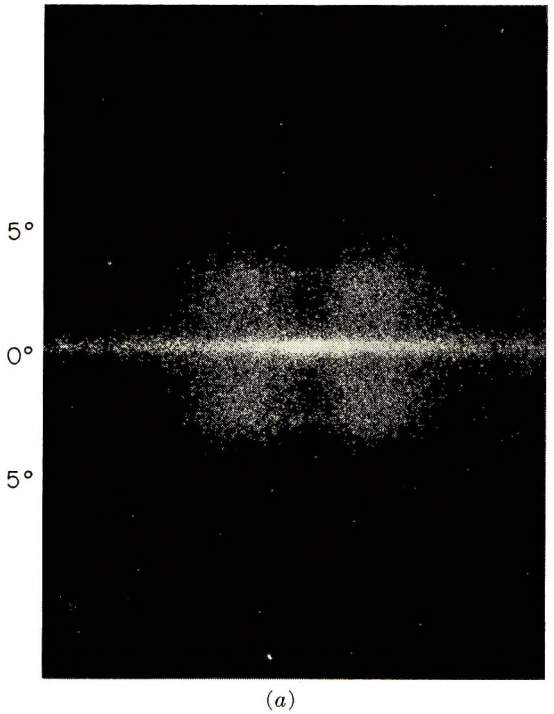

(*a*)

(*b*)

Fig. 4. H_V scattering pattern obtained from a radial section of Eastern spruce: (*a*) fibers normal to the incident beam and along its direction of polarization; (*b*) specimen normal to the incident beam, but fiber direction rotated 45° to its direction of polarization.

Experimental and Results

The experimental arrangement used for recording data reported in this paper has been described earlier.[2] It allows more convenient and more accurate measurements than scattering observations on a microscope stage, since the latter has fixed optical components and lower light intensity. The laser source is normal to the sample which is mounted between glass microscope slides. The light is vertically polarized and its scattering component is analyzed after passage through either a vertically or a horizontally oriented analyzer. The resulting scattering patterns are referred to as V_V and H_V respectively, the subscript showing the polarization mode of the incident light.

Light-scattering photographs in the H_V mode (Figs. 4–7) are especially useful for analysis of anisotropic structures since scattering due to fluctuations in density is absent here. Light-scattering photographs in the V_V mode, where the analyzer is vertically directed, are shown in Figures 8–10. From the similarity of the H_V and V_V scattering patterns, especially when the fibers are irradiated with light polarized 45° to their orientation direction (cf. Figs. 4*b* and 8*b*, 6*b* and 9*b*). It is apparent that anisotropic scattering is the main contributor to the scattering envelope. Because of random density fluctuations, regenerated cellulosic structures[2,3] usually show a strong V_V scattering component of circular symmetry around the incoming

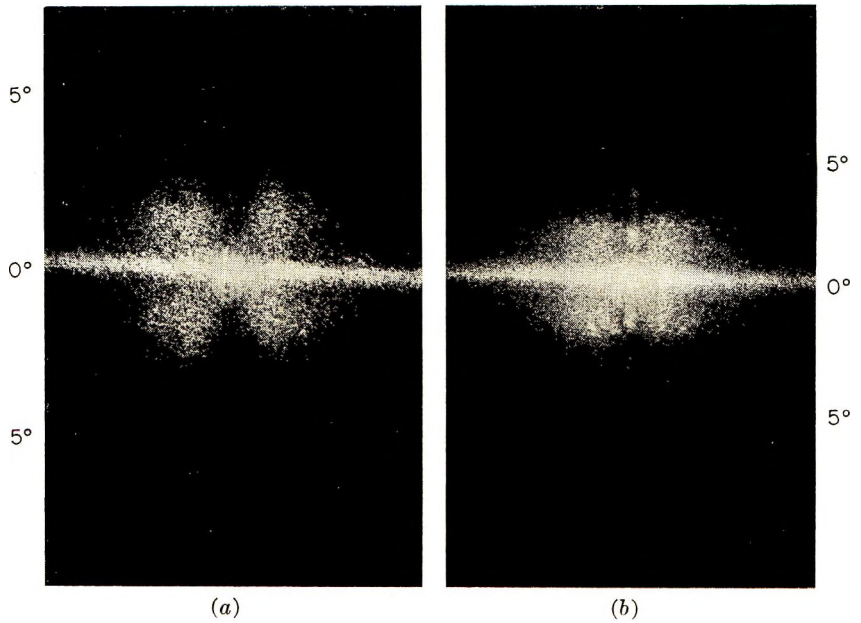

(*a*) (*b*)

Fig. 5. H_V scattering pattern obtained from selected areas of a radial section of Eastern spruce: (*a*) four-leaf clover pattern arising from a random distribution of pits; (*b*) asymmetric four-leaf clover pattern with intensity maxima along the meridian, arising due to an ordered array of pits. The maxima along the equatorial streak are not visible owing to the high intensity.

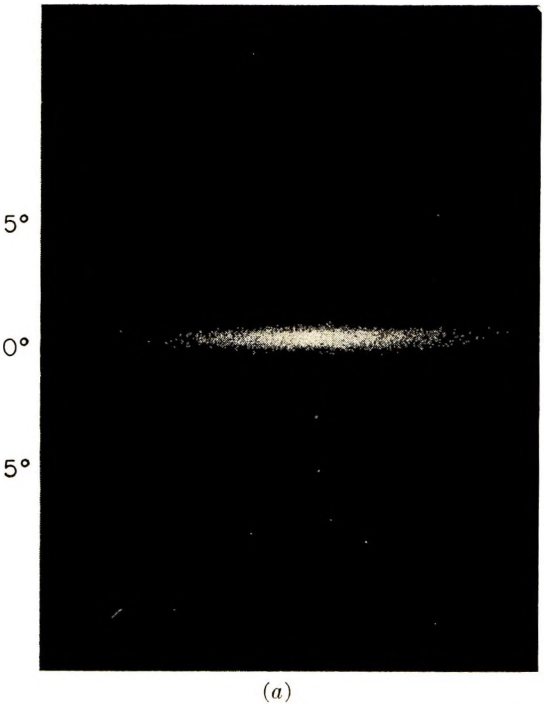

(*a*)

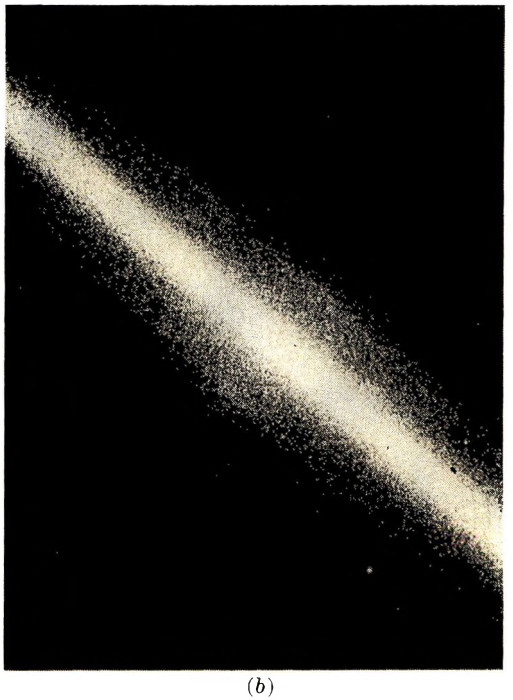

(*b*)

Fig. 6. H_V scattering pattern obtained from a tangential section of Eastern spruce. (*a*), (*b*) sample positioning as in Fig. 4.

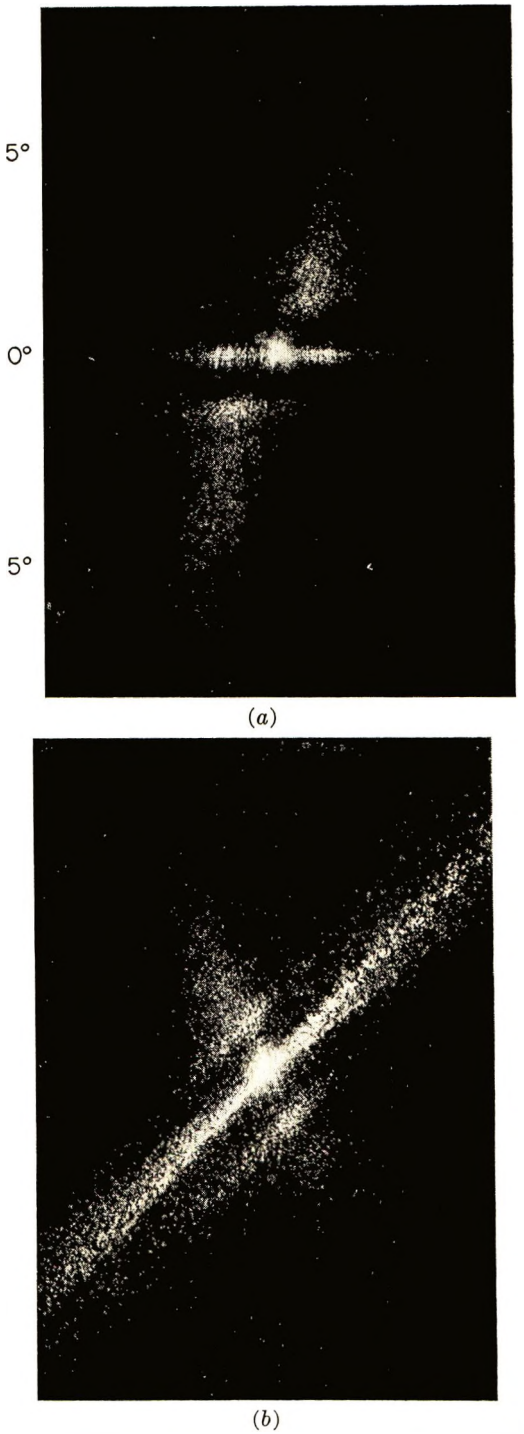

Fig. 7. H_V scattering pattern obtained from a cross section of Eastern spruce: (*a*) sample positioning as in Fig. 3 (*a*); (*b*) sample rotated 45° in its own plane.

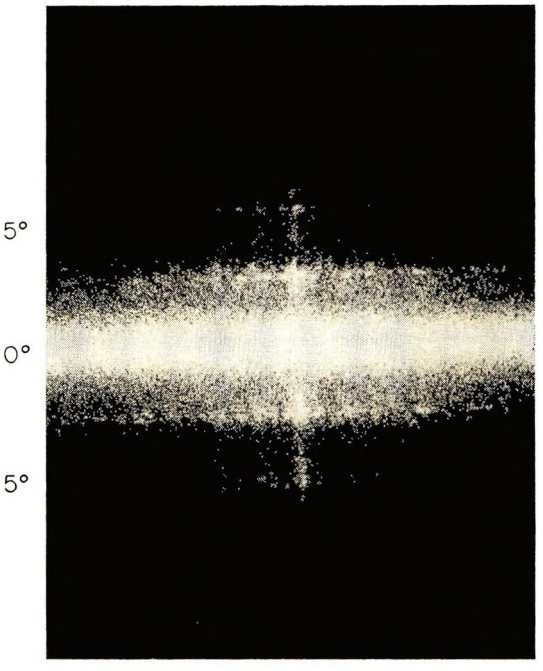

(*a*)

(*b*)

Fig. 8 (*continued*)

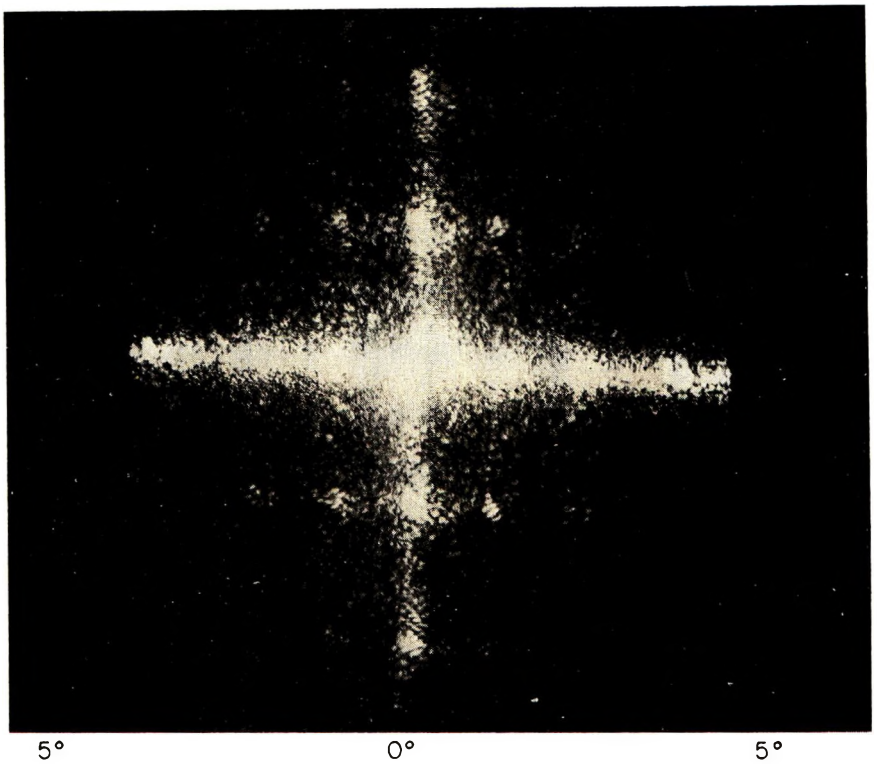

(*c*)

Fig. 8. V_V scattering pattern obtained from a radial section of Eastern spruce: (*a*), (*b*) sample positioning as in Fig. 4; (*c*) same as (*a*), but from an area in which the pits are well arrayed. The intensity of the incident beam was adjusted to bring out maxima along the equatorial direction.

beam in addition to a weak symmetric anisotropic scattering component. However all the V_V scattering envelopes from the wood cuts are strongly asymmetric indicating that major density fluctuations of random character are absent. The most noteworthy difference between V_V and H_V patterns recorded for the same sample when the fibers are oriented in the vertical direction was the much more intense equatorial streak for the former which was due to the density fluctuations due to the persence of the hollow lumens.

Comparing the H_V scattering patterns from the radial and tangential sections, one notes particularly the "four-leaf clover" pattern in Figures 4*a*, 5*a*, and 5*b*. By choosing a proper area in the sample and manipulating the intensity of incident light, one can obtain a nearly symmetrical four-leaf-clover pattern as in Figure 5*a*, which is the theoretically expected pattern for a random distribution of pits (area I in Fig. 11). In areas where the pits tend to be arranged in a two-dimensional lattice (area II in Fig. 11), a cloverleaf pattern with discrete intensity maxima along the meridan (Fig.

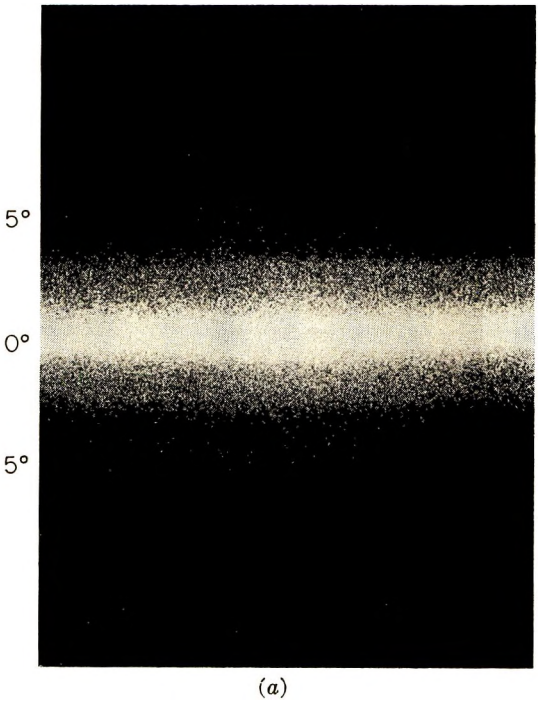

(*a*)

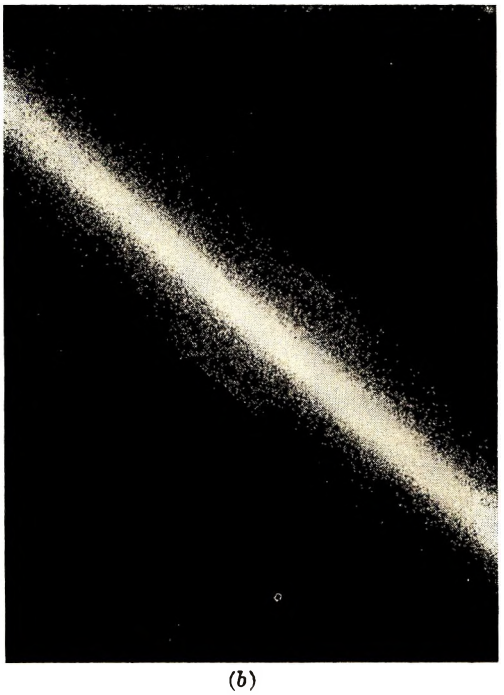

(*b*)

Fig. 9. V_V scattering pattern obtained from a tangential section of Eastern spruce: (*a*), (*b*) sample positioning as in Fig. 4.

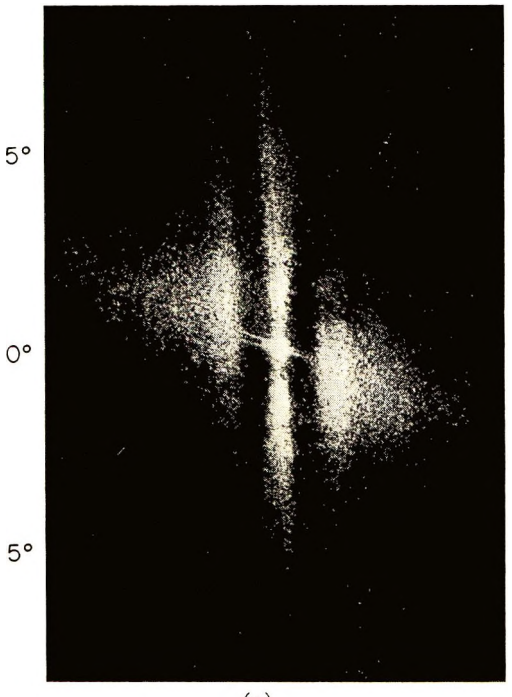

(*a*)

(*b*)

Fig. 10. V_V scattering pattern obtained from a cross section of Eastern spruce: (*a*), (*b*) sample positioning as in Fig. 7. The two principal scattering directions are non-orthogonal (see text).

5*b*) was found. Finally, by reducing the intensity of the incident light, the equatorial streak may be seen to show definite maxima as in Figure 8*c* for the V_V mode.

The pronounced effect of fiber orientation on the scattered intensity in the H_V mode is due to the fact that the induced dipole is a vector quantity and the magnitude of the observed scattering depends on the component of the vector with respect to the analyzer. Evidently, when the fiber axis is at 45° with respect to crossed Nicols one has the best compromise between the induced dipole and the magnitude of its component that is passed by the analyzer. The significance of the observation relates to the basic anisotropic character of the wood fiber: with respect to anisotropy the larger part of the fiber behaves as if the optic axes are oriented along the

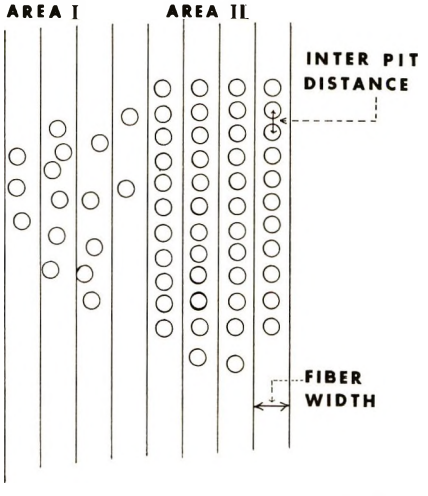

Fig. 11. Schematic diagram of the "randomly" distributed (area I) and regularly arrayed (area II) organizations of the pits in a radial section of Eastern spruce.

fiber axis. Thus, while at 0° there is a maximum induced dipole, this dipole vector has no component to be transmitted by the crossed analyzer. Only in the vicinity of the pits is there a nearly radially symmetric structure which scatters independent of fiber orientation and this is responsible for the cloverleaf.

For V_V scattering, the effect of fiber orientation is much less pronounced. A good example of the grating analog aspect of wood sections are the scattering patterns from the Eastern spruce cross sections. As shown in Figure 3, the fiber cross sections are parallelograms rather than squares or rectangles, and this is reflected in the angular relation of the two principal scattering directions (Figs. 7 and 10). The scattering maxima tend to streak out, and this may be due to the variation in the size of the parallelograms in the cross section.

Discussion

The pronounced equatorial scattering with maxima suggest an overall organized rodlike anisotropic superstructure due to the orientation of the microfibrils in the main part of the cell walls. According to morphologists this orientation is predominantly helical in the fiber direction (10). The scattered intensity of the H_V envelopes increases when the fiber axis is rotated in a plane 45° to the polarization direction of the incoming beam (Figures 4*b* and 6*b*). This indicates a steep helical fiber orientation or a rodlike aggregation well oriented along the fiber direction.

Since a gas laser is used as the illumination source, the incoming light is spatially coherent, and diffraction maxima are created by distinct anisotropy and density fluctuations at the pit center and boundaries. When several pits are aligned along the fiber wall, scattering maxima similar to those from a diffraction grating are created. As expected, the spacing varies with the pit size, an increase causing a corresponding decrease in the layer line spacing. This was shown for a series of tangential cuts of Eastern white pine all exhibiting the general scattering features of the similar sample of Eastern spruce.

Another periodicity, perpendicular to the fiber axis, is visible in some of the scattering photographs of radial sections where well-defined layer-lines are seen (Figs. 4*b*, 8*b*, and 8*c*). The intensity maxima in Figure 4*b* and in Figure 8 bear a remarkable resemblance to the layer lines and row lines of a classical x-ray fiber diagram. Indeed it would seem that the bordered pits form a diffraction grating with an average unit cell whose orthogonal dimensions are slightly different. The pit-to-pit distance represents both a density and an anisotropy fluctuation period since the same spacings are found in both V_V and H_V scattering.

Measurement of the spacings of the two orders of maxima along the meridian in Figures 5*b* and 6*b* using the classical condition for scattering maxima ($d \sin \theta = n\lambda$)[9] gives a spacing of $d = 20\ \mu$, and a similar calculation in the direction perpendicular to the fiber axis (Figs. 4*b*, 8*b*, and 8*c*) shows a characteristic row line spacing of 30 μ. The former is the pit-to-pit distance along the fiber direction and corresponds roughly to the pit size. The latter obviously arises due to the interference of the pits along adjacent fibers. This approximates to the fiber width. Figure 11 is a schematic which summarizes the situation.

Figure 12 represents the H_V scattering patterns obtained from the optical microscope and the light scattering unit for the pits along the ray crossings (Fig. 12*a*). Comparison of Figures 12*b*, 12*c*, and 8*c* shows that the pits along the ray crossings are of the same nature (with respect to the size of the pits and thickness of the fibers) as those along the fibers but are much better organized in a regular two-dimensional lattice and give rise to a much sharper scattering pattern. However, the spherulitic anisotropic scattering, which gives rise to the four-leaf-clover pattern in the H_V mode, is less distinct in Figure 12*c*.

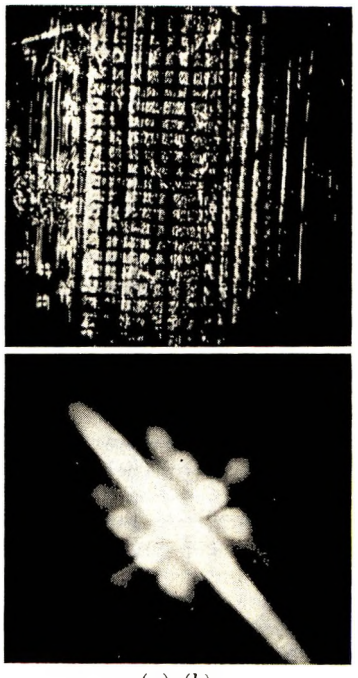

(*a*), (*b*)

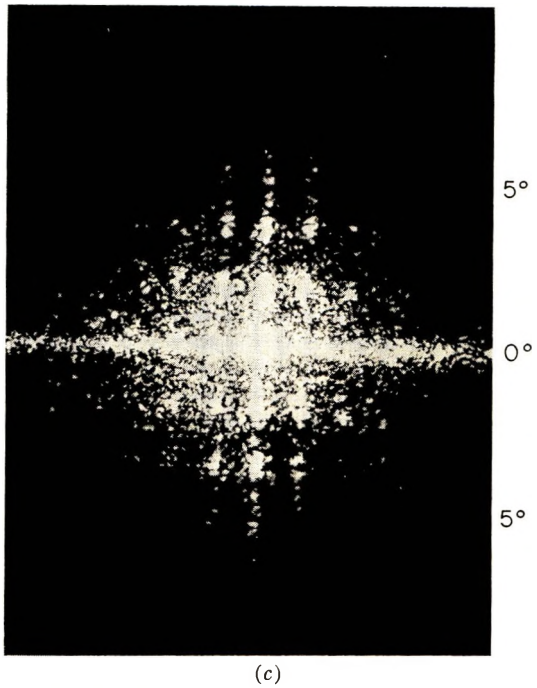

(*c*)

Fig. 12. Selected area H_V scattering from the pits along the ray crossings in a radial section of Eastern spruce: (*a*) area of the specimen (ray crossings) exposed to the incident beam to get the patterns in (*b*) and (*c*); (*b*) scattering pattern for the pits along ray crossings obtained by using the optical microscope and rotating the fiber axis through 45°; (*c*) pattern obtained by using the light-scattering unit, fiber axis as in (*a*).

The spherulitic scattering component visible in Figures 4*a* and 5*a* is likewise due to the large number of bordered pits in the scattering area. The fourfold cloverleaf is often recorded from polymer films and powders where the superstructural anisotropic organization is mainly spherical or disklike.[11] The wood pits are differentiations of the cell wall where cavities are defined.[8] The cellulose microfibrils are deposited in the pit border such that an anisotropic ringlike organization is created. This is comparable to a negatively birefringent disklike spherulite with the center removed. The H_V scattering envelope from an anisotropic disk is similar in shape to the scattering envelope from an anisotropic sphere of the same dimensions in the angular range of the first scattering maximum.[11] It has furthermore been demonstrated[12] that the change in scattered intensity distribution is minor in the small-angle range when an anisotropic sphere contains an isotropic center, even of considerable dimensions. It is therefore expected that the bordered pit can be sufficiently well approximated with a disklike continuously anisotropic spherulite. This allows the calculation of an average pit size by measuring the scattering angle for maximum scattered intensity in the direction for $\mu = 45°$.[11] The size obtained (diameter = 20 μ) agrees with the estimations from the polarizing photomicrographs (Figs. 1 and 2) and the previous calculation on the basis of the spacings of the intensity maxima along the meridian. It should be noted, however, that interpit distance and pit diameter need not coincide. In Figure 5*b* the meridional maximum and the position of the deformed cloverleaf center from the origin are different; this indicates that the pit-to-pit distance is greater than the pit diameter. This type of information is difficult to assess from polarization micrographs alone.

Figure 5*a* for the H_V scattering shows an asymmetry in the cloverleaf pattern due to the bordered pits. Asymmetry of this nature could arise from deformation of spherulites to an ellipsoidal shape. The likelier explanation in this case is that inter-pit interference along a single fiber is responsible for the asymmetry. Indeed, careful experiments with two individual starch granules aligned vertically, as the pits are, in Figure 5*a*, lead to a spherulite envelope which appears elongated in the horizontal direction. Unpublished theoretical calculations[13] also support this view.

Conclusions

The qualitative analysis of the scattering data indicates that the scattering method is promising for morphological analysis of wood. A more detailed quantitative approach should include theoretical calculations of model structures assumed on the basis of what is presently known about the superstructural organization of wood. These could then be compared with directly recorded and densitometrically evaluated scattering envelopes. Such an approach should lead to a better understanding of wood morphology. As a method of analysis, light scattering provides a nondestructive texture probe which responds to the overall distribution of microfibrillar orientation and void content in the cell walls. Use of a light source of

sufficient intensity, such as the laser, for the investigations described here would make it possible to record wood fiber properties under dynamic conditions and correlate them with mechanical measurements. A high-speed deformation arrangement coupled with a fast scattering-detection method has recently been described and is being applied to the deformation analysis of various polymers.[14]

The present status of solid-state light scattering both from the theoretical and experimental point of view certainly justifies a far greater use of the method than has heretofore been found. Recent developments in the area of optical diffractometry[9] have considerably advanced our interpretative ability. In fact, scattering under the conditions used in this report can be thought of in terms of an optical analog experiment, in which the diffraction mask is the sample itself. As such, the optical interaction between the bordered pits becomes immediately apparent. The similarity between the V_V and the H_V scattering patterns, when the sample is in the 45° position, leads one to conclude that the main anisotropy and density fluctuations are of similar origin. The scattering streak at right angles to the fiber axes and discrete intensity maxima along the streak suggest a well oriented superstructure in the tracheid direction.

Part of this work was performed at the College of Forestry, Syracuse, N. Y. Embedded wood sections were kindly supplied by Dr. W. A. Côté, of the College of Forestry.

References

1. J. Borch and R. H. Marchessault, *J. Colloid Interface Sci.*, **27**, 355 (1968).
2. J. Borch and R. H. Marchessault, in *Proceedings of the Sixth Cellulose Conference* (*J. Polym. Sci. C*, **28**), R. H. Marchessault, Ed., Interscience, New York, 1969, p. 153.
3. E. V. Beebe, R. L. Coalson, and R. H. Marchessault, in *Small Angle Scattering From Fibrous and Partially Ordered Systems* (*J. Polym. Sci. C*, **13**), R. H. Marchessault, Ed., Interscience, New York, 1966, p. 103.
4. F. A. Bettelheim, *J. Polym. Sci. A-2*, **5**, 1043 (1967).
5. F. A. Bettelheim and E. A. Balasz, *Biochim. Biophys. Acta*, **158**, 309 (1968).
6. Y. W. Lim, Ph.D. thesis, N. Y. State University, College of Forestry, Syracuse, N. Y. 1969.
7. M. B. Rhodes, Ph.D. Thesis, University of Massachusetts, Amherst, Mass. 1966.
8. W. Leise, in *Cellular Ultrastructure of Woody Plants*, W. A. Côté, Jr., Ed., Syracuse Univ. Press, Syracuse, N. Y., 1965, p. 271.
9. S. G. Lipson and H. Lipson, *Optical Physics*, Cambridge Univ. Press, Cambridge, England, 1969, p. 192.
10. H. Harada, in *Cellular Ultrastructure of Woody Plants*, W. A. Côté, Jr., Ed., Syracuse Univ. Press, Syracuse, N. Y., 1965, p. 215.
11. R. S. Stein, in *Newer Methods of Polymer Characterization*, B. Ke, Ed., Interscience, New York, 1964, p. 185.
12. J. Borch, A. Sarko, and R. H. Marchessault, *Stärke*, **21**, 279 (1969).
13. J. Borch, Ph.D. thesis, N. Y. State University, College of Forestry, Syracuse, N. Y., 1969.
14. R. S. Stein, *Polym. Eng. Sci.*, **9**, 320 (1969).

Received July 6, 1970

JOURNAL OF POLYMER SCIENCE: PART A-2 VOL. 9, 331–343 (1971)

Adsorption of Polydimethylsiloxanes from Solution on Glass

B. V. ASHMEAD and M. J. OWEN, *Research Department, Midland Silicones Limited, Barry, South Wales, United Kingdom*

Synopsis

The adsorption of polydimethylsiloxane polymers from solution on glass has been studied. The amount of polymer adsorbed depends markedly on the solvent because of specific solvent–surface interactions. The presence of silanol groups in the polymer, particularly as endgroups, markedly increases the amount of polymer adsorbed. Large differences are shown between the adsorption of the commercially available, and fully trimethylsilylated polydimethylsiloxanes of narrow molecular weight distribut on. Possible adsorption mechanisms are discussed.

INTRODUCTION

The adsorption of polymers from dilute solution on glass and a variety of other substrates has received considerable attention. Several reviews have been published summarizing the subject.[1,2] The adsorption of polydimethylsiloxane polymers from dilute solution has also been investigated.[3–7] In all these studies, not very well defined polymers have been used. They have, in general, been materials with broad molecular weight distributions, and no attempt has been made to investigate the effect of endgroups on the adsorption behavior. In their paper, Perkel and Ullman[3] suggest that terminal silanol groups will strongly increase the adsorption of polydimethylsiloxanes.

Current studies on polymer adsorption have stressed the need to look at well defined materials, especially materials with narrow molecular weight distributions. We report here the adsorption of polydimethylsiloxanes with a narrow molecular weight distribution ($\bar{M}_w/\bar{M}_n < 2$) and with both silanol and trimethylsilyl endgroups.

Ideally, measurements of the amounts adsorbed should be undertaken from a theta solvent which itself is not preferentially adsorbed to enable true comparisons to be made between the sizes of the polymer coils adsorbed on the substrate and in free solution. This is not possible, because all the theta solvents for polydimethylsiloxanes at room temperature (e.g. methyl ethyl ketone, 2-butanone, ethyl acetate) are expected to be strongly adsorbed on the glass surface.

The effect of solvent on the adsorption behavior of one particular polymer has been investigated, all remaining measurements being made from two solvents, *n*-hexane and benzene.

EXPERIMENTAL

Adsorbent

300 mesh Pyrex glass powder from Jencons, Ltd., Hemel Hempstead, U.K., was used as the adsorbent. The surface area, 0.64 m^2/g, was determined by the B.E.T. method at $-196°C$ by using krypton (cross-sectional area 20.2 $Å^2$) as adsorbate.

Palmitic acid adsorption from carbon tetrachloride gave an estimate of the surface area as 0.22 m^2/g. This value was independent of the powder treatment.

Solvents

AnalaR grades were used in each case. The solvents were allowed to stand over molecular sieve (type 4A) for at least two weeks before use and were handled only over argon in the dry box.

Polymers

These were all materials of narrow molecular weight distribution prepared by the anionic polymerization of hexamethylcyclotrisiloxane.[8] Trimethylsilyl end-blocked materials were obtained by refluxing the polymer with excess hexamethyldisilazane for at least 24 hr, distilling off the remaining disilazane, and reprecipitating the polymer with methanol from benzene solution. All polymers were thoroughly dried before use, initially at room temperature in a vacuum oven; subsequently, small samples were heated at 110°C under vacuum for at least 24 hr. GPC analysis showed that this treatment did not affect the molecular weight distribution of any of the polymers.

TABLE I
Characterization of Polymers

Polymer	$\bar{M}_n$	$\bar{M}_w/\bar{M}_n$	
A	37,300	1.37	Partially trimethylsilylated
B	37,300	1.37	Exhaustively trimethylsilylated
C	58,000	1.51	α,ω-Hydroxy end-blocked
D	58,000	1.51	Exhaustively trimethylsilylated
E	119,300	1.24	Exhaustively trimethylsilylated
F	177,000	1.33	Exhaustively trimethylsilylated
G	28,000	5.88	MS 200/1000
H	58,000	3.88	MS 200/12,500
J	100,000	2.68	MS 200/60,000

Three commercially available polydimethylsiloxane fluids were also used. These were Midland Silicones, Ltd., 200 fluids of viscosity 1,000 cS, 12,500 cS, and 60,000 cS, and were used as received.

Molecular weight determinations were made on all the polymers both for $\bar{M}_n$ and $\bar{M}_w$, the latter by light scattering for the narrow distribution materials and by calculation from the GPC trace for the 200 fluids.

A summary of the polymers used with their molecular weights and the nature of the endgroup is given in Table I.

Technique

Perkel and Ullman[3] showed that the adsorption of polydimethylsiloxanes from solution on glass and iron was very sensitive to traces of water. We did not attempt to investigate the effect of water on the adsorption, but always used glass dried to the same extent. A 7g portion of the glass powder was weighed into a small adsorption tube fitted with a Teflon high-vacuum stopcock. The tubes were attached to a high-vacuum line, evacuated to a pressure of better than 0.005 mm Hg, and heated for 5 hr at 280°C. They were removed from the line while under vacuum and transferred to the dry box, which had previously been purged with dry argon. Ten milliliters of a solution of the polymer of known concentration was pipetted onto the powder and the tube shaken for at least 14 hr at room temperature (20°C). The supernatant liquid was analyzed by an infrared technique after shaking. Use was made of the symmetric deformation of the methyl group (1261 cm^{-1}) to determine polymer concentrations. With methyl ethyl ketone and 1% ethyl acetate in benzene as solvent, use had to be made of the peak at 810 cm^{-1} (methyl rocking and Si-C stretch vibrations). Matched sodium chloride cells (1-mm path length) were used with a Perkin-Elmer 237 infrared spectrophotometer. Beer's Law plots of the polymers in the solvent of interest were used to measure polymer concentrations after adsorption.

The amount of polymer adsorbed Γ was determined from:

$$\Gamma = (V/M)(C_i - C_f)$$

where V is the volume of polymer solution used, M is the mass of glass powder, and C_i, C_f are the initial and final (equilibrium) polymer solution concentration, respectively.

Surface Area Measurement

The surface area of the glass powder was determined by adsorbing palmitic acid from carbon tetrachloride solution. The quantity of acid adsorbed was obtained from the difference between the palmitic acid concentration in the solution before and after adsorption, determined by measuring the infrared peak of the carboxyl group (1712 cm^{-1}). It was assumed that each fatty acid molecule occupied 20.5 $Å^2$ of the surface.[9]

The glass powder was treated in two ways: (a) by the procedure described above, (b) by heating 7 g in air at 125°C for 20 hr. No differences in the isotherm could be detected for the two treatments.

RESULTS

Effect of Solvent on Adsorption

Strong absorption of some of the solvents in the infrared region at 1261 and 810 cm^{-1} did not permit the concentration to be measured by infrared spectroscopy. For these solvents, mixtures with benzene were used to study their effect on the adsorption.

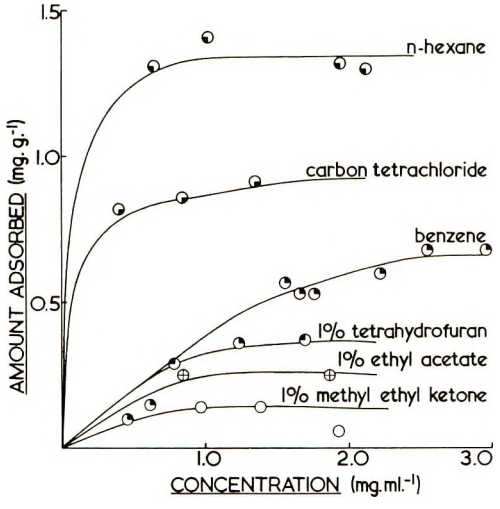

Fig. 1. Adsorption of polydimethylsiloxanes on glass from different solvents.

Isotherms for the adsorption of polymer A from *n*-hexane, carbon tetrachloride, benzene, and 1% (volume/volume) of methyl ethyl ketone, tetrahydrofuran, and ethyl acetate in benzene are shown in Figure 1. "Negative" adsorption of the siloxane from methyl ethyl ketone (a theta solvent at 20°C) was measured (Table II).

TABLE II
Adsorption of Polymer A from Methyl Ethyl Ketone

Initial concentration, mg/ml	Final concentration, mg/ml	Amount adsorbed, mg/g
1.00	1.04	−0.06
1.03	1.04	−0.02
1.52	1.60	−0.11

Dependence of Adsorption on Polymer Endgroup

Figure 2 shows the isotherms for the adsorption of a material which has and has not been fully trimethylsilylated (polymers A and B). It can be seen that the removal of the free silanol groups in the polymer by hexamethyldisilazane markedly reduces the adsorption. These materials are not, however, well defined for the amount of silanol group present.

More striking is the adsorption of an α,ω-hydroxy end-blocked material (polymer C) compared with the fully trimethylsilylated material (polymer

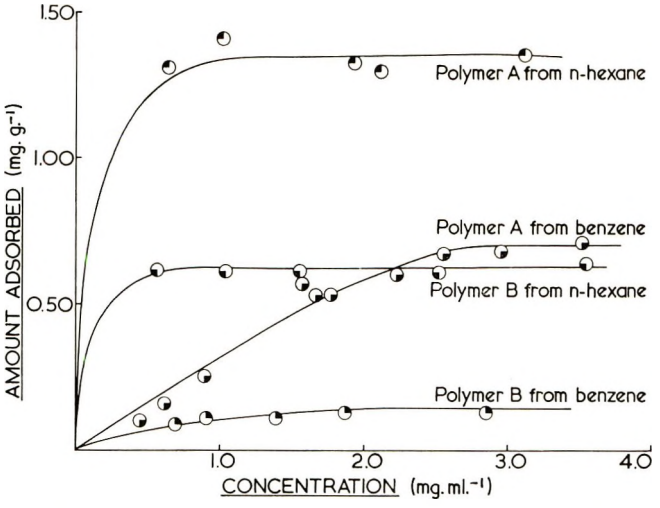

Fig. 2. Adsorption of partially and fully trimethylsilylated polydimethylsiloxanes from benzene and *n*-hexane.

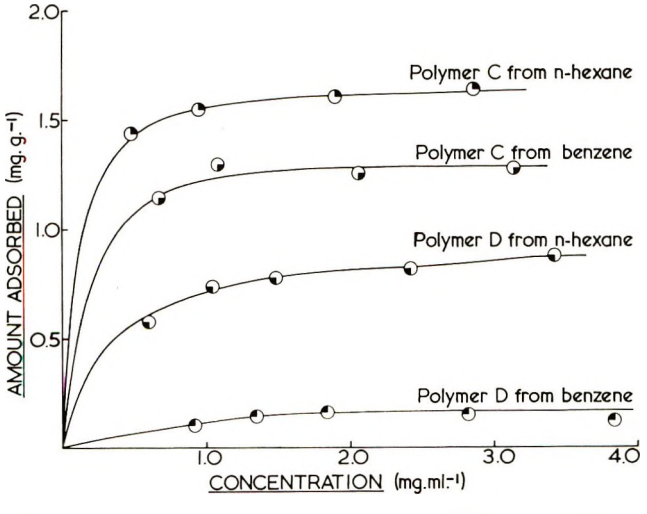

Fig. 3. Adsorption of α,ω-hydroxy end-blocked and fully trimethylsilylated polydimethylsiloxanes from benzene and *n*-hexane.

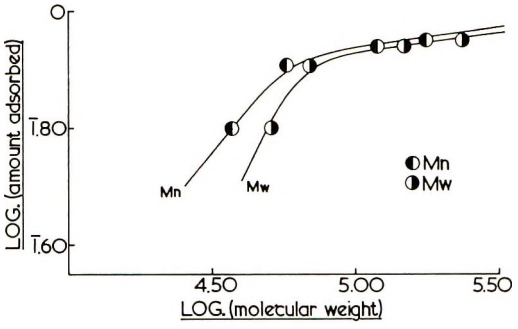

Fig. 4. Effect of molecular weight on the adsorption of fully trimethylsilylated polydimethylsiloxanes from *n*-hexane.

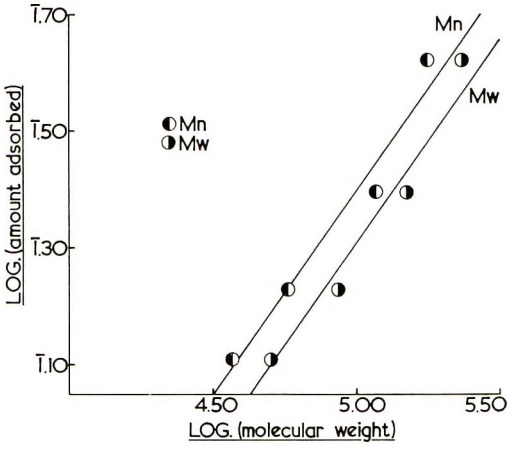

Fig. 5. Effect of molecular weight on the adsorption of fully trimethylsilylated polydimethylsiloxanes from benzene.

D). Figure 3 presents isotherms for these materials adsorbed from both *n*-hexane and benzene. The amount adsorbed from *n*-hexane solution is reduced by half, from 1.60 mg/g to 0.81 mg/g and from benzene by a factor of eight, from 1.28 mg/g to 0.16 mg/g.

Adsorption as a Function of Molecular Weight

In view of the effect of silanol groups, the materials used in this section were exhaustively trimethylsilylated. Isotherms were constructed for each polymer in the usual manner, the saturation value Γ_0 being noted. This could be related to the molecular weight by the empirical relationship:

$$\Gamma_0 = K\bar{M}_w^a$$

Plots of log Γ_0 against both log $\bar{M}_w$ and log $\bar{M}_n$ with both *n*-hexane and benzene as solvent are shown in Figures 4 and 5. The constants K and a are summarized in Table III.

TABLE III
Effect of Molecular Weight on Adsorption of Trimethylsilylated Polymers

Solvent	Molecular weight variable	K[a]	a
n-Hexane	$\bar{M}_w$, min. slope	0.41	0.06
"	$\bar{M}_w$, max. slope	3.3×10^{-5}	0.91
"	$\bar{M}_n$, min. slope	0.42	0.06
"	$\bar{M}_n$, max. slope	9.1×10^{-5}	0.62
Benzene	$\bar{M}_w$	$(6.4 \pm 0.5) \times 10^{-5}$	0.70 ± 0.06
"	$\bar{M}_n$	$(7.8 \pm 0.6) \times 10^{-5}$	0.70 ± 0.07

[a] Calculated by expressing Γ_0 in mg/g.

The values quoted in n-hexane are the maximum and minimum slopes found for the curved plots (Fig. 4), and no attempt has been made to introduce an error as in the benzene case. The errors in the benzene case appear to be very large but it must be noted that very small amounts of polymer are being adsorbed.

Adsorption of Commercially Available Materials

These materials were used as received. No attempt was made to remove any silanol groups or the low molecular weight material present. Plots of log Γ_0 against log $\bar{M}_w$ and log $\bar{M}_n$ with benzene as solvent are shown in Figure 6, the constants K and a being summarized in Table IV.

TABLE IV
Effect of Molecular Weight on Adsorption of Commercially Available Polymers

Solvent	Molecular weight variable	K[a]	a
Benzene	$\bar{M}_w$	0.5×10^{-2}	0.41
Benzene	$\bar{M}_n$	8.1×10^{-2}	0.16

[a] Calculated by expressing Γ_0 in mg/g.

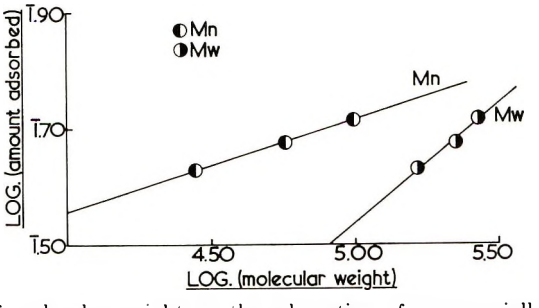

Fig. 6. Effect of molecular weight on the adsorption of commercially available polydimethylsiloxanes from benzene.

DISCUSSION

The isotherms for the adsorption of siloxanes on glass are similar to those observed for other polymers with the use of glass and metals as adsorbents.

The amount of material adsorbed in the plateau region of the isotherm (i.e., surface saturation) is far in excess of the amount in a monolayer when the polymer molecule is fully extended on the adsorbent surface. Zisman[10] has shown that for a monolayer of polydimethylsiloxane in such a configuration on water, the cross-sectional area of each $[(CH_3)_2SiO]$ unit is 22.7 Å^2. The weight of polymer in this configuration occupying 1 g of a powder of surface area 0.22 m^2/g would be 0.119 mg. It seems more relevant to use here the fatty acid figure rather than the krypton figure, since the palmitic acid situation more closely resembles the polymer in solution.

With methyl ethyl ketone (MEK) as solvent, no adsorption could be measured. With small amounts of oxygen-containing solvents in benzene, adsorption is significantly lower than with pure benzene. MEK is a theta solvent for polydimethylsiloxanes at 20°C, whereas benzene is a good solvent.[11] One would expect more polymer to be adsorbed from a theta solvent than from a good solvent, but this is not found experimentally.

In this system, therefore, solvent–surface interactions are sufficiently important to affect the adsorption markedly and must be considered.

We know that MEK is strongly adsorbed. The solvents containing oxygen reduce the adsorption and they too must be adsorbed on the hydroxylated surface. No figures are available for the adsorption of these materials on glass, but the shift in the hydroxyl stretching frequency $\Delta\nu_{OH}$ in the infrared spectrum of silica on the vapor adsorption of these materials suggests them to be strongly adsorbed. Values are summarized in Table V. This table reveals a drastic difference in the $\Delta\nu_{OH}$ values for

TABLE V
Infrared Frequency Shifts on the Adsorption of Various Vapors on Silica

Vapor	$\Delta\nu_{OH}$, cm^{-1}
n-Hexane	45,[a] 30[b]
Carbon tetrachloride	45,[b] 60[c]
Benzene	125,[d] 110,[a] 120[b]
Methyl ethyl ketone	330[d]
Ethyl acetate	270[d]
Tetrahydrofuran	475[d]

[a] Data of Kiselev and Lygin.[12]
[b] Data of Hertl and Hair.[13]
[c] Data of Hasegawa and Low.[14]
[d] Data of Elkington and Curthoys.[15]

the adsorption of saturated *n*-hexane molecules possessing only σ-bonds and, therefore, affecting only the nonspecific interaction with silica, and for the adsorption of molecules which interact specifically with the hydroxyl groups of the silica surface.

The differences in the amounts adsorbed from benzene and *n*-hexane can further be explained by considering a study of the adsorption of benzene and *n*-hexane on silica[16] as a function of the temperature at which the silica was heat-treated. It was found that the adsorption of benzene decreased with increasing adsorbent degassing temperature, while the adsorption of *n*-hexane increased over the same temperature range. The adsorption of benzene was greater than that of *n*-hexane, the heats and free energies of benzene adsorption also being greater in the temperature region studied. A π-complex between the proton of the Si-OH group and a benzene molecule is predicted, which accounts for the enhanced benzene adsorption on silica. In the case of the adsorption of polydimethylsiloxane from benzene, it is clear that the benzene molecules are preferentially adsorbed on the hydroxyl groups. With *n*-hexane as solvent, the polydimethylsiloxane can adsorb on what is effectively a greater surface area since the solvent is not as strongly adsorbed.

The effect of the polymer–solvent interaction on the adsorption must also be considered. The solvating power of a solvent for a polymer can be shown by examination of the Mark-Houwink relation $[\eta] = KM^a$. For a theta solvent, a is 0.5; for a good solvent a is larger than 0.5, generally 0.6–0.7. Benzene is a good solvent for siloxanes ($a = 0.68$ at 20°C).[11] The corresponding parameter has not been measured in *n*-hexane, although we have unpublished evidence that indicates it to be a better solvent than benzene.

Perkel[17] has shown by intrinsic viscosity–molecular weight measurements that the very similar solvent to *n*-hexane, *n*-heptane is a better solvent than benzene.

Thus, neglecting any possible solvent–surface interaction, more siloxane should be adsorbed from benzene than from *n*-hexane. The fact that this is not the case clearly shows that the solvent–surface interaction is the predominant effect.

The nature of the endgroup has been found to affect the adsorption behavior of several polymer systems. Howard and McConnell[18] found that esterification of the hydroxyl endgroups in the poly(ethylene oxide)–charcoal–benzene system markedly reduces the adsorption of low molecular weight species, an effect most pronounced with the hexanoate. The effect falls off with increasing molecular weight and is not noticeable for $\bar{M}_n > 10^4$.

The effect with siloxanes is clearly noticeable with much greater molecular weights. Perkel and Ullman[3] suggest that terminal silanol groups will strongly increase the adsorption of siloxane polymers, although they do not support this statement with experimental evidence.

Similar effects have been noticed for the adsorption of poly(methyl methacrylate)[19] where a large increase in the amount of polymer adsorbed is brought about by a small fraction of free carboxyl groups in the polymer. Here, the presence of strong polar groups enhances adsorption.

The adsorption of polyvinyl acetate from solution[20] is another such example. The polymer containing the highest percentage of hydroxyl

groups is adsorbed the most, although the relative increase in adsorption caused by a small percentage of hydroxyl groups on the polymer is greater than that obtained by further increasing the hydroxyl content.

In our present study, the glass surface still contains several hydroxyl groups after it has been heated at 280°C. Free hydroxyl groups in the polymer would possess a relatively high affinity for this surface, certainly greater than that of the $-Si(CH_3)_2OSi(CH_3)_2O-$ chain.

We have interpreted the results for the adsorption of the fully trimethylsilylated materials from *n*-hexane in the same way as Burns and Carpenter.[21] They assume that the molecules are adsorbed in a monolayer as distorted random coils of radius R_a which can be calculated (in Å) from:

$$R_a = (S_m/\pi)^{1/2}$$
$$= (S\bar{M}_w/6.023\pi\Gamma_0)^{1/2}$$

where S_m is the area occupied by a single molecule, S is the specific surface area of adsorbent, $\bar{M}_w$ is the weight-average molecular weight, and Γ_0 is the specific adsorption (mg/g).

Table VI shows the results of such calculations. Values are also included for the radius of gyration of free chains in solution and the compression of the coils on adsorption, i.e., the ratio of the adsorbed coil radius to the radius of gyration of the molecules in solution.

TABLE VI
Comparison of Radii of Free and Adsorbed Molecules

Polymer	$\bar{M}_w$	Radius free coil, Å		Γ_0, mg/g	Radius, adsorbed coil, Å	Compression	
		Theta solvent	Good solvent			Good solvent	Theta solvent
B	51,000	66.3	66.3	0.63	30.7	0.46	0.46
D	87,400	86.8	90.8	0.81	35.4	0.39	0.41
E	148,000	113	122	0.87	44.5	0.36	0.39
F	235,000	142	158	0.89	55.4	0.35	0.39

Values for the chain dimensions in the theta solvent have been calculated from intrinsic viscosity data.[11] As we have no appropriate intrinsic viscosity data for *n*-hexane, values in the good solvent in Table VI have been determined by using the volume expansion factor relevant to benzene. The figures in *n*-hexane will probably be slightly greater than this.

No attempt has been made to compare the values obtained in benzene solution in this way, since no estimate of the amount of benzene in the surface can be made.

The values in the table indicate that a significant degree of compression of the coils occurs upon adsorption, more so than when polystyrene is absorbed from cyclohexane on aluminum.[21] The degree of compression also increases with increasing molecular weight. This model is rather simplified and supposes that the coils are adsorbed separately. Probably, the

TABLE VII
Molecular Weight Dependence of Adsorption of Commercially Available Materials from Benzene

$K \times 10^2$ [a]	a	Source
2.1	0.41	This study
1.8	0.40	Perkel and Ullman

[a] Calculated by expressing Γ_0 in mg/m².

coils are entangled on the surface, a fact which cannot be considered on such a model.

The theoretical considerations of Silberberg[22] predict that the plot of log (amount adsorbed) against log (molecular weight) will be curved with a slope decreasing with increasing molecular weight. This is the case with *n*-hexane as solvent. The low value of the constant a found at the high molecular weight end then agrees with the value zero found for many other polymer systems.

Our measurements on the adsorption of commercially available materials agree very closely with those of Perkel and Ullman.[3] The comparison is made in Table VII by expressing the amounts adsorbed in mg.m.$^{-2}$. This would suggest that we have a very comparable system, i.e., our powders, solvents, etc., have been similarly dried.

Perkel and Ullman[3] suggest that the siloxane is adsorbed by mechanism I (Fig. 7). This mechanism will probably explain the adsorption of the fully trimethylsilylated materials, but is not adequate for the commercially available polymers. By the nature of their preparation, the commercially avail-

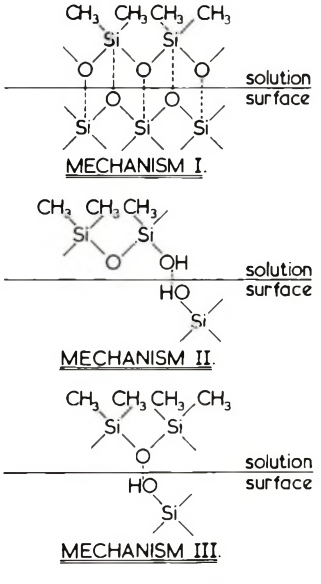

Fig. 7. Some possible mechanisms of adsorption.

able siloxanes must contain some hydroxyl groups, and these groups will greatly affect the adsorption mechanism.

Consider the adsorption from benzene, a solvent which is strongly adsorbed on the hydroxylated surface. On trimethylsilylation of the polymer, considerably less polymer is adsorbed, but there is a greater dependence on molecular weight. Adsorption of the silanol containing materials can occur through a hydrogen-bonding mechanism between hydroxyls on the surface and in the polymer (mechanism II). Further links with the surface may occur by mechanism I. From energetic considerations, mechanism II would be similar to benzene adsorption on a hydroxylated surface whereas mechanism I must be considerably weaker.

With the trimethylsilylated materials, adsorption from benzene could only occur by mechanism I, benzene being preferentially adsorbed on SiOH and obscuring large areas of the surface. Such a system would give rise to the observed situation where less polymer is adsorbed, but a greater dependence on molecular weight arises since the polymer is attached to the surface at fewer anchor points.

With *n*-hexane as solvent, solvent adsorption does not occur. Once again, less trimethylsilylated material is adsorbed than is the case with silanol-containing polymers, but in this instance there is, so it seems, a tendency for the trimethylsilylated polymers to lie flatter in the surface than is the case with the silanol containing materials. The polymers have a greater surface area available to them with *n*-hexane as solvent than with benzene as solvent. As the molecular weight dependence in *n*-hexane is less with the trimethylsilylated materials than with the silanol-containing materials, the polymer must be attached to the surface at more anchor points in the former case than in the latter. In *n*-hexane, the trimethylsilylated polymers must interact with the surface through the surface hydroxyl groups by a mechanism such as III, a mechanism that cannot apply in benzene solution.

Our thanks are due to Dr. R. H. Ottewill of the University of Bristol for the krypton surface area determination and to Dr. W. G. Davies of this department for the preparation of some of the polymers and the light-scattering determinations.

References

1. R. R. Stromberg and G. M. Kline, *Modern Plastics*, **38**, 123, 241 (1961).

2. R. R. Stromberg, in *Treatise on Adhesion and Adhesives*, Vol. I, R. L. Patrick, Ed., Dekker, New York, 1967.

3. R. Perkel and R. Ullman, *J. Polym. Sci.*, **54**, 127 (1961).

4. T. Yoshida, T. Sato, and T. Tanaka, *J. Paint Technol.*, **39**, 194 (1967).

5. B. I. Tul'bovich and E. I. Priimak, *Zh. Fiz. Khim.*, **43**, 963 (1969).

6. B. I. Tul'bovich, F. A. Slisarenko, V. I. Klyaev, and S. I. Sorokin, *Izv. Vyssh. Ucheb. Zaved. SSR, Khim. i Khim. Tekhnol.*, **9**, 892 (1966).

7. A. V. Kiselev, V. N. Novikova, and Yu. A. El'tekov, *Proc. Acad. Sci. U.S.S.R. Phys. Chem. Sect.*, **149**, 210 (1963).

8. W. G. Davies and T. C. Kendrick, to be published. W. G. Davies, B. Eliott, and T. C. Kendrick, U.S. Patent 3,481,898, Dec. 1969.

9. N. K. Adam, *Proc. Roy. Soc.* (London), **A99,** 336 (1921).
10. H. W. Fox, P. W. Taylor, and W. A. Zisman, *Ind. Eng. Chem.*, **39,** 1401 (1947).
11. V. Crescenzi and P. J. Flory, *J. Amer. Chem. Soc.*, **86,** 141 (1964).
12. A. V. Kiselev and V. I. Lygin, *Surface Sci.*, **2,** 236 (1964).
13. W. Hertl and M. L. Hair, *J. Phys. Chem.*, **72,** 4676 (1968).
14. M. Hasegawa and M. J. D. Low, *J. Colloid Interface Sci.*, **30,** 378 (1969).
15. P. A. Elkington and G. Curthoys, *J. Phys. Chem.*, **72,** 3475 (1968).
16. A. V. Kiselev, in *The Structure and Properties of Porous Materials*, D. H. Everett and F. S. Stone, Eds., Academic Press, New York, 1958, pp. 195–226.
17. R. Perkel and R. Ullman, Technical Report, Office of Naval Research. Project Nonr-83919, May 1960.
18. G. J. Howard and P. McConnell, *J. Phys. Chem.*, **71,** 2981 (1967).
19. S. Ellerstein and R. Ullman, *J. Polym. Sci.*, **55,** 123 (1961).
20. J. Koral, R. Ullman, and F. R. Eirich, *J. Phys. Chem.*, **62,** 541 (1958).
21. H. Burns and D. K. Carpenter, *Macromolecules*, **1,** 384 (1968).
22. A. Silberberg, *J. Phys. Chem.*, **66,** 1884 (1962).

Received May 19, 1970
Revised August 24, 1970

JOURNAL OF POLYMER SCIENCE: PART A-2 VOL. 9, 345–362 (1971)

Normal Stress and Shear Stress in a Viscoelastic Liquid Under Steady Shear Flow: Effect of Molecular Weight Heterogeneity

HIROSHI ENDO,* TERUO FUJIMOTO, and MITSURU NAGASAWA,
Department of Synthetic Chemistry, Nagoya University, Chikusa-ku, Nagoya, Japan

Synopsis

Under steady shear flow, the normal stress and the shear stress in both dilute and concentrated solutions of monodisperse poly-α-methylstyrenes and their blends were measured. It was confirmed that the molecular theories of Rouse and Zimm extended to concentrated solutions can explain the relation between the zero-shear normal stress coefficient and the zero-shear steady-flow viscosity for both monodisperse and polydisperse systems. Shear-rate dependence of steady-flow viscosity can be understood fairly well by the molecular entanglement concept proposed by Graessley so long as the polymer is monodisperse or the amount of the higher molecular weight component is high. However, zero-shear viscosity of blended systems cannot be explained quantitatively by the theory of Graessley. The shear-rate dependence of steady-state compliance of blended systems was also observed, and it can well be explained by the theory of Tanaka, Yamamoto, and Takano which interpreted the shear rate-dependent steady-state compliance in terms of the relaxation time spectrum and its variation with shear rate.

INTRODUCTION

Simultaneous measurements of shear stress and normal stress difference are useful in clarifying the effect of molecular characteristics of linear polymers on their rheological properties under steady shear flow. Then, in addition to viscosity η, which is a measure of energy dissipation, the steady-state compliance J_e, which is a measure of stored energy, can be calculated. That is, the shear stress P_{21} and the normal stress difference $P_{11} - P_{22}$ are related to the shear rate $\dot{\gamma}$ by

$$P_{21} = \eta\dot{\gamma} \tag{1}$$

$$P_{11} - P_{22} = \psi_{12}\dot{\gamma}^2 \tag{2}$$

It is assumed that

$$P_{22} - P_{33} = 0 \tag{3}$$

* Present address: Plastics Research Laboratory No. 1, Mitsubishi Petrochemical Company, Ltd., Toho-cho, Yokkaichi-shi, Mie, Japan.

When the shear rate is low, the viscosity η and the normal stress coefficient ψ_{12} are constants. As the shear rate increases, however, they begin to deviate from the initial values. The steady-state compliance J_e is calculated from[1]

$$J_e = (P_{11} - P_{22})/2(P_{21} - P_{21}^s)^2 \quad (4)$$

where P_{21}^s is the shear stress in the solvent at the same shear rate and is calculated as

$$P^s_{21} = \nu_s \eta_s \dot{\gamma}$$

where ν_s is the volume fraction of solvent and η_s is the solvent viscosity.

As is well known, the steady-flow viscosity of concentrated solutions of linear polymers or of undiluted polymers is proportional to $M^{3.5}$ (M denoting molecular weight) and is approximately determined by the weight-average molecular weight in heterogeneous polymers. On the other hand the normal stress difference may be proportional to M^7 or M^8 and hence is very sensitive to the molecular weight distribution of the polymer. The steady-state compliance is also determined by a higher average molecular weight. It is our impression that the effect of molecular weight heterogeneity on the normal-stress difference or steady-state compliance has not yet been adequately studied, even though the effect of molecular weight distribution on viscosity has been studied fairly extensively. The purpose of the present work is to clarify the effect of molecular weight heterogeneity on J_e by using samples of very narrow molecular weight distribution prepared in this laboratory.

EXPERIMENTAL

Samples

The (nearly) monodisperse poly-α-methylstyrene samples used in this work were prepared by an anionic polymerization method.[2] Low and high molecular weight tails were removed by two fractional precipitations from benzene with addition of methanol. The weight-average to number-average molecular weight ratio $\bar{M}_w/\bar{M}_n$ is believed to be less than 1.01 in every case.[3] Examples of sedimentation patterns of the samples before fractionation have been given by Soda et al.,[4] and the sedimentation pattern of a sample after fractionation was also shown elsewhere.[5] Studies of column fractionation and sedimentation velocity[2,3] showed the polymer to have such sharp molecular weight distributions that it can be assumed to be monodisperse, even for calculating z-average and $z + 1$-average molecular weights of polymer mixtures. The molecular weights of the nine samples used are listed in Table I. The number-average and weight-average molecular weights were determined, respectively, with a Hewlett-Packard Mechrolab Model 502 high-speed membrane osmometer and a modified Shimazu light-scattering photometer. The technique for the measurement of those molecular weights was reported in previous papers.[5-7] Five

TABLE I
Molecular Characteristics of Monodisperse Samples

Sample	$\bar{M}_n \times 10^{-4}$	$\bar{M}_n \times 10^{-4}$	$\bar{M}_w/\bar{M}_n$
PαS-3	14.2		
PαS-4-1	26.5		
PαS-4-2	27.5		
PαS-5′	33.2		
PαS-6	43.8	44.4	1.01
PαS-7	68.0	69.4	1.02
PαS-9	118	119	1.01
PαS-10		124	
PαS-12		182	
PαS-13		130	

blended samples were prepared from two monodisperse polymers with molecular weights of 1.82×10^6 (PαS-12) and 3.32×10^5 (PαS-5′) and another blend was prepared from polymers with molecular weights of 1.82×10^6 (PαS-12) and 1.42×10^5 (PαS-3). Number-average, weight-average, z-average and $z + 1$-average molecular weights of the blended samples were calculated from the number average molecular weights of the original monodisperse samples and are listed in Table II. Kanechlor (a chlorinated diphenyl with viscosity 0.693 poises at 25.0°C) was used as a solvent.

TABLE II
Molecular Characteristics of Blends of Monodisperse Samples

Sample	W_2[a]	$\bar{M}_n \times 10^{-4}$	$\bar{M}_w \times 10^{-4}$	$\bar{M}_z \times 10^{-4}$	$\bar{M}_{z+1} \times 10^{-4}$	$\bar{M}_{z+1}\bar{M}_z/M_w \times 10^{-4}$
PαS-5′	0.000	33.2	33.2	33.2	33.2	33.2
B-1[b]	0.051	34.7	40.7	67.3	125	207
B-2[b]	0.100	36.2	48.1	89.5	148	275
B-3[b]	0.252	41.8	70.7	130	169	309
B-4[b]	0.500	56.1	108	159	177	262
B-5[b]	0.720	80.7	140	172	180	221
PαS-12	1.000	182	182	182	182	182
B-6[c]	0.500	27.0	98.3	170	181	312

[a] W_2 denotes the weight fraction of higher molecular weight component.
[b] Blend of two monodisperse samples with $M = 1.82 \times 10^6$ and $M = 3.32 \times 10^5$.
[c] Blend of two monodisperse samples with $M = 1.82 \times 10^6$ and $M = 1.46 \times 10^5$.

Apparatus

The Weissenberg rheogoniometer, model R-17, manufactured by Sangamo Controls Ltd. was used. It is a cone-and-plate viscometer with facilities for oscillatory input and for normal-stress measurement. Details of the instrument are given in the literature.[8–10] The reliability and reproducibility of the instrument were examined earlier.[11] In the present work, platens 5 cm in diameter and with a 2° angle were used with a torsion bar 2 mm in diameter. Experiments were generally carried out according to the

instruction manual supplied by the manufacturer. The experimental procedure has been reported in a previous paper.[11] The temperature was held at 25.0 ± 0.05°C as measured by a thermocouple of 0.01° sensitivity.

RESULTS

Examples of shear stress $P_{21} - P_{21}^s$ and normal stress difference $P_{11} - P_{22}$ measured as a function of shear rate $\dot{\gamma}$ are shown in Figure 1. The shear rate dependence of $\eta - v_s\eta_s$ and ψ_{12} for 7% solutions of monodisperse and blended samples are shown in Figures 2 and 3, respectively. In these figures as well as in all other figures, the solvent contribution to the total shear

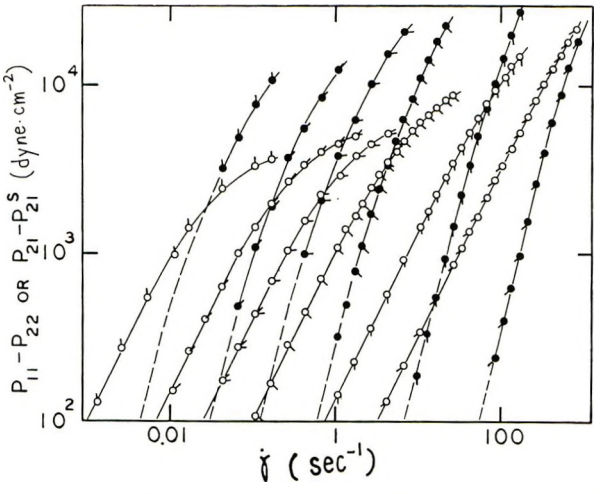

Fig. 1. Plots of (○) log $(P_{21}-P_{21}^s)$ and (●) log $(P_{11}-P_{22})$ vs. log $\dot{\gamma}$ for 7% solutions of monodisperse samples of various molecular weights: (○, ●) 3.00×10^6; (○, ●) 1.82×10^6; (○, ●) 1.19×10^6; (○, ●) 6.94×10^5; (○, ●) 3.32×10^5; (○, ●) 1.46×10^5.

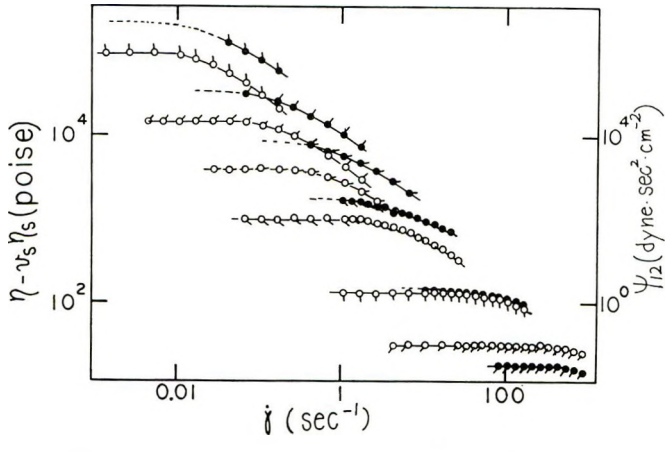

Fig. 2. Plots of (○) log $(\eta-v_s-\eta_s)$ and (●) log ψ_{12} vs. log $\dot{\gamma}$ for 7% solutions of monodisperse samples. Symbols are the same as in Fig. 1.

stress is subtracted as $v_s\eta_s$. Moreover, when applying the theories presented for dilute solution to our present experimental data, we subtract $v_s\eta_s$ instead of η_s. However, the solvent contribution is not appreciable even for 2% solutions when reduced viscosity is discussed. The η results are quite similar to the results reported for molten monodisperse polystyrene.

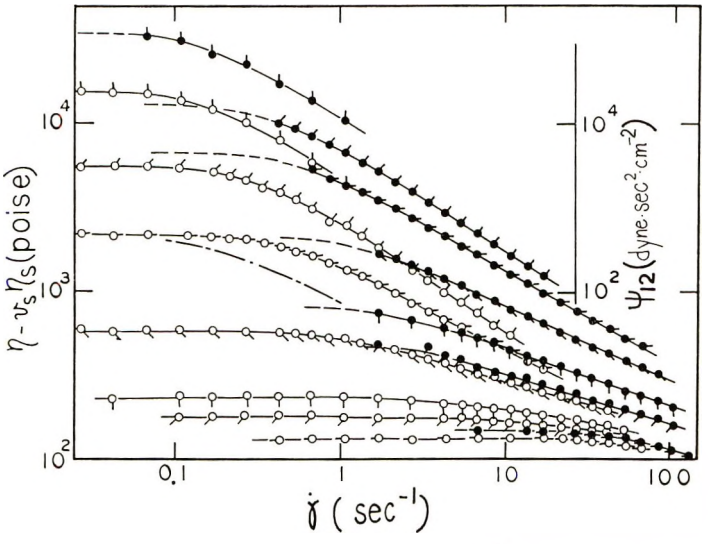

Fig. 3. Plots of (O) log $(\eta\text{-}v_s\eta_s)$ and (●) log ψ_{12} vs. log $\dot{\gamma}$ for 7% solutions of blended samples for various weight fractions of the higher molecular weight component W_2: (○, ●) 1.00; (◔, ◐) 0.720; (◑, ◒) 0.500; (◕, ◕) 0.252; (◔, ◔) 0.100; (○, ●) 0.051; (○, ●) 0.00; the chain line (–·–) indicates the values calculated from eq. (14).

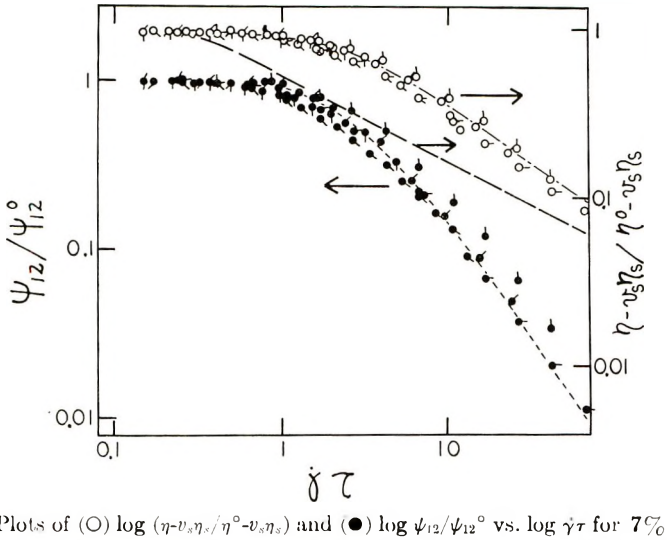

Fig. 4. Plots of (O) log $(\eta\text{-}v_s\eta_s/\eta^\circ\text{-}v_s\eta_s)$ and (●) log $\psi_{12}/\psi_{12}^\circ$ vs. log $\dot{\gamma}\tau$ for 7% solutions of monodisperse samples; circles are coded as in Fig. 1; (–·–) Graessley's theory (– –) Bueche's theory; (- -) calculated as $\psi_{12}/\psi_{12}^\circ = (\eta\text{-}v_s\eta_s/\eta^\circ\text{-}v_s\eta_s)^2$ from Graessley's theory.

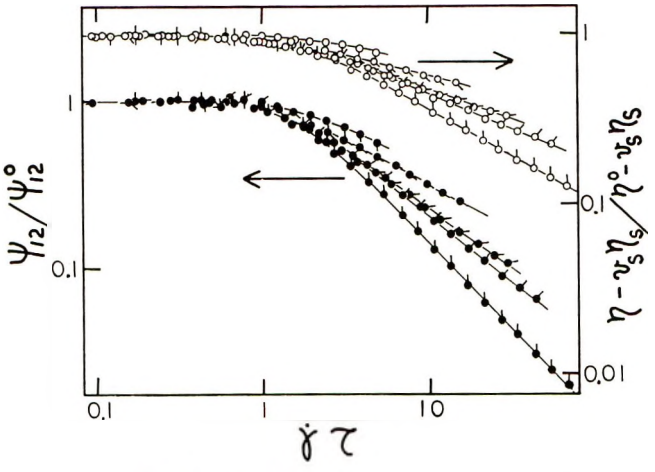

Fig. 5. Plots of (○) log $(\eta - v_s\eta_s/\eta^{\circ} - v_s\eta_s)$ and (●) log $\psi_{12}/\psi_{12}^{\circ}$ vs. log $\dot{\gamma}\tau$ for 2% solutions of monodisperse samples of various molecular weights: (○, ●) 3.00×10^6; (○, ●) 1.82×10^6; (○, ●) 1.14×10^6; (○, ●) 6.94×10^5; (○, ●) 4.96×10^5; (○, ●) 2.75×10^5.

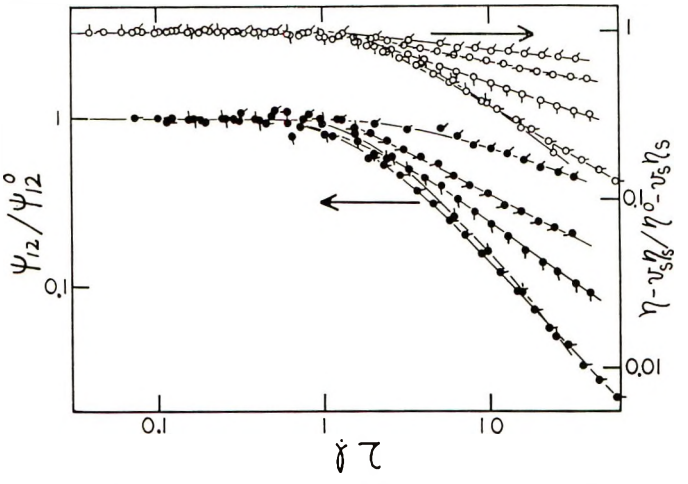

Fig. 6. Plots of (○) log $(\eta - v_s\eta_s/\eta^{\circ} - v_s\eta_s)$ and (●) log $\psi_{12}/\psi_{12}^{\circ}$ vs. log $\dot{\gamma}\tau$ for solutions of various concentrations of a monodisperse samples with $M = 1.82 \times 10^6$ at various concentrations (in weight per cent): (○, ●) 7.00; (○, ●) 3.50; (○, ●) 1.68; (○, ●) 0.801; (○, ●) 0.400.

renes by other investigators.[12,13] in that η becomes very much less dependent on molecular weight as $\dot{\gamma}$ increases. Plots of log $(\eta - v_s\eta_s)$ versus log $\dot{\gamma}$ for the monodisperse polymers approach a limiting line with a slope of about -0.8 at high $\dot{\gamma}$.[14,15] The plots of log ψ_{12} versus log $\dot{\gamma}$ for the monodisperse polymers also appears to approach a limiting line. As has often been reported, η and ψ_{12} for polydisperse samples deviate from Newtonian behavior at lower shear rates than is the case for the monodisperse samples. The same data are replotted in Figures 4–7 in the form log $(\eta - v_s\eta_s)/$

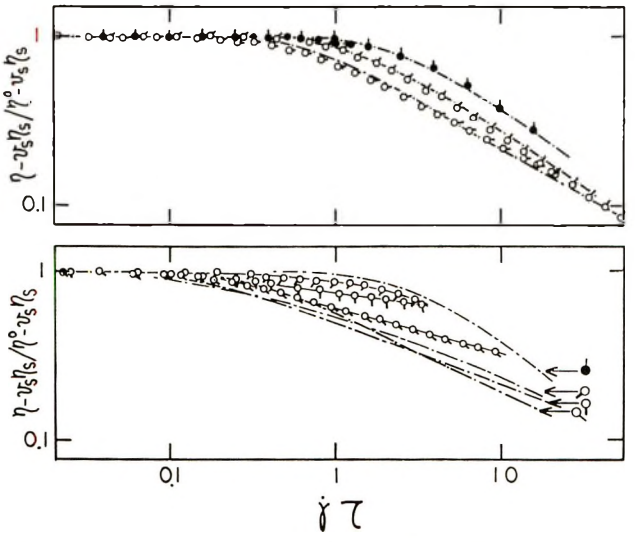

Fig. 7. Plots of log $(\eta - v_s\eta_s/\eta^\circ - v_s\eta_s)$ vs. log $\dot{\gamma}\tau$ for 7% solutions of blended samples: at various weight fractions W_2 of the higher molecular weight component: (●) 1.00; (○) 0.720; (○) 0.500; (○) 0.252; (○) 0.100; (○) 0.051; (●) 0. (●) Data on the monodisperse samples used for blending; (—·—) theoretical curves calculated from eq. (27) of ref. 15.

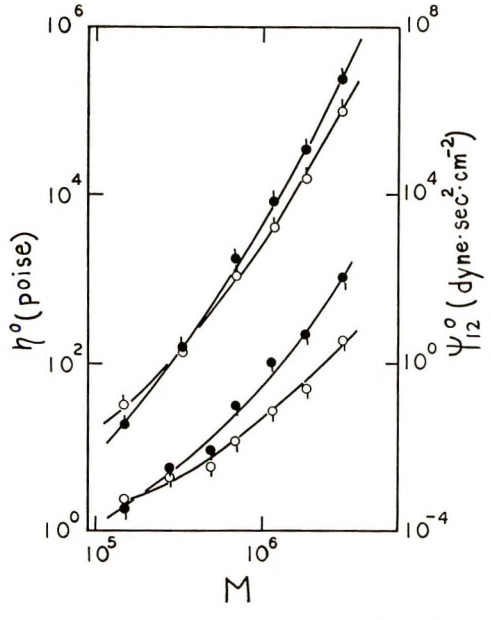

Fig. 8. Plots of (○) log η° and (●) log ψ_{12}° vs. log M for (○, ●) 7% solutions and (○, ●) 2% solutions of monodisperse samples.

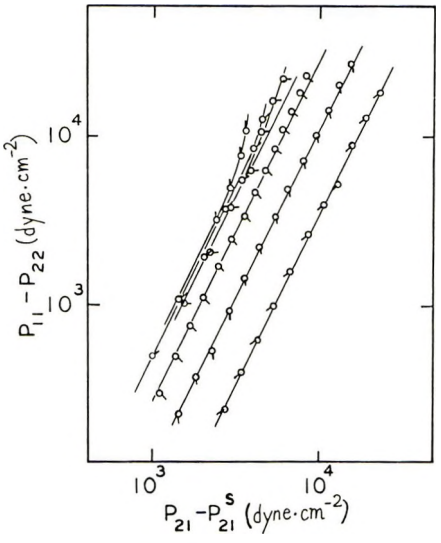

Fig. 9. Plots of log (P_{11}-P_{22}) vs. log (P_{21}-P_{21}^s) for 7% solutions of monodisperse samples. Symbols are the same as in Fig. 1.

($\eta^0 - v_s\eta_s$) or log ψ_{12}/ψ_{12}^0 vs. log $\dot{\gamma}\tau$, where η^0 and ψ_{12}^0 are the zero-shear viscosity and the normal stress coefficient, respectively, and τ is calculated from[16,17]

$$\tau = 12(\eta^0 - v_s\eta_s)M/\pi^2 cRT \tag{5}$$

Here, c is the concentration in g/cm^3, R is the gas constant, and T is the absolute temperature. It can be seen that the experimental data for 7% monodisperse polymer solutions fall approximately on a single curve. At lower concentrations, however, $(\eta - v_s\eta_s)/(\eta^0 - v_s\eta_s)$ does not form a single curve as can be seen in Figure 5, though the departure from Newtonian flow occurs at approximately the same value of $\dot{\gamma}\tau$ in each case. Examples of plots of log $(\eta - v_s\eta_s)/(\eta^0 - v_s\eta_s)$ and log ψ_{12}/ψ_{12}^0 versus log $\dot{\gamma}\tau$ at different concentrations for the sample of molecular weight 1.82×10^6 (PαS-12) are shown in Figure 6. At concentration as high as 7%, the observed values become almost independent of concentration. From the plot in Figure 7, it can be seen that $(\eta - v_s\eta_s)/(\eta^0 - v_s\eta_s)$ deviates from Newtonian behavior at lower values of $\dot{\gamma}\tau$ for polydisperse polymers than for monodisperse samples.

In Figure 8, log η^0 and log ψ_{12}^0 obtained at the limit of zero shear rate in Figure 2 are plotted against log M for both 2% and 7% solutions. If the concentration is low, η^0 must be proportional to M^α, α being a constant between 0.5 and unity. As the concentration increases, however, it is well known that the viscosity is determined by entanglements between polymer coils so that η^0 becomes proportional to $M^{3.5}$. In Figure 8, we can see that a 2% solution is not concentrated enough for the viscosity to be dominated by entanglements. At 7% concentration, the exponent is about 3, and the

proportionality of η^0 to $M^{3.5}$ can be observed only when M is higher than 10.[6] Strictly speaking, therefore, even a concentration of 7% may not be quite high enough, but, this does not affect our remaining discussion. The normal-stress coefficient $\psi_{12}{}^0$ in 7% solutions is found to be proportional to M^8 in the limit of high molecular weight.

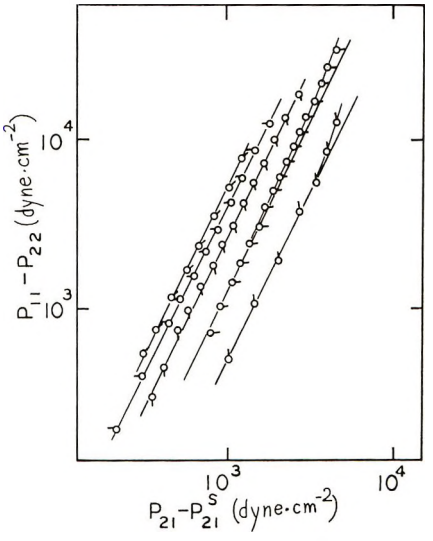

Fig. 10. Plots of log (P_{11}-P_{12}) vs. log (P_{21}-$P_{21}{}^s$) for solutions of various concentrations of a monodisperse sample with $M = 1.82 \times 10^6$. Symbols are the same as in Fig. 6.

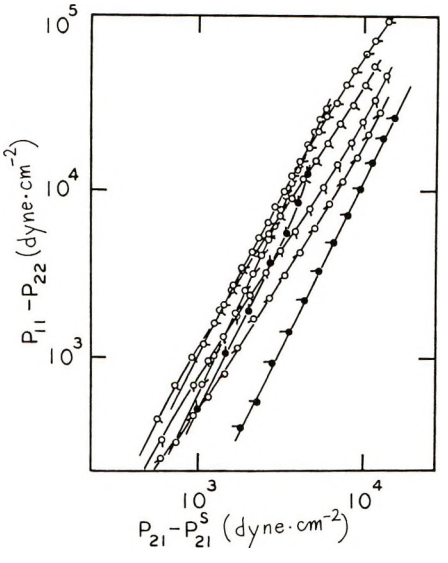

Fig. 11. Plots of log (P_{11}-P_{22}) vs. log (P_{21}-$P_{21}{}^s$) for 7% solutions of blended samples. Symbols are the same as in Fig. 7.

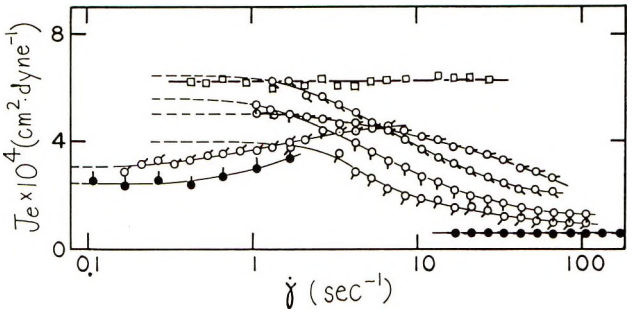

Fig. 12. Plots of J_e vs. log $\dot{\gamma}$ for 7% solutions of blended samples: (□) blend of samples PαS-3 and PαS-12; other symbols are the same as in Fig. 7.

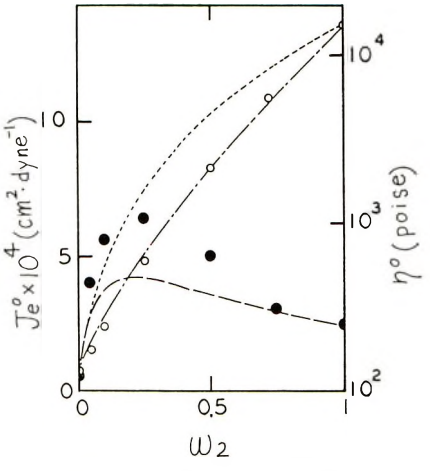

Fig. 13. Plots of (○) η° and (●) log J_e° vs. W_2 for 7% solutions of blended samples: (–·–) calculated from eq. (9);[18] (– –) calculated from eq. (8);[19] (---) calculated from eq. (10).[14,15]

The data in Figure 1 are replotted in the form of log $(P_{11} - P_{22})$ versus log $(P_{21} - P_{21}^s)$ in Figure 9. Figures 10 and 11 show similar plots for monodisperse samples at various concentrations and for blended samples at 7%. It can be seen that experimental plots generally give a straight line with slope 2. However, it is to be pointed out that the plots for monodisperse samples of high molecular weight show an upward deviation from the straight lines as the shear rate increases, whereas the plots for blended samples show a downward deviation. In practice, the slopes for blended samples appear to be lower than 2. The deviation can be observed more easily at high concentration.

From the data in Figures 9–11, J_e can be calculated by using eq. (4). Since the data for monodisperse samples in Figure 9 show only upward deviations from the straight lines, it is clear that J_e for monodisperse samples is a constant or increases with $\dot{\gamma}$. Therefore, it may be enough for us to show two examples of J_e for monodisperse samples in Figure 12 in relation to

the behavior of blended samples. In Figure 12, J_e for blended samples calculated by the same method are semilogarithmically plotted against log $\dot{\gamma}$. It is important to note that J_e decreases with $\dot{\gamma}$ for blended samples, whereas J_e for monodisperse samples increases. One blended sample still shows an increase in J_e with $\dot{\gamma}$, but this may be due to the low content of low molecular weight component. If either the molecular weight or concentration is low, J_e is a constant independent of $\dot{\gamma}$, but we expect that it would change if we could make measurements at higher shear rates. Besides, in a 50/50 blend of the two monodisperse samples of molecular weight 1.82×10^6 (PαS-12) and 1.42×10^5 (PαS-3), J_e did not show a $\dot{\gamma}$ dependence in our experimental range of shear rate, as is shown in Figure 12.

For the blended samples, the zero-shear viscosity η^0 and zero-shear steady-state compliance J_e^0 are shown in Figure 13. The values of η^0 for blended samples always lie between the values of η^0 for pure components,

TABLE III
η^0 and J_e^0 for 2% Solutions of Monodisperse Samples

Sample	η^0, poise	$J_e^0 \times 10^4$, cm²/dyne
PαS-3	2.44	0.580
PαS-4-2	4.40	1.10
PαS-6	5.90	1.60
PαS-7	12.4	3.60
PαS-10	28.2	6.75
PαS-12	50.8	9.50
PαS-13	188	17.5

TABLE IV
η^0 and J_e^0 for 7% Solutions of Monodisperse Samples

Sample	$\eta^0 \times 10^{-3}$, poise	$J_e^0 \times 10^4$, cm²/dyne
PαS-3	0.0325	0.175
PαS-5′	0.134	0.580
PαS-7	1.10	1.40
PαS-9	4.10	2.15
PαS-12	15.3	2.50
PαS-13	103	2.80

TABLE V
η^0 and J_e^0 for Solutions of Various Concentrations of a Monodisperse Sample with $M = 2.65 \times 10^5$

Concentration, wt-%	$\eta^0 \times 10^{-1}$, poise	$J_e^0 \times 10^5$, cm²/dyne
0.802	0.161	103
1.66	0.340	14.3
3.50	1.28	8.00
6.99	10.0	5.15
8.09	16.8	5.00

TABLE VI
η^0 and J_e^0 for Solutions of Various Concentrations of a Monodisperse Sample with $M = 1.82 \times 10^6$

Concentration, wt-%	$\eta^0 \times 10^{-2}$, poise	$J_e^0 \times 10^4$, cm²/dyne
0.400	0.0260	26.0
0.801	0.0640	20.5
1.68	0.254	13.3
3.50	3.62	6.35
7.00	153	2.50

TABLE VII
η^0 and J_e^0 for 7% Solutions of Blended Samples

Sample	W_2	$\eta^0 \times 10^{-3}$, poise	$J_e^0 \times 10^4$, cm²/dyne
PαS-5′	0.000	0.134	0.580
B-1	0.051	0.176	3.75
B-2	0.100	0.243	5.60
B-3	0.252	0.600	7.45
B-4	0.500	2.17	5.00
B-5	0.720	5.60	2.90
PαS-12	1.000	15.3	2.50
B-6	0.500	1.43	6.20

whereas J_e^0 for blended samples exceeds the values of J_e^0 for both pure components and shows a maximum. This behavior of η^0 and J_e^0 for blended samples is in agreement with the results reported by other investigators.[18] The values of η^0 and J_e^0 for both monodisperse samples and blended samples are listed in Tables III–VII.

DISCUSSION

Effect of Molecular Heterogeneity on Zero-Shear Viscosity and Zero-Shear Steady-State Compliance J_e^0

If the polymer solution is so dilute that there is no intermolecular interaction between polymers, the viscosity of a blended sample at a constant concentration is given by the average of the viscosities of the components on a molar basis:

$$\eta_b^0 - v_s\eta_s = \sum_i (\eta_i^0 - v_s\eta_s)P(M_i) \tag{6}$$

where subscripts b and i indicate the blend and component i, respectively, and $P(M_i)$ indicates the number fraction of component i. If there is strong interaction between polymers, i.e., if the viscosity is determined by entanglements between polymer chains, η_b cannot be given by such a simple relationship as eq. (6). Ferry presented the following equations based on his

discussion of the relaxation spectrum of a mixture of two monodisperse polymers.[19]

$$\eta_b^0 = w_1\eta_1^0\zeta_{0b}/\zeta_{01} + w_2\eta_2^0\zeta_{0b}/\zeta_{02} \tag{7}$$

$$J_{eb}^0 = w_1J_{e1}^0(M_1/M_w)^2 + w_2J_{e2}^0(M_2/M_w)^2 \tag{8}$$

Here ζ_0 is the translational friction coefficient per monomer unit and w_i is the weight fraction of component i. As we cannot calculate η_b^0 directly from eq. (7), while J_{eb}^0 can be calculated from eq. (8) without arbitrary constants, we compare our experimental data on η_b^0 with the equation

$$\eta_b^0 = D(\eta_1^0)^{v_1}(\eta_2^0)^{v_2}[1 + v_2(N_{21} - 1)]/N_{21}^{v_2} \tag{9}$$

where v indicates the volume fraction of each component polymer. Equation (9) was obtained from eq. (7) and includes two arbitrary constants, N_{21} and D.[18] In Figure 13, the chain line denotes the values of η_b^0 calculated from eq. (9) with $D = 1$ and $N_{21} = 7.05$, values chosen to give the best fit to the experimental data and with v replaced by w. Agreement between theory and experiments is satisfactory.

Calculated values of J_{eb}^0 from eq. (8) are shown in Figure 13 by the broken line. Thus, eq. (8) does explain the experimental results qualitatively. It is to be stressed that J_{eb}^0 calculated from eq. (8) has its maximum value at about the same value of w_2 as is found experimentally. However, the quantitative agreement is not satisfactory.

Graessley [eq. (21) in ref. 15] presented the relation

$$\eta_b^0 = [\sum_i \eta_i^0 P(M_i)](M_w/M_n) \tag{10}$$

This equation is found not to give good agreement with the observed values of η_b^0 as can be seen in Figure 13.

Normal Stress Coefficient at Zero Shear Rate

A molecular theory[20] expresses the relation between the shear stress and the normal stress difference by

$$(P_{11} - P_{22})/(P_{21} - P_{21}^s)^2 = \gamma M/cRT \tag{11}$$

where γ is a constant, the value of which is 0.8 for free-draining molecules and 0.4 for nondraining molecules.[20] Thus, from eqs. (1), (2), and (11), we have

$$\psi_{12}^0 = \gamma M(\eta - v_s\eta_s)^2/cRT \tag{12}$$

These equations were originally derived for dilute polymer solutions. According to Ferry[19] and Bueche,[21] however, they can also be applied to concentrated polymer solutions though an effective frictional coefficient of a monomer in concentrated solutions is different from that in dilute solutions. Concerning the molecular weight in eqs. (11) and (12), Ferry

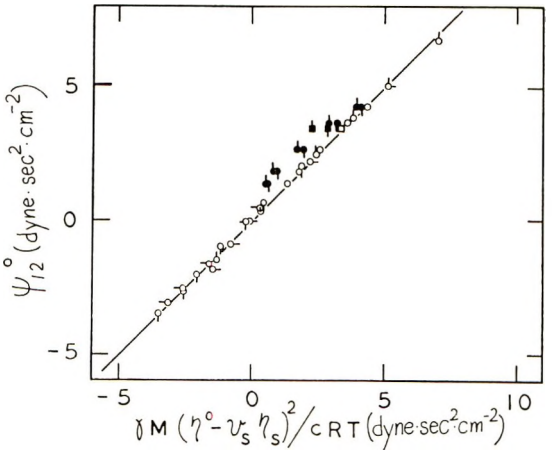

Fig. 14. Plots of log ψ_{12}° vs. log $\gamma M(\eta^{\circ}-v_s\eta_s)^2/cRT$ for all samples: (Ⓞ) 7% solutions of monodisperse samples; (Ⓠ) 2% solutions of monodisperse samples; (O-) solutions of various concentrations of monodisperse sample with $M = 1.82 \times 10^6$; (-O) solutions of various concentrations of monodisperse sample with $M = 2.65 \times 10^5$; (○) 7% solutions of blended samples of two monodisperse samples with $M = 1.82 \times 10^6$ and $M = 3.32 \times 10^5$ [calculated with $M = M_{z+1}M_z/M_w$ in eq. (12)]; (□) 7% solution of a blended sample of two monodisperse samples with $M = 1.82 \times 10^6$ and $M = 1.46 \times 10^5$ [calculated with $M = M_{z+1}M_z/M_w$ in eq. (12)]; (●) 7% solutions of blended samples corresponding to (○) [calculated with $M = \bar{M}_n$ (pip up) and $M = M_w$ (pip down) in eq. (12)]; (■) 7% solution of a blended sample corresponding to (□) [calculated with $M = \bar{M}_n$ (pip up) and $M = \bar{M}_w$ (pip down) in eq. (12)]; (——) theoretical relation.

pointed out[19] on the basis of the Rouse theory that for heterogeneous samples M should be taken as

$$M = M_{z+1}M_z/M_w \tag{13}$$

In his textbook, Middleman collected published data on ψ_{12}^0 and compared them with eq. (12) by using the weight-average or viscosity-average molecular weight.[22] These data, however, deviate from the theoretical line by more than one decade in log ψ_{12}^0 and scatter, mainly on the left side of the theoretical line. According to Middleman,[22] the reason for the scattering of these data is not absolutely clear but might mostly be due to polymer heterogeneity. The values of ψ_{12}^0 for our present samples can be estimated from the data at the limit of zero shear rate in Figures 2 and 3. Since the plot of log $(P_{11} - P_{22})$ versus log $(P_{21} - P_{21}^s)$ has a slope of 2.0 over a wide range of $\dot{\gamma}$, as is shown in Figures 9–11, and η^0 can easily be established, as in Figures 2 and 3, we can estimate the limiting values of ψ_{12}^0 from these data. The estimated values appear to be reasonable. They are plotted against $\gamma M(\eta^0 - v_s\eta_s)^2/cRT$ in Figure 14, assuming $\gamma = 0.8$. The molecular weight defined by eq. (13) is used for blended samples. As demanded by eq. (12), the plot of the data defines a good straight line of unit slope through ten decades. If we use M_n or M_w in eq. (12), however, the plots for blended samples are far from the theoretical prediction as shown

by black points in Figure 14. Therefore, considering that the samples cited by Middleman may have broad molecular weight distributions, we may conclude that the scattering of experimental data is mainly attributable to polydispersity of the polymers studied, as Middleman speculated. Thus, the modified molecular theories of Rouse[16] and Zimm[17] can predict the limiting behavior of linear polymer solutions under steady shear flow rather well. However, even if we define the molecular weight for blended samples by eq. (13), the agreement between the molecular theory and the experimental results may not be perfect. The deviation of the data for blended polymers from the theoretical line found in Figure 14 is amplified in Figure 13. However, it is to be pointed out that the theories of Rouse[16] and Zimm[17] cannot give the shear-rate dependence of ψ_{12} and η.

Shear-Rate Dependence of η and ψ_{12}

Middleman[22] also compared the published data and the Bueche[23] theory of non-Newtonian viscosity of molten polymer and concentrated polymer solutions. Comparison of our experimental results and that theory is given in Figure 4. As pointed out by Middleman, agreement is qualitatively good but, quantitatively is not satisfactory despite the fact that our samples are highly monodisperse.

A quite understandable idea about the dependence of entanglement density on shear rate was recently presented by Graessley.[14,15] In Figure 4, the values calculated from Graessley's theory[15] are indicated by a chain curve with the horizontal position determined so as to give the best fit to our experimental data. Agreement between the theory and our experimental results is quite satisfactory. In particular, as $\dot{\gamma}$ increases, all curves in Figure 2 approach a limiting line with the slope of about -0.8 as Graessley predicted.[14,15]

The effect of molecular weight distribution on non-Newtonian viscosity has also been studied by Graessley[15] and Middleman.[22] According to Middleman, even for the viscosity at high shear rate, the shear rate dependence of η_b of a polydisperse polymer is expressed by

$$\frac{\eta_b - v_s\eta_s}{\eta_b^0 - v_s\eta_s} = \sum_i M_i^2 \left(\frac{\eta_i - v_s\eta_s}{\eta_i^0 - v_s\eta_s}\right) P(M_i)/M_w M_n \qquad (14)$$

Comparison of this equation with the present experimental data shows that the contribution of the component of higher molecular weight is overestimated; that is, the calculated decrease in η_b with $\dot{\gamma}$ is much steeper than is observed. An example is shown in Fig. 2b.

On the basis of his entanglement mechanism, Graessley derived a complicated expression for the non-Newtonian viscosity of a polydisperse sample. Following his suggestions for determining the parameters and functions $\theta(\dot{\gamma},n)$, $h(\dot{\gamma},n)$ and $g(\dot{\gamma},n)$, we can obtain $\eta_b - v_s\eta_s/\eta_b^0 - v_s\eta_s$ as a function of $\dot{\gamma}\tau$. Calculated values are shown in Figure 7 for comparison with the observed values. When the amount of the higher molecular weight compo-

nent is greater than 50%, agreement between the calculated values and the experimental values is splendid, but, when the amount of the lower molecular weight component is higher, agreement is qualitative but not completely satisfactory. The reason for the unsatisfactory agreement might be due to formation of an insufficient number of entanglements in the low molecular weight sample at 7% concentration.

As cited by Middleman, ψ_{12}/ψ_{12}^0 decreases with $\dot{\gamma}$ twice as rapidly as $\eta - v_s\eta_s/\eta^0 - v_s\eta_s$ at low shear rate. At high shear rate, however, this relation between ψ_{12}/ψ_{12}^0 and $\eta - v_s\eta_s/\eta^0 - v_s\eta_s$ does not hold, since J_e also depends on $\dot{\gamma}$. The shear-rate dependence of J_e can be more easily understood on a molecular basis than that of ψ_{12} and is discussed below.

Shear-Rate Dependence of J_e

The many phenomenological theories concerning the $\dot{\gamma}$ dependence of J_e have been summarized by Spriggs et al.[24] White and Metzner[25] derived J_e independent of $\dot{\gamma}$, while Spriggs[26] predicted J_e to decrease as $\dot{\gamma}$ increases. On the other hand, Tanner[27] predicted J_e to increase as $\dot{\gamma}$ increases. Williams and Bird[28] predicted a dependence of J_e on $\dot{\gamma}$ that is greatly affected by the choice of parameters. Williams also derived a $\dot{\gamma}$-dependent J_e.[29] In most experiments so far reported, J_e was found to be either independent of or to decrease with $\dot{\gamma}$.[24,30] However, the recent data of Graessley and Segel[31] show that J_1 increases with $\dot{\gamma}$ for monodisperse polymers, whereas J_e decreases with $\dot{\gamma}$ if the sample has a broad molecular weight distribution. In our experiments, too, all three types of the behavior of J_e (independent of $\dot{\gamma}$, increasing and decreasing with $\dot{\gamma}$) are observed. For monodisperse polymers, J_e is independent of $\dot{\gamma}$ or increases with $\dot{\gamma}$ at high shear rates if either the molecular weight or the concentration is high. For blended samples, however, we can see that J_e is a decreasing function of $\dot{\gamma}$ except for one sample. Thus, our results agree with those of Graessley but cannot be explained by any of the continuum theories cited above.

Recently, Tanaka et al.[32] published an interesting paper in which the $\dot{\gamma}$ dependence of J_e is interpreted in terms of the shape of the relaxation time spectrum $H(\tau)$ and its variation with shear rate. That is, the $\dot{\gamma}$ dependence of J_e is mainly determined by the slope of the plot of $\log H(\tau)$ versus $\log \tau$ at the long-relaxation-time end of the relaxation spectrum. They conclude that J_e will increase with $\dot{\gamma}$ if the slope is higher than $-1/2$, but will decrease with $\dot{\gamma}$ if the slope is less than $-1/2$. In practice, the relaxation-time spectrum for monodisperse polymers is of the box type with a slope higher than $-1/2$.[33,34] It is expected, moreover, that the long-time end of the relaxation time spectrum is changed by mixing two monodisperse samples of different molecular weights and may become more flat.[33] Presumably, considering these experimental facts, Tanaka et al. speculated that J_e would increase with $\dot{\gamma}$ if the polymer is monodisperse, whereas J_e would decrease with $\dot{\gamma}$ if the polymer is polydisperse. Their speculation is well supported by our experimental results. The polydisperse sample that shows an increasing J_e

with $\dot{\gamma}$ in Figure 12 may still have a box-type relaxation spectrum because it contains only a slight amount of the low molecular weight component.

Thus, we may conclude that the shear-rate dependence of J_e is greatly affected by molecular weight distribution and the effect of molecular weight distribution may be interpreted in terms of the relaxation time spectrum, as Tanaka et al. predicted. However, it should be added that the variation in the relaxation spectrum may be affected by other factors, and the molecular weight distribution may not be the only reason for such complicated changes in J_e with $\dot{\gamma}$.[35]

This work was motivated by the work of Professor Misazo Yamamoto and his co-workers. We wish to thank Professor Yamamoto for his continued advice and discussions, and also Mr. Mototsugu Sakai for his helpful discussions.

References

1. B. D. Coleman and H. Markovitz, *J. Appl. Phys.*, **35**, 1 (1964).
2. T. Fujimoto, N. Ozaki, and M. Nagasawa, *J. Polym. Sci. A*, **3**, 2259 (1965).
3. A. Yamamoto, I. Noda, and M. Nagasawa, *Polym. J.*, **1**, 304 (1970).
4. A. Soda, T. Fujimoto, and M. Nagasawa, *J. Phys. Chem.*, **71**, 4274 (1967).
5. I. Noda, Y. Yamada, and M. Nagasawa, *J. Phys. Chem.*, **72**, 2890 (1968).
6. I. Noda, S. Saito, T. Fujimoto, and M. Nagasawa, *J. Phys. Chem.*, **71**, 4048 (1967).
7. T. Kato, K. Miyaso, and M. Nagasawa, *J. Phys. Chem.*, **72**, 2161 (1968).
8. A. Jobling and J. E. Roberts, *Weissenberg Rheogoniometer Instruction Manual*, Sangamo Controls Ltd., Bogner Regis, England.
9. K. Weissenberg, *Testing of Materials by Means of the Rheogoniometer*, Sangamo Controls Ltd., Bogner Regis, England.
10. A. Jobling and J. E. Roberts, in *Rheology—Theory and Applications*, F. R. Eirich, Ed., Vol. II, Academic Press, New York, 1958, Chap. 13.
11. H. Endo and M. Nagasawa, *J. Polym. Sci. A-2*, **8**, 371 (1970).
12. R. A. Stratton, *J. Colloid Interface Sci.*, **22**, 517 (1966).
13. D. P. Wymann and L. J. Elyash, *J. Polym. Sci. A*, **3**, 681 (1965).
14. W. W. Graessley, *J. Chem. Phys.*, **43**, 2696 (1965).
15. W. W. Graessley, *J. Chem. Phys.*, **47**, 1942 (1967).
16. P. E. Rouse, *J. Chem. Phys.*, **21**, 1272 (1953).
17. B. Zimm, *J. Chem. Phys.*, **24**, 269 (1956).
18. K. Ninomiya, J. D. Ferry, and Y. Oyanagi, *J. Phys. Chem.*, **67**, 2297 (1963).
19. J. D. Ferry, *Viscoelastic Properties of Polymers*, Wiley, New York, 1961.
20. M. C. Williams, *J. Chem. Phys.*, **42**, 2988 (1965).
21. F. Bueche, *Physical Properties of Polymers*, Interscience, New York, 1962.
22. S. Middleman, *The Flow of High Polymers*, Interscience, New York–London, 1968.
23. F. Bueche, *J. Chem. Phys.*, **22**, 1570 (1954).
24. T. W. Spriggs, J. D. Huppler, and R. B. Bird, *Trans. Soc. Rheol.*, **10**:**1**, 191 (1966).
25. J. L. White and A. B. Metzner, *J. Polym. Sci.*, **7**, 1867 (1963).
26. T. W. Spriggs, *Chem. Eng. Sci.*, **20**, 931 (1965).
27. R. I. Tanner, *ASLE Trans.*, **8**, 179 (1965).
28. M. C. Williams and R. B. Bird, *Phys. Fluids*, **5**, 1126 (1962).
29. M. C. Williams, *AIChE J.*, **13**, 955 (1967).
30. K. Osaki, *Kobunshi*, **17**, 497 (1968).
31. W. W. Graessley and L. Segel, *Macromolecules*, **2**, 49 (1969).

32. T. Tanaka, M. Yamamoto, and Y. Takano, *J. Macromol. Sci. (Phys.)*, in press.
33. A. V. Tobolsky, *Properties and Structure of Polymers*, Wiley, New York, 1960.
34. T. Fujimoto, N. Ozaki, and M. Nagasawa, *J. Polym. Sci. A-2*, **6**, 120 (1968).
35. M. Sakai and M. Nagasawa, to be published.

Received February 4, 1970
Revised August 24, 1970

JOURNAL OF POLYMER SCIENCE: PART A-2 VOL. 9, 363-368 (1971)

Dispersion and Polar Contributions to Surface Tension of Poly(methylene Oxide) and Na-Treated Polytetrafluoroethylene

D. H. KAELBLE and E. H. CIRLIN, *Science Center, North American Rockwell Corporation, Thousand Oaks, California 91360*

Synopsis

Average values for dispersion γ_s^d and polar γ_s^d contributions of the solid surface tension $\gamma_s = \gamma_s^d + \gamma_s^p$ for poly(methylene oxide) (PMO) and Na-treated polytetrafluoroethylene (PTFE) are determined by a new computational analysis of wettability data. PMO displays $\gamma_s^d = 21.8 \pm 0.9$ and $\gamma_s^p = 11.5 \pm 1.5$ dyn/cm while Na-treated PTFE displays $\gamma_s^d = 36.1 \pm 3.0$ and $\gamma_s^p = 14.5 \pm 2.9$ dyne/cm. These surfaces present the highest fractional surface polarity $p_s = \gamma_s^p/\gamma_s = 0.29$–$0.35$ yet encountered for organic polymers or oriented monolayers. These unusual surface tension properties are correlated with surface chemistry and adhesion phenomena.

A new computational method for analyzing wettability data has recently been reported[1] which defines average values of the (London) dispersion $\bar{\gamma}_s^d$ and (Keesom) polar $\bar{\gamma}_s^p$ components of the surface tension $\bar{\gamma}_s = \bar{\gamma}_s^d + \bar{\gamma}_s^p$ of a solid. This method augments or replaces the standard graphical method of plotting the cosine of the contact angle θ versus liquid surface tension γ_L, and extrapolating to $\cos\theta = 1.0$ to determine the critical surface tension γ_c of the organic solid surface.[2] In order to further explore the value of the new computational analysis we have added more liquids with graduated values of γ_L^d and γ_L^p to the scheme of analysis and obtained new computed values of γ_s^d, γ_s^p and γ_s for polymer surfaces characterized by controlled variations in surface chemistry. Polyethylene (PE) and poly(methylene oxide) (PMO) represent one pair of polymers whose surface properties should reflect the replacement of nonpolar methylene by a polar ether oxygen in the main chain. Skived polytetrafluoroethylene (PTFE) and the sodium-treated surface of this polymer represent a second pair of surfaces whose dispersion-polar surface tension properties should shift because of the defluorination, graphitization, and possible attachment of polar carbonyl or hydroxyl groups produced by Na treatment.[3–5]

Literature values[6,7] of γ_L^d and γ_L^p for the eleven liquids utilized in the contact-angle measurements are tabulated in Table I. Contact-angle measurements were conducted at 22°C in the B-100 environmental chamber of the NRL contact angle apparatus (Rame-Hart, Inc., Mountain Lakes, N. J.) by use of the sessile-drop method with drop volume regulated

TABLE IA
Experimental Wettability Data for Nonpolar and Polar Polymer Surfaces[a]

Liquid	γ_L, dyne/cm	γ_L^d, dyne/cm	γ_L^p, dyne/cm	cos θ (measured) PE (Marlex 6009)	PMO (Delrin 500)	PTFE (Teflon)	Na-treated PTFE
Water	72.8	21.8	51.0	−0.225	0.284	−0.454	0.612
Glycerol	63.4	37.0	23.4	−0.009	0.399	−0.242	0.766
Formamide	58.2	39.5	18.7	0.165	0.508	−0.131	0.974
Diiodomethane	50.8	48.5	2.3	0.570	0.566	−0.018	0.906
α-Br-naphthalene	44.6	44.6	.0	0.755	0.358	0.250	0.937
Polyglycol E-200[b]	43.5	28.2	15.3	0.390	0.707	0.026	0.972
" 15-200[b]	36.6	26.0	10.6	0.669	0.839	0.165	0.975
" P-1200[b]	31.3	24.5	6.8	0.900	0.956	0.391	0.960
Hexadecane	27.6	27.6	.0	1.000		0.688	
Ethanol (abs.)[b]	22.6	17.1	5.5			0.776	
n-Heptane	20.3	20.3	.0			0.924	

[a] Data of Fowkes,[6] unless otherwise noted.
[b] Data of Dann.[7]

TABLE IB
Computed Solid Surface Tension Properties of Polar and Nonpolar Polymer Surfaces

Solid surface	Pair Calculations by eq. (1)	$\bar{\gamma}_s^d$, dyne/cm	$\bar{\gamma}_s^p$, dyne/cm	$\bar{\gamma}_s$, dyne/cm
PE (Marlex 6009)	24	30.9 ± 0.9	0.5 ± 0.1	31.4 ± 0.9
PMO (Delrin 500)	18	21.8 ± 0.9	11.5 ± 1.4	33.3 ± 1.0
PTFE (Teflon)	34	16.9 ± 0.7	1.1 ± 0.5	18.0 ± 0.6
Na-treated PTFE	18	36.1 ± 3.0	14.5 ± 2.9	50.6 ± 1.3

to 3.0 μl in order to eliminate gravitation effects. At least 10 contact angles were determined for each liquid-solid interaction with a normal reproducibility of $\pm 2°$ for θ. Table I summarizes the average value of cos θ obtained from these measurements. The polymer surfaces (1) polyethylene, (2) polymethylene oxide, and (3) skived polytetrafluoroethylene were obtained in film form from commercial sources and cleaned ultrasonically with Tide detergent in distilled water followed by copious washing in distilled water and drying. The clean surface of skived polytetrafluoroethylene was etched by immersion in Tetra-Etch (H. L. Gore & Associates, Inc., Newark, N. J.) a proprietary organic dispersion of sodium, for the few seconds required to develop uniform darkening of the surfaces. The surfaces were then rinsed with carbon tetrachloride and 3% HCl to remove organic and inorganic residue, followed by copious washing with distilled water, ultrasonic cleaning in Tide-water solution, water rinsing, and drying to produce solid surface (4).

Experimental values of work of adhesion obtained by use of the familiar Young equation, $W_a = \gamma_L(1 + \cos \theta)$, were analyzed in pairs by the determinant method already described[1] for all simple combinations that exceeded the test condition:

$$D = [(\gamma_L^d)_i(\gamma_L^p)_j]^{1/2} - [(\gamma_L^d)_j(\gamma_L^p)_i]^{1/2} \geq \pm 10$$

This test condition excludes liquid pairs which contribute linear dependence in the simultaneous solution of the following theoretical expressions for work of adhesion:

$$\left.\begin{aligned}(W_a/2)_i &= (\gamma_{Li}^d\gamma_s^d)^{1/2} + (\gamma_{Li}^p\gamma_s^p)^{1/2}\\ (W_a/2)_j &= (\gamma_{Lj}^d\gamma_s^d)^{1/2} + (\gamma_{Lj}^p\gamma_s^p)^{1/2}\end{aligned}\right\} \quad (1)$$

which form the basis of the computational analysis.

The number of applications of eq. (1) for mean values of $\bar{\gamma}_s^d$, $\bar{\gamma}_s^p$, and $\bar{\gamma}_s$ for each surface and the accompanying calculated standard deviations from the mean values are summarized in the lower portion of Table IB The calculated surface properties for PE and PTFE shown in Table I compare closely with those provided by previous calculations[1] based upon

wettability data of Fox and Zisman.[8] Table I and previous analyses[1] show that PE and PTFE display essentially nonpolar surface properties, where $\bar{\gamma}^d \approx \bar{\gamma}_s$, and the computed solid surface tension and the standard value for critical surface tension γ_c are comparable. The new data for PE and PTFE surfaces thus reconfirm previous estimates for surface tension properties.

The interesting new information developed by this study is displayed by PMO and sodium-treated PTFE. Table I shows that PMO displays a $\bar{\gamma}_s^d$ value 30% lower than that of PE. The fractional surface polarity $p = \bar{\gamma}_s^p/\bar{\gamma}_s$ for PE is $p = 0.016$, while for PMO $p = 0.346$, indicating strong polar contributions to surface interaction. The high ratio p(PMO)/p(PE) = 21.6 can be attributed to the exposed ether oxygens of the PMO main chain which act as strong proton acceptors in interfacial interactions with the hydrogen-bonding liquids of Table I. The total surface tensions $\bar{\gamma}_s = \bar{\gamma}_s^d + \bar{\gamma}_s^p$ for the two polymers differ by only 1.4 dyne/cm. Standard extrapolation of cos θ versus $\bar{\gamma}_L$ curves to cos $\theta = 1.0$ provides values of $\bar{\gamma}_l \approx \bar{\gamma}_s$ which are essentially equivalent for the two polymers and thus give no indication of the surface property differences clearly shown by the new computational analysis.

The surface property differences for PTFE and the sodium-treated surface of this polymer are also clearly illustrated through the computational analysis by eq. (1). Sodium-treated PTFE displays a 114% increase in $\bar{\gamma}_s^d$ over untreated PTFE and a fractional-surface-polarity ratio of p(Na-treated PTFE)/p(PTFE) = 6.2, which indicate a dramatic increase in polar contributions to surface interactions. Sodium-treated PTFE exhibits the highest value of total surface tension, $\bar{\gamma}_s = 50.3$ dyne/cm, of any polymer or oriented monolayer surface analyzed by the computational method. An analysis[1] by this method of wettability data of Schonhorn and Ryan[9] for a gold-nucleated PTFE surface showed surface properties ($\gamma_s^d = 36.3 \pm 1.2$, $\bar{\gamma}_s^p = 9.3 \pm 1.2$, $\bar{\gamma}_s = 45.6 \pm 0.8$) which approach but do not exceed those shown in Table I for Na-treated PTFE. Both gold-nucleated and Na-treated PTFE display strong polar contributions to surface tension, which evidently explain their strong bonding to polar epoxy resin adhesives.[2,3,9] The molecular processes for increasing the surface energy of gold-nucleated PTFE are ascribed to surface morphology,[9] while in Na-treated PTFE they are more clearly related to changes in surface chemistry.

The previous comprehensive analysis of 25 polymeric and oriented monolayer surfaces revealed consistent correlations between surface tension properties, as expressed by $\bar{\gamma}_s^d$ and $\bar{\gamma}_s^p$, and surface composition of organic solids.[1] This report reinforces and extends these surface-property and surface-chemistry correlations by including a more diverse group of wetting liquids. It is quite evident that the theory of interfacial interaction leading to eq. (1) accommodates hydrogen-bonded, polar, and nonpolar liquids and solids. The surface properties of water, alcohols, amides, aromatics, halogenated, and hydrocarbon liquids are successfully combined in a single scheme of analysis.

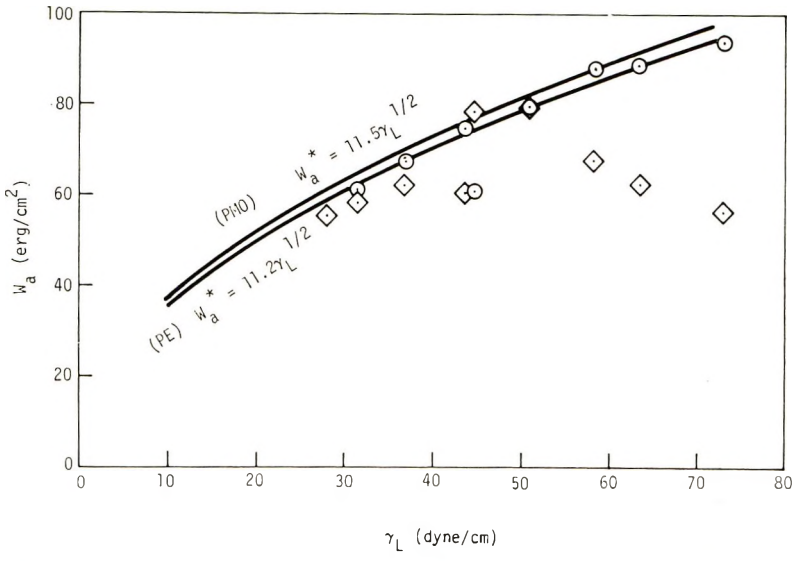

Fig. 1. Comparison of theoretical functions for maximum work of adhesion W_a^* vs. liquid surface tension γ_L with experimental values of W_a for (◊) PE and (⊙) PMO.

The general theory from which eq. (1) is obtained as a special case describes the interfacial work of adhesion by the relations (2) and (3):[10]

$$W_a = 2\Phi_{Ls}(\gamma_s\gamma_L)^{1/2} \tag{2}$$

where

$$\Phi_{Ls} = (d_L d_s)^{1/2} + (p_L p_s)^{1/2} + \Delta_{Ls} \tag{3}$$

Equation (3) describes the bonding efficiency factor Φ_{Ls} through dispersion ($d = \gamma^d/\gamma$) and polar ($p = \gamma^p/\gamma$) fractional contributions to surface tension and an excess term Δ_{Ls} which accounts for specific associative or chemical interactions not defined by generalized van der Waals forces. Equation (1) assumes that $\Delta_{Ls} = 0$ and represents a special case of eq. (2) for which the maximum value of bonding efficiency is $\Phi_{Ls} = 1.0$. A significant test of eq. (1) is obtained by plotting the function:

$$W_a^* = 2(\gamma_L\bar{\gamma}_s)^{1/2} \quad \Phi_{Ls} = 1.0 \tag{4}$$

against the experimental work of adhesion $W_a = \gamma_L(1 + \cos\theta)$ for the data of Table I.

The curves of Figure 1 illustrate the closely aligned functions W_a^* for PE ($2\bar{\gamma}_s^{1/2} = 11.2$) and for PMO ($2\bar{\gamma}_s^{1/2} = 11.5$). None of the experimental W_a values seriously exceed the predictions of eq. (4). The more widely separated curves of Figure 2 are defined by $2\bar{\gamma}_s^{1/2} = 8.48$ for PTFE and $2\bar{\gamma}_s^{1/2} = 14.24$ for Na-treated PTFE. Figure 2 shows no serious excess interaction with the possible exception of formamide on Na-treated PTFE. These figures reconfirm the applicability of eq. (1) in defining a broad range of liquid-solid interactions. The experimental values of W_a shown

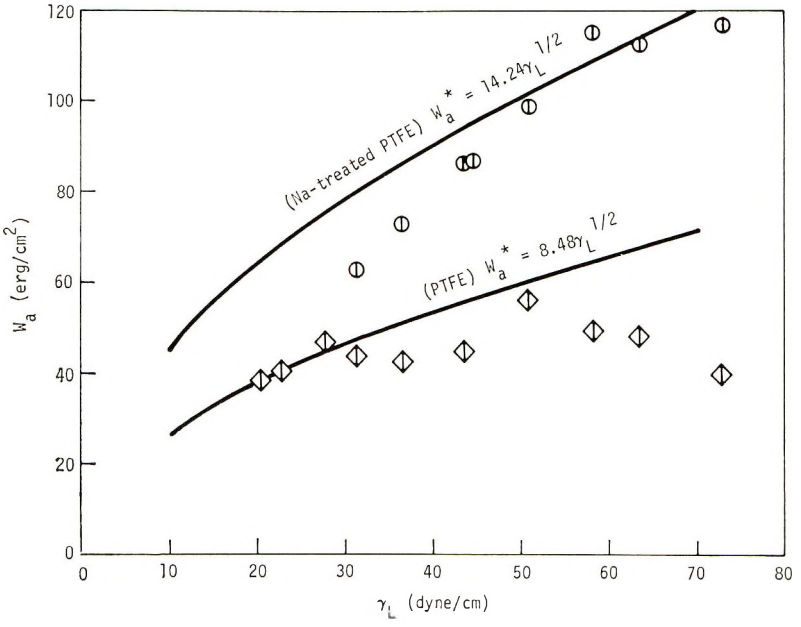

Fig. 2. Comparison of theoretical functions of W_a^* vs. γ_L with experimental values of W_a for (◊) PTFE and (⊕) Na-treated PTFE.

in Figure 1 for PE and Figure 2 for PTFE tend to follow a parabolic function due to the steady lowering of Φ_{Ls} below unity as the fractional polarity p_L of the liquids increases with γ_L.[1] Alternatively, the experimental data for W_a versus γ_L fail to display the parabolic form for PMO in Figure 1 and Na-treated PTFE in Figure 2, since polar interactions increase Φ_{Ls} toward unity as γ_L and p_L increase when the substrate surface is polar.

References

1. D. H. Kaelble, *J. Adhesion*, **2**, No. 2, 66 (1970).
2. W. A. Zisman, in *Adhesion and Cohesion*, P. Weiss, Ed., Elsevier, Amsterdam, 1962, p. 176.
3. A. A. Benderly, *J. Appl. Polym. Sci.*, **6**, 221 (1962).
4. V. P. Sanoilou and M. N. Kulygina, *Inst. Exp. Techniques*, **1963**, 994 (1963).
5. J. T. Martin, in *Adhesion and Adhesives*, Vol. 2, T. Houwink and G. Salomon, Eds., Elsevier, Amsterdam, pp. 95–96.
6. F. M. Fowkes, in *Treatise on Adhesion and Adhesives*, R. L. Patrick, Ed., Dekker, New York, 1967, Chap. 9.
7. J. R. Dann, *J. Colloid Interface Sci.*, **32**, 302 (1970).
8. H. W. Fox and W. A. Zisman, *J. Colloid Interface Sci.*, **5**, 514 (1950); *ibid.*, **7**, 428 (1952).
9. H. Schonhorn and F. W. Ryan, *J. Adhesion*, **1**, 43 (1969).
10. D. H. Kaelble, *Physical Chemistry of Adhesion*, Chap. 4, Interscience, New York, in press.

Received May 27, 1970
Revised August 17, 1970

JOURNAL OF POLYMER SCIENCE: PART A-2 VOL. 9, 369–372 (1971)

Annealing Effects and the α Relaxation in Drawn Polyethylene

C. P. BUCKLEY and N. G. McCRUM,
Department of Engineering Science,
University of Oxford, Oxford, England

Stachurski and Ward[1,2] have observed the α-relaxation in cold-drawn sheets of linear polyethylene (LPE) to consist of several, small, irregular relaxations, closely spaced together in the temperature region between 0°C and the melting point. This complex structure is taken by Stachurski and Ward[2] to be experimental support for the three α_c relaxation theories of Hoffman, Williams and Passaglia.[3] The purpose of the present note is to provide experimental evidence for a simpler interpretation of the data: in brief, it will be shown that the complex structure is an experimental artifact and does not support therefore the theories of Hoffman et al.

The theoretical premise of viscoelastic spectrometry is that temperature affects principally the relaxation time and, to a lesser extent, the limiting moduli. If the physical state of the specimen is changed, then the experimental results may not be interpreted within the framework of the theory of linear viscoelasticity. It is not possible under this circumstance to use the assumption of frequency–temperature equivalence. The experiments of Stachurski and Ward were performed on LPE specimens drawn at room temperature and not annealed: the measurements of mechanical loss, however, were taken at temperatures above room temperature. It is to be anticipated that annealing would commence as soon as the specimen was heated above room temperature and would accelerate as the temperature approached the melting point. The measured mechanical loss would thus be determined by the pattern of mechanical anisotropy of the original drawn specimen, and also by the effect of the complex thermal history encountered during the experiment. This interpretation of the results of Stachurski and Ward was confirmed by the following experiments. In the first experiment the conditions of Stachurski and Ward's experiment were reproduced to obtain multiple damping peaks. In the second experiment (which forms part of a wider study to be reported elsewhere) the effects of a controlled annealing schedule on both density and mechanical damping were studied.

A quenched sheet, $^1/_8$ in. thick, of LPE (Rigidex type 2) was drawn $\times 7$ at room temperature, at constant width, producing a voided sheet of high c-axis orientation of the crystallites. A torsion specimen was then cut with torsion axis parallel to the draw direction and experiments performed using

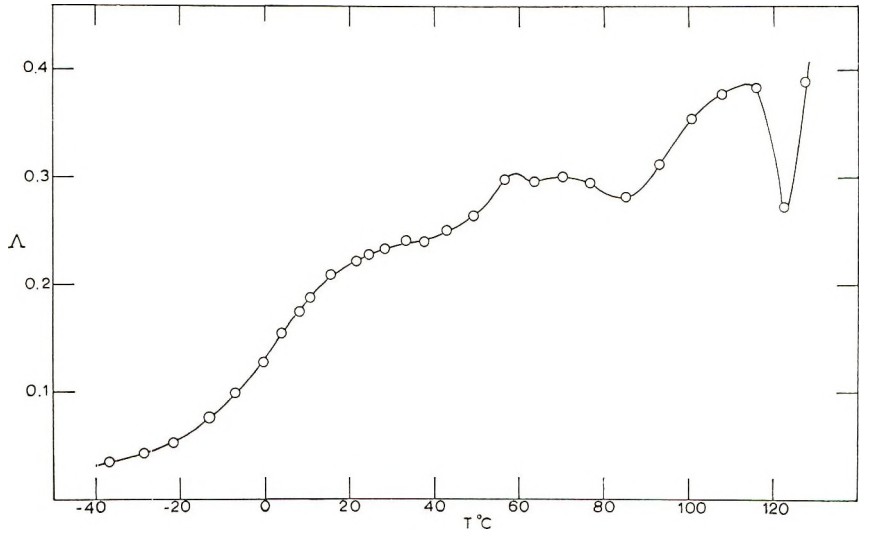

Fig. 1. Logarithmic decrement Λ vs. temperature T at a frequency of 0.67 Hz for specimen A of cold-drawn LPE (torsion axis parallel to draw direction).

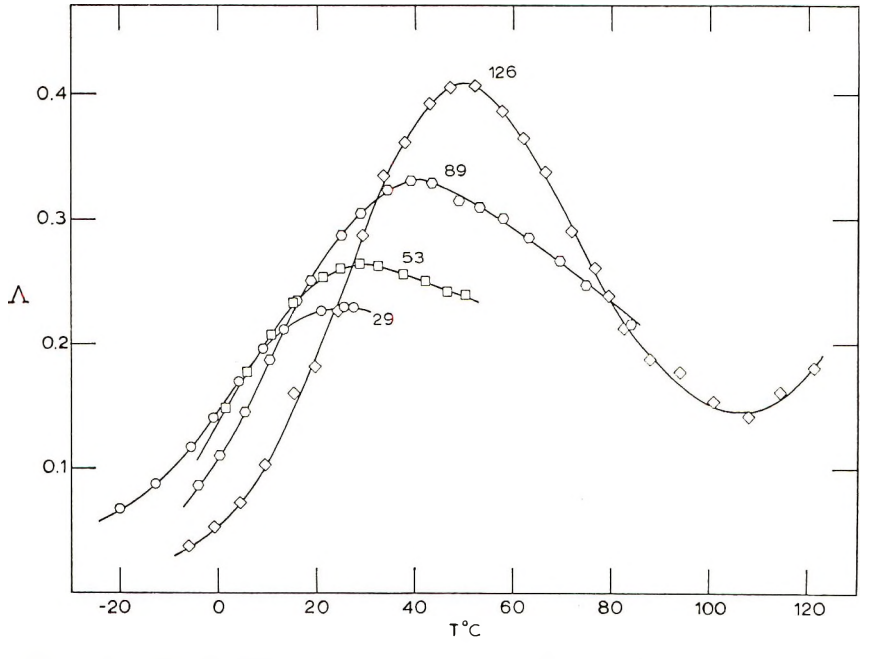

Fig. 2. Logarithmic decrement Λ vs. temperature T at a frequency of 0.67 Hz for specimen B of cold-drawn LPE (torsion axis parallel to draw direction) after annealing for 6 hr at the temperatures T_A as shown.

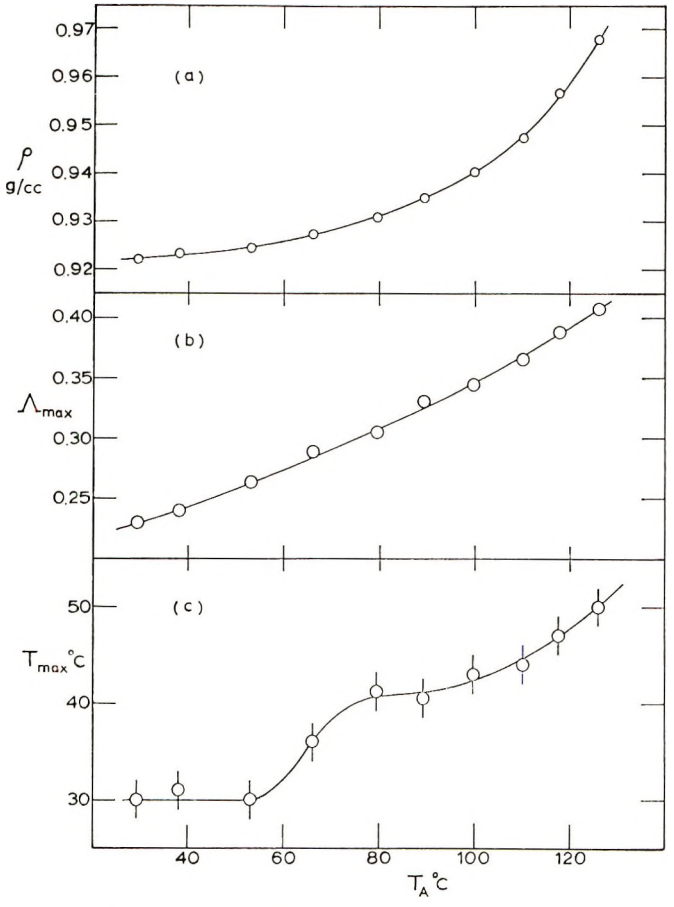

Fig. 3. Specimen B of cold-drawn LPE annealed at successively higher temperatures T_A for 6 hr: (*a*) density ρ g/cc (measured at 25°C) vs. T_A; (*b*) peak value Λ_{max} at the α peak, obtained from $\Lambda(T)$ plots at 0.67 Hz, vs. T_A; (*c*) temperature T_{max} of the α peak, obtained from $\Lambda(T)$ plots at 0.67 Hz, vs. T_A.

a torsion pendulum at a constant frequency of 0.67 ± 0.04 Hz. Specimen A, prepared in this way and having a density of 0.891 g/cc (at 25°C), was mounted in the pendulum and logarithmic decrement Λ recorded in the temperature range −40°C to 128°C. Above room temperature the time-temperature schedule is important. The temperature was raised in steps of between 5 and 8°C, between $^1/_2$ and 1 hr being allowed for the system to equilibrate at each new temperature. Results are shown in Figure 1, where the multiple peaks reported before[1,2] are in evidence. It is of note that during the course of this experiment the density increased to 0.956 g/cc (at 25°C) and the length decreased by 20%, with corresponding changes in thickness. Clearly the specimen underwent considerable recovery during the experiment.

Specimen B (prepared under the same conditions as specimen A) was

studied in experiments designed to discover the effects of controlled annealing upon the α-relaxation. It was mounted in the torsion pendulum and close to it in the thermal jacket of the pendulum was placed a dummy specimen cut from the same region of the drawn sheet. The pendulum was then heated to 29°C, maintained at that temperature for 6 hr to allow the specimen and dummy to anneal, and then cooled slowly to room temperature. The dummy specimen was removed from the pendulum, the density determined, and then replaced. Measurements of Λ were then obtained from −20°C up to temperatures slightly below the annealing temperature, 29°C. The pendulum was then heated to the second annealing temperature of 38°C and the above sequence repeated exactly. In this way experiments were performed for a set of ten annealing temperatures T_A between T_A = 29°C and T_A = 126°C. Representative data for four values of T_A are shown in Figure 2. It is noteworthy that for no value of T_A was there any evidence of multiple structure in the α peak. Features of the $\Lambda(T)$ curves and the density, as a function of T_A are summarized in Figure 3. It is clear that the properties considered here show drastic changes even for values as low as T_A = 29°C. With increasing annealing temperature, the single α peak increases in intensity and moves to higher temperatures. The density of the specimen (measured at 25°C) also increases systematically from 0.922 g/cc (T_A = 29°C) to 0.965 g/cc (T_A = 126°C). There can be no doubt that specimen A underwent comparable drastic changes during the experiment in which $\Lambda(T)$ was determined. For this reason it is clear that the multiple peaks shown in Figure 1 are an experimental artifact. This view is supported by previous results obtained on annealed drawn sheets of LPE, in which there is no sign of multiple peaks.[2,4]

It has long been recognized that thermal history is also significant in mechanical loss experiments in undrawn polyethylene.[5] In this case the most likely causes are annealing-induced changes in density (particularly significant in quenched specimens) and possibly also the removal of moulded in stresses. Another effect which must be considered is that of premelting. In drawn LPE annealed at 127.5°C for 168 hr the onset of premelting is observed in the region 70–90°C.[6] There can be therefore no simple interpretation of viscoelastic experiments even on well annealed, drawn LPE at temperatures in the region of 70–90°C and above.

This work was supported by the Science Research Council.

References

1. Z. H. Stachurski and I. M. Ward, *J. Polym. Sci. A-2*, **6**, 1083 (1968).
2. Z. H. Stachurski and I. M. Ward, *J. Macromol. Sci. (Phys.), B3*, 445 (1969).
3. J. D. Hoffman, G. Williams, and E. Passaglia, in *Transitions and Relaxations in Polymers* (*J. Polym. Sci. C*, **14**), R. F. Boyer, Ed., Interscience, New York, 1966, p. 173.
4. K. Oka and T. Kawaguchi, *Repts. Progr. Polym. Phys. Japan*, **9**, 385 (1966).
5. A. H. Willbourn, *Trans. Faraday Soc.* **54**, 717 (1958).
6. H. Goddar, G. F. Schmidt, and E. W. Fischer, *Makromol. Chem.*, **127**, 286 (1969).

Received July 10, 1970

JOURNAL OF POLYMER SCIENCE: PART A-2 VOL. 9, 373-375 (1971)

Intrinsic Viscosity of Polyelectrolytes in Salt Solutions

R. YEH and A. ISIHARA, *Statistical Physics Laboratory, Department of Physics and Astronomy, State University of New York, Buffalo, New York*

Synopsis

The dependence of the intrinsic viscosity of polyelectrolytes on the concentration of added salt is given satisfactorily by a formula obtained recently. A new viscosity–molecular weight relation gives satisfactory agreement with experiments.

The properties of dilute solutions of flexible chain polymers are determined by the distribution $W(r)$ of chain segments about the molecular center of gravity.[1,2] In the presence of excluded volume effects, however, the evaluation of the distribution function has been performed only to a first-order[3] approximation. Therefore, we have recently proposed a distribution function which expresses volume effects in a compact and satisfactory way.[4] It is given by

$$W(\mathbf{r}) = A(9/\pi Nb^2) \exp\left\{(9r^2/Nb^2)^{3/2} - (cNb^2z/4r^2)\right\} \tag{1}$$

where c is a parameter to be determined so as to produce the best agreement with experiments, N is the number of segments in a single polymer molecule, and z is defined by

$$z = (3/2\pi)^{3/2}(\beta/b^3)N^{1/2} \tag{2}$$

β denoting the excluded volume integral for disconnected segments and b the effective bond length. In the absence of an excluded-volume effect c is zero; in general it is supposed to be of the order of unity.

Like the distribution function proposed by Bueche, the above function enables us to evaluate some average distances in closed form.[4,5] As a result the intrinsic viscosity is given by

$$[\eta] = \frac{\pi Nab^2/6m}{1 + (6a/\pi^{1/2}b)N^{1/2}f(z)} \frac{1 + 3(cz)^{1/2} + 3cz}{1 + 3(cz)^{1/2}} \tag{3}$$

where

$$f(z) = \exp\{3(cz)^{1/2}\}[1 + 3(cz)^{1/2}]^{-1} \int_0^\infty \exp\{-y - (9cz/4y)\}\, dy \tag{4}$$

where a is the effective radius of the segments considered as spheres and m is the mass of a segment.

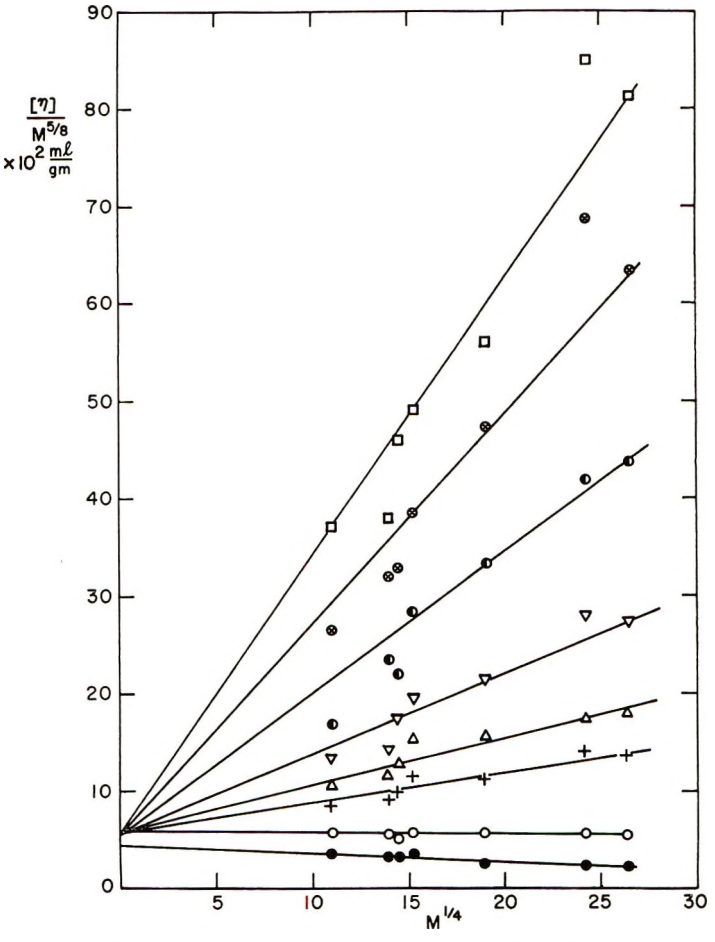

Fig. 1. Plots of $[\eta]/M^{5/8}$ vs. $M^{1/4}$ for sodium polyacrylate in sodium bromide solutions at 15°C at various values of c_s: (●) 1.506; (○) 0.502; (+) 1.00×10^{-1}; (△) 5.02×10^{-2}; (▽) 2.51×10^{-2}; (◐) 1.00×10^{-2}; (⊗) 5.02×10^{-3}; (□) 2.51×10^{-3}.

We note that $f(z)$ approaches unity when $z \ll 1$ and varies as $z^{-1/4}$ when $z \gg 1$. Making use of this property and the fact that β is defined for all segment interaction potentials, one can apply the above viscosity formula to polyelectrolyte solutions. For an intersegmental potential function $\phi(r) \propto e^{-\kappa r}/r$, with κ^{-1} denoting the thickness of the ion atmosphere, one can use κr as an integration variable for β. Thus, we have $\beta \propto \kappa^{-2}$, i.e., $\beta \propto c_s^{-1}$, where c_s is the concentration of added salt.

On the basis of these observations, let us now examine various special cases.

High Salt Concentration. In this case the screened Coulomb interaction is of very short range and behaves effectively like a hard-core interaction. Since z is small, eq. (3) implies that

$$[\eta]/M = A_1 + A_2 c_s^{-1} M^{1/2} \tag{5}$$

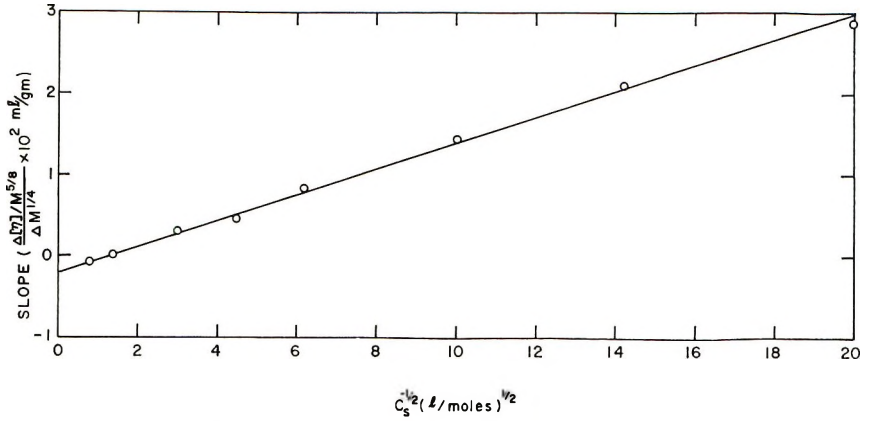

Fig. 2. Slopes of the straight lines in Fig. 1 plotted against $c_s^{-1/2}$.

where M is the molecular weight of the polymer; that is, the quantity $[\eta]/M$ is inversely proportional to the concentration of added salt. Such a dependence has been observed by experiments.

Low Salt Concentration. For low concentration of added salt, the Debye-Hueckel approximation is not valid. The dependence of $[\eta]$ on c_s is generally complicated.[6-8]

Intermediate Salt Concentration. Most experimental data fall in the range of intermediate c_s. In this range z is large, yet the screened Coulomb potential is of short range in comparison with the effective radius of the polymer. Equation (3) reduces to

$$[\eta]/M^{5/6} = K + Bc_s^{-1/2}M^{1/4} \tag{6}$$

Figure 1 compares this theoretical relation with the experimental data of Takahashi and Nagasawa.[9] As we see, the experimental points corresponding to the same concentration c_s fall on a straight line. From the intercept of the straight lines we find $K = 5.5 \times 10^2$ ml/g.

According to eq. (6) the slopes of such straight lines should be proportional to $c_s^{-1/2}$. This prediction is satisfactory, as Figure 2 shows. From this graph we find $B = 1.08 \times 10^{-2}$ (l.-mole)$^{1/2}$/g.

This work was supported by the National Science Foundation.

References

1. A. Isihara and E. Guth, *Fortschr. Hochpolym. Forsch.* **5**, 283 (1967).
2. A. Isihara, *Fortschr. Hochpolym. Forsch.*, **5**, 531 (1968).
3. R. Yeh and A. Isihara, *J. Chem. Phys.*, **51**, 1215 (1969).
4. R. Yeh and A. Isihara, *J. Polym. Sci. A-1*, **8**, 861 (1970).
5. F. Bueche, *J. Chem. Phys.*, **21**, 208 (1953).
6. Z. Alexandrowicz, *J. Chem. Phys.*, **47**, 377 (1967).
7. S. Imai, *J. Chem. Phys.*, **50**, 2107 (1969).
8. G. S. Manning, *J. Chem. Phys.*, **51**, 924 (1969).
9. A. Takahashi and M. Nagasawa, *J. Amer. Chem. Soc.*, **86**, 543 (1964).

Received July 16, 1970
Revised September 4, 1970

NOTES

Dispersion of Dilute Polymer Solution in Small-Diameter Tubing

Introduction

It has been shown[1] that the loss of resolution in gel-permeation chromatography and other liquid chromatographic separations depends to a large degree on dispersion of the solute in the connecting tubing. A recent study[2] of band broadening due to axial dispersion in small-diameter tubing showed that the elution curves of polystyrene solutions are not only highly unsymmetrical, but also exhibits an anomaly in the form of bimodal curves. This anomaly has also been observed by other investigators.[3]

In many cases, the anomaly has been observed for solutions of polystyrene of narrow molecular weight distribution ($\bar{M}_w/\bar{M}_n \approx 1.06$) flowing through a relatively short length of tubing (141–285 in.). Consequently, the possibility of molecular weight fractionation of the polystyrene solute in such a short tube is considered remote, as was pointed out by Yau et al.[4] An axial dispersion model[1] based on molecular diffusion and convection without solute intermolecular interaction yields elution curves which are either skewed or symmetrical and Gaussian, depending on the length of the tubing, flow rate, and molecular diffusivity of the solute. However, the model does not account for the bimodal elution curve observed for high molecular weight polystyrene.

It is our belief that the anomaly observed in the elution curve of high molecular weight polystyrene solution is due to solute intermolecular interaction (possibly entanglement),

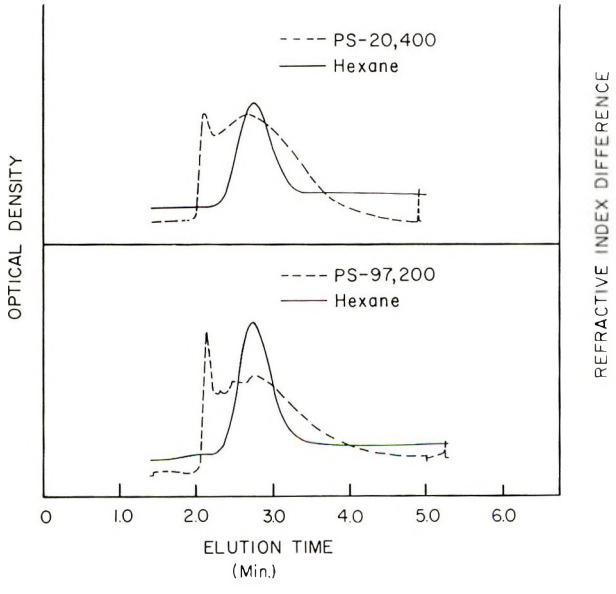

Fig. 1. Elution curves of hexane and polystyrene through Teflon tubing (146 in. long, 0.1 cm ID) at 1 ml/min flow rate: (--) ultraviolet optical density; (——) refractive index difference.

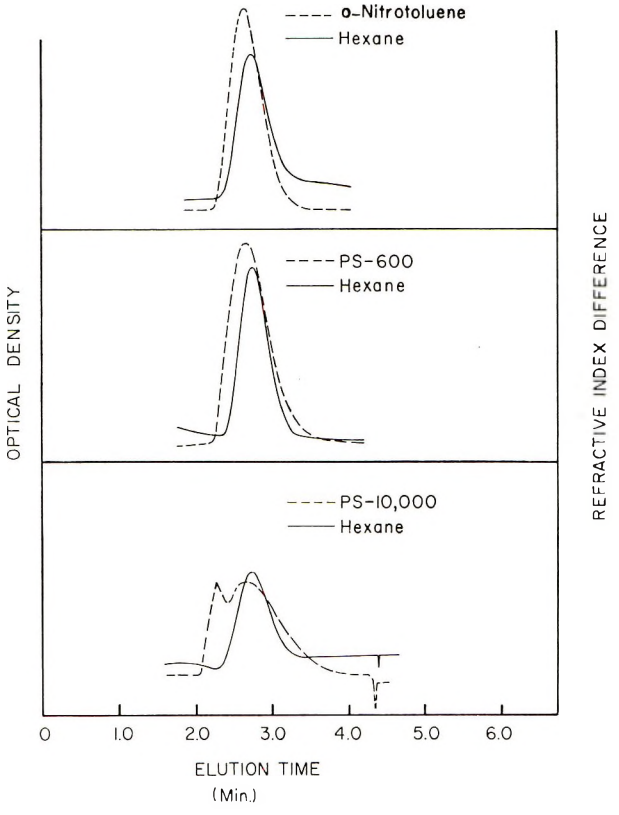

Fig. 2. Elution curves of hexane, *o*-nitrotoluene, and polystyrene through Teflon tubing (146 in. long, 0.1 cm ID) at 1 ml/min flow rate: (--) ultraviolet optical density, (——) refractive index difference.

and not a solution viscosity effect (sometimes referred to as "fingering"). Fingering should result in the distortion of the solution (solute and solvent) velocity profile, while solute intermolecular interaction is assumed to distort only the solute velocity profile. Simultaneous measurement of the elution of the solute and the solvent should clarify the cause of this anomaly. If bimodal elution curves are observed for both the solvent and solute, then fingering is likely to be the cause of the anomaly; if not, a difference between the velocity profiles of the solute and the solvent may perhaps be inferred. A two-detector system connected in series can be used effectively to measure independently the elution of both the solvent and the high molecular weight solute. These measurements should designate which of the two possibilities is correct.

Experimental

The principal equipment used was the DuPont Model 820 LC apparatus, modified by replacing the chromatographic column with either Teflon or stainless steel tubing, 146 in. long and 0.1 cm in ID. The main modification was done on the sample injection block, where the chromatographic column connector was replaced by a 5 cm × 0.64 cm OD brass tubing with an ID of 0.1 cm. Stainless steel tubing, 10 cm, 0.1 cm ID, was silver soldered to the 0.64 cm brass tubing to which the 146 in. of Teflon or stainless steel tubing being studied was connected.

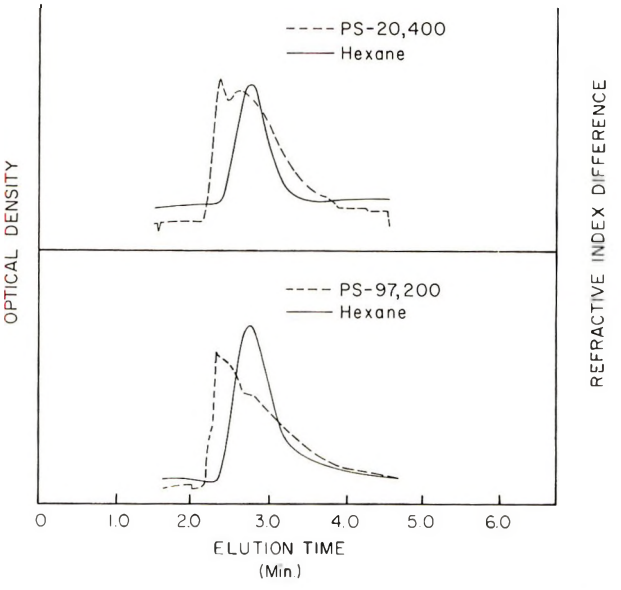

Fig. 3. Elution curve of hexane and polystyrene through stainless steel tubing (146 in. long, 0.1 cm ID) at 1 ml/min flow rate: (--) ultraviolet optical density; (——) refractive index difference.

A 254 nm ultraviolet photometer and a Fresnel type differential refractometer connected in series (the ultraviolet detector was ahead of the refractometer cell) were used as the detector system. The ultraviolet and refractometer cells had volumes of 7 and 3 μl, respectively. The volume of the connecting tubing between the ultraviolet photometer and refractometer was 60 μl. The solvent pump was of the "pulseless" type, and the sample injection system was of the septum type.

Polystyrenes (Pressure Chemical Co., $\bar{M}_w/\bar{M}_n$ 1.02–1.10) of 600, 10,000, 20,400, and 97,200 molecular weights and *o*-nitrotoluene were each dissolved in a 20:80 (by volume) hexane–chloroform solvent mixture to make 0.2% solutions. To prevent undissolved foreign matter from getting to the detector, the solutions were filtered through a sintered metal filter. Spectrophotometric grade *n*-hexane and chloroform (which are transparent to the ultraviolet at 254 nm) were used to minimize ultraviolet background absorption and interference with the monitoring of the solute elution. At the appropriate times, 4–6 μl of each solution was injected into the chloroform solvent stream. The solvent flow rate was maintained at 1 ml/min.

The elution of polystyrene was detected by changes in the ultraviolet absorbance of the solvent stream in the ultraviolet photometer cell with time. Hexane elution, on the other hand, was detected by the change in refractive index of the carrier solvent stream with time. Since the concentration of polystyrene in the solutions is very low (0.2%) relative to hexane (20%), the contribution of polystyrene to changes in refractive index of the solvent stream is negligible compared to that of hexane. The attenuation of the refractive index detector was adjusted high enough so that the signal fell within the bounds of the recorder chart. At this attenuation, the refractive index detector was insensitive to the polystyrene concentration in the solution.

Discussion of Results

Figure 1 shows the elution curve through the Teflon tubing of the 20,400 and 97,200 molecular weight polystyrene solutions along with the corresponding elution curve of the

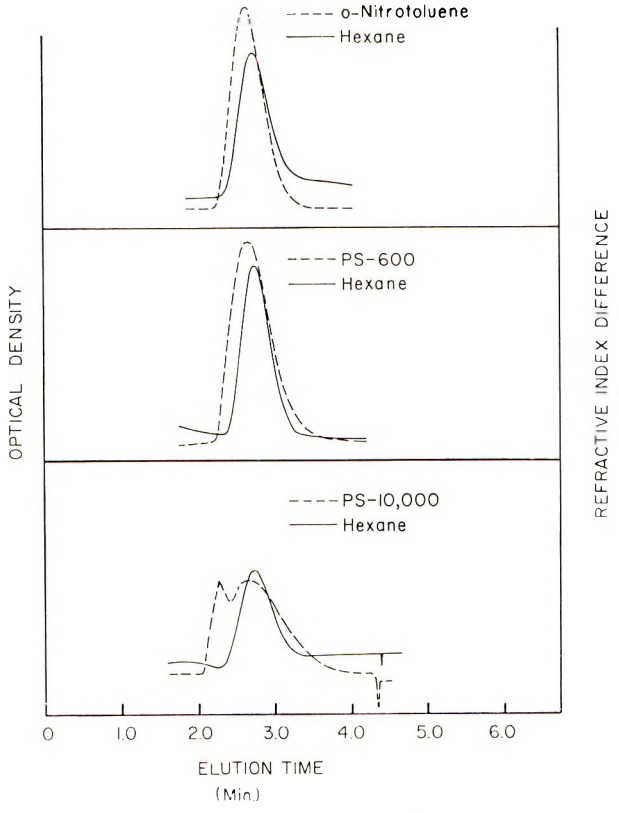

Fig. 4. Elution curves of hexane, *o*-nitrotoluene, and polystyrene through stainless steel tubing (146 in. long, 0.1 cm ID) at 1 ml/min flow rate: (--) ultraviolet optical density; (——) refractive index difference.

hexane solvent. It is evident that the bimodal anomaly occurs in the polystyrene elution, but not in the solvent elution. The hexane solvent curve approaches a Gaussian shape which agrees with the theoretical curve based on Taylor diffusion[5] in tubing.

The possibility of a malfunctioning ultraviolet photometer and cell, which can cause anomalies in the elution curve of polystyrene, was checked by substituting the high molecular weight polystyrene with *o*-nitrotoluene and with polystyrene of molecular weight 600. Figure 2 shows the elution curves of *o*-nitrotoluene and PS-600 to be free of the bimodal anomaly. This shows that the bimodal elution curve of the higher molecular weight polystyrene is not an artifact, but is highly dependent on the molecular weight of the solute.

Figures 3 and 4 show that essentially the same results were obtained for the elution of polystyrene and hexane through the stainless steel tubing. The main difference between the elution curves through the Teflon and stainless steel tubing is the tailing and skewness of the curve. A satisfactory explanation for the above difference in elution of polystyrene through stainless steel and Teflon tubing is presently not available. It could be attributed to differences in wettability of the Teflon and stainless steel tubing. This is, however, only a conjecture.

It is clear from Figures 1–4 that the shape of the elution curve of hexane is unaffected by the solute molecular weight and reflects Taylor's criteria for axial dispersion in laminar parabolic flow.[1,5] In contrast, the high molecular weight polystyrene elution curve is

bimodal with very sharp initial peak. This suggests a distortion in the velocity profile of the high molecular weight polymer solute. One can roughly deduce the shape of the polymer solute velocity profile from the shape of its elution curve. The very sharp initial peak of the polystyrene elution curve perhaps indicates a velocity profile which is "pluglike" near the tube axis with very sharp decrease in velocity near the tube wall. The above explanation of the very sharp initial peak of polystyrene elution curve seems to be reasonable when one considers that for a true plug flow with negligible molecular diffusion, a pulse input of solution into the mobile phase will result in a pulse response (no dispersion in the tubing) at the detector. This odd flow behavior of polymer solutes in the tubing is perhaps due to the low shear stress near the tube axis which can result in a higher probability for solute intermolecular entanglement than nearer the tubing wall where the shear stress is greatest. This explanation is of course mainly an interesting conjecture at this time.

The author wishes to extend special recognition to Professor Joseph Biesenberger whose ideas greatly contributed to this paper and Professor Costas Gogos and Dr. R. J. Gritter for their helpful suggestions.

References

1. J. A. Biesenberger and A. Ouano, *J. Appl. Polym. Sci.*, **14**, 471 (1970).
2. A. Ouano and J. A. Biesenberger, *J. Appl. Polym. Sci.*, **14**, 483 (1970).
3. F. Billmeyer and R. Kelley, *J. Chromog.*, **34**, 322 (1968).
4. W. W. Yau, C. Malone, and H. Suchan, paper presented at Symposium on GPC, American Chemical Society Meeting, Houston, Feb. 22, 1970.
5. G. I. Taylor, *Proc. Roy. Soc.* (London), **219A**, 186 (1953).

IBM Research Laboratory
San Jose, California 95114

AUGUSTUS C. OUANO

Received May 20, 1970
Revised September 10, 1970

Composition Equation for Block Copolymers

For binary anionic copolymers with long block-type monomer sequences, O'Driscoll has derived the following composition equation[1]

$$y = (k_A' k_{AA}/k_B' k_{BB})x^2 \tag{1}$$

where $x \equiv [A]/[B]$ is the ratio of the concentrations of the two monomers A and B in the feed mixture, and y is the ratio of the numbers of A and B units incorporated in the polymer. Here, k_{AA}, for example, is the rate constant for the addition of A to a polymer chain whose end comonomer is also A. The rate of production of the active monomer species A is assumed to be proportional to [A] with the rate constant k_A', and a similar assumption for active B is also made. In discussing some experimental data, he has also used[1] the following form of composition equation

$$y = Kx^a \tag{2}$$

where K is a constant and the value of a ranges from unity to 2.

Equation (1) is derived[1] under numerous restrictive conditions. One of the assumptions or approximations used in the derivation is neglect of the "crossover" reactions compared to homopropagation steps. Another is a stricter version of the steady state assumption which amounts to setting the ratio of the concentrations of the two active polymer species to be constant independent of time. As for eq. (2), no theoretical derivation or justification has been so far advanced for $1 < a < 2$.

In this note, we point out that the conventional binary copolymer composition equation[2,3] can give not only a composition equation for block copolymers [similar to eq. (1) in form but under more general conditions], but also a theoretical explanation of eq. (2) with $1 < a < 2$, occasionally observed for limited ranges of x.

As is well known, if chain propagation by monomer addition predominates over other steps, and if this monomer addition is influenced by the species of comonomer unit at the end of the growing chain, but not by the penultimate and previous comonomer units, we obtain[2,3]

$$y = [(1 + r_A x)/(r_B + x)]x \tag{3}$$

where the reactivity ratios r_A and r_B are defined by

$$\begin{aligned} r_A &\equiv k_{AA}/k_{AA} \\ r_B &\equiv k_{BB}/k_{BA} \end{aligned} \tag{4}$$

Equation (3) holds whether the copolymerization proceeds by a free-radical or ionic mechanism, as long as the above-mentioned conditions are met. If we denote by P_{AB} the conditional probability of finding a B as a randomly selected monomer unit in the polymer chain given that its immediate predecessor is an A, we may express the conditional possibilities by[4]

$$\begin{aligned} P_{AA} &= r_A x/(1 + r_A x) \\ P_{BA} &= x/(r_B + x) \\ P_{AB} &= 1/(1 + r_A x) \\ P_{BB} &= r_A/(r_B + x) \end{aligned} \tag{5}$$

The persistence ratio[5] ρ is given for this case by

$$\rho = (1 + r_A x)(r_B + x)/(r_B + 2x + r_A x^2) = (1 + r_A x)/(1 + y) \tag{6}$$

Now, if both r_A and r_B are very large, eq. (3) simplifies to

$$y = (r_A/r_B)x^2 = (k_{BA}k_{AA}/k_{AB}k_{BB})x^2 \tag{7}$$

for any value of x neither too large nor too small. In other words, eq. (7) holds so long as

$$1/r_A \ll x \ll r_B. \tag{8}$$

The larger the values of r_A and r_B, the wider is the range of x for which eq. (7) is valid. Although both eqs. (1) and (7) show that y is proportional to x^2, the proportionality constants of the two equations have completely different physical significance and different magnitudes (unless $k_A'/k_B' = k_{BA}/k_{AB}$ by coincidence). Also, with the range of x given by eq. (8), we have from eqs. (5) and (6)

$$\begin{gathered} P_{AB}, P_{BA} \approx 0 \\ P_{AA}, P_{BB} \approx 1 \\ \rho \rightarrow \infty \end{gathered} \tag{9}$$

which all indicate formation of very long blocks of A alternating with very long blocks of B.

If only one of the reactivity ratios is very large or small, we have four less restrictive limiting forms of the composition equation. For example, if r_A is very large, we obtain from eq. (3)

$$y = r_A x^2/(r_B + x) \qquad x \gg 1/r_A \tag{10}$$

for which eq. (5) gives

$$\begin{aligned} P_{AA} &\approx 1 \\ P_{AB} &\approx 0 \end{aligned} \tag{11}$$

indicating the tendency of comonomer A to form long blocks. We note that the data used by O'Driscoll which fit eq. (2) with $a = 1.3$ can also fit eq. (3) or eq. (10) for the given limited range of x used for the experiments. For more decisive comparison experimental data for a much wider range of x must be used. In a recent publication,[6] it is noted that the value of a in eq. (2) varies as a function of the composition range investigated in those cases where a is not exactly equal to unity or 2. This indicates the approximate nature of eq. (2) in general.

Note added in proof: If we start with the standard copolymer composition equation that takes into account of penultimate effects as well as terminal effects, we can obtain Eq. (2) with $a = 3$ and 4 in addition to $a = 0$, 1, and 2 as special cases.

References

1. K. F. O'Driscoll, *J. Polym. Sci.*, **57**, 721 (1962).
2. F. R. Mayo and F. M. Lewis, *J. Amer. Chem. Soc.*, **66**, 1594 (1944).
3. T. Alfrey and G. Goldfinger, *J. Chem. Phys.*, **12**, 205 (1944).
4. G. Goldfinger and T. Kane, *J. Polym. Sci.*, **3**, 462 (1948).
5. B. D. Coleman and T. G Fox, *J. Polym. Sci. A-2*, **1**, 3183 (1963).
6. T. Higashimura, T. Masuda, and K. F. O'Driscoll, *J. Polym. Sci. B*, **6**, 841 (1968).

Chong Wha Pyun*

Mellon Institute
Carnegie-Mellon University
Pittsburgh, Pennsylvania 15213

Received August 25, 1970

* Present address: Department of Chemistry, Lowell Technological Institute, Lowell, Mass. 01854.

The *Journal of Polymer Science* publishes results of fundamental research in all areas of high polymer chemistry and physics. The *Journal* is selective in accepting contributions on the basis of merit and originality. It is not intended as a repository for unevaluated data. Preference is given to contributions that offer new or more comprehensive concepts, interpretations, experimental approaches, and results. Part A-1 *Polymer Chemistry* is devoted to studies in general polymer chemistry and physical organic chemistry. Contributions in physics and physical chemistry appear in Part A-2 *Polymer Physics*. Contributions may be submitted as full-length papers or as "Notes." Notes are ordinarily to be considered as complete publications of limited scope.

Three copies of every manuscript are required. They may be submitted directly to the editor: For Part A-1, to C. G. Overberger, Department of Chemistry, University of Michigan, Ann Arbor, Michigan 48104; and for Part A-2, to T. G Fox, Mellon Institute, Pittsburgh, Pennsylvania 15213. Three copies of a short but comprehensive synopsis are required with every paper; no synopsis is needed for notes. Books for review may also be sent to the appropriate editor. Alternatively, manuscripts may be submitted through the Editorial Office, c/o H. Mark, Polytechnic Institute of Brooklyn, 333 Jay Street, Brooklyn, New York 11201. All other correspondence is to be addressed to Periodicals Division, Interscience Publishers, a Division of John Wiley & Sons, Inc., 605 Third Avenue, New York, New York 10016.

Detailed instructions on preparation of manuscripts are given frequently in Parts A-1 and A-2 and may also be obtained from the publisher.